

**Modeling of Combined Physical - Mechanical
Moisture Induced Damage in Asphaltic Mixes**

N. Kringos

ISBN/EAN 978-90-9021765-9

Modeling of Combined Physical-Mechanical Moisture Induced Damage in Asphaltic Mixes

Proefschrift

ter verkrijging van de graad van doctor
aan de Technische Universiteit Delft,
op gezag van de Rector Magnificus prof.dr.ir. J.T. Fokkema
voorzitter van het College voor Promoties,
in het openbaar te verdedigen op maandag 4 juni 2007 om 15:00 uur
door

Niki KRINGOS

CIVIEL INGENIEUR
Geboren te Utrecht

Dit proefschrift is goedgekeurd door de promotoren:

Prof. dr. ir. J. Blaauwendraad
Prof. A.P.S. Selvadurai, MS, PhD, DSc

Toegevoegd promotor:

Dr. A. Scarpas, BSc, MSc, PhD

Samenstelling Promotiecommissie:

Rector Magnificus, voorzitter
Prof. dr. ir. J. Blaauwendraad
Prof. A.P.S. Selvadurai, MS, PhD, DSc
Dr. A. Scarpas, BSc, MSc, PhD
Prof. A.C. Collop, BSc, MSc, PhD
Dr. J. Youtcheff, BSc, MSc, PhD
Prof. M. Zaman, BSc, MSc, PhD
Prof. dr. ir. S. van der Zwaag
Prof. A. Drescher, BSc, MSc, PhD

Technische Universiteit Delft, voorzitter
Technische Universiteit Delft, promotor
McGill University, promotor
Technische Universiteit Delft, toegevoegd promotor
University of Nottingham
US Federal Highway Administration
University of Oklahoma
Technische Universiteit Delft
University of Minnesota, reserve lid

Copyright © 2007 by N. Kringos

ISBN/EAN 978-90-9021765-9

Printed in Delft, The Netherlands

Acknowledgements

The phrase “beware of Greeks bearing gifts” is a friendly warning against trickery and deception. The phrase, of course, refers to the famous Trojan Horse in which the Greek soldiers were hiding to trick the people of Troy. You could also interpret the phrase as a warning that you can never really know what you get yourself involved in until you actually jump in.

Working toward my PhD was, in a way, quite similar to this. It started with a Greek Professor offering me to work on an interesting project (the gates of Troy opened), it developed itself into a project which turned out to offer more exciting challenges than expected (the horse was filled with soldiers), and, finally, science won me over (they burned down Troy...). Well, maybe the analogy goes somewhat rusty towards the end. The point I want to make though is, that one can never tell in advance how a research project will turn out scientifically, how its outcome will be perceived by the industry and, on a personal note, whether one will benefit from doing the doctoral research.

With regard to the scientific outcome of my research, this dissertation serves as a testimony for the work and, as such, it may be judged by the reader. Regarding the perception of the industry, in general, and ignoring the occasional unavoidable skeptics, the acceptance and support of the industry has been and continues to be overwhelming and very gratifying. As far as the personal benefit from doing the doctoral degree is concerned, in addition to personal growth and gained scientific insight, what has made the entire experience very rewarding for me was the interaction with (inter)national colleagues, the setting-up of new collaborations and the team spirit of the research group in TU Delft that I became part of.

Having defined, in a nutshell, what made the horse interesting for me, I would like to acknowledge the soldiers who came out of it, and, without whom this research project would have turned out quite differently.

First and foremost I owe enormous gratitude to Dr. Tom Scarpas, who not only offered me a wonderful opportunity to tackle a tricky research topic, but who allowed me to participate in the scientific community, made me interact with industrial representatives, helped me organize and teach in international courses and workshops, gave me visibility, provided me with a solid technical background and gave me the tools to further develop myself. Tom taught me that more can be achieved by working with a team of people, even though ‘one smart person knows more than a thousand fools’ and ‘the work will always be done by a busy person’...

Secondly, I would like to express my gratitude to my two promotors, Professor Johan Blaauwendraad from TU Delft and Professor Patrick Selvadurai from McGill University, Canada. Professor Blaauwendraad has helped me by always asking the difficult questions and forcing me to stay on track with my work. Patrick has been an enormous help in defining the physical phenomena and setting-up relevant benchmarks. The time I spent with him in McGill University working on my research was very valuable and I feel honored to have him as a co-promotor.

I owe a lot of gratitude to the ‘Scarpas -alias CAPA-3D- group’, which consists of ir. Cor Kasbergen, Dr. Xueyan Liu and ir. Yani Sutjiadi. Collectively, they create a

pleasant working environment and present a strong body of knowledge. Individually, I owe gratitude to Cor for putting up with me –full stop–. Cor has contributed tremendously to my finite element programming and was a key-figure in coupling RoAM with CAPA-3D. I owe gratitude to Xueyan for helping me figure out the necessary balance laws and for criticizing my equations. Yani has been a tremendous help in more things than I can mention, I acknowledge her most for her willingness to help all of us in all aspects of our research and chase us when we tend to miss our deadlines.

This project would have not been possible without the generous financial support of Ooms Nederland holding. I owe Dr. Arian de Bondt, Head of the Ooms Research and Development Department, gratitude for this. I cannot emphasize enough how important I feel it is that industry get involved into fundamental research. This does not mean that the industry should dictate the research done at universities, but that the industry should see the benefit of investing in long-term developments which will, eventually, lead to improved products and technology. Dr. de Bondt believed in our research approach from the very beginning and for this I thank him.

Our research has been very well received, both nationally and internationally, which led to several fruitful collaborations, among which the most important ones were with: the Turner Fairbank Highway Research Center of the US Federal Highway Administration, for which I owe gratitude to Dr. Jack Youtcheff and Audrey Copeland, the Nottingham Transportation Engineering Centre, for which I owe gratitude to Prof. Steve Brown and Prof. Andrew Collop and the Oklahoma Transportation Centre, for which I thank Prof. Musharraf Zaman. Furthermore, I owe gratitude to the Association of Asphalt Paving Technologists for acknowledging my research by awarding it with a very generous award. In addition to these, I also owe gratitude to the Dutch Ministry of Public Works, who has been very supportive of our research and who continues to support us in our efforts, for this I thank Dr. Sandra Erkens and Dr. Fons van Reisen.

Finally, I thank my parents and my sister Dionne Sofia for never letting me forget that, even when computer programs don't converge or deadlines are missed, life still goes on. Just like the Trojan Horse brought the end of the 10 year old Trojan war, this dissertation is the end of my 4 years quest towards a PhD degree, which has groomed me, hopefully, for a long and exciting career in science.

Niki Kringos
May 2007, Delft

	<i>page</i>
Chapter 1 Introduction	
1.1 Moisture damage in practice	1
1.2 Aim of this research	4
1.3 Content overview	5
Chapter 2 Identification of Processes	
2.1 Moisture infiltration into an asphaltic mix	7
2.2 Weakening of the mastic-aggregate bond	8
2.3 Weakening of the asphaltic mastic	11
2.4 Pumping action due to traffic loading	12
2.5 New approach towards moisture induced damage	13
Chapter 3 Simulation of the Physical Processes Inducing Moisture Damage in Asphaltic Mixes	
3.1 Introduction	15
3.2 Moisture flow into an asphalt mix	15
3.2.1 Generic mass balance equation	15
3.2.2 Moisture mass balance in an asphaltic mix	17
3.2.3 Moisture diffusion	21
3.3 Moisture induced damage of the mastic film	23
3.4 Conclusions	26

Chapter 4 Numerical Formulations of Physical Moisture Damage Inducing Processes

4.1 Introduction	27
4.2 Numerical approximation of the flow equation	27
4.2.1 Galerkin finite element formulation	27
4.2.2 Numerical integration	30
4.2.3 In time approximation	35
4.3 Numerical approximation of the mastic transport equation	38
4.3.1 Introduction	38
4.3.2 Hybrid Lagrangian-Eulerian approximation	39
4.3.3 Particle tracking method	42
4.3.4 Galerkin formulation of the governing equation	43
4.3.5 In time approximation	47
<i>Appendix 4.1 Weak formulation</i>	<i>51</i>
<i>Appendix 4.2 Time approximation methods</i>	<i>53</i>
<i>Appendix 4.3 Arbitrary Eulerian Lagrangian descriptions</i>	<i>57</i>

Chapter 5 Comparison to closed form solutions

5.1 Introduction	63
5.2 Diffusion equation	63
5.3 Advective transport	67

Chapter 6 Material Parameter Determination

6.1 Introduction	73
6.2 Work of adhesion measurements	74
6.3 Moisture diffusion coefficients measurements	76
6.3.1 Moisture sorption principle	76
6.3.2 Adsorption of moisture on the outside of the film	79
6.3.3 Experimental procedure	81
6.3.4 Determination of mastic diffusion coefficients	83
6.4 Mastic desorption measurement	95
<i>Appendix 6.1 Experimental determination of Work of Adhesion</i>	<i>97</i>

Chapter 7 Elasto-Visco Plastic Constitutive Model for Mastic

7.1 Introduction	101
7.2 Mastic constitutive model	102
7.2.1 Elast-visco-plastic material response	102
7.2.2 Multiplicative decompositions	103
7.2.3 Local dissipation model	105
7.2.4 Elasto-plastic component	106
7.2.5 Elasto-plastic stress reduction procedure	110
7.2.5.1 Elasto-plastic Trial elastic state	110
7.2.5.2 Elasto-plastic Flow rule discretization	111
7.2.5.3 Elasto-plastic Return mapping procedure	112
7.2.6 Visco-elastic component	114
7.2.7 Visco-elastic stress reduction procedure	116
7.2.7.1 Visco-elastic Trial elastic state	116
7.2.7.2 Visco-elastic Flow rule discretization	117
7.2.7.3 Visco-elastic Return mapping procedure	117
7.3 Parameter determination	120
7.3.1 Procedure	120
7.3.2 Creep recovery example	125
<i>Appendix 7.1: Derivations for the yield response</i>	<i>129</i>
<i>Appendix 7.2: Yield surface</i>	<i>139</i>

Chapter 8 Effect of moisture on the aggregate-mastic bond

8.1 Introduction	149
8.2 Methodology	149
8.3 Experimental results	152
8.3.1 Sample preparation	152
8.3.2 Direct tension results	152
8.3.3 RoAM moisture infiltration simulation results	153
8.3.4 Mastic-aggregate bond strength degradation	154
8.4 Conclusions	157

Chapter 9	Combined physical-mechanical moisture induced damage finite element model	
9.1	Introduction	159
9.2	Physical moisture induced damage parameters	160
9.3	Mechanical moisture induced damage	161
9.4	Coupling of RoAM with CAPA-3D	163
9.5	Combined physical and mechanical moisture induced damage constitutive model	164
9.5.1	Introduction	164
9.5.2	Elasto-plastic component	165
9.5.3	Visco-elastic component	167
9.5.4	Stress reduction procedure	170
9.6	Numerical parametric study of moisture induced damage	171
9.6.1	Introduction	171
9.6.2	Mastic thickness versus aggregate-mastic bond strength degradation	172
9.6.3	Combined physically-mechanically generated damage on a micro-scale asphalt mix	178
9.6.3.1	Introduction	178
9.6.3.2	Mechanical loading conditions	180
9.6.3.3	Parametric simulation scheme	182
9.6.3.4	Material properties	183
9.6.3.5	Moisture induced damage simulations	184
Chapter 10	Conclusions and recommendations	221
	References	225
	Summary	233
	Samenvatting	235
	Curriculum Vitae	237

1.1 Moisture damage in practice

Practice and many studies have shown that asphalt wearing surfaces which are exposed to moisture generally start losing aggregates prematurely through a damage phenomenon that has become known as asphalt ‘stripping’ or ‘ravelling’ [Davidson 1993], [Curtis 1991, 1993], [Fromm 1979], [Graf 1986], [Hicks 1991], [Ishai 1972], [Kanitpong 2003], [Khandhal 1992, 1994, 2001a], [Lytton 2002], [Majidzadeh 1968], [McGennis 1984], [Riedel 1953], [Scholz 1993], [Scott 1978] [Stuart 1990], [Takallou 1984], [Taylor 1983], [White 1987]. Stripping is generally contributed to moisture infiltration into the asphalt, causing a weakening of the bituminous binder that holds the aggregates together, known as the asphalt mastic, and a weakening of the aggregate-mastic bond. Due to the continuing action of moisture and traffic load, progressive dislodgement of the aggregates can occur. This initial stripping rapidly progresses into a more severe degradation of the wearing surface, and ultimately leads to pothole formation, Fig. 1.1.1.



Fig. 1.1.1: Moisture induced damage in asphalt (a) raveling (b) potholing

In countries that suffer from large amounts of rainfall, like the Netherlands, the asphalt wearing surfaces are often constructed of open graded asphaltic mixes. The high permeability of these wearing surfaces ensures a fast drainage of the water away from the surface, avoiding hydroplaning and bad visibility conditions due to ‘splash and spray’, Fig. 1.1.2, and thus improving the overall road safety. An added benefit of these mixes turned out to be the ability to not only absorb moisture, but also to absorb a part of the traffic noise that is generated upon wheel-pavement contact, creating so-called ‘silent asphalts’. Therefore, open graded asphaltic mixes seem an ideal solution for a densely populated country, where many living communities are at close proximity to the major highways and where, with a growing twenty four hour economy, road safety and pleasant driving conditions are necessary boundary conditions.

In the Netherlands these mixes are referred to as Zeer Open Asphalt Beton, or with its acronym ZOAB, and in the US as open graded friction courses. Unfortunately, because of the open structure of these mixes, moisture resides more or less permanently within the mix. As a result, ravelling occurs far too early in their service life and progresses much faster than in other mixes [Kandhal 2001b], [Smith 1992], [Erkens 2005]. Currently, in order to keep these mixes at an acceptable quality standard, a lot of extra maintenance is required, which makes them quite expensive.



Fig. 1.1.2: (a) Bad road visibility conditions and (b) ‘splash and spray’ [Erkens 2005]

Currently, pavement engineers try to prevent moisture induced damage to the pavement by selecting asphaltic mixes that perform well in the prescribed moisture sensitivity tests, by adding anti-stripping agents to the mix and by maximizing the quality control at all stages from hot mix processing to the finished compacted asphalt mix and by designing a proper pavement drainage system.

The *quality control* issue is of great importance in the pavement industry to avoid a difference between the designed asphalt mix composition with the material characteristics as determined in the asphalt laboratory, and the asphalt mix which is actually constructed on the road. For instance, with regard to moisture induced damage, it may occur that the asphalt mix components are exposed to moisture, even before construction, Fig. 1.1.3 [Cheng 2003], [Fwa 1994], [Huber 2005], [Rice 1958]. Since most aggregates and asphalt binders do absorb moisture when exposed to a wet environment, a binder with a significantly changed stiffness characteristics and an initially damaged mix would end up on the pavement, Fig. 1.1.4.



Fig. 1.1.3: Wet asphalt mix components before construction [Huber 2005]

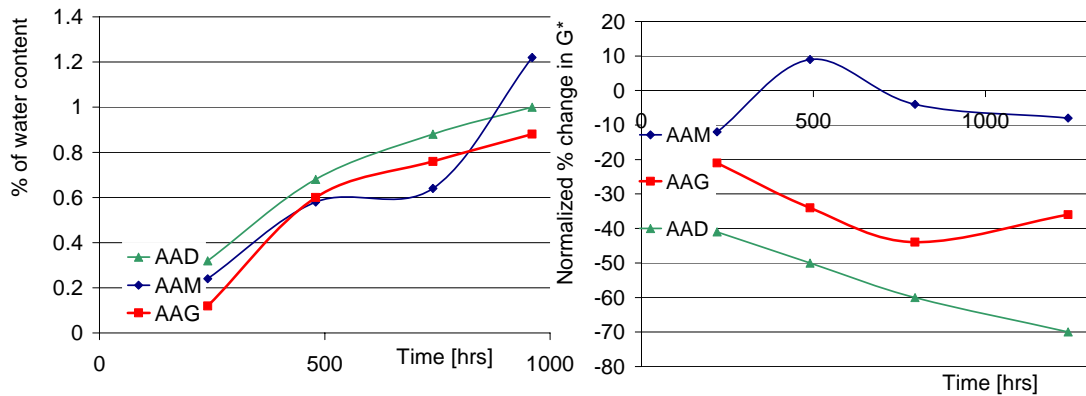


Fig. 1.1.4: Moisture infiltration in bitumen [Huber 2005]
 (a) moisture absorption in three SHRP binders
 (b) binder stiffness change due to moisture infiltration

To evaluate the moisture sensitivity of an asphaltic mix a-priori, several moisture sensitivity experiments are used. Most of these experiments resulted from a major research effort in the later 1970s and during the 1980s under the National Cooperative Highway Program of USA [Epps 2000]. In the mid 1980s the US Congress funded a Strategic Highway Research Program for the amount of 150 million US\$ [Harman 2006] to undertake asphalt binder research, among which improved performance-related testing to evaluate moisture susceptibility. In these efforts, evaluation of moisture induced damage in asphaltic mixes is generally approached from a mechanical point of view, where evaluation of the moisture susceptibility of an asphalt mix most often is evaluated using a mechanical test, performed on dry and wet specimens, e.g. [Airey 2002], [Kennedy 1991], [Khosla 2000], [Lottman 1974], [Terrel 1994].

Such moisture damage evaluation methods produce a set of moisture index ratios, Fig. 1.1.5. The unfortunate realization is that, even though they seem to constitute a quick and simple way of comparing the moisture susceptibility of mixes, they are highly subject to the specific test boundary conditions, they do not give any fundamental insight into the causes and evolution of the damage in time within the mix, nor can they be used for mix improvements. Given the fact that asphalt is a composite material which, for every different aggregate type, every different bitumen source, every different mastic composition, every different mix compaction etc., leads to basically a completely different material with changed characteristics, it would take an isolation of each characteristic to get any information regarding the controlling parameters, which is practically impossible in such a test.

In addition to this, often, anti-stripping additives, such as hydrated lime and surfactants, are added in the asphalt mix to improve the bond between the asphalt binder and the aggregates, e.g. [Anderson 1982], [Coplantz 1987], [Kennedy 2001], [Lottman 1990], [Maupin 1983], [Tunncliffe 1997]. However, the long-term effect of such additives is not always well understood, nor do they provide a general solution to the problem of moisture induced damage over a range of materials and construction practices.

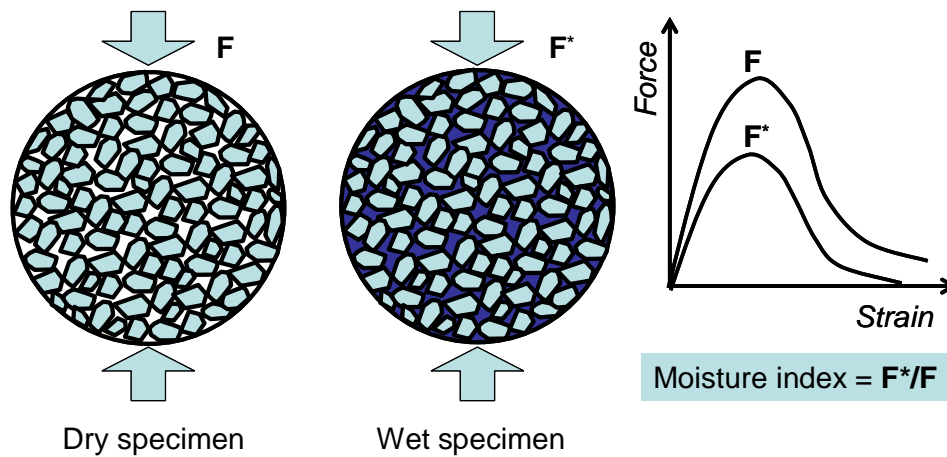


Fig. 1.1.5: Traditional moisture damage evaluation method

1.2 Aim of this research

As illustrated in the above, moisture induced damage in asphaltic mixes is recognized by the asphalt community and the road authorities as a major issue, in particular in open graded asphalts, resulting to the need for frequent maintenance operations. This does not only imply high maintenance costs, but also temporary closure of traffic and hence increased road congestion. Given the high costs for the road authorities and the inconvenience for the road users, it is greatly desired to shift the solution from a repair philosophy to a prevention one.

Prevention of a problem inherently implies *knowledge* of the causes of the problem. Currently, mix designers have no a-priori knowledge of the engineering properties of the mix at the time of purchase of the mix components. They purchase a particular type of bitumen from one supplier and a particular aggregate from another, both based on individual specifications, without actual knowledge if these components will interact favourably with each other.

Given the awareness of the problem of moisture induced damage in asphaltic mixes and the lack of quantified fundamental knowledge of its causes and solutions, this thesis is aiming at developing a more fundamental approach towards the identification and quantification of the moisture induced damage processes and their mechanical manifestations. The important *starting-point* of this thesis is that the problem of moisture induced damage in asphalt can not be solved by mechanical considerations alone. Clearly, our current asphalt wearing surfaces show that moisture has an effect on the material characteristics of the asphalt components and their bond. This implies that moisture makes a physical change to the material, which exhibits itself in the early development of damage patterns which, without the moisture, may have not occurred or may have occurred in a much later stage of its service life.

Therefore, in this research, both *physical and mechanical moisture damage* inducing processes are taken into consideration. Furthermore, in order to acquire fundamental insight into the processes which cause moisture damage, the asphalt mix is considered on a micro-scale. This implies that the experimental characterization and the computational simulations of the moisture damage inducing processes are dealt with at mix component level; i.e. the aggregates, the mastic, the bond between the

aggregates and the mastic and the (macro) pore space. Each of these contribute to the mechanical performance of the mix as well as to its moisture susceptibility.

The aim of this research is therefore the *development of a computational tool for the fundamental analysis of combined mechanical and moisture induced damage of asphaltic mixes which includes both physical and mechanical moisture damage inducing processes*. Such a tool can greatly contribute to an improved material selection procedure and give insight into the various competing damage inducing processes within the asphalt mix. To achieve this aim, the physical and mechanical moisture induced damage processes are identified, the controlling parameters are determined, an experimental framework to quantify these parameters is set-up and the numerical tools are developed and are demonstrated in this dissertation. In the following a short overview is given of the structure of the text.

1.3 Content overview

In the following chapter a detailed description is given of the moisture damage inducing processes in asphalt, where a separation is made between physical and mechanical processes.

Chapter 3 of this dissertation treats the physical moisture damage inducing processes by deriving the governing equation of the processes, Chapter 4 shows their numerical formulation, Chapter 5 compares simulations of the physical processes with closed form solutions and Chapter 6 describes an experimental plan to determine the necessary model parameters.

In Chapter 7 the mechanical constitutive finite element model for the asphalt components are given and Chapter 8 describes a new methodology to determine the aggregate-mastic bond strength as a function of moisture content.

Finally, Chapter 9 develops the combined physical-mechanical moisture induced model and shows micro-scale simulations and Chapter 10 gives the conclusions and recommendations of this research.

Identification of Processes

2.1 Moisture infiltration into an asphaltic mix

Moisture induced damage in asphaltic mixes is obviously only an issue if the moisture is initially able to penetrate into the mix. For the identification and simulation of the moisture damage inducing processes in asphaltic mixes, it is therefore important to identify the various moisture infiltration modes.

First of all, water may enter the mix due to rainfall, which may cause water flow through the connected macro-pores of the asphalt wearing surface, Fig. 2.1.1(a). This is especially the case for open graded mixes that are designed to have a high permeability such as the Dutch ZOAB mixes. Secondly, stationary moisture may reside in the macro-pores of the mix, either in liquid or vapour form, Fig. 2.1.1(b). This can, for instance, be caused by residual moisture after rainfall, a wet subgrade under the wearing surface or a humid environment. Finally, as is mentioned in the previous chapter, moisture may be present inside the aggregates even before construction of the wearing surface, due to inadequate drying procedures of the aggregates Fig. 2.1.1(c). [Stuart 1990], [Huber 2005], [Fwa 1994], [Rice 1958]

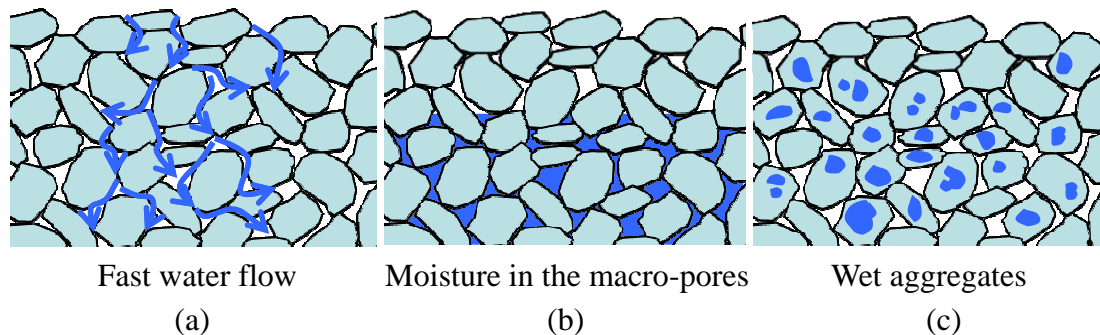


Fig. 2.1.1: Moisture penetration into the asphalt mix

In addition to rainfall, fast water flow through the connected macro-pores of the asphalt mix may also result locally from a saturated wearing surface, when subjected to traffic loading. This phenomenon is often referred to as ‘pumping action’ [Kandhal 1992, 1994], [Kiggundu 1988], [Taylor 1983] and shall be discussed in more detail further on in this chapter.

From the above possible modes for moisture infiltration into an asphaltic mix, some are more relevant for open graded asphaltic mixes and others are more relevant for densely graded ones. Regardless of the mix composition, asphaltic mixes with moisture will suffer in due time from moisture induced damage. In practice, this damage exhibits itself as a dislodging process of the aggregates, a process which has become known as *ravelling* or *stripping* of the asphaltic mix [Lytton 2002]. The dislodging of aggregates from an asphalt wearing surface may show either a

pronounced *cohesive* (i.e. within the mastic) or a pronounced *adhesive* (i.e. within the aggregate-mastic bond) failure pattern, or a combination thereof, Fig. 2.1.2.

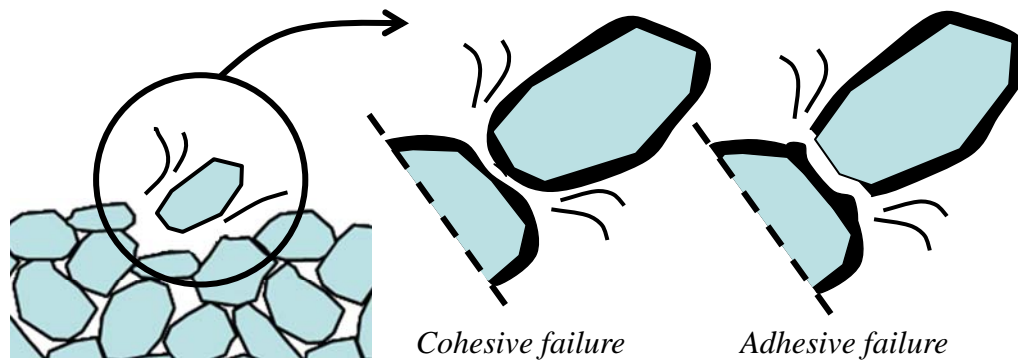


Fig. 2.1.2: Cohesive versus adhesive dislodging of an aggregate from the mix

Once the wearing surface starts to degrade, progressive physical moisture induced damage, in combination with traffic loading, may lead to even more severe forms of moisture induced damage, like pothole forming. The ravelling or stripping of an asphaltic wearing surface is a failure pattern which is undoubtedly related to a combined action of mechanical damage and moisture infiltration, where, weakening of the mastic film will promote a cohesive failure pattern and weakening of the aggregate-mastic bond will promote a pronounced adhesive failure pattern.

In the following, the processes which results into the weakening of the asphalt components are identified.

2.2 Weakening of the aggregate-mastic bond

The properties of the aggregate-mastic bond play a crucial role in the performance of asphaltic mixes. The reason that asphalt mixes do not qualify as 'unbound granular materials' is the presence of the mastic component, which serves as the binding 'glue' that holds the aggregate matrix together under loading. Essential in this is the *adhesion* of the mastic to the surface of the aggregates. An asphaltic mix which consists of a mastic-aggregate combination which has 'bad adhesion' will have bad mechanical performance and will show undoubtedly a pronounced adhesive failure pattern.

It is known that mastic-aggregate adhesion improves with an increased aggregate surface roughness, Fig. 2.2.1(a). Clearly, more surface area to adhere to will create a better bond, since the transferred loads will be spread over a larger area. Since mastic is mixed with the aggregates while it is in liquid form, an increased aggregate surface roughness will maximize the mechanical interlock between the mastic and the aggregates, due to the ability of mastic to flow into the surface pores of the aggregates while in liquid form, and thus creating mastic 'fingers' inside of the aggregate surface when it solidifies, Fig. 2.2.1(b). Such mastic fingers greatly improve the strength of the mastic-aggregate bond, since it requires additional forces to 'unlock' them from the aggregate. However, the interlocking phenomenon rely on the ability of the mastic to come into close contact to the aggregate surface. An asphalt mix which has a mastic component which is not able to spread properly on the aggregate surface, will not benefit from the increased adhesive bond, as described above, since it will not be able to fill some of the surface pores Fig. 2.2.1(c). The 'spreading capacity' of mastic on an

aggregate surface is often referred to as the ‘wetting’ capacity of the mastic, and can be related to the surface energy properties of the components.

Adhesion is often categorised as thermodynamic, chemical or mechanical adhesion. *Thermodynamic adhesion* refers to equilibrium of interfacial forces or energies, work of adhesion and wetting, *chemical adhesion* refers to adhesion involving chemical bonding at the interface and *mechanical adhesion* arises from the mechanical interlocking over substantial portions of the interface. Despite the various definitions for adhesion, none seem to be completely satisfactory or generally accepted. However, a satisfactory definition for the adhesion of a mastic film on an aggregate surface should somehow account for the thermodynamical as well as the physio-chemical and mechanical aspects of adhesion. Nevertheless, the physio-chemical phenomena which contribute to the adhesion of two materials will, and should, manifest themselves into the mechanical bond properties, which are measurable. The behaviour of the mastic-aggregate interface can therefore be modelled, based on thermodynamically sound relationships in which the physio-chemistry is controlled by internal state variables.

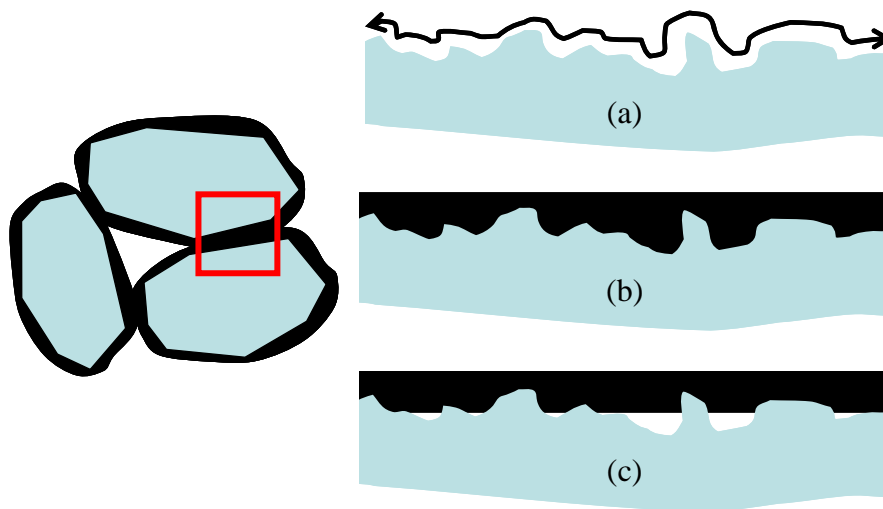


Fig. 2.2.1: Mastic-aggregate interface surface characteristics
 (a) rough aggregate surface (b) good mastic wetting (c) bad mastic wetting

In the previous section, several moisture infiltration modes were discussed. However, having moisture in either a stationary or a moving fashion inside of the macro-pores of the asphalt mix, does not explain directly the weakening of the aggregate-mastic bond. Clearly, for the interface to be weakened, moisture must first be able to reach it. Disregarding, for the time being, the possibility of moisture being present in the aggregate itself, and assuming a continuous mastic film without any cracks, moisture can only reach the aggregate-mastic interface by moving through the mastic film. Since mastic has a negligible porosity, the only physical process which explains moisture infiltration into the mastic is molecular diffusion [Cheng 2002, 2003], [Thunqvist 2001], [Masad 2005].

In Fig. 2.2.2 a schematic is given of an aggregate, coated in mastic film, which is exposed to a stationary moisture field. Initially, the mastic is exposed to moisture at the moisture-aggregate interface and the mastic film and the aggregate-mastic interface have zero moisture content. Then, moisture shall gradually start infiltrating through the mastic film, because of the moisture concentration gradient difference

inside the mastic. Depending on the moisture diffusion coefficients of the mastic and on the thickness of the mastic film, moisture will eventually reach the aggregate-mastic interface. Common sense indicates that one molecule of moisture reaching the interface, will not cause an abrupt debonding effect. As moisture diffusion through the mastic film continues and the moisture concentration gradient diminishes, a significant amount of moisture will reach the aggregate-mastic interface and shall cause progressive debonding of the mastic from the aggregate, Fig. 2.2.3. An asphaltic mix with poor moisture diffusion characteristics of the mastic and an aggregate-mastic bond which is sensitive to moisture, shall eventually exhibit a predominantly adhesive failure pattern, when exposed to moisture for long periods.

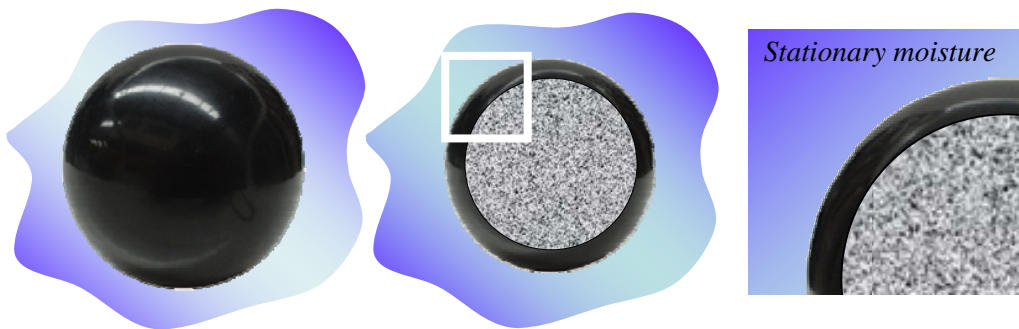


Fig. 2.2.2: A coated aggregate exposed to a stationary moisture field

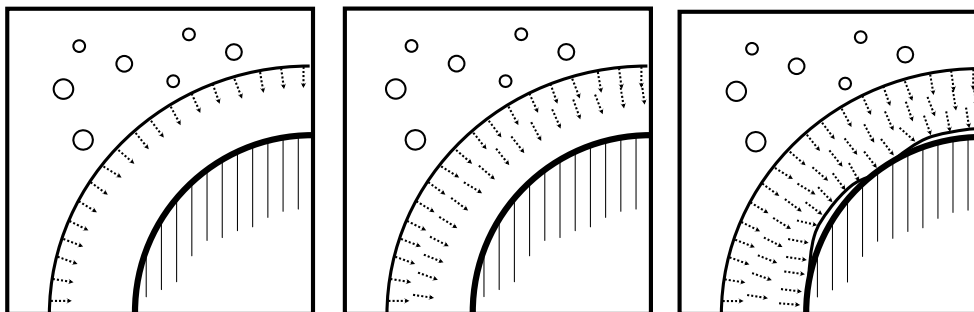


Fig. 2.2.3: Damage of the mastic-aggregate bond due to moisture infiltration

2.3 Weakening of the asphaltic mastic

As discussed in section 2.1, asphaltic mixes with an open graded structure are often designed to serve as a drainage system of the pavement. This means that, at wet periods, water flows through the connecting macro-pores of the mix. Fig. 2.3.1.

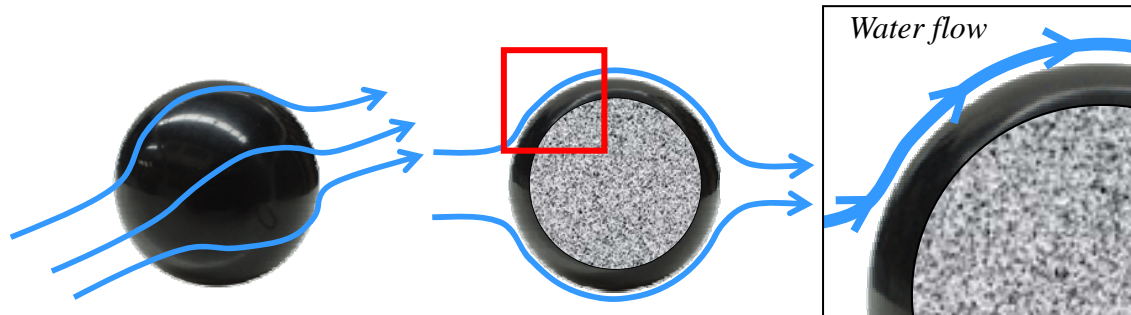


Fig. 2.3.1: A coated aggregate exposed to a water flow field

Depending on the mastic desorption characteristics, the ongoing action of water flowing past the mastic film may have a ‘scraping’ effect on the films and cause mastic particles to be removed. This is a physical moisture induced damage process that continues in the presence of a fast water flow, and which depends on the desorption characteristics of the mastic.

The loss of mastic particles as a consequence of a fast water flow is referred to as ‘washing away’ of the mastic, Fig. 2.3.2.

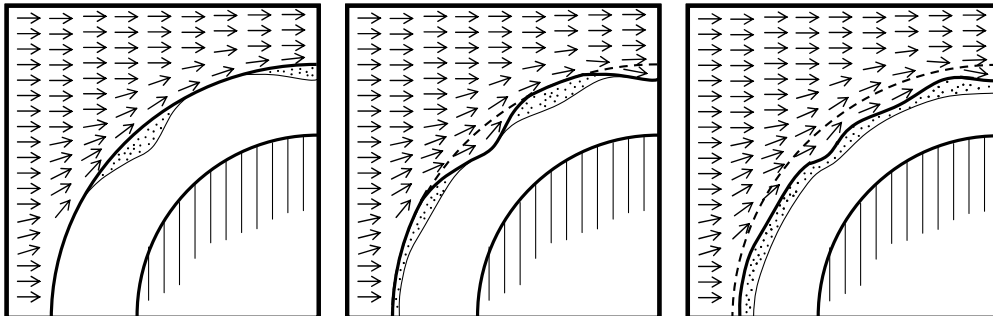


Fig. 2.3.2: Loss of mastic concentration due to a water flow field

As described in the previous section, moisture can infiltrate into the mastic film via molecular diffusion. The building-up of moisture content inside of the mastic, may locally cause a weakening of the mastic itself and can actually assist the washing away effect by increasing the desorption characteristics of the mastic, causing an even greater loss of mastic concentration, Fig. 2.3.3.

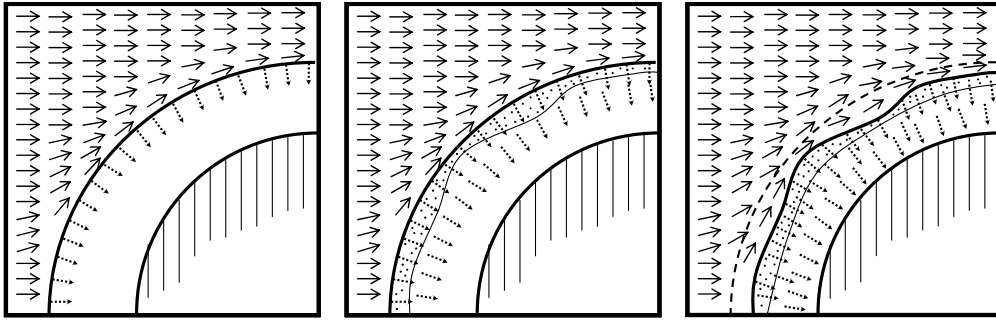


Fig. 2.3.3: Increased loss of mastic due to weakening of the mastic, caused by moisture diffusion

In practice, the loss of concentration of mastic means that the asphalt mix is slowly losing the flexibility of its binding component and, as such, is becoming weaker and more prone to a cohesive failure pattern, Fig. 2.1.2(b).

In addition to this, thinner mastic films and/or more porous mastic films will promote the movement of moisture towards the aggregate-mastic interface, and therefore contribute also to the loss of the aggregate-mastic bond.

The ‘washing away’ effect shall also be referred to from here on as *advective transport* of the mastic, since this is the approach which is used in this research for its simulation.

2.4 Pumping action due to traffic loading

Another process which is identified in this research as a contributor to moisture induced damage is due to the combination of a wet asphaltic mix, exposed to traffic loading. When some of the macro-pores in an asphaltic pavement are saturated, the fast traffic load will locally cause intense water pressure fields in these pores. These excess pore pressures shall even be generated away from the actual wheel path, since the water has no time to redistribute itself within the mix, Fig. 2.4.1. These pore pressures contribute extra stresses within the asphaltic mix, which may cause added mechanical damage within the asphalt components. [Kandhal 1992, 1994], [Kiggundu 1988], [Taylor 1983]

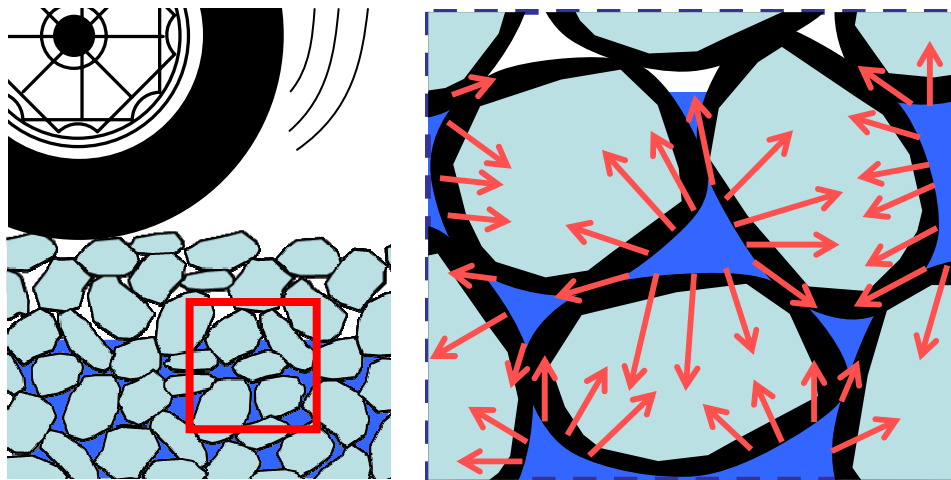


Fig. 2.4.1: Pumping action on a pavement

In contrast to the previously described processes, pumping action is categorized in this research as a *mechanical* moisture induced damage process, since it is directly related to the application of loading to the asphaltic mix. However, this process does have implications for the physical moisture induced damage processes. For example, the intense pore pressures will locally create a fast water flow field which contributes to the washing away of the mastic particles which, in turn, affects the diffusivity characteristics of the mastic. Obviously, mechanical damage of the material, which would also occur under dry circumstances is also included in the model and is discussed in Chapter 7.

2.5 New approach towards moisture induced damage

Clearly, all the above described processes are in reality coupled, and it is their combined effect which results into the eventual moisture damage pattern that the asphalt wearing surface shall exhibit.

In summary, in this research, moisture induced damage processes are divided into physical and mechanical processes:

The *physical* processes that are included as important contributors to moisture induced damage are molecular diffusion of moisture and a ‘washing away’ process of the mastic, named from here on advective transport, due to a fast water flow field. Fig. 2.5.1(a).

The *mechanical* damage process that is identified as a contributor to moisture damage is the occurrence of intense water pressure fields inside the mix caused by traffic loads and referred to as ‘*pumping action*’.

In this research, these physical material degradation processes interact with a model for the mechanical damage to produce the overall moisture-mechanical damage in the mix, Fig. 2.5.1(b).

Eventually, moisture induced damage will follow from the combined effect of the physical and mechanical moisture damage inducing processes, which result into a weakening of the mastic and a weakening of the aggregate mastic bond, Fig. 2.5.1(c).

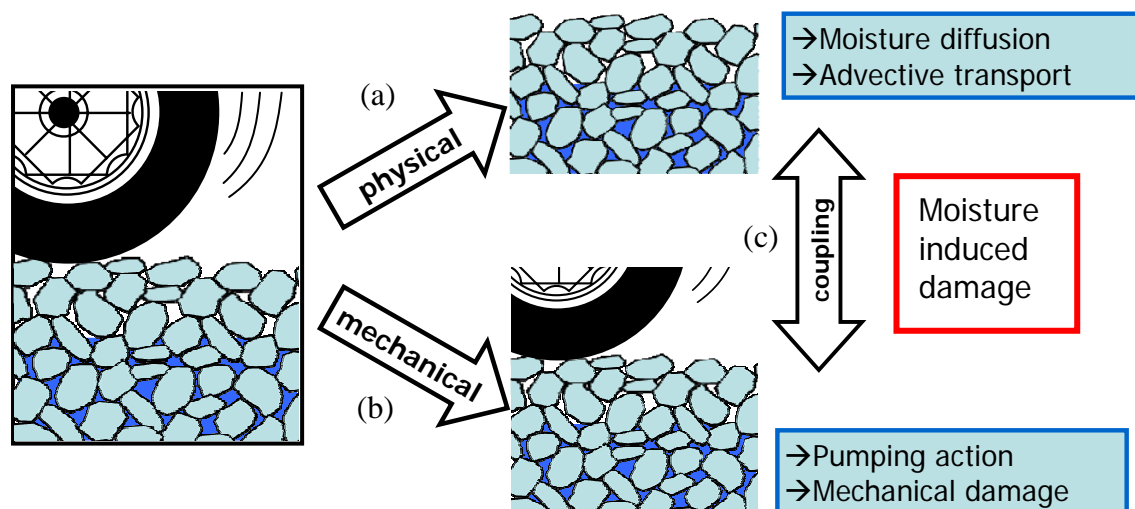


Fig. 2.5.1: Schematic of the new approach towards moisture induced damage

The above described processes are implemented in a new finite element tool, named RoAM (Raveling of Asphaltic Mixes), which was developed in this research as a sub-system of the finite element system CAPA-3D. The formulations and numerical implementation of the physical moisture induced damage processes, Fig. 2.5.1(a), are derived in Chapter 3 and 4 of this dissertation, the mechanical moisture induced damage processes, Fig. 2.5.1(b), and related issues are discussed in Chapter 7 of the text. In Chapter 8 and 9 of this dissertation the formulations of the coupling between the physical and the mechanical moisture induced damage processes and several simulations with the developed tool are shown.

Simulation of the Physical Processes Inducing Moisture Damage in Asphaltic Mixes

3.1 Introduction

This dissertation aims at the development of a computational finite element tool for the fundamental analysis of moisture induced damage of asphaltic mixes, in which the physical and mechanical moisture induced damage processes, as described in the previous chapter, are included. This new tool is named RoAM (Raveling of Asphaltic Mixes), and is developed in this research as a sub-system of the finite element system CAPA-3D. [Scarpas 2000].

In this research, the asphaltic mix is considered on a micro-scale. This implies that the experimental characterization and the computational simulations of the moisture damage inducing processes are dealt with at mix component level; i.e. the aggregates, the mastic, the aggregates-mastic interface and the macro-pores. Each of these components has its own permeability, porosity and hydraulic conductivity characteristics, whereby the macro-pores in the mix are modeled by assigning substantially higher values for each of these characteristics. The macro-permeability of the asphalt mix would therefore result from the arrangements of the components within the finite element mesh. From here on, when in the text reference is made to the various material characteristics of the components, unless stated otherwise, the micro-scale characteristics are intended.

In this chapter, the formulations that are needed for the simulation of the physical moisture induced damage processes are derived and the terminology used in later chapters is established.

3.2 Moisture flow in an asphalt mix

3.2.1 Generic Mass Balance Equation

The mass balance equation of water flowing through a differential volume can be established by considering a fluid flow with velocity field \underline{v} given by

$$\underline{v} = u\mathbf{e}_1 + v\mathbf{e}_2 + w\mathbf{e}_3 \quad (3.1)$$

Consider the rate of fluid mass out of a differential volume $dx_1dx_2dx_3 = d\Omega$, Fig. 3.2.1.

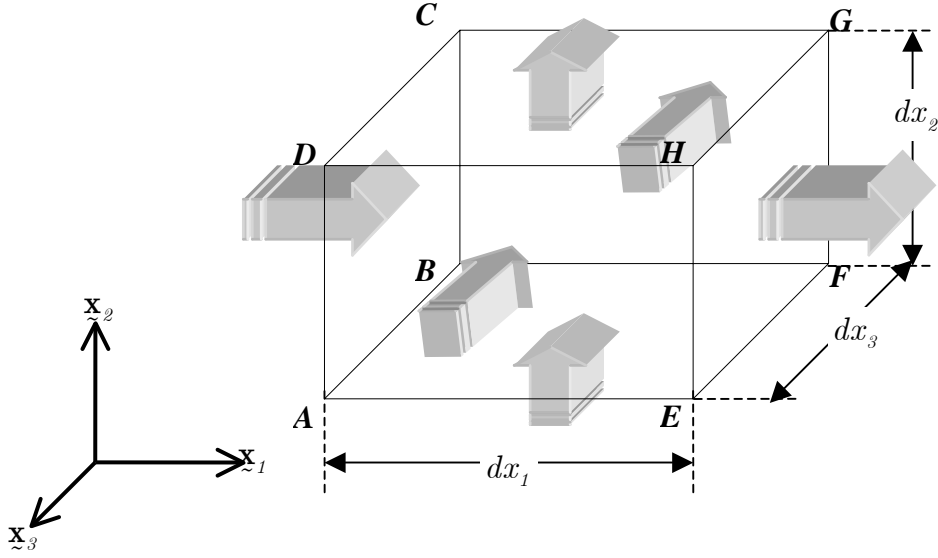


Fig. 3.2.1: Fluid flow through a differential volume

The fluid mass that flows in through the face $ABCD$ during time interval dt is

$$F_{in}^{ABCD} = \rho u dx_2 dx_3 dt \quad (3.2)$$

in which ρ is the density of the fluid. The fluid mass that flows out of the face $EFGH$ during time dt is

$$F_{out}^{EFGH} = \left(\rho u + \frac{\partial}{\partial x_1} (\rho u) dx_1 \right) dx_2 dx_3 dt \quad (3.3)$$

Similar expression can be obtained for mass flow in and out of the other faces. The net mass that passes through the differential volume $d\Omega$ during dt is

$$F_{net}^{dV} = F_{out}^{dV} - F_{in}^{dV} = \left[\frac{\partial}{\partial x_1} (\rho u) + \frac{\partial}{\partial x_2} (\rho v) + \frac{\partial}{\partial x_3} (\rho w) \right] d\Omega dt \quad (3.4)$$

which can be rewritten as

$$F_{net}^{dV} = \text{div}(\rho \mathbf{v}) d\Omega dt \quad (3.5)$$

The increase in fluid mass during dt is

$$F_{increase}^{dV} = \frac{\partial \rho}{\partial t} d\Omega dt \quad (3.6)$$

Hence the mass balance equation for a fluid in the spatial description can be found to be

$$F_{increase}^{dV} + F_{net}^{dV} = \left[\frac{\partial \rho}{\partial t} + \text{div}(\rho \mathbf{v}) \right] d\Omega dt = 0 \quad (3.7)$$

or

$$\frac{\partial \rho}{\partial t} + \text{div}(\rho \mathbf{v}) = 0 \quad (3.8)$$

The same philosophy of water mass conservation can be applied for an asphaltic mix, whereby the mix is considered as a non-homogeneous composite material, as discussed earlier.

The movement of moisture in an asphaltic mix is, however, not solely due to a potential gradient driven flow, as discussed in the above. Moisture can also move, through the asphalt component via a molecular diffusion process. Moisture diffusion is considered to be a microscopic process, which is driven by a moisture concentration gradient and the molecular diffusion characteristics of the host material, for instance the mastic.

Here, the approximation is made that the existence of a relatively slow moisture diffusion flux through the components of the mix will not influence the fast water flow through the mix, since the time-scales differ greatly. The governing equations for the simulation of the water flow are discussed in the following section and the governing equation of moisture diffusion will be discussed in section 3.2.3.

3.2.2 Moisture Mass Balance in an Asphaltic Mix

Consider a volume v of an asphaltic mix. The mass of the water m present in this volume is

$$m = \int_v \phi S \rho_w \, dv \quad (3.9)$$

where ρ_w is the water density, ϕ is the effective porosity of the component under consideration

$$\phi = \frac{V_{\text{pores}}}{V_{\text{total}}} \quad (3.10)$$

and S is the degree of saturation in the component under consideration

$$S = \frac{V_{\text{water}}}{V_{\text{pores}}} \quad (3.11)$$

As shown in the previous section, the change of water mass that can take place as a result of net fluid flow out of the volume v across the boundary surface $\partial\Omega$ is described by the net transport of mass flux

$$F_a = \int_{\partial\Omega} \rho_w \mathbf{v} \cdot \mathbf{n} \, ds \quad (3.12)$$

where \mathbf{v} is the water flow velocity and \mathbf{n} is the outward unit normal to $\partial\Omega$.

If the water mass is conserved (i.e. neglecting chemical reactions or phase changes), the rate of change in fluid mass in the region is equal to the water flux out of the region

$$\frac{Dm}{Dt} = -F_a \quad (3.13)$$

Based on the above, the water mass balance can be written as

$$\frac{D}{Dt} \int_v \phi S \rho_w \, dv = - \int_{\partial\Omega} \rho_w \underline{z} \cdot \underline{n} \, ds \quad (3.14)$$

Applying the divergence theorem, the r.h.s. of Eq. (3.14) can be rewritten as

$$\frac{D}{Dt} \int_v \phi S \rho_w \, dv = - \int_{\Omega} \operatorname{div}(\rho_w \underline{z}) \, dv \quad (3.15)$$

Since the region of integration v depends on time itself, integration and time differentiation do not commute. Therefore, the total time derivative needs to be rewritten according to Reynolds' transportation theory

$$\frac{D}{Dt} \int_v \phi S \rho_w \, dv = \int_{\Omega} \left[\frac{\partial}{\partial t} (\phi S \rho_w) + \operatorname{div}(\phi S \rho_w \underline{z}_a) \right] \, dv \quad (3.16)$$

where \underline{z}_a is the velocity of the deforming asphalt components due to the water pressure.

Substituting Eq. (3.16) into Eq. (3.15) yields

$$\int_{\Omega} \left[\frac{\partial}{\partial t} (\phi S \rho_w) + \operatorname{div}(\phi S \rho_w \underline{z}_a) \right] \, dv = - \int_{\Omega} \operatorname{div}(\rho_w \underline{z}) \, dv \quad (3.17)$$

Since the balance of mass must be true for an arbitrary volume element, the integral sign can be removed, and the water mass balance equation in the asphalt mix becomes

$$\frac{\partial}{\partial t} (\phi S \rho_w) + \operatorname{div}(\phi S \rho_w \underline{z}_a) = - \operatorname{div}(\rho_w \underline{z}) \quad (3.18)$$

The first term of Eq. (3.18) can be expanded as

$$\frac{\partial}{\partial t} (\phi S \rho_w) = S \rho_w \frac{\partial \phi}{\partial t} + \phi S \frac{\partial \rho_w}{\partial t} + \phi \rho_w \frac{\partial S}{\partial t} \quad (3.19)$$

Substituting this into Eq. (3.18) gives

$$\left(S \rho_w \frac{\partial \phi}{\partial t} + \phi S \frac{\partial \rho_w}{\partial t} + \phi \rho_w \frac{\partial S}{\partial t} \right) + \operatorname{div}(\phi S \rho_w \underline{z}_a) = - \operatorname{div}(\rho_w \underline{z}) \quad (3.20)$$

The second term in Eq. (3.18) can be expanded as follows

$$\begin{aligned} \operatorname{div}(\phi S \rho_w \underline{z}_a) &= S \rho_w \operatorname{div}(\phi \underline{z}_a) + \phi \underline{z}_a \cdot \nabla(S \rho_w) \\ &\approx S \rho_w \operatorname{div}(\phi \underline{z}_a) \end{aligned} \quad (3.21)$$

whereby making the approximation that $\nabla(S \rho_w) \rightarrow 0.0$

Substituting this into Eq. (3.20) gives

$$\left(S \rho_w \frac{\partial \phi}{\partial t} + \phi S \frac{\partial \rho_w}{\partial t} + \phi \rho_w \frac{\partial S}{\partial t} \right) + S \rho_w \operatorname{div}(\phi \underline{z}_a) = - \operatorname{div}(\rho_w \underline{z}) \quad (3.22)$$

this can be conveniently rearranged into

$$\left(\phi S \frac{\partial \rho_w}{\partial t} + \phi \rho_w \frac{\partial S}{\partial t} \right) + S \rho_w \left(\frac{\partial \phi}{\partial t} + \text{div}(\phi \mathbf{z}_a) \right) = -\text{div}(\rho_w \mathbf{z}) \quad (3.23)$$

The second term in Eq. (3.23) can be replaced, following mass continuity of the asphalt mix components:

$$\begin{aligned} \frac{D}{Dt}(1-\phi)\rho_a &= \frac{\partial}{\partial t}(1-\phi)\rho_a + \text{div}((1-\phi)\rho_a \mathbf{z}_a) = 0 \\ &= \rho_a \frac{\partial}{\partial t}(1-\phi) + \rho_a \text{div}((1-\phi)\mathbf{z}_a) + (1-\phi)\mathbf{z}_a \cdot \nabla \rho_a \underset{\rightarrow 0}{=} 0 \\ &= -\rho_a \frac{\partial \phi}{\partial t} + \rho_a \text{div}(\mathbf{z}_a - \phi \mathbf{z}_a) = 0 \\ &= -\frac{\partial \phi}{\partial t} + \text{div} \mathbf{z}_a - \text{div}(\phi \mathbf{z}_a) = 0 \end{aligned} \quad (3.24)$$

From which it can be seen that

$$\frac{\partial \phi}{\partial t} + \text{div}(\phi \mathbf{z}_a) = \text{div} \mathbf{z}_a \quad (3.25)$$

Substituting this into Eq. (3.23) gives

$$\left(\phi S \frac{\partial \rho_w}{\partial t} + \phi \rho_w \frac{\partial S}{\partial t} \right) + S \rho_w \text{div} \mathbf{z}_a = -\text{div}(\rho_w \mathbf{z}) \quad (3.26)$$

The flux of the asphalt mix velocity due to the water pressure can also be interpreted as a change in the effective porosity of that material [Selvadurai 2000]

$$\text{div} \mathbf{z}_a = \frac{d\phi}{dp} \frac{\partial p}{\partial t} = \alpha \frac{\partial p}{\partial t} \quad (3.27)$$

in which α is the consolidation coefficient of the asphalt components.

Replacing this into Eq. (3.26) yields

$$\left(\phi S \frac{\partial \rho_w}{\partial t} + \phi \rho_w \frac{\partial S}{\partial t} \right) + S \rho_w \alpha \frac{\partial p}{\partial t} = -\text{div}(\rho_w \mathbf{z}) \quad (3.28)$$

It may also be assumed that the degree of saturation is pressure dependent, $S = S(p)$, and therefore

$$\frac{\partial S}{\partial t} = \frac{\partial S}{\partial p} \frac{\partial p}{\partial t} \quad (3.29)$$

Replacing this into Eq. (3.28), and assuming the water incompressible $\frac{\partial \rho_w}{\partial t} \rightarrow 0$, gives

$$\left(\phi \rho_w \frac{\partial S}{\partial p} + S \rho_w \alpha \right) \frac{\partial p}{\partial t} + \text{div}(\rho_w \mathbf{z}) = 0 \quad (3.30)$$

Postulating Darcy's law for the movement of the water within the components of the mix

$$\underline{\mathbf{v}} = -\underline{\underline{\mathbf{K}}}\nabla\Phi \quad (3.31)$$

where the hydraulic gradient Φ is defined as the sum of the pressure potential and the datum potential

$$\Phi = \frac{p}{\rho_w g} + z \quad (3.32)$$

where g is the gravity, and the hydraulic conductivity tensor $\underline{\underline{\mathbf{K}}}$ is related to the intrinsic permeability tensor $\underline{\underline{\mathbf{k}}}$ via

$$\underline{\underline{\mathbf{K}}} = \frac{\rho_w g}{\mu} \underline{\underline{\mathbf{k}}} = \frac{\rho_w g}{\mu} \begin{bmatrix} k_{xx} & k_{xy} & k_{xz} \\ k_{xy} & k_{yy} & k_{yz} \\ k_{xz} & k_{zy} & k_{zz} \end{bmatrix} \quad (3.33)$$

where μ is the dynamic viscosity of the water.

Substituting Eq. (3.32) and Eq. (3.33) into Eq. (3.31), Darcy's law can be rewritten as

$$\underline{\mathbf{v}} = -\frac{1}{\mu} \underline{\underline{\mathbf{k}}} (\nabla p + \rho_w g \nabla z) \quad (3.34)$$

Substituting Eq. (3.34) into Eq. (3.30) and rearranging the terms, gives

$$\text{div} \left(\rho_w \frac{1}{\mu} \underline{\underline{\mathbf{k}}} (\nabla p + \rho_w g \nabla z) \right) = \left(S \rho_w \alpha + \phi \rho_w \frac{\partial S}{\partial p} \right) \frac{\partial p}{\partial t} \quad (3.35)$$

The product of the effective porosity and the degree of saturation can be replaced by the moisture content θ

$$\theta = \frac{V_{\text{water}}}{V_{\text{total}}} = \frac{V_{\text{pores}}}{V_{\text{total}}} \cdot \frac{V_{\text{water}}}{V_{\text{pores}}} = \phi S \quad (3.36)$$

which gives

$$\text{div} \left(\rho_w \frac{1}{\mu} \underline{\underline{\mathbf{k}}} (\nabla p + \rho_w g \nabla z) \right) = \left(\frac{\theta}{\phi} \rho_w \alpha + \phi \rho_w \frac{dS}{dp} \right) \frac{dp}{dt} \quad (3.37)$$

Replacing the water pressure p with the reference pressure head

$$h = \frac{p}{\rho_w g} \quad (3.38)$$

gives

$$\text{div} \left(\frac{\rho_w g}{\mu} \underline{\underline{\mathbf{k}}} (\rho_w \nabla h + \rho_w \nabla z) \right) = \rho_w \left(\frac{\theta}{\phi} \alpha \rho_w g + \phi \frac{dS}{dh} \right) \frac{dh}{dt} \quad (3.39)$$

Dividing Eq. (3.39) by ρ_w gives

$$\operatorname{div}\left(\frac{\rho_w \mathbf{g}}{\mu} \mathbf{k}(\nabla h + \nabla z)\right) = \left(\frac{\theta}{\phi} \alpha \rho_w \mathbf{g} + \phi \frac{dS}{dh}\right) \frac{dh}{dt} \quad (3.40)$$

Defining the modified compressibility of each component as

$$\alpha^* = \alpha \rho_w \mathbf{g} \quad (3.41)$$

which can be substituted into Eq. (3.40) as follows

$$\operatorname{div}\left(\frac{\rho_w \mathbf{g}}{\mu} \mathbf{k}(\nabla h + \nabla z)\right) = \left(\frac{\theta}{\phi} \alpha^* + \phi \frac{dS}{dh}\right) \frac{dh}{dt} \quad (3.42)$$

The term between brackets on the right side of Eq. (3.42) can be replaced by the storage coefficient L

$$L = \frac{\theta}{\phi} \alpha^* + \phi \frac{dS}{dh} \quad (3.43)$$

Substituting this into Eq. (3.42) gives

$$\operatorname{div}\left(\frac{\rho_w \mathbf{g}}{\mu} \mathbf{k}(\nabla h + \nabla z)\right) = L \frac{dh}{dt} \quad (3.44)$$

Since $\mathbf{y} = -\frac{\rho_w \mathbf{g}}{\mu} \mathbf{k}(\nabla h + \nabla z)$, the governing equation for the water balance in the asphalt components can be formulated as

$$L \frac{dh}{dt} + \operatorname{div}(\mathbf{y}) = 0 \quad (3.45)$$

3.2.3 Moisture diffusion through the mastic film

The movement of moisture through the mastic film is considered to be a process that occurs on molecular level. To simulate the process of moisture diffusion into the components of the asphalt mix, Fick's phenomenological law of diffusion is employed [Fick 1855].

The diffusion flux of moisture \mathbf{J}_d is defined as

$$\mathbf{J}_d = -\mathbf{D} \nabla C_m \quad (3.46)$$

where C_m is the current moisture concentration in the material. The diffusion of the material is determined by the diffusion tensor \mathbf{D}

$$\mathbf{D} = \sum_{i,j} D_{ij} \mathbf{e}_i \otimes \mathbf{e}_j = a_m \tau \delta_{ij} \quad (3.47)$$

where a_m is the molecular diffusion coefficient, τ is the tortuosity of the material and δ_{ij} is the Kronecker delta.

Eq. (3.46) assumes that the process of moisture diffusion into the mastic film is solely attributed to mixing on a micro-scale, depending on a spatial gradient of moisture concentration.

Posing the conservation of mass principle, it can be found

$$\frac{\partial}{\partial t} C_m = -\text{div}(\underline{\mathbf{J}}_d) = \text{div}(\underline{\mathbf{D}} \nabla C_m) \quad (3.48)$$

which is also known as Fick's second law.

The moisture content θ within the material is defined as

$$\theta = \frac{C_m}{C_m^{\max}} \quad (3.49)$$

where C_m^{\max} is the maximum moisture concentration uptake of the material. The mass of moisture, present in the mastic at time t is therefore controlled by both the diffusivity $\underline{\mathbf{D}}$ and the maximum moisture concentration C_m^{\max} uptake in the mastic, Fig. 3.2.2.

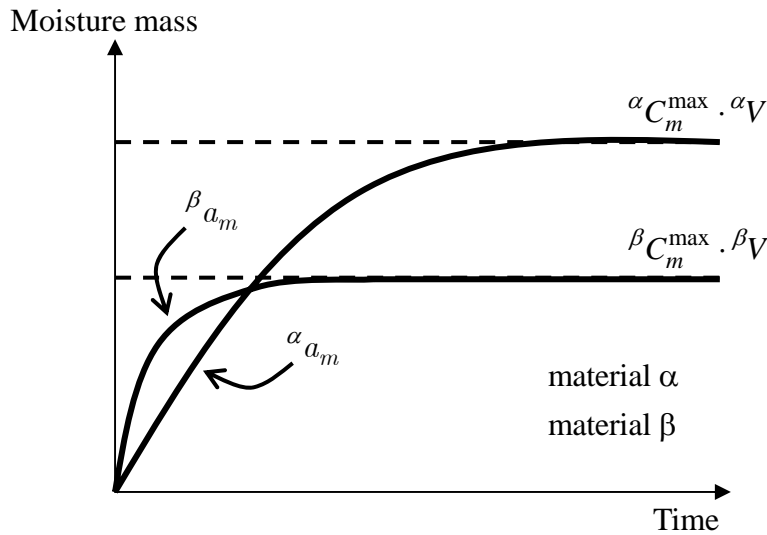


Fig. 3.2.2: Schematic of moisture diffusion in two different materials

From Fig. 3.2.2 it can be seen that a material which has a high moisture diffusion coefficient (material β) does not necessary have the highest moisture uptake. Even though material α has a lower diffusion coefficient, it eventually absorbs a bigger amount of moisture, due to its higher moisture uptake capacity, ${}^{\alpha} C_m^{\max}$.

Due to the differences in time scales, the mass balance law for water which infiltrates into the asphalt mix via a pressure gradient driven process, as discussed in the previous section, and moisture which infiltrates into the mix via a concentration gradient driven diffusion process, are modelled separately.

3.3 Moisture inducing damage of the mastic film

The mastic film is an important component in asphaltic mixes; it is the ‘glue’ that keeps the aggregates together. It also gives the visco-elasto-plastic and self-healing characteristic to the asphalt. Damage of the mastic, due to moisture infiltration is modeled in this research via two physical processes. The first is related to a weakening of the mastic due to moisture diffusion and the second is related to an erosion of the mastic, due to traffic related high water pressures in the macro-pores of the asphalt mix.

In this section, the governing equation for the modeling of erosion of mastic, or loss of mastic concentration, due to water pressure is derived.

Considering an asphaltic mix exposed to water, mastic particles can be present in the mix in two different forms: adsorbed or desorbed. Adsorbed mastic particles are still part of the mix and contribute to the overall mix characteristics. Desorbed mastic particles have been separated from the mix and are being transported via the water out of the mix, they are no longer contributing to the mechanical or physical characteristics of the asphalt.

In the following the mastic that is desorbed from the mix, and is no longer contributing to the mechanical strength of the mastic, is shown as the dissolved mastic concentration C_d

$$C_d = \frac{M_{\text{desorbed_mastic}}}{V_{\text{water}}} \quad (3.50)$$

The mastic which is still part of the asphalt is shown as the adsorbed mastic content C_a

$$C_a = \frac{\rho^m}{\rho_0^m} \quad (3.51)$$

where ρ_0^m is the, undamaged, reference density of the mastic and ρ^m is the current density.

Considering the spatial scalar field $C = C(\mathbf{x}, t)$ that describes the concentration of mastic at time t . Assuming C to be continuously differentiable, the current amount of mastic mass $m(t)$ in some three-dimensional region Ω with volume v given time t may be characterized by the scalar-valued function

$$m(t) = \int_{\Omega} C(\mathbf{x}, t) dv \quad (3.52)$$

The concentration mastic at a given place in the asphalt mix can consist of desorbed or adsorbed mastic particles

$$C(\mathbf{x}, t) = \phi S C_d + \rho_0^m C_a \quad (3.53)$$

where ϕ is the porosity and S is the degree of saturation at time t on location \mathbf{x} .

The change of mastic mass in the volume Ω might take place as a result of an advective and a diffusive flux across the boundary surface $\partial\Omega$.

The advective flux F_a is defined as

$$\mathbf{F}_a = \int_{\partial\Omega} \mathbf{C}_d \mathbf{z} \cdot \mathbf{n} \, ds \quad (3.54)$$

The diffusive flux \mathbf{F}_d is defined as

$$\mathbf{F}_d = - \int_{\partial\Omega} \mathbf{D}_m \nabla C_d \cdot \mathbf{n} \, ds \quad (3.55)$$

where \mathbf{D}_m is the diffusion/dispersion tensor and \mathbf{n} denotes the outward unit normal acting along the boundary surface $\partial\Omega$

The diffusion/dispersion tensor [Bear, 1972] is depicted as

$$\mathbf{D}_m = \sum_{i,j} D_{ij} \mathbf{e}_i \otimes \mathbf{e}_j = a_m \tau \theta \delta_{ij} + a_t |\mathbf{z}| \delta_{ij} + (a_l - a_t) \frac{z_i z_j}{|\mathbf{z}|} \quad (3.56)$$

where a_m is the molecular diffusion coefficient, τ is the tortuosity, a_t is the transverse dispersivity and a_l is the longitudinal dispersivity.

Similar to the mass balance of moisture, the mastic mass balance can be written as

$$\frac{D}{Dt} \int_v (\phi S C_d + \rho_0^m C_a) \, dv = - \int_{\Omega} \text{div} (C_d \mathbf{z} - \mathbf{D}_m \nabla C_d) \, dv \quad (3.57)$$

where v is a moving volume containing a constant amount of material and Ω is a fixed volume in space that instantaneously coincides with the moving material volume v .

The term on the left of Eq. (3.57) is the total time derivative of the spatial distribution of the mastic mass. Since the region of interest depends on time itself, integration and time differentiation do not commute. Therefore, the total time derivative needs to be rewritten according to Reynolds' transport theorem

$$\frac{D}{Dt} \int_v (\phi S C_d + \rho_0^m C_a) \, dv = \int_{\Omega} \frac{\partial}{\partial t} (\phi S C_d + \rho_0^m C_a) \, dv + \int_{\partial\Omega} (\phi S C_d + \rho_0^m C_a) \text{div} \mathbf{z}_c \, ds \quad (3.58)$$

where \mathbf{z}_c can be considered as the consolidation velocity.

Eq. (3.58) shows that the rate of change of mass, considered in a moving material volume v , is equal to the rate of change of the mass taken over the fixed volume Ω and the flux through the bounding surface $\partial\Omega$.

Applying the divergence theorem to Eq. (3.58) and after substituting in Eq. (3.57), it results

$$\begin{aligned} \int_{\Omega} \frac{\partial}{\partial t} (\phi S C_d + \rho_0^m C_a) \, dv + \int_{\Omega} \text{div} (C_d \mathbf{z}) \, dv - \int_{\Omega} \text{div} (\mathbf{D}_m \nabla C_d) \, dv \\ = - \int_{\Omega} \text{div} \left[(\phi S C_d + \rho_0^m C_a) \mathbf{z}_c \right] \, dv \end{aligned} \quad (3.59)$$

Since the volume element is arbitrary, Eq. (3.59) can be written without integral signs

$$\frac{\partial}{\partial t}(\phi S C_d + \rho_0^m C_a) + \text{div}(C_d \mathbf{v}) - \text{div}(\mathbf{D}_m \nabla C_d) = -\text{div}\left[(\phi S C_d + \rho_0^m C_a) \mathbf{v}_c\right] \quad (3.60)$$

The consolidation term can be replaced by

$$\begin{aligned} \text{div}\left[(\phi S C_d + \rho_0^m C_a) \mathbf{v}_c\right] &= (\phi S C_d + \rho_0^m C_a) \text{div} \mathbf{v}_c + \mathbf{v}_c \text{grad}(\phi S C_d + \rho_0^m C_a) \\ &\approx (\phi S C_d + \rho_0^m C_a) \text{div} \mathbf{v}_c \end{aligned} \quad (3.61)$$

where the second term on the r.h.s. of Eq. (3.61)₁ is a product of two small vectors and is therefore neglected.

The divergence of the consolidation velocity of a porous material can be approximated by

$$\text{div} \mathbf{v}_c = \alpha \frac{dp}{dt} \quad (3.62)$$

where α is the compressibility coefficient of the component under consideration.

Substituting Eq. (3.62) and Eq. (3.61) into Eq. (3.60) results to

$$\frac{\partial}{\partial t}(\phi S C_d + \rho_0^m C_a) + \text{div}(C_d \mathbf{v}) - \text{div}(\mathbf{D}_m \nabla C_d) = -(\phi S C_d + \rho_0^m C_a) \alpha \frac{\partial p}{\partial t} \quad (3.63)$$

Replacing the moisture content ϕS by θ , according to Eq. (3.36), the governing equation becomes

$$\frac{\partial(\theta C_d + \rho_0^m C_a)}{\partial t} + \text{div}(C_d \mathbf{v}) - \text{div}(\mathbf{D}_m \cdot \nabla C_d) = -(\theta C_d + \rho_0^m C_a) \alpha \frac{\partial p}{\partial t} \quad (3.64)$$

where $\frac{\partial(\theta C_d + \rho_0^m C_a)}{\partial t}$ represents the change of mass accumulation, $\text{div}(C_d \mathbf{v})$ represents the net change of mass flux due to advection, $\text{div}(\mathbf{D}_m \cdot \nabla C_d)$ is the net mass flux due to dispersion and diffusion and $(\theta C_d + \rho_0^m C_a) \alpha \frac{\partial p}{\partial t}$ is the change of mass 'production' due to consolidation of the medium.

The change of mass accumulation term of Eq. (3.64) can be expanded into

$$\frac{\partial(\theta C_d + \rho_0^m C_a)}{\partial t} = \frac{\partial(\theta C_d)}{\partial t} + \frac{\partial(\rho_0^m C_a)}{\partial t} = \theta \frac{\partial C_d}{\partial t} + C_d \frac{\partial \theta}{\partial t} + \rho_0^m \frac{\partial C_a}{\partial t} \quad (3.65)$$

The advective flux term of Eq. (3.64) can be written as

$$\text{div}(C_d \mathbf{v}) = C_d \text{div} \mathbf{v} + \mathbf{v} \nabla C_d \quad (3.66)$$

From the balance of the fluid mass in Eq.(3.45) the divergence of the velocity field is known

$$\text{div} \mathbf{v} = -L \frac{\partial h}{\partial t} \quad (3.67)$$

Substituting Eq. (3.67) into the advective flux term Eq. (3.66) yields

$$\operatorname{div}(\mathbf{v}C_d) = -C_d L \frac{\partial h}{\partial t} + \mathbf{v} \nabla C_d \quad (3.68)$$

Substituting Eq. (3.68), Eq. (3.65), Eq. (3.41) and Eq. (3.38) into Eq. (3.64) yields the governing equation of the mastic:

$$\theta \frac{\partial C_d}{\partial t} + \rho_0^m \frac{\partial C_a}{\partial t} + \mathbf{v} \nabla C_d - \operatorname{div}(\mathbf{D}_{z_m} \cdot \nabla C_d) = -(\theta C_d + \rho_0^m C_a) \alpha^* \frac{\partial h}{\partial t} + \left(L \frac{\partial h}{\partial t} - \frac{\partial \theta}{\partial t} \right) C_d \quad (3.69)$$

The relationship between the adsorbed mastic content C_a and the desorbed concentration of mastic C_d can be described via an isotherm. The type of isotherm that is used in the analysis to define this relationship (e.g. linear, Langmuir, Freundlich) can be based on experimental data and shows the desorption characteristics of the mastic in the presence of a water field. A few examples of isotherms can be found in Fig. 3.3.1, based on the Langmuir relation

$$C_a = \frac{\alpha C_d}{1 + \beta C_d} \quad (3.70)$$

where α and β are coefficients of the Langmuir isotherm.

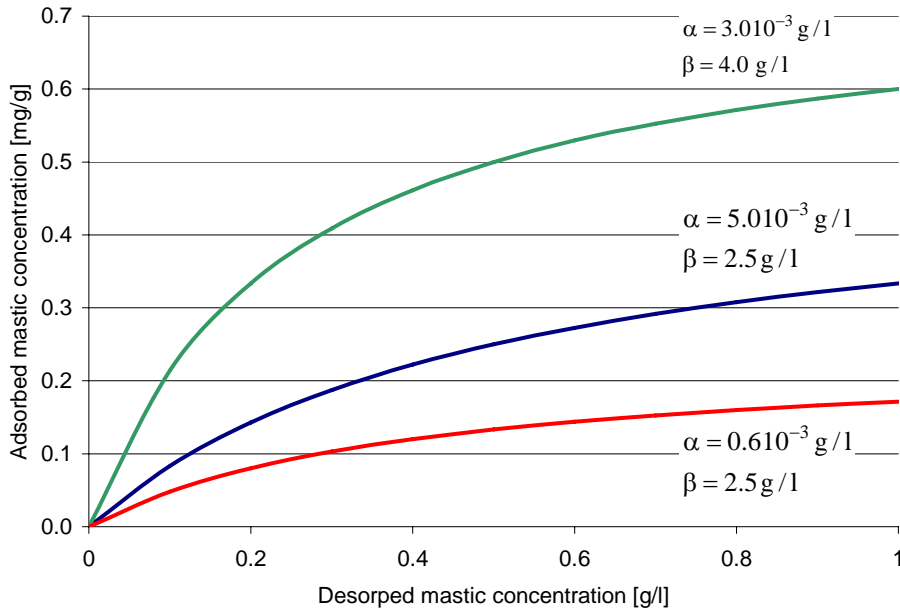


Fig. 3.3.1: Examples of desorption isotherms, based on the Langmuir relation

3.4 Conclusions

In this chapter, the formulations that are needed for the simulation of the physical moisture induced damage processes were derived and the terminology used in later chapters was established. In the following chapter the here presented formulations are formulated in notation, suitable for implementation into the finite element method.

Numerical Formulations of Physical Moisture Damage Inducing Processes

4.1 Introduction

In the previous chapter, the governing equations for the simulation of water flow and advective transport were derived as part of the physical moisture inducing damage processes. These equations need to be restructured, to become applicable for implementation into the finite element method. As mentioned previously, the aim of this research was the development of a computational finite element tool to enable a fundamental approach towards moisture induced damage in asphaltic mixes. To do so, RoAM was developed as a new sub-system of CAPA-3D to simulate the physical moisture damage processes. The interaction between RoAM and CAPA-3D results to a computational tool which enables the simulation of combined physical and mechanical moisture induced damage. In this chapter the numerical formulations of the physical moisture induced damage processes, as discussed in the previous chapter, are derived. The mechanical moisture induced damage processes are discussed from Chapter 7 on.

4.2 Numerical Approximation of the Flow Equation

4.2.1 Galerkin finite element formulation

The flow equation was derived in Eq. (3.36) as

$$L(h) \frac{\partial h}{\partial t} - \text{div} \left(\underset{\approx}{\mathbf{K}} \{ \nabla h + \nabla z \} \right) = 0 \quad (4.1)$$

Before applying the finite element method to solve Eq. (4.1), it is necessary to transform the equation into a more suitable form. To do so, the so called weak formulation can be derived. Originally the weak formulation has been introduced by mathematicians to investigate the behavior of the solution of partial differential equations, and to prove existence and uniqueness of the solution. Later on numerical schemes have been based on this formulation which leads to an approximate solution in a constructive way.

The weak form of Eq. (4.1) can be derived by multiplying both terms by a function w_i and integrate over the domain

$$\int_{\mathbf{v}} w_i \left(L(h) \frac{\partial h}{\partial t} - \text{div} \left(\underset{\approx}{\mathbf{K}} \{ \nabla h + \nabla z \} \right) \right) dV = 0 \quad (4.2)$$

whereby w_i are so called test or weighting functions, see Appendix 4.1 for more details.

Splitting the integral in Eq. (4.2), gives

$$\int_{\mathcal{V}} w_i L(h) \frac{\partial h}{\partial t} dV - \int_{\mathcal{V}} w_i \operatorname{div} \left(\underset{\sim}{\mathbf{K}} \{ \nabla h + \nabla z \} \right) dV = 0 \quad (4.3)$$

For sake of convenience, the Darcy's flux term is temporarily replaced by the velocity vector $\underset{\sim}{\mathbf{v}}$

$$\underset{\sim}{\mathbf{K}} \{ \nabla h + \nabla z \} = \underset{\sim}{\mathbf{v}} \quad (4.4)$$

The second integral in Eq. (4.3) can then be written as

$$\int_{\mathcal{V}} w_i \operatorname{div} \left(\underset{\sim}{\mathbf{K}} \{ \nabla h + \nabla z \} \right) dV = \int_{\mathcal{V}} w_i \operatorname{div} \underset{\sim}{\mathbf{v}} dV \quad (4.5)$$

It can be shown that the r.h.s. of Eq. (4.5) can be reformulated as

$$\int_{\mathcal{V}} w_i \operatorname{div} \underset{\sim}{\mathbf{v}} dV = \int_{\mathcal{V}} \left(\operatorname{div} (w_i \underset{\sim}{\mathbf{v}}) - \nabla w_i \cdot \underset{\sim}{\mathbf{v}} \right) dV \quad (4.6)$$

From the divergence theorem, the volume integral over the divergence term in Eq. (4.6) can be replaced by a surface integral

$$\int_{\mathcal{V}} \operatorname{div} (w_i \underset{\sim}{\mathbf{v}}) dV = \int_{\mathcal{S}} w_i \underset{\sim}{\mathbf{v}} \cdot \underset{\sim}{\mathbf{n}} dS \quad (4.7)$$

Based on the above, Eq. (4.3) can be rewritten as

$$\int_{\mathcal{V}} w_i L(h) \frac{\partial h}{\partial t} dV - \int_{\mathcal{S}} w_i \underset{\sim}{\mathbf{v}} \cdot \underset{\sim}{\mathbf{n}} dS + \int_{\mathcal{V}} \nabla w_i \cdot \underset{\sim}{\mathbf{v}} dV = 0 \quad (4.8)$$

Back substituting Eq. (4.4) into Eq. (4.8) gives

$$\int_{\mathcal{V}} w_i L(h) \frac{\partial h}{\partial t} dV - \int_{\mathcal{S}} w_i \underset{\sim}{\mathbf{n}} \cdot \underset{\sim}{\mathbf{K}} \{ \nabla h + \nabla z \} dS + \int_{\mathcal{V}} \nabla w_i \cdot \left(\underset{\sim}{\mathbf{K}} \{ \nabla h + \nabla z \} \right) dV = 0 \quad (4.9)$$

By rearranging Eq. (4.9), the weak form of the flow equation is found as

$$\int_{\mathcal{V}} w_i L(h) \frac{\partial h}{\partial t} dV + \int_{\mathcal{V}} \nabla w_i \cdot \left(\underset{\sim}{\mathbf{K}} \nabla h \right) dV = \int_{\mathcal{S}} w_i \underset{\sim}{\mathbf{n}} \cdot \underset{\sim}{\mathbf{K}} \{ \nabla h + \nabla z \} dS - \int_{\mathcal{V}} \nabla w_i \cdot \left(\underset{\sim}{\mathbf{K}} \nabla z \right) dV \quad (4.10)$$

By using the finite element method to solve the above equation, the following approximations can be made

$$h = h_j N_j \quad (4.11)$$

$$w_i = N_i \quad (4.12)$$

where Eq. (4.12) follows from the Galerkin criterion, h_j is the hydraulic head amplitude at nodal point j and N_i and N_j are the shape functions of the nodal points i and j , respectively.

The shape functions for the 8-noded serendipity elements are defined as

$$N_k(\xi, \eta, \zeta) = \frac{1}{8}(1 + \xi\xi_k)(1 + \eta\eta_k)(1 + \zeta\zeta_k) \quad k = 1, 2, \dots, 8 \quad (4.13)$$

Substituting the hydraulic head and the weighting function into Eq. (4.10) gives

$$\begin{aligned} \sum_{j=1}^n \left(\int_V N_i L(h) N_j dV \right) \frac{dh_j}{dt} + \sum_{j=1}^n \left(\int_V \nabla N_i \mathbf{K} \nabla N_j dV \right) h_j \\ = \int_S N_i \mathbf{n} \cdot \mathbf{K} (\nabla h + \nabla z) dS - \int_V \nabla N_i \mathbf{K} \nabla z dV \end{aligned} \quad (4.14)$$

Which can be written in matrix form as

$$[M] \left\{ \frac{dh}{dt} \right\} + [S] \{h\} = \{B\} + \{G\} \quad (4.15)$$

where

$$[M] = \sum_{j=1}^n \left(\int_V N_i L(h) N_j dV \right) \quad (4.16)$$

represents the mass matrix resulting from the storage term,

$$[S] = \sum_{j=1}^n \left(\int_V \nabla N_i \mathbf{K} \nabla N_j dV \right) \quad (4.17)$$

represents the stiffness matrix resulting from the action of conductivity,

$$\{B\} = \int_S N_i \mathbf{n} \cdot \mathbf{K} (\nabla h + \nabla z) dS \quad (4.18)$$

represents the boundary conditions, where the pressure head or the pressure gradient can be described as a boundary condition, and

$$\{G\} = - \int_V \nabla N_i \mathbf{K} \nabla z dV \quad (4.19)$$

represents the load vectors from gravity, and finally

$$\left\{ \frac{dh}{dt} \right\} = \sum_{j=1}^n \frac{dh_j}{dt} \quad (4.20)$$

and

$$\{h\} = \sum_{j=1}^n h_j \quad (4.21)$$

Reformulation of the flow equation into a summation of matrices, allows for the implementation of the numerical approximation of this non-linear equation. The first step for this approximation is the replacements of the integrals by the Gaussian summations convention, to allow for a numerical integration.

4.2.2 Numerical integration

In order to complete the matrices of Eq. (4.15), the integrals on the r.h.s. of Eq. (4.16) through Eq. (4.19) need to be evaluated for every element in the mesh:

$$M_{ij}^e = \int_{V^e} N_i^e L(h) N_j^e dV \quad (4.22)$$

$$S_{ij}^e = \int_{V^e} \nabla N_i^e \mathbf{K} \nabla N_j^e dV \quad (4.23)$$

$$B_i^e = \int_S N_i^e \mathbf{n} \cdot \mathbf{K} (\nabla h + \nabla z) dS \quad (4.24)$$

$$G_i^e = - \int_V \nabla N_i^e \mathbf{K} \nabla z dV \quad (4.25)$$

Since Eq. (4.22) - Eq. (4.25) are written in global coordinates and the shape functions in Eq. (4.13) are in local coordinates, a mapping between the two coordinate systems is needed

$$\begin{aligned} x_1 &= \sum_{i=1}^n N_i(\xi, \eta, \zeta) x_{1i} \\ x_2 &= \sum_{i=1}^n N_i(\xi, \eta, \zeta) x_{2i} \\ x_3 &= \sum_{i=1}^n N_i(\xi, \eta, \zeta) x_{3i} \end{aligned} \quad (4.26)$$

where x_1, x_2 and x_3 are the actual coordinates in the global coordinate system, x_{1i}, x_{2i} and x_{3i} are the actual coordinates of the nodes i , where $1 \leq i \leq n$, and N_i are the same shape functions as Eq. (4.13). The fact that the same interpolation functions are used for the interpolation of the element coordinates and the hydraulic pressures is the basis of the isoparametric finite element formulation.

The differential volume dV over which Eq. (4.22), Eq. (4.23) and Eq. (4.25) are integrated can be expressed in the global coordinates as

$$dV = dx_1 dx_2 dx_3 \quad (4.27)$$

where the volume dV is contained by the vectors $d\mathbf{x}_1$, $d\mathbf{x}_2$ and $d\mathbf{x}_3$

$$\begin{aligned} d\mathbf{x}_1 &= dx_1 \mathbf{e}_1 \\ d\mathbf{x}_2 &= dx_2 \mathbf{e}_2 \\ d\mathbf{x}_3 &= dx_3 \mathbf{e}_3 \end{aligned} \quad (4.28)$$

with $\mathbf{e}_1, \mathbf{e}_2$ and \mathbf{e}_3 as the normalized unit coordinate (base) vectors of the global system.

Since a volume that is contained by the vectors \mathbf{u} , \mathbf{w} and \mathbf{y} , can be found from

$$dV = (\underline{\mathbf{u}} \times \underline{\mathbf{w}}) \cdot \underline{\mathbf{v}} = \det \begin{bmatrix} u_1 & w_1 & v_1 \\ u_2 & w_2 & v_2 \\ u_3 & w_3 & v_3 \end{bmatrix} \quad (4.29)$$

Eq. (4.27) can be also found from

$$dV = (d\mathbf{x}_1 \times d\mathbf{x}_2) \cdot d\mathbf{x}_3 = \det \begin{bmatrix} dx_1 & 0 & 0 \\ 0 & dx_2 & 0 \\ 0 & 0 & dx_3 \end{bmatrix} = dx_1 dx_2 dx_3 \quad (4.30)$$

This differential volume dV needs to be ‘mapped’ into a differential volume that is defined in the local coordinate system

$$d\hat{v} = d\xi d\eta d\zeta \quad (4.31)$$

Using the same philosophy as above, the differential volume $d\tilde{v}$ is contained by the vectors

$$\begin{aligned} d\tilde{\xi} &= d\xi \hat{\mathbf{e}}_1 \\ d\tilde{\eta} &= d\eta \hat{\mathbf{e}}_2 \\ d\tilde{\zeta} &= d\zeta \hat{\mathbf{e}}_3 \end{aligned} \quad (4.32)$$

with $\hat{\mathbf{e}}_1, \hat{\mathbf{e}}_2$ and $\hat{\mathbf{e}}_3$ as the normalized unit coordinate (base) vectors of the local system.

The vectors that contain the global differential volume can be expressed in the local coordinates as

$$\begin{aligned} d\mathbf{x}_1 &= dx_1 \mathbf{e}_1 = \frac{\partial x_1}{\partial \xi} d\tilde{\xi} + \frac{\partial x_1}{\partial \eta} d\tilde{\eta} + \frac{\partial x_1}{\partial \zeta} d\tilde{\zeta} \\ d\mathbf{x}_2 &= dx_2 \mathbf{e}_2 = \frac{\partial x_2}{\partial \xi} d\tilde{\xi} + \frac{\partial x_2}{\partial \eta} d\tilde{\eta} + \frac{\partial x_2}{\partial \zeta} d\tilde{\zeta} \\ d\mathbf{x}_3 &= dx_3 \mathbf{e}_3 = \frac{\partial x_3}{\partial \xi} d\tilde{\xi} + \frac{\partial x_3}{\partial \eta} d\tilde{\eta} + \frac{\partial x_3}{\partial \zeta} d\tilde{\zeta} \end{aligned} \quad (4.33)$$

Using the above definitions, the differential global volume can be found from the differential local volume as

$$dV = \det \begin{bmatrix} \frac{\partial x_1}{\partial \xi} d\tilde{\xi} & \frac{\partial x_2}{\partial \xi} d\tilde{\xi} & \frac{\partial x_3}{\partial \xi} d\tilde{\xi} \\ \frac{\partial x_1}{\partial \eta} d\tilde{\eta} & \frac{\partial x_2}{\partial \eta} d\tilde{\eta} & \frac{\partial x_3}{\partial \eta} d\tilde{\eta} \\ \frac{\partial x_1}{\partial \zeta} d\tilde{\zeta} & \frac{\partial x_2}{\partial \zeta} d\tilde{\zeta} & \frac{\partial x_3}{\partial \zeta} d\tilde{\zeta} \end{bmatrix} = \det \begin{bmatrix} \frac{\partial x_1}{\partial \xi} & \frac{\partial x_2}{\partial \xi} & \frac{\partial x_3}{\partial \xi} \\ \frac{\partial x_1}{\partial \eta} & \frac{\partial x_2}{\partial \eta} & \frac{\partial x_3}{\partial \eta} \\ \frac{\partial x_1}{\partial \zeta} & \frac{\partial x_2}{\partial \zeta} & \frac{\partial x_3}{\partial \zeta} \end{bmatrix} d\tilde{\xi} d\tilde{\eta} d\tilde{\zeta} = \det[\mathbf{J}] d\hat{v} \quad (4.34)$$

where

$$[J] = \begin{bmatrix} \frac{\partial x_1}{\partial \xi} & \frac{\partial x_2}{\partial \xi} & \frac{\partial x_3}{\partial \xi} \\ \frac{\partial x_1}{\partial \eta} & \frac{\partial x_2}{\partial \eta} & \frac{\partial x_3}{\partial \eta} \\ \frac{\partial x_1}{\partial \zeta} & \frac{\partial x_2}{\partial \zeta} & \frac{\partial x_3}{\partial \zeta} \end{bmatrix} \quad (4.35)$$

is called the Jacobian tensor. The determinant of this matrix is often referred to as ‘the jacobian’ and relates the volume from one coordinate system to another.

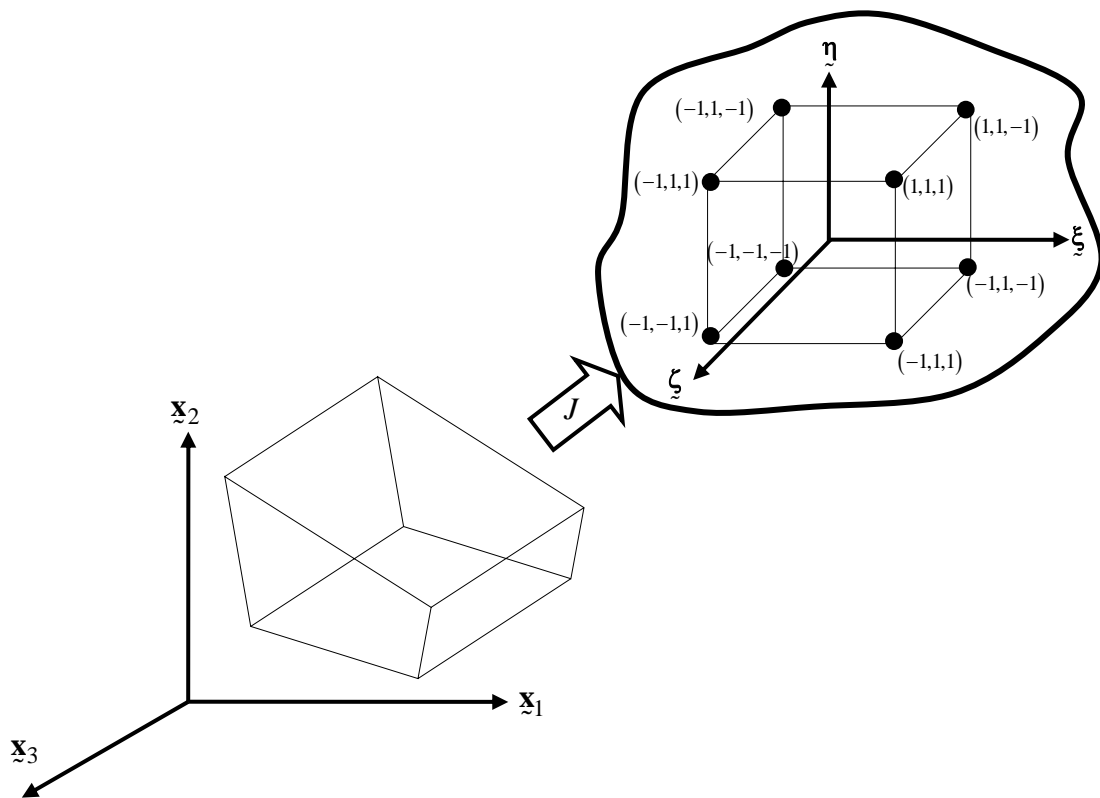


Figure 4.2.1 Mapping of an element in a global Cartesian coordinate system into a local isoparametric coordinate system

Following Eq. (4.34), an integral over a global differential volume can be replaced by a local volume integral as

$$\int_e dV = \int_{-1}^1 \int_{-1}^1 \int_{-1}^1 J d\hat{v} = \int_{-1}^1 \int_{-1}^1 \int_{-1}^1 J d\xi d\eta d\zeta \quad (4.36)$$

Using Eq. (4.36) and the Gaussian quadrature rule, a function $g(x_1, x_2, x_3)$ that is integrated over a differential volume dV can be found as a summation over the integration points

$$\int_e g(x_1, x_2, x_3) dV = \int_{-1}^1 \int_{-1}^1 \int_{-1}^1 g(\xi, \eta, \zeta) J d\xi d\eta d\zeta \quad (4.37)$$

$$= \sum_{i=1}^n \sum_{j=1}^n \sum_{k=1}^n g(\xi_i, \eta_j, \zeta_k) w_i w_j w_k$$

where w_i are the associated weight functions of the i^{th} Gaussian point, and n are the number of integration points.

Eq. (4.37) can be used to replace the volume integrals in Eq. (4.22), Eq. (4.23) and Eq. (4.25).

Eq. (4.18) makes use of a surface integral. In order to find the mapping function that brings a differential surface area dS from the global coordinate system to a differential surface area $d\xi d\eta$ in the local coordinate system, a surface S is defined by the function

$$S = f(x_1, x_3) \quad (4.38)$$

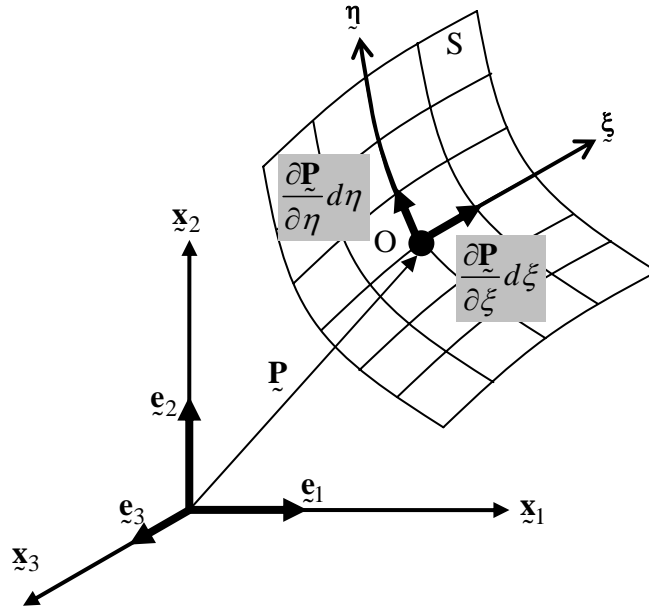


Figure 4.2.2: Defining a surface area in a local coordinate system

On this surface, a point O is located, Figure 4.2.2, whose location is defined by a vector $\tilde{\mathbf{P}}$

$$\tilde{\mathbf{P}} = \begin{Bmatrix} x_1 \\ x_2 \\ x_3 \end{Bmatrix} = x_1 \mathbf{e}_1 + x_2 \mathbf{e}_2 + x_3 \mathbf{e}_3 \quad (4.39)$$

The tangent vectors to the coordinate curves at point O are given by

$$\mathbf{u} = \frac{\partial \tilde{\mathbf{P}}}{\partial \eta} d\eta \quad (4.40)$$

$$\underline{\mathbf{v}} = \frac{\partial \underline{\mathbf{P}}}{\partial \underline{\xi}} d\underline{\xi} \quad (4.41)$$

The area contained by two vectors $\underline{\mathbf{u}}$ and $\underline{\mathbf{v}}$ can be found as the magnitude of their cross product

$$dS = |\underline{\mathbf{u}} \times \underline{\mathbf{v}}| \quad (4.42)$$

where the cross product can be found from

$$\underline{\mathbf{u}} \times \underline{\mathbf{v}} = \det \begin{bmatrix} \mathbf{e}_1 & \mathbf{e}_2 & \mathbf{e}_3 \\ u_1 & u_2 & u_3 \\ v_1 & v_2 & v_3 \end{bmatrix} \quad (4.43)$$

Substituting Eq. (4.40) and Eq. (4.41) into Eq. (4.43) gives

$$\frac{\partial \underline{\mathbf{P}}}{\partial \underline{\eta}} d\underline{\eta} \times \frac{\partial \underline{\mathbf{P}}}{\partial \underline{\xi}} d\underline{\xi} = \det \begin{bmatrix} \mathbf{e}_1 & \mathbf{e}_2 & \mathbf{e}_3 \\ \frac{\partial P_1}{\partial \eta} d\eta & \frac{\partial P_2}{\partial \eta} d\eta & \frac{\partial P_3}{\partial \eta} d\eta \\ \frac{\partial P_1}{\partial \xi} d\xi & \frac{\partial P_2}{\partial \xi} d\xi & \frac{\partial P_3}{\partial \xi} d\xi \end{bmatrix} = \det \begin{bmatrix} \mathbf{e}_1 & \mathbf{e}_2 & \mathbf{e}_3 \\ \frac{\partial P_1}{\partial \eta} & \frac{\partial P_2}{\partial \eta} & \frac{\partial P_3}{\partial \eta} \\ \frac{\partial P_1}{\partial \xi} & \frac{\partial P_2}{\partial \xi} & \frac{\partial P_3}{\partial \xi} \end{bmatrix} d\underline{\xi} d\underline{\eta} \quad (4.44)$$

where the determinant term can be rewritten as

$$\begin{aligned} \det \begin{bmatrix} \mathbf{e}_1 & \mathbf{e}_2 & \mathbf{e}_3 \\ \frac{\partial P_1}{\partial \eta} & \frac{\partial P_2}{\partial \eta} & \frac{\partial P_3}{\partial \eta} \\ \frac{\partial P_1}{\partial \xi} & \frac{\partial P_2}{\partial \xi} & \frac{\partial P_3}{\partial \xi} \end{bmatrix} &= \det \begin{bmatrix} \mathbf{e}_1 & \mathbf{e}_2 & \mathbf{e}_3 \\ \frac{\partial x_1}{\partial \eta} & \frac{\partial x_2}{\partial \eta} & \frac{\partial x_3}{\partial \eta} \\ \frac{\partial x_1}{\partial \xi} & \frac{\partial x_2}{\partial \xi} & \frac{\partial x_3}{\partial \xi} \end{bmatrix} \\ &= \mathbf{e}_1 \det \begin{bmatrix} \frac{\partial x_2}{\partial \eta} & \frac{\partial x_3}{\partial \eta} \\ \frac{\partial x_2}{\partial \xi} & \frac{\partial x_3}{\partial \xi} \end{bmatrix} - \mathbf{e}_2 \det \begin{bmatrix} \frac{\partial x_1}{\partial \eta} & \frac{\partial x_3}{\partial \eta} \\ \frac{\partial x_1}{\partial \xi} & \frac{\partial x_3}{\partial \xi} \end{bmatrix} + \mathbf{e}_3 \det \begin{bmatrix} \frac{\partial x_1}{\partial \eta} & \frac{\partial x_2}{\partial \eta} \\ \frac{\partial x_1}{\partial \xi} & \frac{\partial x_2}{\partial \xi} \end{bmatrix} \\ &= \mathbf{e}_1 J_{x_1} - \mathbf{e}_2 J_{x_2} + \mathbf{e}_3 J_{x_3} \\ &= \begin{bmatrix} J_{x_1} \\ -J_{x_2} \\ J_{x_3} \end{bmatrix} \end{aligned} \quad (4.45)$$

Back substituting the result of Eq. (4.45) into Eq. (4.44) gives

$$\frac{\partial \mathbf{P}}{\partial \eta} d\eta \times \frac{\partial \mathbf{P}}{\partial \xi} d\xi = \begin{Bmatrix} J_{x_1} \\ -J_{x_2} \\ J_{x_3} \end{Bmatrix} d\xi d\eta \quad (4.46)$$

Finally, the new expression for the surface dS can be found by taking the norm of this vector

$$dS = \left| \frac{\partial \mathbf{P}}{\partial \eta} d\eta \times \frac{\partial \mathbf{P}}{\partial \xi} d\xi \right| = \left| \begin{Bmatrix} J_{x_1} \\ -J_{x_2} \\ J_{x_3} \end{Bmatrix} d\xi d\eta \right| = \sqrt{J_{x_1}^2 + J_{x_2}^2 + J_{x_3}^2} d\xi d\eta \quad (4.47)$$

Based on the above, to map a surface integral from the global to the local coordinate system, the following convention can be used

$$\int_S F(x_1, x_2, x_3) dS = \int_{-1}^1 \int_{-1}^1 \phi(\xi, \eta) \sqrt{J_x^2 + J_y^2 + J_z^2} d\xi d\eta \quad (4.48)$$

Eq. (4.48) can be used to replace the surface integral of Eq. (4.24). Rewriting this integral using the Gaussian quadrature rule, gives

$$\begin{aligned} \int_S F(x_1, x_2, x_3) dS &= \int_{-1}^1 \int_{-1}^1 \phi(\xi, \eta) \sqrt{J_x^2 + J_y^2 + J_z^2} d\xi d\eta \\ &= \sum_{i=1}^n \sum_{j=1}^n \phi(\xi_i, \eta_j) \sqrt{J_x^2 + J_y^2 + J_z^2} w_i w_j \end{aligned} \quad (4.49)$$

In summary, Eq. (4.22) through Eq. (4.25) can be rewritten as

$$M_{\alpha\beta}^e = \sum_{i=1}^n \sum_{j=1}^n \sum_{k=1}^n N_{\alpha}^e L(\mathbf{h}) N_{\beta}^e w_i w_j w_k \quad (4.50)$$

$$S_{\alpha\beta}^e = \sum_{i=1}^n \sum_{j=1}^n \sum_{k=1}^n \nabla N_{\alpha}^e \mathbf{K}_{\approx} \nabla N_{\beta}^e w_i w_j w_k \quad (4.51)$$

$$B_{\alpha}^e = \sum_{i=1}^n \sum_{j=1}^n N_{\alpha}^e \mathbf{n} \cdot \mathbf{K}_{\approx} (\nabla h + \nabla z) \sqrt{J_x^2 + J_y^2 + J_z^2} w_i w_j \quad (4.52)$$

$$G_{\alpha}^e = - \sum_{i=1}^n \sum_{j=1}^n \sum_{k=1}^n \nabla N_{\alpha}^e \mathbf{K}_{\approx} \nabla z w_i w_j w_k \quad (4.53)$$

4.2.3 In time approximation

In paragraph 4.2.1, the flow equation was reformulated in matrix form as

$$[M] \left\{ \frac{dh}{dt} \right\} + [S] \{h\} = \{B\} + \{G\} \quad (4.54)$$

In the previous section it is explained how the integrations over the volume and the surface are performed numerically and results in a system of ordinary differential equations of the shape Eq. (4.54). In order to solve this system of equations any classical method for the solution of ordinary differential equations may be used. In general a distinction is made between explicit and implicit methods and between one-step and multi-step methods. In Appendix 4.2 a more detailed description of time approximation methods is given.

In RoAM a so called α -method of time integration [Bathe 1996], [Hughes 1987], [Press 1989] is implemented, which is a one-step method where the value of α dictates if it is an explicit or implicit method. The one-step method means that, to compute the solution at a certain time-step, only information of the preceding time-step is used and not of older time-steps. The method is considered explicit if the terms are only evaluated at the present time level and implicit if they are also evaluated at the next time level.

To apply the α -method of time integration, the r.h.s. of Eq. (4.54) is replaced by a single force vector

$$[M] \left\{ \frac{dh}{dt} \right\} + [S] \{h\} = \{F\} \quad (4.55)$$

The initial value problem consists of finding a function $\underline{h} = \underline{h}(t)$ satisfying Eq. (4.55) and the initial condition $\underline{h}(0) = \underline{h}_0$, where \underline{h}_0 is given.

The time of simulation $0 \leq t \leq t_E$ can be subdivided into time steps Δt_n with $n = 1$ to n_{TS} , where n_{TS} is the number of time steps and t_E is the end of the simulation.

In the α -method of time integration method Eq. (4.55) can be written as

$$[M] \left\{ \frac{dh}{dt} \right\}_{n+\alpha} + [S] \{h\}_{n+\alpha} = \{F\} \quad (4.56)$$

where $\left\{ \frac{dh}{dt} \right\}_{n+\alpha}$ and $\{h\}_{n+\alpha}$ are the approximations of $\dot{\underline{h}}(t_{n+\alpha})$ and $\underline{h}(t_{n+\alpha})$.

The values of $\{h\}_{n+\alpha}$ are determined on the basis of $\{h\}_n$ and $\{h\}_{n+1}$, where the contribution of each vector depends on a weighting parameter α , taken to be in the interval $[0,1]$:

$$\{h\}_{n+\alpha} = (1-\alpha)\{h\}_n + \alpha\{h\}_{n+1} \quad (4.57)$$

Assuming a constant time step

$$\Delta t_n = \Delta t = \frac{t_E}{n_{TS}} \quad (4.58)$$

the time differential $\left\{ \frac{dh}{dt} \right\}_{n+\alpha}$ can be determined via

$$\left\{ \frac{dh}{dt} \right\}_{n+\alpha} = \frac{1}{\Delta t} (\{h\}_{n+1} - \{h\}_n) \quad (4.59)$$

Substituting Eq. (4.57) and Eq. (4.59) into Eq.(4.56), the flow equation becomes

$$\frac{[M]}{\Delta t} (\{h\}_{n+1} - \{h\}_n) + [S](1-\alpha)\{h\}_n + \alpha[S]\{h\}_{n+1} = \{F\} \quad (4.60)$$

By rearranging Eq.(4.60), the values of $\{h\}_{n+1}$ can be found from

$$\left(\frac{[M]}{\Delta t} + \alpha[S] \right) \{h\}_{n+1} = \{F\} + \left(\frac{[M]}{\Delta t} - [S](1-\alpha) \right) \{h\}_n \quad (4.61)$$

where $[M]$, $[S]$ and $[F]$ are evaluated at $t + \alpha\Delta t$.

For the case of $\alpha = 0$, the above method is also known as the explicit forward Euler method. For the case of $\alpha = 0.5$ the method is known as the Crank-Nicholson, the implicit Heun or the trapezoidal method and for $\alpha = 1.0$ the method is known as the implicit backward Euler method.

Eq. (4.61) can be written as a matrix equation

$$[T]\{h\} = \{Y\} \quad (4.62)$$

where $[T]$ is the matrix, $\{h\}$ is the unknown vector to be found and represents the values of discretized pressure field at a new time, and $\{Y\}$ is the load vector.

For $\alpha = 0.0$

$$\begin{aligned} [T] &= \frac{[M]}{\Delta t} \\ \{Y\} &= \{F\} + \left(\frac{[M]}{\Delta t} - [S] \right) \{h\}_n \end{aligned} \quad (4.63)$$

For $\alpha = 0.5$

$$\begin{aligned} [T] &= \left(\frac{[M]}{\Delta t} + 0.5[S] \right) \\ \{Y\} &= \{F\} + \left(\frac{[M]}{\Delta t} - 0.5[S] \right) \{h\}_n \end{aligned} \quad (4.64)$$

For $\alpha = 1.0$

$$\begin{aligned} [T] &= \left(\frac{[M]}{\Delta t} + [S] \right) \\ \{Y\} &= \{F\} + \frac{[M]}{\Delta t} \{h\}_n \end{aligned} \quad (4.65)$$

4.3 Numerical approximation of the mastic transport equation

4.3.1 Introduction

The mastic transport equation, as presented in Eq. (3.61) combines advective (i.e. flow-field or pressure gradient driven) and diffusive (i.e. concentration gradient driven) transport of the dissolved mastic particles. This combination of advective and diffusive (or dispersive) terms is known to cause some numerical difficulties which generally are not encountered in the governing equation of the flow field. The nature of diffusion-advection equations can be conveniently characterized by the dimensionless Peclet number

$$P_e = |\underline{v}|h / \alpha_m \quad (4.66)$$

where \underline{v} is the velocity vector, h is a characteristic length and α_m is the molecular diffusion coefficient. For example, in the case when an inert species is spreading due to molecular diffusion and advection in a one-dimensional velocity field, the governing equation can be written as

$$\frac{\partial C}{\partial t} = \frac{\partial^2 C}{\partial x^2} - P_e \frac{\partial C}{\partial x} \quad (4.67)$$

where C is the concentration of species.

Clearly, when the Peclet number is small, diffusion dominates and the equation is parabolic in character. However, when the Peclet number is large, advection dominates and the character of the equation becomes hyperbolic. In non-uniform flow fields, like the ones occurring through an asphalt mix, where the velocity is not constant, the Peclet number may vary from point to point both in space and time. As a result of this variation, the diffusion-advection equation may vary in character within a given field and time, being predominantly parabolic in some regions and predominantly hyperbolic in others. Physically, this means that the way of transport of a particle can vary from place to place as well as in time. This poses a challenge on the capabilities of the numerical tool to actually capture the concentrations correctly. Since this problem is known for quite some time, several methods have been developed over the years to treat it. The most conventional numerical methods for solving this problem can be classified into three major categories: Eulerian, Lagrangian or mixed Lagrangian-Eulerian. In Appendix 4.3 a more detailed discussion about these three methods is given.

In the Eulerian approach the equation is discretized by a finite difference or finite element grid fixed in space, where the Eulerian form of the transport equation is solved at the nodes of the grid. Since the advective and diffusive terms in this method still need to be solved simultaneously, the numerical instabilities as described above need to be avoided. The Eulerian approach often uses weighting functions that are one or two orders higher than the base functions as a form of stabilization, where the weighting factors are dependent on the direction of the flow. A popular method within this category is the streamline upwinding by the Petrov Galerkin method (SUPG) [Hughes 1987], [Belytschko 2001].

In the Lagrangian approach, either a deforming grid or a fixed grid in deforming coordinates is used, where the physical quantities are computed at a set of point moving with the fluid. The numerical instabilities are in this case avoided because the advective term is no longer treated explicitly by solving the Lagrangian form of the transport equation in grids moving with the particles. Lagrangian approaches are less popular than the other methods for solving the transport equation because of the complexities arising from the highly distorting grid.

In a mixed Lagrangian-Eulerian approach a combination of the two above methods is used. The method employs, just like the Eulerian method, a fixed grid. However, the advective term is computed via a Lagrangian approach using a particle tracking method. This way the advective term vanished from the governing equation, which then can be solved with either finite difference, finite element or some other variant numerical method [Neuman, 1981], [Neuman, 1984], [Hughes, 1987], [Belytschko, 2001], [Franca, 2005].

In RoAM the latter approach has been implemented, where the Lagrangian concentrations are computed via a single-step reverse tracking method [Galeati, 1992] and the diffusive part is computed via a Eulerian finite element method. In the following the numerical approximation of the mastic transport equation is further elaborated.

4.3.2 Hybrid Lagrangian-Eulerian formulation

The mastic transport equation is simulating the movement of dissolved mastic particles inside a partially or fully saturated asphalt mix, where both advective transport and gradient driven (diffusion) processes are considered.

The mastic transport equation was derived in Eq. (3.61), and is repeated here for the sake of convenience

$$\begin{aligned} \theta \frac{\partial C_d}{\partial t} + \rho_0^m \frac{\partial C_a}{\partial t} + \mathbf{v} \cdot \nabla C_d - \text{div} \left(\mathbf{D}_m \cdot \nabla C_d \right) \\ = - \left(\theta C_d + \rho_0^m C_a \right) \alpha^* \frac{\partial h}{\partial t} + \left(L \frac{\partial h}{\partial t} - \frac{\partial \theta}{\partial t} \right) C_d \end{aligned} \quad (4.68)$$

This equation involves two unknowns, the adsorbed C_a and the desorbed C_d mastic particles. In order to solve this equation, a relation between these two quantities must be defined. In addition to the Langmuir relationship, which was discussed in chapter 3, other relationships that can be chosen are, for instance, a linear isotherm

$$C_a = K_d C_d \quad (4.69)$$

where K_d is the desorption coefficient, or a nonlinear (Freundlich) isotherm

$$C_a = \gamma C_d^n \quad (4.70)$$

where γ is the Freundlich coefficient and n is a power index [Bear 1990]. The choice of the isotherm and the corresponding parameters, should follow from experimental data, see chapter 8 for a more detailed discussion.

By choosing the *linear* isotherm for the adsorbed-desorbed mastic relation, Eq. (4.68) becomes

$$\begin{aligned} (\theta + \rho_0^m K_d) \frac{\partial C_d}{\partial t} + \mathbf{v} \nabla C_d = \operatorname{div}(\mathbf{D}_m \cdot \nabla C_d) \\ - \alpha^* \frac{\partial h}{\partial t} (\theta + \rho_0^m K_d) C_d + \left(L \frac{\partial h}{\partial t} - \frac{\partial \theta}{\partial t} \right) C_d \end{aligned} \quad (4.71)$$

By choosing the *non-linear* isotherm, i.e. Eq. (4.70), Eq. (4.68) becomes

$$\begin{aligned} \theta \frac{\partial C_d}{\partial t} + \rho_0^m \frac{dC_a}{dC_d} \frac{\partial C_d}{\partial t} + \mathbf{v} \nabla C_d = \operatorname{div}(\mathbf{D}_m \cdot \nabla C_d) - (\theta C_d + \rho_0^m C_a(C_d)) \alpha^* \frac{\partial h}{\partial t} \\ + \left(L \frac{\partial h}{\partial t} - \frac{\partial \theta}{\partial t} \right) C_d \end{aligned} \quad (4.72)$$

Eq. (4.71) and Eq. (4.72) describe the transport of mastic from an Eulerian (or fixed) framework for a linear and a non-linear constitutive relation, respectively.

As discussed previously, the combination of advective and dispersive/diffusive terms in the mastic transport equation could cause numerical difficulties. These difficulties have been well documented in the literature and various attempts to handle them have been summarized by many authors, e.g. [Neuman 1981], [Kinzelbach 1987], [Lobo Ferreira 1987], [Casulli 1990], [Selvadurai 2005,2006].

In RoAM, a Lagrangian-Eulerian method is implemented. Lagrangian-Eulerian methods generally solve the advective part of the problem by a ‘method of characteristics’ and the diffusive part by Eulerian grid methods, such as finite elements. The traditional ‘method of characteristics’ is explicit and tracks particles forward in a manner which is computationally intensive. Therefore, in RoAM a modified method is used which is implicit and has good numerical stability. In this method the path lines of the particles are traced backwards according to a single step reverse algorithm [Neuman 1981], [Douglas and Russel 1982], [Baptista 1984], [Casulli 1987]. In Appendix 4.3 a more detailed discussion about Lagrangian, Eulerian and hybrid formulations is given.

Following [Neuman 1981, 1984], the total time derivative of C_d is computed by

$$\begin{aligned} \frac{DC_d(\mathbf{x}, t)}{Dt} &= \frac{\partial C_d(\mathbf{x}, t)}{\partial t} + \frac{\partial C_d(\mathbf{x}, t)}{\partial x_i} \frac{\partial x_i}{\partial t} \\ &= \frac{\partial C_d(\mathbf{x}, t)}{\partial t} + \nabla C_d \mathbf{v}^* \end{aligned} \quad (4.73)$$

where \mathbf{v}^* is the velocity of a particle that moved in the flow field, also known as the ‘seepage velocity’ and is equal to

$$\mathbf{v}^* = \frac{\mathbf{v}}{(\theta + \rho_0^m K_d)} \quad (4.74)$$

Eq. (4.73) describes changes with time along particle lines. For convenience, the arguments (\mathbf{x}, t) of the tensor quantities are omitted in the following.

The partial time derivative $\frac{\partial C_d}{\partial t}$ can therefore, according to the above, also be written as

$$\frac{\partial C_d}{\partial t} = \frac{DC_d}{Dt} - \nabla C_d \mathbf{v}^* \quad (4.75)$$

By substituting Eq. (4.75) into the l.h.s. of Eq. (4.71), the l.h.s. of the governing equation with the linear isotherm becomes

$$\begin{aligned} (\theta + \rho_0^m K_d) \frac{\partial C_d}{\partial t} + \mathbf{v} \nabla C_d &= (\theta + \rho_0^m K_d) \left(\frac{DC_d}{Dt} - \nabla C_d \mathbf{v}^* \right) + \mathbf{v} \nabla C_d \\ &= \frac{DC_d}{Dt} (\theta + \rho_0^m K_d) + \nabla C_d (\mathbf{v} - \mathbf{v}^* (\theta + \rho_0^m K_d)) \end{aligned} \quad (4.76)$$

Substituting the seepage velocity, Eq. (4.74), into Eq. (4.76), the advective term vanishes

$$(\theta + \rho_0^m K_d) \frac{\partial C_d}{\partial t} + \mathbf{v} \nabla C_d = \frac{DC_d}{Dt} (\theta + \rho_0^m K_d) \quad (4.77)$$

Back substituting Eq. (4.77) into Eq. (4.71) gives the governing equation (for a linear isotherm) in a Lagrangian formulation

$$\frac{DC_d}{Dt} (\theta + \rho_0^m K_d) = \text{div}(\mathbf{D}_{\tilde{z}_m} \cdot \nabla C_d) - \alpha^* \frac{\partial h}{\partial t} (\theta + \rho_0^m K_d) C_d + \left(L \frac{\partial h}{\partial t} - \frac{\partial \theta}{\partial t} \right) C_d \quad (4.78)$$

Similarly, by substituting Eq. (4.75) into Eq. (4.72), the temporal term in the governing equation with the non-linear isotherm becomes

$$\begin{aligned} \theta \frac{\partial C_d}{\partial t} + \mathbf{v} \nabla C_d &= \theta \left(\frac{DC_d}{Dt} - \nabla C_d \mathbf{v}^* \right) + \mathbf{v} \nabla C_d \\ &= \theta \frac{DC_d}{Dt} + \nabla C_d (\mathbf{v} - \mathbf{v}^* \theta) \end{aligned} \quad (4.79)$$

Where now the seepage velocity \mathbf{v}^* is defined as

$$\mathbf{v}^* = \frac{\mathbf{v}}{\theta} \quad (4.80)$$

Substituting this into Eq. (4.79), again the advective term vanishes

$$\theta \frac{\partial C_d}{\partial t} + \mathbf{v} \nabla C_d = \theta \frac{DC_d}{Dt} \quad (4.81)$$

Back substituting Eq. (4.81) into Eq. (4.72) gives the governing equation (for a nonlinear concentration isotherm) in a Lagrangian formulation

$$\begin{aligned} \theta \frac{DC_d}{Dt} + \rho_0^m \frac{dC_a}{dC_d} \frac{\partial C_d}{\partial t} &= \text{div}(\mathbf{D}_{\tilde{z}_m} \cdot \nabla C_d) - (\theta C_d + \rho_0^m C_a(C_d)) \alpha^* \frac{\partial h}{\partial t} \\ &\quad + \left(L \frac{\partial h}{\partial t} - \frac{\partial \theta}{\partial t} \right) C_d \end{aligned} \quad (4.82)$$

Both Eq. (4.78) and Eq. (4.82) no longer include the hyperbolic advective term. The equations could now be solved using a full implementation of the Lagrangian approach, i.e. using a moving coordinate system. Because of the challenges occurring due to a highly deforming grid, in RoAM a mixed Lagrangian-Eulerian approach is implemented, whereby the advective term of the total material time derivative $\frac{DC_d}{Dt}$ is separately evaluated in a Lagrangian manner by a single-step reverse particle tracking methodology. In the following this methodology is explained.

4.3.3 Particle tracking method

By formulating the total material time derivative of the desorbed concentration and replacing the partial time derivative of the governing equation, Eq. (4.78) and Eq. (4.82) no longer include the advective term [Baptista 1984], [Casulli 1987, 1990], [Douglas 1982], [Galeati 1992], [Kinzelbach 1987], [Neuman 1981, 1984].

The material time derivative $\frac{DC_d}{Dt}$ can now be approximated from

$$\frac{DC_d(\mathbf{x}, t)}{Dt} = \frac{C_d(\mathbf{x}_{t+\Delta t}, t + \Delta t) - C_d^*(\mathbf{x}_t^*, t)}{\Delta t} \quad (4.83)$$

To find the concentration C_d^* at time t , consider a fictitious particle that moves from a location \mathbf{x}_i^* at time t to a new location \mathbf{x}_i at time $t + \Delta t$, the latter coinciding with node n , Figure 4.3.1.

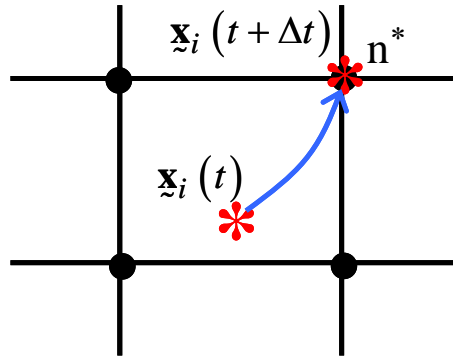


Figure 4.3.1: Movement of a fictitious particle

Since the movement of the particle is along the characteristic line with the seepage velocity \mathbf{v}^* , the initial particle location $\mathbf{x}_i^*(t)$ can be found from

$$\mathbf{x}_i^*(t) = \mathbf{x}_i(t + \Delta t) - \int_t^{t+\Delta t} \mathbf{v}^* dt \quad (4.84)$$

where the time integral is taken along the particle flow path.

If $\mathbf{x}_i^*(t)$ is located outside of the element under consideration $\Delta\tau(\mathbf{x}_t)$ must be found such that

$$\mathbf{x}_i^*(t) = \mathbf{x}_i(t + \Delta\tau) - \int_t^{t+\Delta\tau(\mathbf{x}_i^*)} \mathbf{v}^* dt \quad (4.85)$$

will be located within the element boundaries.

Once the backward particle position $\mathbf{x}_i(t)$ is known, the corresponding concentration $C_d^*(\mathbf{x}_i^*, t)$ can be obtained by interpolating between nodal values according to

$$C_d^*(\mathbf{x}_i^*, t) = \sum_{j=1}^n C_j(t) N_j(\mathbf{x}_i^*(t)) \quad (4.86)$$

The diffusion equation $\text{div}(\mathbf{D}_{\tilde{z}_m} \cdot \nabla C_d)$ is then solved using a fixed (Eulerian) coordinate system. The particle tracking procedure is explained in more detail in section 4.3.5.

4.3.4 Galerkin formulation of the governing equations

4.3.4.1 Linear isotherm

The weak form [Hughes 1987], see Appendix 4.1, of the Lagrangian governing equation with the linear isotherm, can be found by multiplying Eq. (4.78) with a weighting function w_i and integration over the domain

$$\int_V w_i \left[\frac{DC_d}{Dt} (\theta + \rho_0^m K_d) - \text{div}(\mathbf{D}_{\tilde{z}_m} \cdot \nabla C_d) + \alpha^* \frac{\partial h}{\partial t} (\theta + \rho_0^m K_d) C_d - \left(L \frac{\partial h}{\partial t} - \frac{\partial \theta}{\partial t} \right) C_d \right] dV = 0 \quad (4.87)$$

Integrating by parts gives

$$\begin{aligned} \int_V w_i \frac{DC_d}{Dt} (\theta + \rho_0^m K_d) dV - \int_V w_i \text{div}(\mathbf{D}_{\tilde{z}_m} \cdot \nabla C_d) dV \\ + \int_V w_i \alpha^* \frac{\partial h}{\partial t} (\theta + \rho_0^m K_d) C_d dV - \int_V w_i \left(L \frac{\partial h}{\partial t} - \frac{\partial \theta}{\partial t} \right) C_d dV = 0 \end{aligned} \quad (4.88)$$

The diffusion term is temporarily replaced by a vector

$$\mathbf{D}_{\tilde{z}_m} \cdot \nabla C_d = \mathbf{s} \quad (4.89)$$

It can be shown that

$$\begin{aligned} - \int_V w_i \text{div}(\mathbf{s}) dV &= - \int_V (\text{div}(w_i \mathbf{s}) - \mathbf{s} \cdot \nabla w_i) dV \\ &= - \int_V \text{div}(w_i \mathbf{s}) dV + \int_V (\mathbf{s} \cdot \nabla w_i) dV \end{aligned} \quad (4.90)$$

By making use of the divergence theorem, the first volume integral on the r.h.s. of Eq. (4.90) can be replaced by a surface integral

$$\int_V \text{div}(w_i \underline{s}) dV = \int_S (w_i \underline{s} \cdot \underline{n}) dS \quad (4.91)$$

Back substituting Eq. (4.89) through Eq. (4.91) into Eq. (4.88), yields

$$\begin{aligned} \int_V w_i \frac{DC_d}{Dt} (\theta + \rho_0^m K_d) dV - \int_S \underline{n} w_i \underline{D}_m \cdot \nabla C_d dS + \int_V (\underline{D}_m \cdot \nabla C_d \nabla w_i) dV \\ + \int_V w_i \alpha^* \frac{\partial h}{\partial t} (\theta + \rho_0^m K_d) C_d dV - \int_V w_i \left(L \frac{\partial h}{\partial t} - \frac{\partial \theta}{\partial t} \right) C_d dV = 0 \end{aligned} \quad (4.92)$$

The variable desorbed concentration term can be approximated by a summation of the nodal values j multiplied by a shape function N_j

$$C_d = \sum_{j=1}^n N_j C_j^d \quad (4.93)$$

Since the weighting functions w_i can be taken equal to the shape functions N_i , in the Galerkin method

$$w_i = N_i \quad (4.94)$$

Replacing Eq. (4.93) and Eq. (4.94) into Eq. (4.92) and summing over the volumes of the individual elements, the finite element approximation of the governing equation (with a linear isotherm) becomes

$$\begin{aligned} \sum_{j=1}^n \left(\int_V N_i (\theta + \rho_0^m K_d) N_j dV \right) \frac{DC_j^d}{Dt} + \sum_{j=1}^n \left(\int_V (\nabla N_i \underline{D}_m \cdot \nabla N_j) dV \right) C_j^d \\ + \sum_{j=1}^n \left(\int_V N_i \alpha^* \frac{\partial h}{\partial t} (\theta + \rho_0^m K_d) N_j dV \right) C_j^d \\ - \sum_{j=1}^n \left(\int_V N_i \left(L \frac{\partial h}{\partial t} - \frac{\partial \theta}{\partial t} \right) N_j dV \right) C_j^d = \int_S \underline{n} N_i \underline{D}_m \cdot \nabla C_d dS \end{aligned} \quad (4.95)$$

Recall that the storage term L consists of the following terms

$$L = \alpha^* \frac{\theta}{\phi} + \phi \frac{\partial S}{\partial h} \quad (4.96)$$

The saturation S was shown in the previous chapter as the moisture content θ divided by the porosity ϕ

$$S = \frac{\theta}{\phi} \quad (4.97)$$

Replacing Eq. (4.97) into Eq. (4.96)

$$L = \alpha^* \frac{\theta}{\phi} + \frac{\partial \theta}{\partial h} \quad (4.98)$$

Since the storage term is multiplied by the rate of the hydraulic head in Eq. (4.95), the partial derivative of the moisture content w.r.t. the hydraulic head becomes the rate of moisture content

$$L \frac{\partial h}{\partial t} = \left(\alpha^* \frac{\theta}{\phi} + \phi \frac{\partial S}{\partial h} \right) \frac{\partial h}{\partial t} = \alpha^* \frac{\theta}{\phi} \frac{\partial h}{\partial t} + \frac{\partial \theta}{\partial t} \quad (4.99)$$

Substituting Eq.(4.99) into Eq. (4.95), gives

$$\begin{aligned} & \sum_{j=1}^n \left(\int_{\mathbf{v}} N_i (\theta + \rho_0^m K_d) N_j dV \right) \frac{DC_j^d}{Dt} + \sum_{j=1}^n \left(\int_{\mathbf{v}} (\nabla N_i \underline{\underline{D}}_m \cdot \nabla N_j) dV \right) C_j^d \\ & + \sum_{j=1}^n \left(\int_{\mathbf{v}} N_i \alpha^* \frac{\partial h}{\partial t} (\theta + \rho_0^m K_d) N_j dV \right) C_j^d \\ & - \sum_{j=1}^n \left(\int_{\mathbf{v}} N_i \left(\alpha^* \frac{\theta}{\phi} \frac{\partial h}{\partial t} \right) N_j dV \right) C_j^d = \int_{\mathbf{s}} N_i \mathbf{n} \cdot \underline{\underline{D}}_m \cdot \nabla C_d dS \end{aligned} \quad (4.100)$$

Eq. (4.100) can be written in the following matrix format

$$[\mathbf{M}] \left\{ \frac{DC_d}{Dt} \right\} + ([\mathbf{D}] + [\mathbf{K}]) \{C_d\} = \{Q\} + \{B\} \quad (4.101)$$

where the mass matrix $[\mathbf{M}]$ is given by

$$M_{ij} = \sum_e \left(\int_{\mathbf{v}_e} N_i^e (\theta + \rho_0^m K_d) N_j^e dV \right) \frac{DC_j^d}{Dt} \quad (4.102)$$

the diffusion matrix $[\mathbf{D}]$ is given by

$$D_{ij} = \sum_e \left(\int_{\mathbf{v}_e} (\nabla N_i^e \underline{\underline{D}}_m \cdot \nabla N_j^e) dV \right) \quad (4.103)$$

the matrix $[\mathbf{K}]$ associated with the first order terms is given by

$$K_{ij} = \sum_e \left(\int_{\mathbf{v}_e} N_i^e \left[\alpha^* \frac{\partial h}{\partial t} (\theta + \rho_0^m K_d) - \alpha^* \frac{\theta}{\phi} \frac{\partial h}{\partial t} \right] N_j^e dV \right) \quad (4.104)$$

and the boundary condition vector $\{B\}$ is given by

$$B_i = \int_{\mathbf{s}_e} N_i^e \mathbf{n} \cdot \underline{\underline{D}}_m \cdot \nabla C_d dS \quad (4.105)$$

where either a concentration or a concentration flux can be given as boundary conditions.

4.3.4.2 Non-linear isotherm

Using the same procedure as above for the governing equation with the non-linear isotherms, Eq. (4.82), the weak form can be written as

$$\begin{aligned} & \int_{\mathbf{V}} w_i \theta \frac{DC_d}{Dt} dV + \int_{\mathbf{V}} w_i \rho_0^m \frac{dC_a}{dC_d} \frac{\partial C_d}{\partial t} dV - \int_{\mathbf{V}} w_i \operatorname{div}(\underline{D}_m \cdot \nabla C_d) dV \\ & + \int_{\mathbf{V}} w_i \left(\theta C_d + \rho_0^m C_a(C_d) \right) \alpha^* \frac{\partial h}{\partial t} dV - \int_{\mathbf{V}} w_i \left(L \frac{\partial h}{\partial t} - \frac{\partial \theta}{\partial t} \right) C_d dV = 0 \end{aligned} \quad (4.106)$$

Since the isotherm between the adsorbed and desorbed mastic particles is not linear here, the hydraulic rate term in Eq. (4.106) needs to be slightly rewritten into

$$\begin{aligned} \int_{\mathbf{V}} w_i \left(\theta C_d + \rho_0^m C_a \right) \alpha^* \frac{\partial h}{\partial t} dV &= \int_{\mathbf{V}} w_i \left(\theta C_d + \rho_0^m \left(C_a + \frac{dC_a}{dC_d} C_d - \frac{dC_a}{dC_d} C_d \right) \right) \alpha^* \frac{\partial h}{\partial t} dV \\ &= \int_{\mathbf{V}} w_i \left(\theta C_d + \rho_0^m \frac{dC_a}{dC_d} C_d \right) \alpha^* \frac{\partial h}{\partial t} dV \\ &\quad + \int_{\mathbf{V}} w_i \rho_0^m \left(C_a - \frac{dC_a}{dC_d} C_d \right) \alpha^* \frac{\partial h}{\partial t} dV \end{aligned} \quad (4.107)$$

Back substituting Eq. (4.107) into Eq. (4.106) gives

$$\begin{aligned} & \int_{\mathbf{V}} w_i \theta \frac{DC_d}{Dt} dV + \int_{\mathbf{V}} w_i \rho_0^m \frac{dC_a}{dC_d} \frac{\partial C_d}{\partial t} dV - \int_{\mathbf{V}} w_i \operatorname{div}(\underline{D}_m \cdot \nabla C_d) dV \\ & + \int_{\mathbf{V}} w_i \left(\theta C_d + \rho_0^m \frac{dC_a}{dC_d} C_d \right) \alpha^* \frac{\partial h}{\partial t} dV + \int_{\mathbf{V}} w_i \rho_0^m \left(C_a - \frac{dC_a}{dC_d} C_d \right) \alpha^* \frac{\partial h}{\partial t} dV \\ & - \int_{\mathbf{V}} w_i \left(L \frac{\partial h}{\partial t} - \frac{\partial \theta}{\partial t} \right) C_d dV = 0 \end{aligned} \quad (4.108)$$

By following the same procedure as for the governing equation with the linear isotherm, the finite element approximation of Eq. (4.108) can be found as

$$\begin{aligned} & \sum_{j=1}^n \left(\int_{\mathbf{V}} N_i \theta N_j dV \right) \frac{DC_j^d}{Dt} + \sum_{j=1}^n \left(\int_{\mathbf{V}} N_i \rho_0^m \frac{dC_a}{dC_d} N_j dV \right) \frac{\partial C_j^d}{\partial t} \\ & + \sum_{j=1}^n \left(\int_{\mathbf{V}} (\nabla N_i \underline{D}_m \cdot \nabla N_j) dV \right) C_j^d \\ & + \sum_{j=1}^n \left(\int_{\mathbf{V}} N_i \alpha^* \frac{\partial h}{\partial t} \left(\theta + \rho_0^m \frac{dC_a}{dC_d} \right) N_j dV \right) C_j^d \\ & - \sum_{j=1}^n \left(\int_{\mathbf{V}} N_i \left(\alpha^* \frac{\theta}{\phi} \frac{\partial h}{\partial t} \right) N_j dV \right) C_j^d \\ & = \int_{\mathbf{S}} N_i \mathbf{n} \cdot \underline{D}_m \cdot \nabla C_d dS - \int_{\mathbf{V}} N_i \alpha^* \frac{\partial h}{\partial t} \rho_0^m \left(C_a - \frac{dC_a}{dC_d} C_d \right) dV \end{aligned} \quad (4.109)$$

Eq. (4.109) can be written in the following matrix representation

$$\left(\left[\mathbf{M}^I \right] \left\{ \frac{DC_d}{Dt} \right\} + \left[\mathbf{M}^{II} \right] \left\{ \frac{dC_d}{dt} \right\} \right) + ([D] + [K]) \{C_d\} = \{Q\} + \{B\} \quad (4.110)$$

where the mass matrices $\left[\mathbf{M}^I \right]$ and $\left[\mathbf{M}^{II} \right]$ are given by

$$M_{ij}^I = \sum_e \left(\int_{V_e} N_i^e \theta N_j^e dV \right) \quad (4.111)$$

$$M_{ij}^{II} = \sum_e \left(\int_{V_e} N_i^e \rho_0^m \frac{dC_a}{dC_d} N_j^e dV \right) \quad (4.112)$$

the dispersion matrix $[D]$, the matrix $[K]$, associated with the first order terms, and the load vector $\{B\}$ are equal to Eq. (4.103) through Eq. (4.105), respectively.

The vector $\{Q\}$ is associated with all zero-order derivative terms and is given by

$$Q_i = \int_{V_e} N_i^e \alpha^* \frac{\partial h}{\partial t} \rho_0^m \left(C_a - \frac{dC_a}{dC_d} C_d \right) dV \quad (4.113)$$

Similar to the flow equation, a Gaussian quadrature is used for the numerical integration of the above matrices.

4.3.5 In time approximation

The time approximation of the mastic transport equation is, similar to the flow equation, performed via the α -method of time integration [Bathe 1996], [Hughes 1987], [Press 1989]. However, since for the approximation of the mastic-transport equation a hybrid Lagrangian-Eulerian formulation is used, the time integration of the mastic transport equation is somewhat different than for the flow equation, and is discussed in the following.

For the case of a linear relation between the absorbed and desorbed mastic particles, the mastic transport equation was found as

$$[M] \frac{D}{Dt} \{C_d\} + ([D] + [K]) \{C_d\} = \{F\} \quad (4.114)$$

where the vectors on the r.h.s. of Eq. (4.101) are here replaced by a single load vector $\{F\}$.

Following the α -method of time integration, as described in section 4.2.3, Eq. (4.114) should be evaluated as

$$[M] \frac{D}{Dt} \{C_d\}_{n+\alpha} + ([D] + [K]) \{C_d\}_{n+\alpha} = \{F\} \quad (4.115)$$

with

$$\{C_d\}_{n+\alpha} = (1-\alpha)\{C_d\}_n + \alpha\{C_d\}_{n+1} \quad (4.116)$$

and

$$\frac{D}{Dt}\{C_d\}_{n+\alpha} = \frac{1}{\Delta t}(\{C_d\}_{n+1} - \{C_d\}_n) \quad (4.117)$$

where $[M]$, $[D]$, $[K]$ and $\{F\}$ are evaluated at $n + \alpha$ (i.e. $t + \alpha\Delta t$).

However, as discussed in section 4.3.3, the material time derivative of C_d is approximated by

$$\frac{D}{Dt}\{C_d\} = \frac{1}{\Delta\tau}(\{C_d\}_{n+1} - \{C_d^*\}_n) \quad (4.118)$$

where $\{C_d^*\}$ is the Lagrangian concentration vector at time t at location \underline{x}_i^* and where $\Delta\tau \leq \Delta t$.

Therefore, Eq. (4.115) is becomes

$$\frac{[M]}{\Delta\tau}(\{C_d\}_{n+1} - \{C_d^*\}_n) + ([D] + [K])\{C_d\}_{n+\alpha} = \{F\} \quad (4.119)$$

with

$$\{C_d\}_{n+\alpha} = (1-\alpha)\{C_d^*\}_n + \alpha\{C_d\}_{n+1} \quad (4.120)$$

Substituting Eq. (4.120) into Eq. (4.119) gives

$$\frac{[M]}{\Delta\tau}(\{C_d\}_{n+1} - \{C_d^*\}_n) + (1-\alpha)([D] + [K])\{C_d^*\}_n + \alpha([D] + [K])\{C_d\}_{n+1} = \{F\} \quad (4.121)$$

By rearranging Eq. (4.121), it is found that

$$\left(\frac{[M]}{\Delta\tau} + \alpha([D] + [K])\right)\{C_d\}_{n+1} = \left(\frac{[M]}{\Delta\tau} + (\alpha-1)([D] + [K])\right)\{C_d^*\}_n + \{F\} \quad (4.122)$$

from which $\{C_d\}_{n+1}$ can be found since the r.h.s. is known.

For the nonlinear relation between the desorbed and the adsorbed mastic, Eq. (4.110), can be approximated with the α -method of time integration as

$$\left([M^I]\frac{D}{Dt}\{C_d\} + [M^{II}]\frac{d}{dt}\{C_d\}_{n+\alpha}\right) + ([D] + [K])\{C_d\}_{n+\alpha} = \{F\} \quad (4.123)$$

with Eq. (4.120) and

$$\frac{d}{dt}\{C_d\}_{n+\alpha} = \frac{1}{\Delta t}(\{C_d\}_{n+1} - \{C_d\}_n) \quad (4.124)$$

Similar to the mastic transport equation for the linear case, the total material time derivative is computed from

$$\frac{D}{Dt}\{C_d\} = \frac{1}{\Delta\tau}\left(\{C_d\}_{n+1} - \{C_d^*\}_n\right) \quad (4.125)$$

where $\{C_d^*\}_n$ is the Lagrangian concentration vector at time t at location \mathbf{x}_i^* and where $\Delta\tau \leq \Delta t$.

Substituting Eq. (4.120), Eq. (4.124) and Eq. (4.125) into Eq. (4.123) gives

$$\begin{aligned} \frac{[M^I]}{\Delta\tau}\left(\{C_d\}_{n+1} - \{C_d^*\}_n\right) + \frac{[M^{II}]}{\Delta t}\left(\{C_d\}_{n+1} - \{C_d\}_n\right) + (1-\alpha)([D]+[K])\{C_d^*\}_n \\ + \alpha([D]+[K])\{C_d\}_{n+1} = \{F\} \end{aligned} \quad (4.126)$$

By rearranging Eq. (4.126), it is found that

$$\begin{aligned} \left(\frac{[M^I]}{\Delta\tau} + \frac{[M^{II}]}{\Delta t} + \alpha([D]+[K])\right)\{C_d\}_{n+1} \\ = \frac{[M^I]}{\Delta\tau}\{C_d^*\}_n + \frac{[M^{II}]}{\Delta t}\{C_d\}_n + (\alpha-1)([D]+[K])\{C_d^*\}_n + \{F\} \end{aligned} \quad (4.127)$$

from which $\{C_d\}_{n+1}$ can be found since the r.h.s. is known.

Eq. (4.122) and Eq. (4.127) can be written as a matrix equation

$$[P]\{C_d\} = \{W\} \quad (4.128)$$

where $[P]$ is the matrix, $\{C_d\}$ is the unknown vector to be found and represents the values of discretized concentration field at a new time, and $\{W\}$ is the load vector.

For the case of the linear isotherm:

for $\alpha = 0.0$

$$\begin{aligned} [P] &= \frac{[M]}{\Delta\tau} \\ \{W\} &= \frac{[M]}{\Delta\tau}\{C_d^*\} - ([D]+[K])\{C_d^*\} + \{F\} \end{aligned} \quad (4.129)$$

for $\alpha = 0.5$

$$\begin{aligned} [P] &= \frac{[M]}{\Delta\tau} + 0.5([D]+[K]) \\ \{W\} &= \frac{[M]}{\Delta\tau}\{C_d^*\} - 0.5([D]+[K])\{C_d^*\} + \{F\} \end{aligned} \quad (4.130)$$

for $\alpha = 1.0$

$$\begin{aligned}
[\mathbf{P}] &= \frac{[\mathbf{M}]}{\Delta\tau} + [\mathbf{D}] + [\mathbf{K}] \\
\{\mathbf{W}\} &= \frac{[\mathbf{M}]}{\Delta\tau} \{\mathbf{C}_d^*\} + \{\mathbf{F}\}
\end{aligned}
\tag{4.131}$$

For the case of the non-linear isotherm
for $\alpha = 0.0$

$$\begin{aligned}
[\mathbf{P}] &= \frac{[\mathbf{M}^I]}{\Delta\tau} + \frac{[\mathbf{M}^{II}]}{\Delta t} \\
\{\mathbf{W}\} &= \frac{[\mathbf{M}^I]}{\Delta\tau} \{\mathbf{C}_d^*\} + \frac{[\mathbf{M}^{II}]}{\Delta t} \{\mathbf{C}_d\}_n - ([\mathbf{D}] + [\mathbf{K}]) \{\mathbf{C}_d^*\} + \{\mathbf{F}\}
\end{aligned}
\tag{4.132}$$

for $\alpha = 0.5$

$$\begin{aligned}
[\mathbf{P}] &= \frac{[\mathbf{M}^I]}{\Delta\tau} + \frac{[\mathbf{M}^{II}]}{\Delta t} + 0.5([\mathbf{D}] + [\mathbf{K}]) \\
\{\mathbf{W}\} &= \frac{[\mathbf{M}^I]}{\Delta\tau} \{\mathbf{C}_d^*\} + \frac{[\mathbf{M}^{II}]}{\Delta t} \{\mathbf{C}_d\}_n - 0.5([\mathbf{D}] + [\mathbf{K}]) \{\mathbf{C}_d^*\} + \{\mathbf{F}\}
\end{aligned}
\tag{4.133}$$

for $\alpha = 1.0$

$$\begin{aligned}
[\mathbf{P}] &= \frac{[\mathbf{M}^I]}{\Delta\tau} + \frac{[\mathbf{M}^{II}]}{\Delta t} + [\mathbf{D}] + [\mathbf{K}] \\
\{\mathbf{W}\} &= \frac{[\mathbf{M}^I]}{\Delta\tau} \{\mathbf{C}_d^*\} + \frac{[\mathbf{M}^{II}]}{\Delta t} \{\mathbf{C}_d\}_n + \{\mathbf{F}\}
\end{aligned}
\tag{4.134}$$

The numerical approximations, as discussed in this chapter, lead to systems of equations for the discretized domain in the form of

$$[\mathbf{A}]\{\mathbf{x}\} = \{\mathbf{b}\}
\tag{4.135}$$

where $[\mathbf{A}]$ is a matrix containing coefficients related to grid discretization and material properties, $\{\mathbf{x}\}$ is a vector containing the dependent variables which we are solving for and $\{\mathbf{b}\}$ is a vector containing all the initial and boundary conditions.

To solve this matrix equation, in RoAM a pointwise iterative solver is utilized, which employs the basic successive iterative method, including a Gauss-Seidel and a successive under- and over-relaxation method.

Weak Formulation

Before applying the finite element method to solve a governing equation it is necessary to transform the equation into a more suitable form. To do so, the so called weak formulation can be derived, [Hughes 1987]. Originally the weak formulation has been introduced by mathematicians to investigate the behavior of the solution of partial differential equations, and to prove existence and uniqueness of the solution. Later on numerical schemes have been based on this formulation which leads to an approximate solution in a constructive way. In the following, a brief procedure is given to transform a differential equation into its weak formulation.

Suppose that the following differential equation needs to be solved over the interval $[0,1]$:

$$\nabla^2 u + f = 0 \tag{A 4.1.1}$$

Given the boundary conditions:

$$u(1) = q \tag{A 4.1.2}$$

$$\nabla u(0) = -h \tag{A 4.1.3}$$

Using the weighting function w which fulfils

$$w(1) = 0 \tag{A 4.1.4}$$

Eq. (A 4.1.1) may be written in the weak form

$$-\int_0^1 w(\nabla^2 u + f) dx = 0 \tag{A 4.1.5}$$

Splitting the integral into two parts gives

$$-\int_0^1 w \nabla^2 u dx - \int_0^1 w f dx = 0 \tag{A 4.1.6}$$

Where the Laplacian ∇^2 can be replaced by taking a divergence from a gradient

$$-\int_0^1 w \operatorname{div}(\nabla u) dx - \int_0^1 w f dx = 0 \tag{A 4.1.7}$$

Since it can be shown that

$$w \operatorname{div}(\nabla u) = \operatorname{div}(w \nabla u) - \nabla w \nabla u \tag{A 4.1.8}$$

Eq. (A 4.1.7) can be rewritten as

$$-\int_0^1 \text{div}(w\nabla u) \, dx + \int_0^1 \nabla w \nabla u \, dx - \int_0^1 w f \, dx = 0 \quad (\text{A 4.1.9})$$

According to the divergence theorem an integral over a volume can be transformed into an integral over a surface area as follows

$$\int_V \text{div}(\underline{y}) \, dV = \int_S \underline{n} \cdot \underline{y} \, dS \quad (\text{A 4.1.10})$$

Using this, Eq. (A 4.1.9) becomes

$$-w\nabla u|_0^1 + \int_0^1 \nabla w \nabla u \, dx - \int_0^1 w f \, dx = 0 \quad (\text{A 4.1.11})$$

By satisfying the boundary conditions Eq. (A 4.1.3) and Eq. (A 4.1.4), and rearranging, Eq. (A 4.1.11) can be shown as

$$\int_0^1 \nabla w \nabla u \, dx = \int_0^1 w f \, dx + w(0)h \quad (\text{A 4.1.12})$$

which is known in literature as the weak form of Eq. (A 4.1.1).

Time Approximation Methods

Following [Bathe 1996], [Hughes 1987] and [Press 1989], from Eq. (4.15) the flow equation was reformulated into a matrix formulation

$$[M] \left\{ \frac{dh}{dt} \right\} + [S] \{h\} = \{F\} \quad (\text{A 4.2.1})$$

The initial value problem consists of finding a function $\underline{h} = \underline{h}(t)$ satisfying Eq. (A 4.2.1) and the initial condition $\underline{h}(0) = \underline{h}_0$, where \underline{h}_0 is given.

The time of the simulation $0 \leq t \leq t_E$ can be subdivided into time steps Δt_n with $n = 1$ to n_{TS} , where n_{TS} is the number of time steps and t_E is the end of the simulation.

There are different methods to find approximations of $\left\{ \frac{dh}{dt} \right\}$ and $\{h\}$. In the following the two most commonly used methods are discussed in detail.

The α method of time integration

For this first method Eq. (A 4.2.1) can be written as

$$[M] \left\{ \frac{dh}{dt} \right\}_{n+\alpha} + [S] \{h\}_{n+\alpha} = \{F\} \quad (\text{A 4.2.2})$$

where $\left\{ \frac{dh}{dt} \right\}_{n+\alpha}$ and $\{h\}_{n+\alpha}$ are the approximations of $\dot{\underline{h}}(t_{n+\alpha})$ and $\underline{h}(t_{n+\alpha})$.

The values of $\{h\}_{n+\alpha}$ are determined on the basis of $\{h\}_n$ and $\{h\}_{n+1}$, where the contribution of each vector depends on a weighting parameter α , taken to be in the interval $[0,1]$:

$$\{h\}_{n+\alpha} = (1-\alpha)\{h\}_n + \alpha\{h\}_{n+1} \quad (\text{A 4.2.3})$$

Assuming a constant time step

$$\Delta t_n = \Delta t = \frac{t_E}{n_{TS}} \quad (\text{A 4.2.4})$$

the time differential $\left\{ \frac{dh}{dt} \right\}_{n+\alpha}$ can be determined via

$$\left\{ \frac{dh}{dt} \right\}_{n+\alpha} = \frac{1}{\Delta t} (\{h\}_{n+1} - \{h\}_n) \quad (\text{A 4.2.5})$$

When substituting Eq. (A 4.2.3) and Eq. (A 4.2.5) into Eq. (A 4.2.2), the flow equation becomes

$$\frac{[M]}{\Delta t} (\{h\}_{n+1} - \{h\}_n) + [S](1-\alpha)\{h\}_n + \alpha[S]\{h\}_{n+1} = \{F\} \quad (\text{A 4.2.6})$$

By rearranging Eq. (A 4.2.6), the values of $\{h\}_{n+1}$ can be found from

$$\left(\frac{[M]}{\Delta t} + \alpha[S] \right) \{h\}_{n+1} = \{F\} + \left(\frac{[M]}{\Delta t} - [S](1-\alpha) \right) \{h\}_n \quad (\text{A 4.2.7})$$

where $[M]$, $[S]$ and $[F]$ are evaluated at $t + \alpha\Delta t$.

For the case of $\alpha = 0$, the above method is also known as the explicit forward Euler method. For the cases of $\alpha = 0,5$ and $\alpha = 1,0$, the method is referred to as the implicit Crank-Nicolson (or trapezoidal) and the implicit backward Euler method, respectively.

The Crank-Nicolson algorithm has a truncation error of $O(\Delta t^2)$, but its propagation-of-error characteristics frequently lead to oscillatory nonlinear instability. Both the backward-difference and forward-difference have a truncation error of $O(\Delta t)$. The backward-difference is quite resistant to oscillatory nonlinear instability. On the other hand, the forward difference is only conditionally stable even for linear problems, not to mention nonlinear problems.

Central difference method

Another way of approximating Eq. (A 4.2.1) is via the central difference method, which is an explicit method.

In this method the values of the unknown variables are assumed to vary linearly during the time step Δt_n . The values can therefore be evaluated halfway the time step

$$[M] \left\{ \frac{dh}{dt} \right\}_{n+1/2} + [S] \{h\}_{n+1/2} = \{F\} \quad (\text{A 4.2.8})$$

where $[M]$, $[S]$ and $\{F\}$ are evaluated at $t + \Delta t/2$.

When considering an algorithm with a variable time step, the time increment can be defined as

$$\begin{aligned}\Delta t_{n+1/2} &= t_{n+1} - t_n \\ t_{n+1/2} &= \frac{1}{2}(t_{n+1} + t_n) \\ \Delta t_n &= t_{n+1/2} - t_{n-1/2}\end{aligned}\tag{A 4.2.9}$$

In Fig. A 7.1.1 an illustration of these time steps is given for the case of $n = 1$.

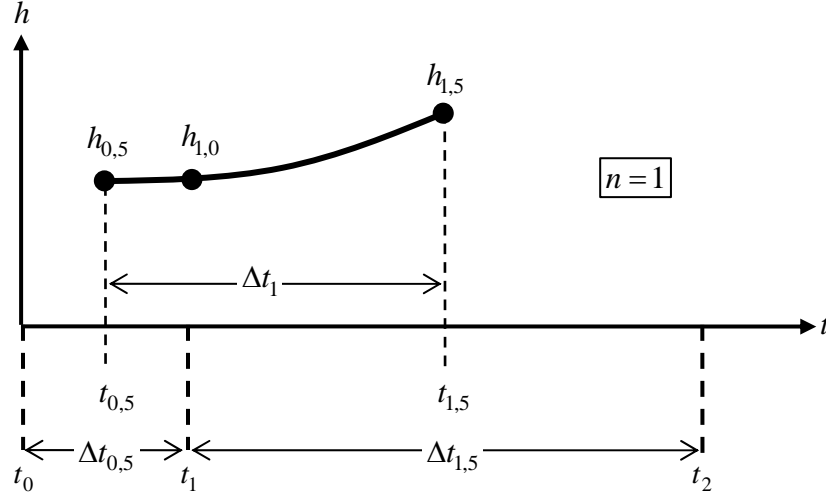


Fig. A 7.1.1:: Example of central difference method for 1 time step, with $\Delta t \neq \text{constant}$

The central difference formula for the vector $\left\{ \frac{dh}{dt} \right\}$ is given by

$$\left\{ \frac{dh}{dt} \right\}_n = \frac{\{h\}_{n+1/2} - \{h\}_{n-1/2}}{\Delta t_n}\tag{A 4.2.10}$$

or

$$\left\{ \frac{dh}{dt} \right\}_{n+1/2} = \frac{\{h\}_{n+1} - \{h\}_n}{\Delta t_{n+1/2}}\tag{A 4.2.11}$$

Substituting Eq. (A 4.2.11) into Eq. (A 4.2.8) gives

$$[M] \left(\frac{\{h\}_{n+1} - \{h\}_n}{\Delta t_{n+1/2}} \right) + [S] \{h\}_{n+1/2} = \{F\}\tag{A 4.2.12}$$

When choosing a constant time step, see Fig. A 7.1.2, i.e.

$$\Delta t_n = \Delta t = \frac{t_E}{n_{TS}}\tag{A 4.2.13}$$

Eq. (A 4.2.11) changes into

$$\left\{ \frac{dh}{dt} \right\}_{n+1/2} = \frac{\{h\}_{n+1} - \{h\}_n}{\Delta t} = \frac{2}{\Delta t} \left(\{h\}_{n+1/2} - \{h\}_n \right) \quad (\text{A 4.2.14})$$

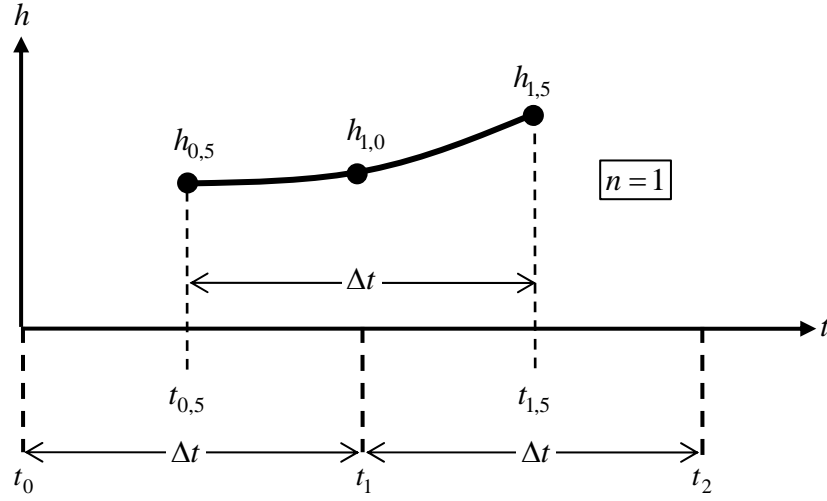


Fig. A 7.1.2: Example of central difference method for 1 time step, with $\Delta t = \text{constant}$

Substituting Eq. (A 4.2.14) into Eq. (A 4.2.8) gives

$$\frac{2}{\Delta t} [\mathbf{M}] \left(\{h\}_{n+1/2} - \{h\}_n \right) + [\mathbf{S}] \{h\}_{n+1/2} = \{F\} \quad (\text{A 4.2.15})$$

which can be rewritten as

$$\left(\frac{2}{\Delta t} [\mathbf{M}] + [\mathbf{S}] \right) \{h\}_{n+1/2} = \{F\} + \frac{2}{\Delta t} [\mathbf{M}] \{h\}_n \quad (\text{A 4.2.16})$$

from which the unknown $\{h\}_{n+1/2}$ can be solved.

The central difference method is among the most popular of the explicit methods in computational mechanics because it is easily implemented and very robust. The disadvantage of this method is that when the time step exceeds a critical value Δt_{crit} , the solution will grow unboundedly.

Arbitrary Lagrangian Eulerian descriptions

Lagrangian and Eulerian description

In a classical continuum, the location of a point before deformation is determined by the position vector $\underline{\mathbf{X}}$ defined in a Cartesian basis system $\{\underline{\mathbf{E}}_I ; I=1,2,3\}$, Fig. 0.1. After deformation, the coordinates of point P are located by position vector $\underline{\mathbf{x}}$ defined w.r.t. an alternative Cartesian basis system $\{\underline{\mathbf{e}}_i ; i=1,2,3\}$. The motion of a particle from the reference to the current position can be viewed as a vector mapping

$$\underline{\mathbf{x}} = \phi(\underline{\mathbf{X}}) \tag{A 4.3.1}$$

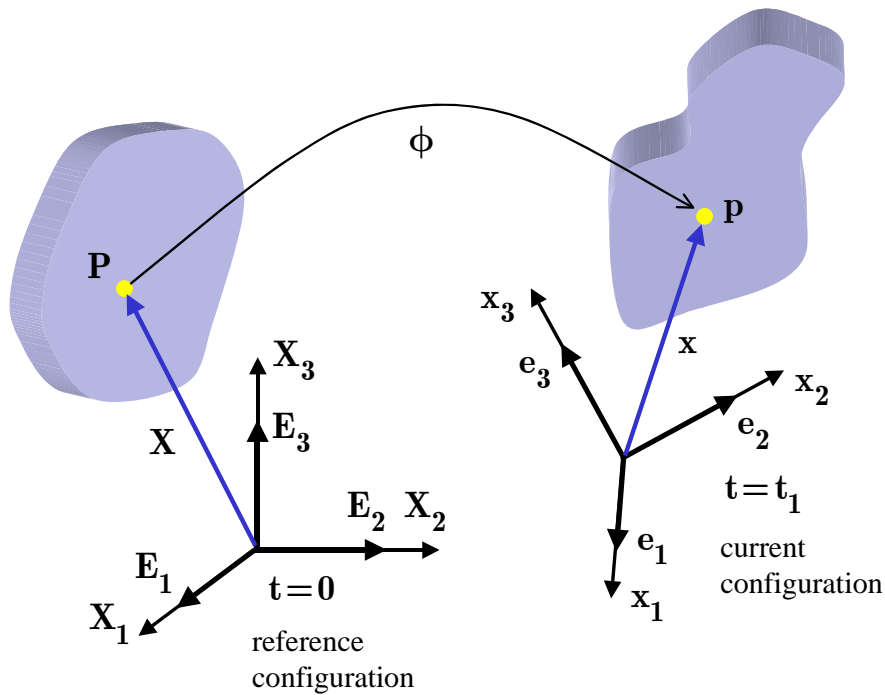


Fig. 0.1: Reference and current configurations of a deformable body

Eq. (A 4.3.1) can be generalized to read

$$\underline{\mathbf{x}} = \phi(\underline{\mathbf{X}}, t) \tag{A 4.3.2}$$

and

$$\underline{\mathbf{X}} = \phi^{-1}(\underline{\mathbf{x}}, t) \tag{A 4.3.3}$$

The so called material (or referential) description is a characterization of the motion (or any other quantity) w.r.t. the material coordinates X_1, X_2, X_3 and time t , given by Eq. (A 4.3.2). In the material description, attention is paid to what happens to a particle as it moves. The material description is also known as the Lagrangian description.

The so called Eulerian (or spatial) description, is a characterization of the motion (or any other quantity) w.r.t. the spatial coordinates x_1, x_2, x_3 and time t , given by Eq. (A 4.3.3). In the Eulerian description attention is paid to what happens to a point in space as time changes.

In fluid mechanics the Eulerian description is most often used, in which all relevant quantities are referred to the position in space at time t . It is not useful to refer the quantities to the material coordinates at $t = 0$, which are in general not known in fluid mechanics. In solid mechanics both types of descriptions are used, even though the Lagrangian description is often preferred.

Hybrids between Lagrangian and Eulerian formulations

In some cases, Lagrangian methods are not suitable. For example, in fluid mechanics problems with high velocity flows, interest is usually focused on a particular spatial subdomain. Similarly, the modeling of processes, such as a seepage or extrusion process, involves fixed spatial domains through which the material flows. These types of problems are more suited to Eulerian elements. In Eulerian finite elements, the elements are fixed in space and material convects through the elements. Eulerian finite elements thus undergo no distortion due to material motion. However, the treatment of constitutive equations and updates is complicated due to the convection of material through the elements.

Unfortunately, the treatment of moving boundaries and interfaces is difficult with Eulerian elements. Therefore, hybrid techniques which combine the advantages of Eulerian and Lagrangian methods have been developed and are often referred to as arbitrary Lagrangian Eulerian (ALE) methods. Eulerian methods can also be viewed as a subset of the ALE methods.

In an ALE method, both the motion of the mesh and the material must be described. The *material* motion is described by Eq. (A 4.3.2). In the ALE formulation, another reference domain $\hat{\Omega}$ is considered, Fig. 0.2.

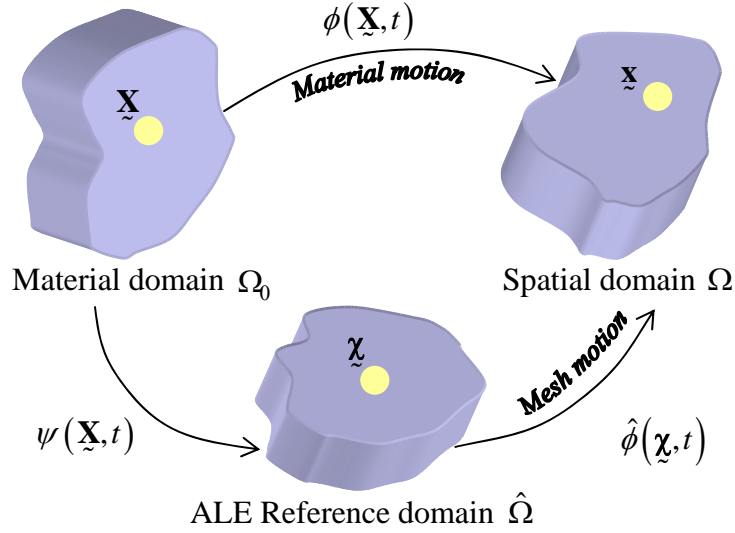


Fig. 0.2: Mapping between Lagrangian, Eulerian and ALE domain

The values of the position of particles in the ALE domain are noted by $\underline{\tilde{\chi}}$

$$\underline{\tilde{\chi}} = \phi(\underline{\tilde{\mathbf{X}}}, t) \quad (\text{A 4.3.4})$$

The coordinates $\underline{\tilde{\chi}}$ are called the ALE coordinates. In most cases $\phi(\underline{\tilde{\mathbf{X}}}, 0) = \underline{\tilde{\mathbf{X}}}$, which means $\underline{\tilde{\chi}}(\underline{\tilde{\mathbf{X}}}, 0) = \underline{\tilde{\mathbf{X}}}$. The referential domain $\hat{\Omega}$ is used to describe the motion of the mesh, independent of the motion of the material. In the implementation, this domain is used to construct the initial mesh. It remains coincident with the mesh throughout the computation, so it can also be considered the computational domain.

The motion of the mesh is described by

$$\underline{\tilde{\mathbf{x}}} = \hat{\phi}(\underline{\tilde{\chi}}, t) \quad (\text{A 4.3.5})$$

The mapping function $\hat{\phi}$ plays a crucial role in the ALE finite element formulation.

As becomes apparent from Fig. 0.2, the ALE coordinates can be related to the material coordinates by a composition of functions

$$\underline{\tilde{\chi}} = \hat{\phi}^{-1}(\underline{\tilde{\mathbf{x}}}, t) = \hat{\phi}^{-1}(\phi(\underline{\tilde{\mathbf{X}}}, t), t) = \psi(\underline{\tilde{\mathbf{X}}}, t) \quad (\text{A 4.3.6})$$

As can be concluded from Eq. (A 4.3.6), the relation between the material coordinates and the ALE coordinates is a function of time.

The material motion can furthermore be expressed as a composition of the mesh motion and the ALE mapping

$$\underline{\tilde{\mathbf{x}}} = \phi(\underline{\tilde{\mathbf{X}}}, t) = \hat{\phi}(\underline{\tilde{\chi}}, t) = \hat{\phi}(\psi(\underline{\tilde{\mathbf{X}}}, t), t) \quad (\text{A 4.3.7})$$

In an ALE algorithm the mesh motion is prescribed or computed. The material motion can then be reconstructed through the above compositions, provided the mapping function ψ is invertible.

Material time derivative and convective velocity

In ALE descriptions, fields are usually expressed as functions of the ALE coordinates $\underline{\chi}$ and time t . The material time derivative (or total time derivative) must then be obtained by the chain rule. Consider a function $f(\underline{\chi}, t)$. The total time derivative of this function can be found as

$$\begin{aligned} \frac{Df(\underline{\chi}, t)}{Dt} &= \frac{\partial f(\underline{\chi}, t)}{\partial t} + \frac{\partial f(\underline{\chi}, t)}{\partial \underline{\chi}} \frac{\partial \underline{\chi}}{\partial t} \\ &= \frac{\partial f(\underline{\chi}, t)}{\partial t} + \frac{\partial f(\underline{\chi}, t)}{\partial \chi_i} \frac{\partial \psi_i(\underline{\mathbf{X}}, t)}{\partial t} \end{aligned} \quad (\text{A 4.3.8})$$

The last term on the r.h.s. of Eq. (A 4.3.8) is defined as the referential particle velocity p_i

$$p_i = \frac{\partial \psi_i(\underline{\mathbf{X}}, t)}{\partial t} = \left. \frac{\partial \chi_i}{\partial t} \right|_{[\underline{\mathbf{X}}]} \quad (\text{A 4.3.9})$$

Substituting Eq. (A 4.3.9) into Eq. (A 4.3.8) gives the following expression for the total time derivative

$$\frac{Df}{Dt} = \frac{\partial f}{\partial t} + \frac{\partial f}{\partial \chi_i} p_i \quad (\text{A 4.3.10})$$

The ALE field variables are often treated as functions of the material coordinates and time. Hence, it is convenient to develop expressions for the material time derivative in terms of the spatial gradient. For this reason the relation between the material velocity, mesh velocity and referential velocity needs to be defined.

Keeping Eq. (A 4.3.7) and Eq. (A 4.3.9) in mind, the material velocity can be found as

$$\begin{aligned} v_j &= \frac{\partial x_j}{\partial t} = \frac{\partial \phi_j(\underline{\mathbf{X}}, t)}{\partial t} = \frac{\partial \hat{\phi}_j(\underline{\chi}, t)}{\partial t} \\ &= \frac{\partial \hat{\phi}_j}{\partial t} + \frac{\partial \hat{\phi}_j(\underline{\chi}, t)}{\partial \chi_i} \frac{\partial \psi_i(\underline{\mathbf{X}}, t)}{\partial t} \\ &= \hat{v}_j + \left. \frac{\partial x_j}{\partial \chi_i} \frac{\partial \chi_i}{\partial t} \right|_{[\underline{\mathbf{X}}]} \\ &= \hat{v}_j + \frac{\partial x_j}{\partial \chi_i} p_i \end{aligned} \quad (\text{A 4.3.11})$$

where \hat{v}_j is the mesh velocity.

The convective velocity \underline{c} is now defined as the difference between the material and the mesh velocities

$$c_j = v_j - \hat{v}_j \quad (\text{A 4.3.12})$$

Substituting Eq. (A 4.3.11) into Eq. (A 4.3.12) yields

$$c_j = \frac{\partial x_j}{\partial \chi_i} p_i \quad (\text{A 4.3.13})$$

Relationship between ALE description and Eulerian and Lagrangian description

The ALE description can be easily again related to the Eulerian and Lagrangian description:

By letting the ALE coordinates coincide with the material coordinates

$$\underline{\chi} = \underline{\mathbf{X}} \quad (\text{A 4.3.14})$$

the mesh motion becomes identical to the material motion, which is the definition of a Lagrangian motion. Or, in other words

$$\underline{\mathbf{X}} = \psi(\underline{\mathbf{X}}, t) = \mathbf{I}(\underline{\mathbf{X}}) \quad (\text{A 4.3.15})$$

By letting the ALE coordinates coincide with the spatial coordinates

$$\underline{\chi} = \underline{\mathbf{x}} \quad (\text{A 4.3.16})$$

the mesh motion becomes

$$\underline{\mathbf{x}} = \hat{\phi}(\underline{\mathbf{x}}, t) = \mathbf{I}(\underline{\mathbf{x}}) \quad (\text{A 4.3.17})$$

Or in other words: the mesh is fixed in space, which is the definition of an Eulerian description.

In summary:

$$\frac{Df}{Dt} = \left\{ \begin{array}{l} \frac{\partial f(\underline{\mathbf{X}}, t)}{\partial t} \quad \text{Lagrangian description} \\ \frac{\partial f(\underline{\mathbf{x}}, t)}{\partial t} + \frac{\partial f}{\partial x_i} \frac{\partial x_i}{\partial t} \Big|_{[\underline{\mathbf{X}}]} = \frac{\partial f(\underline{\mathbf{x}}, t)}{\partial t} + \frac{\partial f}{\partial x_i} v_i \quad \text{Eulerian description} \\ \frac{\partial f(\underline{\chi}, t)}{\partial t} + \frac{\partial f}{\partial \chi_i} \frac{\partial \chi_i}{\partial t} \Big|_{[\underline{\mathbf{X}}]} = \frac{\partial f(\underline{\chi}, t)}{\partial t} + \frac{\partial f}{\partial \chi_i} p_i \quad \text{ALE description} \end{array} \right. \quad (\text{A 4.3.18})$$

Comparison to Closed Form Solutions

5.1 Introduction

In the previous chapters the governing equations of the physical moisture induced damage processes and their finite element formulation are given. Before applying these equations to simulate actual moisture damage phenomena in asphaltic mixes with RoAM, a few benchmarks are performed to verify the correctness of the implemented equations. In the following, diffusion and advective transport simulations with RoAM are compared to closed form solutions.

5.2 Diffusion equation

General solutions of the diffusion equation can be obtained for a variety of initial and boundary conditions provided the diffusion coefficient is constant. Such a solution usually has one of two standard forms. Either it comprised of a series of error functions or related integrals or it is in the form of a trigonometric series. In the following, comparisons are made between the results of RoAM and the analytical solution for diffusion into a semi-infinite medium and a hollow sphere.

Validation 1

An example of a linear diffusion problem that may be solved using an error function is that of a one-dimensional diffusion into a semi-infinite medium with an initial overall concentration $C_0 = 0$ and a constant left boundary condition C_t , Fig. 5.2.1, [Crank, 1975].]

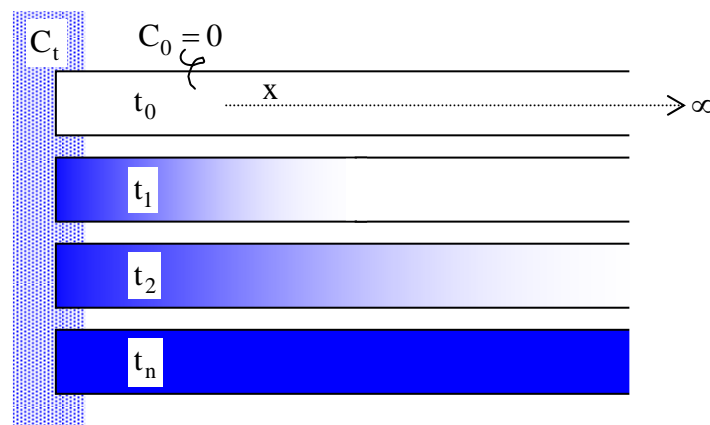


Fig. 5.2.1: One dimensional diffusion into a semi-infinite medium

The diffusion equation for a linear flow reduces to

$$\frac{\partial C}{\partial t} = D \frac{\partial^2 C}{\partial x^2} \quad (5.1)$$

Multiplying both sides of Eq. (5.1) by the Laplace kernel e^{-pt} and integrating over time gives

$$\int_0^{\infty} e^{-pt} \frac{\partial^2 C}{\partial x^2} dt - \frac{1}{D} \int_0^{\infty} e^{-pt} \frac{\partial C}{\partial t} dt = 0 \quad (5.2)$$

where $p > 0$ is a transform parameter.

The first integral can be rewritten as

$$\int_0^{\infty} \left[e^{-pt} \frac{\partial^2}{\partial x^2} C \right] dt = \frac{\partial^2}{\partial x^2} \int_0^{\infty} C e^{-pt} dt \quad (5.3)$$

When defining

$$\tilde{C}(x, p) = \int_0^{\infty} C(x, t) e^{-pt} dt \quad (5.4)$$

Substituting Eq.(5.4) into Eq. (5.3)

$$\int_0^{\infty} \left[e^{-pt} \frac{\partial^2}{\partial x^2} C \right] dt = \frac{\partial^2 \tilde{C}}{\partial x^2} \quad (5.5)$$

Since $\int_a^b u dv = uv|_a^b - \int_a^b v du$ and $d(e^{-pt}) = -pe^{-pt} dt$, the second integral of Eq. (5.2) can be written as

$$\frac{1}{D} \int_0^{\infty} e^{-pt} \frac{\partial C}{\partial t} dt = \frac{C}{D} e^{-pt} \Big|_0^{\infty} + \frac{p}{D} \int_0^{\infty} C e^{-pt} dt \quad (5.6)$$

Using the initial condition of $C_0 = 0$, reduces Eq. (5.6) into

$$\frac{1}{D} \int_0^{\infty} e^{-pt} \frac{\partial C}{\partial t} dt = \frac{p}{D} \int_0^{\infty} C e^{-pt} dt \quad (5.7)$$

Furthermore, utilizing Eq. (5.4)

$$\frac{1}{D} \int_0^{\infty} e^{-pt} \frac{\partial C}{\partial t} dt = \frac{p}{D} \tilde{C} \quad (5.8)$$

Substituting Eq. (5.8) and Eq. (5.5) into Eq. (5.2) gives

$$\frac{\partial^2 \tilde{C}}{\partial x^2} - \frac{p}{D} \tilde{C} = 0 \quad (5.9)$$

Using the boundary condition of $C(0, t) = C_t$, the boundary condition of \tilde{C} can be found as

$$\tilde{C}(0, p) = \int_0^{\infty} C_t e^{-pt} dt = \frac{-1}{p} C_t e^{-pt} \Big|_0^{\infty} = \frac{C_t}{p} \quad (5.10)$$

The solution of Eq. (5.9), subject to the boundary condition of Eq. (5.10) can be found as

$$\tilde{C}(x, p) = \frac{C_t}{p} e^{-(x/\sqrt{D})\sqrt{p}} \quad (5.11)$$

Since the object function of $\tilde{f} = \frac{\alpha}{p} e^{-\beta\sqrt{p}}$ is known to be the function

$f = \alpha \operatorname{erfc}\left(\frac{\beta}{2\sqrt{t}}\right)$, the concentration field can be found from Eq. (5.11) as

$$C(x, t) = C_t \operatorname{erfc}\left(\frac{x}{2\sqrt{Dt}}\right) \quad (5.12)$$

The function $\operatorname{erfc}(y)$ can be found from the error function $\operatorname{erf}(y)$, defined as

$$\operatorname{erfc}(y) = 1 - \operatorname{erf}(z) = 1 - \frac{2}{\sqrt{\pi}} \int_0^y e^{-\eta^2} d\eta \quad (5.13)$$

With Eq. (5.12) a solution is found for the computation of the concentration field in the semi-infinite systems, as posted in Fig. 5.2.1.

The above solution is used to verify the finite element results of the diffusion algorithm of RoAM. For the simulation, a diffusivity $D_x = 1.0 \text{ mm}^2/\text{hr}$, a total length of the mesh $l_x = 100 \text{ mm}$ and 200 elements were used (i.e. $\Delta x = 0.5 \text{ mm}$). A comparison of the normalized concentration values $C(10, t)/C_t$ is shown in Fig. 5.2.2. A good comparison is found. A sensitivity study with respect to the mesh discretization showed that a mesh discretization of 100 and 10 elements give comparable results.

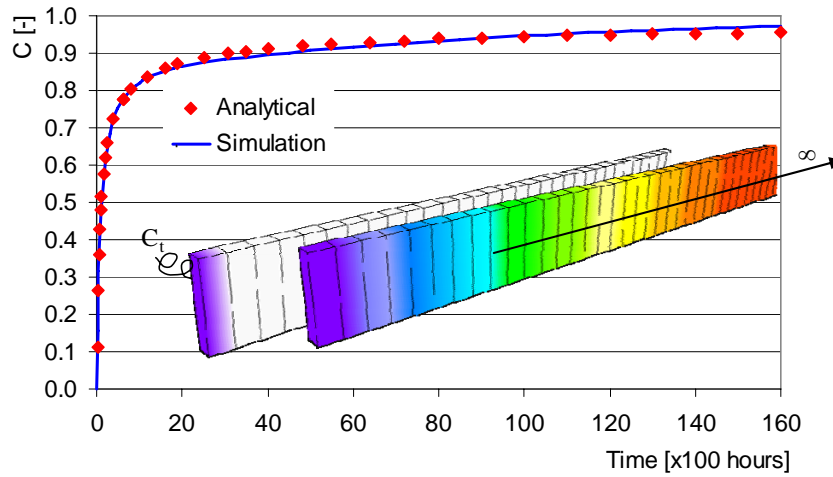


Fig. 5.2.2: Comparison of analytical solution with RoAM simulation.

Validation 2

For the second validation of the diffusion algorithm, the problem of diffusion into a hollow sphere is chosen. In the outset, this example could be related to an aggregate coated in a bituminous mastic film which is exposed to a wet environment. The hollow sphere under consideration has a thickness of $t = r_2 - r_1$, with the outside surface r_2 and the inner surface r_1 , Fig. 5.2.3.

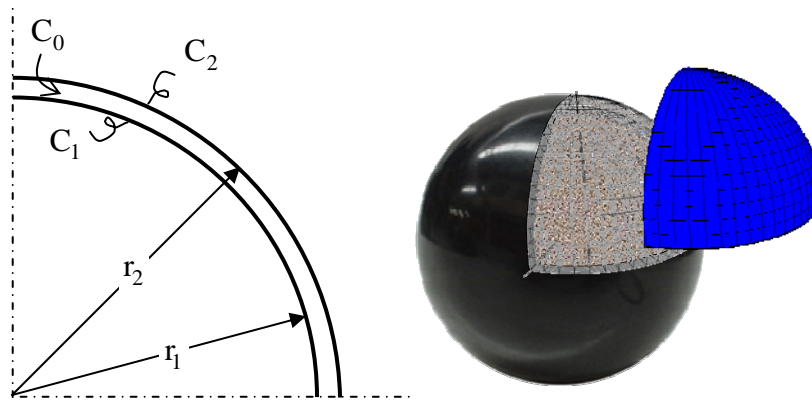


Fig. 5.2.3: One dimensional diffusion into a hollow sphere

If the inside and the outside surfaces are maintained at a constant concentration of C_1 and C_2 , respectively, and the region $r_1 \leq r \leq r_2$ is initially at C_0 , the concentration approaches the steady-state distribution according to the expression [Carslaw and Jaeger, 1959]

$$C = \frac{r_1 C_1}{r} + \frac{(r_2 C_2 - r_1 C_1)(r - r_1)}{r(r_2 - r_1)} + \frac{2}{r\pi} \sum_{n=1}^{\infty} \frac{r_2 (C_2 - C_0) \cos n\pi - r_1 (C_1 - C_0)}{n} \cdot \sin \frac{n\pi(r - r_1)}{r_2 - r_1} \exp \left[\frac{-Dn^2 \pi^2 t}{(r_2 - r_1)^2} \right] \quad (5.14)$$

For the comparison of this solution with the RoAM simulation, an analysis is made with diffusivity $D_r = 0.01 \text{ mm}^2 / \text{hr}$, a radius of the outside service of $r_2 = 200 \text{ mm}$ and a film thickness $t = 14 \text{ mm}$. The finite element mesh is divided in 7 layers of equal thickness, i.e. $\Delta r = 2 \text{ mm}$. The inside concentration is kept at $C_1 = 0.0$ and an initial concentration of $C_0 = 0.0$ is utilized.

The normalized concentration values $C = C(r_{\text{node}}, t) / C_2$ for three nodes in different layers in the mesh are compared to the analytical solution, Fig. 5.2.4. A good comparison is found.

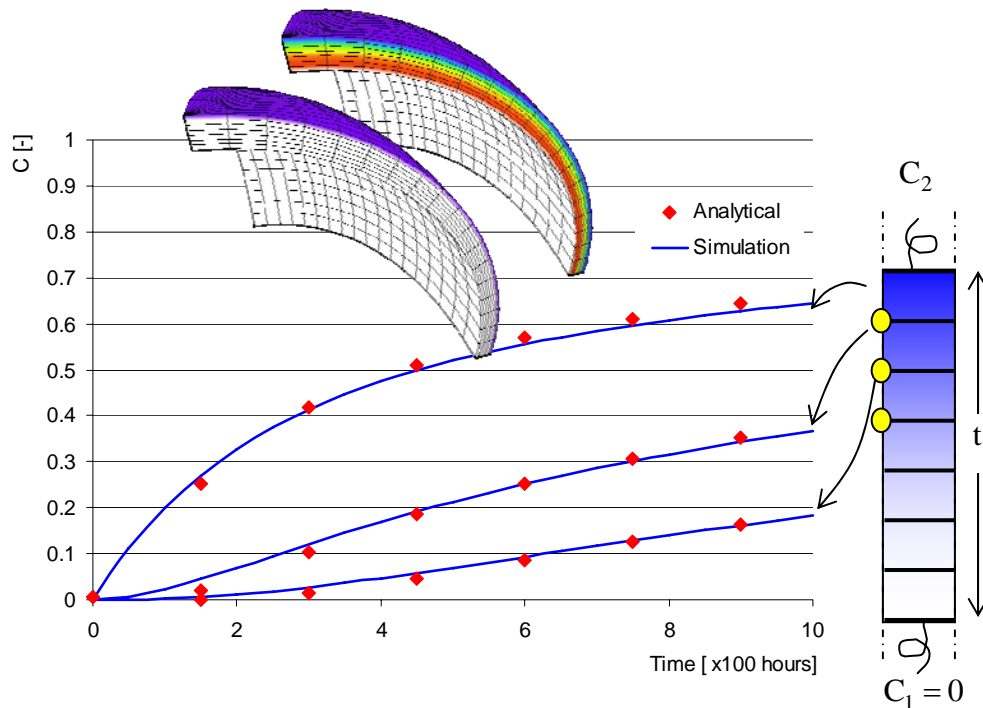


Fig. 5.2.4: Comparison analytical solution and RoAM simulation

5.3 Advective transport

The accurate computational modeling of an advection-diffusion transport equation, especially in the presence of an advection-dominated term, with either a discontinuity or steep gradient of the dependent variable, has been addressed to varying degrees of success in the field of computational fluid dynamics [LeVeque 1992], [Morton 1996]; [Quarteroni and Valli 1997], [Ganzha and Vorozhtsov 1998], [Wang and Hutter 2001]; [Atluri 2004]; [Selvadurai and Dong 2006 (a),(b)]. Higher-order methods require the size of the domain discretization element to be small enough, such that the elemental Péclet number, should not be greater than unity.

When the elemental Péclet number is greater than unity the methods give rise to unrealistic numerical phenomena such as oscillations, negative concentrations and artificial diffusion at regions close to a leading edge with a discontinuous front. For this reason, in conventional higher-order methods for advection dominated problems, a finer mesh is invariably used throughout the region, since the velocity field is usually not known *a priori*. This places a great demand on computational resources,

particularly in simulations involving three-dimensional problems. The first order methods such as the Lax-Friedrich scheme, on the other hand, eliminate the oscillatory behavior at discontinuous fronts, where there is no physical diffusion (i.e. $Pe = \infty$), but gives rise to numerical dispersion in the solution. This feature is generally accepted for purpose of the engineering usage of the procedures, but from a computational point of view gives rise to strong reservations concerning the validity of the procedures developed for the advection-diffusion transport equation for the solution of the purely advective transport problem.

Furthermore, if physical diffusive phenomena are present in the transport problem, it becomes unclear as to whether the diffusive patterns observed in the solution are due to the physical process or an artifact of the numerical scheme.

Evaluating the accuracy of the purely advective transport problem is therefore a necessary pre-requisite to gaining confidence in the application of the computational scheme to the study of the advection-diffusion problem. The real test for a computational scheme developed for modeling the advection dominated transport problem is to establish how accurately the computational scheme can converge to the purely advective transport problem at zero physical diffusion

The validation of the presented numerical approach in RoAM is made by comparing the computational results with two one-dimensional exact closed form solutions involving the advective transport problem.

Validation 1

For the first validation, a finite element mesh of length $L_x = 10$ mm with negligible y and z dimensions is exposed to a water flow field of constant velocities $v_x = v_0$ and $v_y = v_z = 0.0$ mm/s, Fig. 5.3.1. The region is assumed fully saturated and the diffusion tensor \mathbf{D}_m is zero. At time $t = 0.0$ s the region is subjected to a discontinuous desorbed mastic concentration front at the boundary in the form of a Heaviside step function $H(t)$.

These conditions reduce the mastic transport equation, as posted in Chapter 3, to a one dimensional purely advective transport equation of the form

$$\frac{\partial C_d}{\partial t} + v_0 \nabla C_d = 0 \quad (5.15)$$

With the boundary conditions

$$\begin{aligned} C_d(0, t) &= C_0 H(t) \\ C_d(x, 0) &= 0.0 \end{aligned} \quad (5.16)$$

The exact analytical development of the desorbed mastic concentration field can in this case be found as [Selvadurai, 2006]

$$C_d(x, t) = C_0 H \left[t - \frac{x}{v_0} \right] \quad (5.17)$$

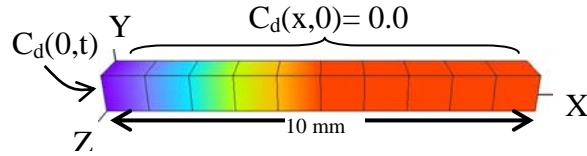


Fig. 5.3.1: Finite element discretization for 10 elements, $h_x = 1.0$ mm

In Fig. 5.3.2 the numerical solutions for $v_0 = 1.0$ mm/s and $C_0 = 1.0$ at $x = 10.0$ mm are compared to the exact analytical solution for various mesh refinements, whereby using a constant Courant number, Cr , equal to 1.0

$$Cr = \frac{|v_x| dt}{h_x} \quad (5.18)$$

where dt is the time step and h_x is the element size.

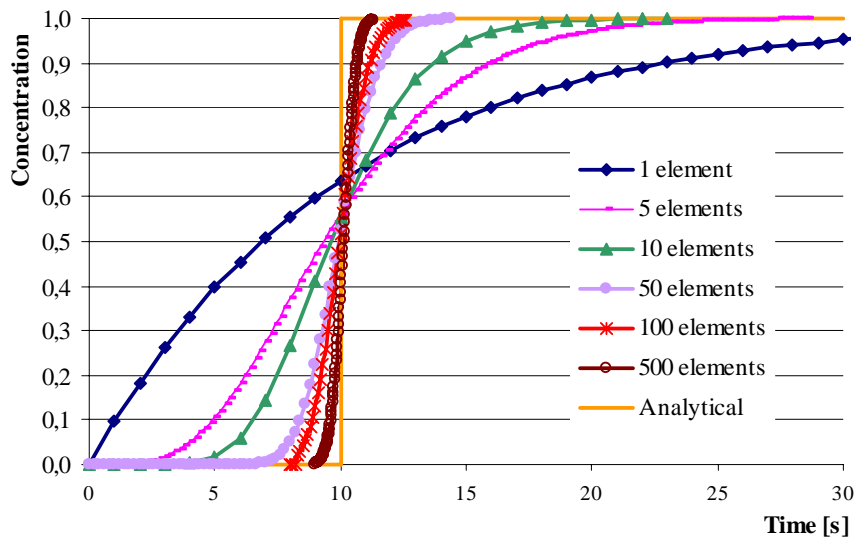


Fig. 5.3.2: Simulation of the advection front, $Cr = 1.0$ at $x=10$ mm

It can be seen from Fig. 5.3.2 that with increased mesh refinement, the numerical diffusion is reduced and the concentration front is simulated quite accurately without oscillatory effects. It may be observed that none of the discretizations exhibit any numerical oscillation.

Varying Cr , i.e. the time-step, shows that for a constant discretization of 50 elements, i.e. $h_x = 0.2$ mm, higher values of Cr actually lead to a better approximation, Fig. 5.3.3. This means that the solution seems to improve for an increasing time-step. The reason for this can be found in the fact that for a larger time-step, less time-steps are needed, which reduces the accumulating numerical error. For Cr values smaller than 1, i.e. a time step of $dt \leq 0.2$ s the solution converges to a constant solution. The particle tracking algorithm automatically reduces the time-step if the particle is not within the boundaries of the element. A finite element mesh with a chosen dt that is too big to capture the particles will therefore automatically be reduced. In this, the algorithm adjusts the Courant number itself if necessary.

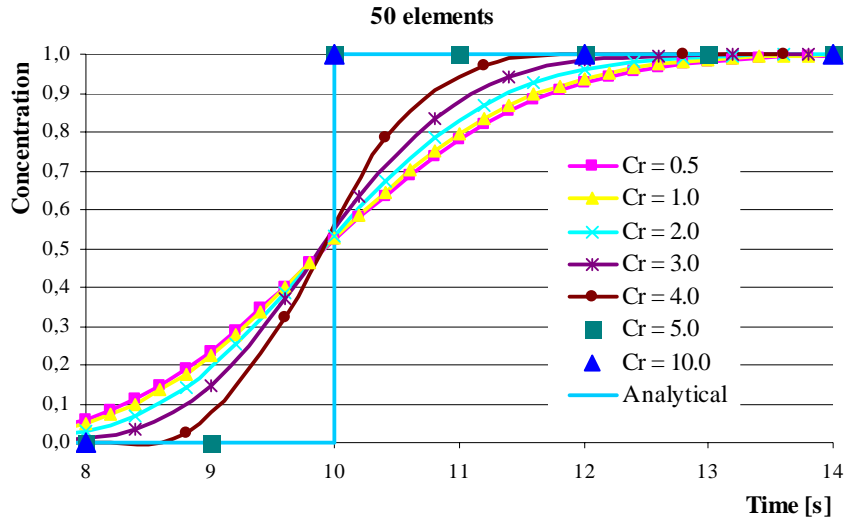


Fig. 5.3.3: Courant number analysis for the mesh with 50 elements

This observation is confirmed by plotting the movement of the concentration front at time $t = 2$ s for Cr values equal to 1.0 and 10, Fig. 5.3.3. The two curves show a distinct difference in numerical dispersion, where the computation with $Cr = 10$ i.e. $dt = 2.0$ s, approximates the advective front quite accurately.

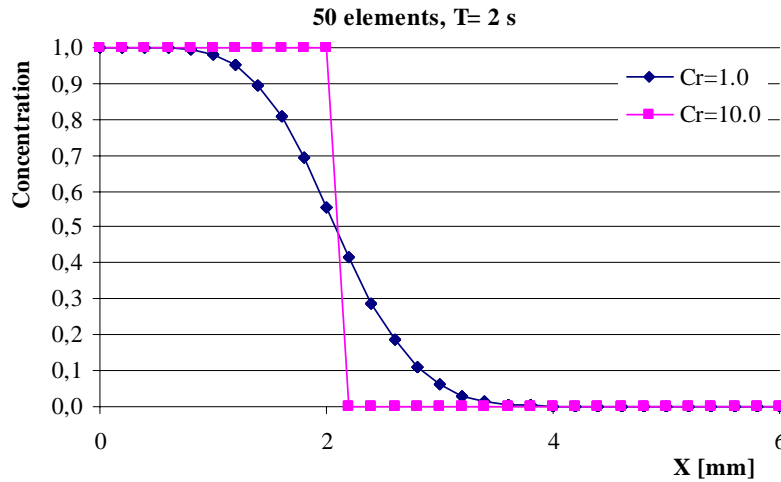


Fig. 5.3.3: Movement of the concentration front at $T = 2$ sec for $Cr = 1.0$ and $Cr = 10$

Validation 2

For the second validation, the same finite element mesh is exposed to a changing flow field of

$$v_x = v_0 \exp(-\lambda t) \tag{5.19}$$

and $v_y = v_z = 0.0$ mm/s. The region is assumed fully saturated with negligible water capacity $\tilde{\theta}$ and a zero diffusion tensor, \mathbf{D}_m . At time $t = 0.0$ s the same boundary conditions as in the first validation are assumed, Eq. (5.16).

These conditions simplify the mastic transport equation to the form

$$\frac{\partial C_d}{\partial t} + v_0 \exp(-\lambda t) \nabla C_d = 0 \quad (5.20)$$

and the developing desorbed mastic concentration field under these conditions can be found analytically as [Selvadurai, 2006]

$$C_d(x, t) = C_0 H \left[\frac{1 - \exp(-\lambda t)}{\lambda} - \frac{x}{v_0} \right] \quad (5.21)$$

Because the velocity field is time dependent, the Courant number is not constant either and can be found from

$$Cr = \beta e^{-0.02t} \quad (5.22)$$

In Fig. 5.3.4 the numerical solutions at $x = 10.0$ mm with $v_0 = 1.0$ mm/s, $C_0 = 1.0$, $\beta = 1.0$ and $\lambda = 0.02 \text{ s}^{-1}$ are compared to the analytical solution Eq. (5.21) for various mesh refinements. It can be seen that for the case under consideration an increased refinement of 500 elements, with $h_x = 0.02$ mm and $dt = 0.02$ s, approximates the analytical solution with negligible numerical dispersion. Again, none of the discretizations showed any signs of numerical oscillations in the approximation.

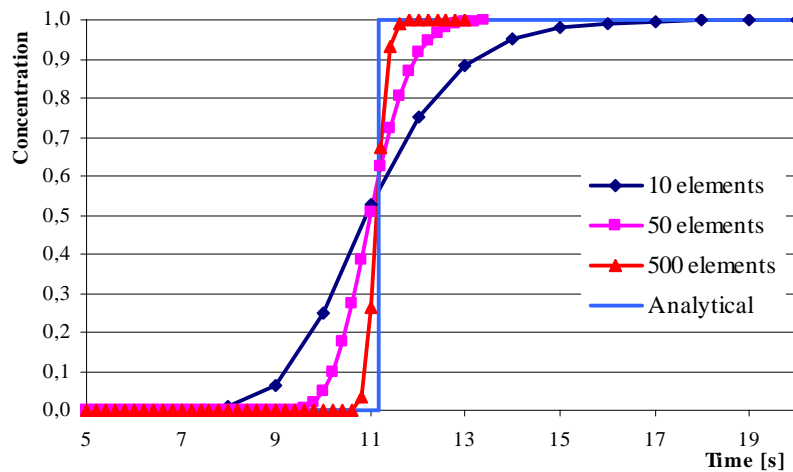


Fig. 5.3.4: Simulation of the advection front, with $Cr = \exp(-0.02t)$

By comparing the solution of the constant finite element discretization of 50 elements with a Cr values with $\beta = 0.5$ and $\beta = 1.0$, it can be shown that a higher Cr value again leads to a more accurate solution, Fig. 5.3.5.

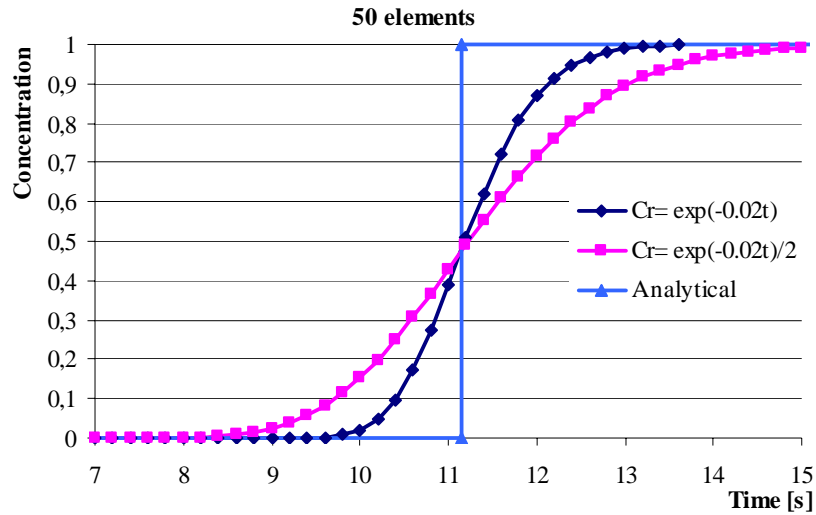


Fig. 5.3.5: Courant number analysis for the mesh with 50 elements

From the above can be seen, that both the diffusion and the advective transport simulations with RoAM can accurately capture the intended phenomena. It was also shown that, the advective transport algorithm is stable under all tested finite element conditions, even though quite a fine finite element discretization is needed to reduce the numerical diffusion to zero.

Material Parameters Determination

6.1 Introduction

In the previous chapters, moisture diffusion and mastic erosion were identified as physical moisture damage inducing processes. More specifically, in chapter 3 and 4 the governing equations and finite element formulations that are needed to simulate these processes are derived and in chapter 5 these formulations are compared with analytical closed form solutions. Table 6.1.1 gives a brief summary of the controlling parameters of these processes.

Table 6.1.1: Summary of controlling parameters

Process	Controlling parameters
<i>Moisture diffusion</i>	<ul style="list-style-type: none"> - Moisture diffusion coefficient D_m [L^2/T] - Maximum moisture capacity C_m^{\max} [M/L^3]
<i>Mastic erosion</i>	<ul style="list-style-type: none"> - Mastic desorption coefficient K_d [L^3/M] - Mastic diffusion coefficient α_m [L^2/T] - Mastic dispersion coefficients $\alpha_{1,t}$ [L]

The actual effect that these moisture induced damage processes have on the mechanical performance of the asphalt components and their bond, is discussed in detail in chapter 8-9.

In this chapter, in section 6.3 and 6.4, experimental procedures are developed for determination of most of the above described controlling parameters.

However, in addition to the moisture induced damage processes which are identified and modeled in this dissertation, a considerable effort has been spent in the USA to develop another approach, commonly referred to as the ‘surface energy approach’, for fundamental characterization of moisture damage in asphalt mixes. And even though this methodology is unrelated to the approach developed in this dissertation, given the relevance to the topic and its timeliness, in section 6.2 this method is briefly discussed.

6.2 Theoretical work of adhesion measurements

In the following, a short background is given of the theory of surface free energies and work of adhesion.

If an attempt is made to push a probe through the surface of a liquid, the probe encounters a resistance to the deformation of the surface; known as surface tension. Surface tension [dyne/cm or erg/cm²] and surface energy [erg/cm² or mJ/m²] are numerically identical for liquids. Techniques for the measurement of the surface tension of liquids have their basis in two types of measurements: probes and surface area increase. The probe methods generally involve the passage of a probe through the surface and the measurement of the force necessary to accomplish that passage. Such methods include the Wilhelmy plate and the du Nuoy ring. Surface area can be used to measure the surface tension of liquids since the minimizing of surface energy is a driving force in nature. It could for instance be measured by placing a clean capillary tube into a pool of liquid and observe the height to which the liquid travels up the tube under the influence of capillary pressure.

According to surface tension theory, the work required for separating reversibly two bulk phases α and β from their equilibrium position is the work of adhesion W_a

$$W_a = \gamma_\alpha + \gamma_\beta - \gamma_{\alpha\beta} \quad (6.1)$$

where γ_i is the surface tension of phase i and $\gamma_{\alpha\beta}$ is the interfacial tension between phases α and β . This equation is known as the Dupré equation [Dupré 1869].

The work of adhesion is also described in literature as the decrease of Gibbs free energy per unit area when an interface is formed from two individual surfaces. Thus, the greater the interfacial attraction, the greater the work of adhesion will be. Rearrangement of (6.1) gives

$$\gamma_{\alpha\beta} = \gamma_\alpha + \gamma_\beta - W_a \quad (6.2)$$

indicating that the greater the interfacial attraction, the smaller the interfacial tension is.

The deepest potential well that is available for the interaction between two atoms or molecules is that formed when they share a pair of electrons. That is, the deepest potential energy well is obtained when a covalent bond is formed. Having the covalent bond in mind, the expression for surface energy can be formulated as:

$$\gamma = \gamma^d + \gamma^p \quad (6.3)$$

where γ^d is the dispersion force component and γ^p is the polar (or acid-based) contribution to the surface energy. Using the hypothesis of Owens and Wendt [1969] it is found:

$$W_a = 2\sqrt{\gamma_1^d \gamma_2^d} + 2\sqrt{\gamma_1^p \gamma_2^p} \quad (6.4)$$

This expression deals only with a situation where the two materials are in contact and no other material is present. In the case of the presence of a third material, such as moisture, which has its own polar and dispersive character it can be shown that

$$W_{a,L} = 2 \left[\gamma_L - \sqrt{\gamma_1^d \gamma_L^d} - \sqrt{\gamma_1^p \gamma_L^p} - \sqrt{\gamma_2^d \gamma_L^d} - \sqrt{\gamma_2^p \gamma_L^p} + \sqrt{\gamma_1^d \gamma_2^d} + \sqrt{\gamma_1^p \gamma_2^p} \right] \quad (6.5)$$

where γ_L is the surface energy of the liquid (water) and γ_L^i are the components of liquid surface energy, i is either d (dispersive) or p (polar).

If the values of the γ_j^i are known, then the predicted *thermodynamic work of adhesion* at an interface in the presence of a liquid can be calculated whereby a negative value of the work of adhesion indicates that the system under consideration is unstable in the presence of moisture.

This, in short, is the theory behind work of adhesion measurements, based on surface energy theory. This theory has been brought forward, mainly by the Texas A&M team, to be utilized for moisture susceptibility characterization of asphaltic mixes [Bhasin 2006], [Masad et al. 2006b], [Zollinger 2005], [Lytton et al. 2005]. In this, the bulk phases α and β are represented by the aggregate and the bitumen and the calculated work of adhesion gives the ‘bond strength’ of the aggregate-mastic interface, with and without moisture.

It has been shown that the actual work needed to break an aggregate-mastic bond is several orders in magnitude higher than the theoretical work of adhesion [Fini 2006]. This clearly indicates that, in addition to Lifshitz van der Waals and acid and base forces, additional bonds are made between the aggregates and the mastic. A more detailed discussion of aggregate-mastic bond properties is given in section 2.2. Additionally, an important factor for moisture susceptibility characterization is the time frame over which moisture damage develops. The surface free energy theory does not account for the time it would take for moisture to reach the aggregate-mastic interface, nor does it include the amount of moisture which would be needed to replace the mastic from the aggregate.

However, if indeed, based on surface energy measurements one would be able to rank mastic-aggregate combinations for the quality of their bond in the presence of moisture, this would constitute a powerful tool for a-priori material selection. In Appendix 6.1 a detailed description is given of the experimental determination of surface tension of the asphalt components.

In the following, a method is given for determination of moisture diffusion coefficients, needed for moisture diffusion simulations.

6.3 Moisture diffusion coefficients measurements

6.3.1 Moisture sorption principle

The moisture sorption experiment is a technique for determination of the moisture diffusion coefficient of the asphalt mix components. It is based on the rate of specimen weight increase due to moisture absorption when the specimen is placed in a conditioning chamber with controlled relative humidity, Fig. 6.3.1.

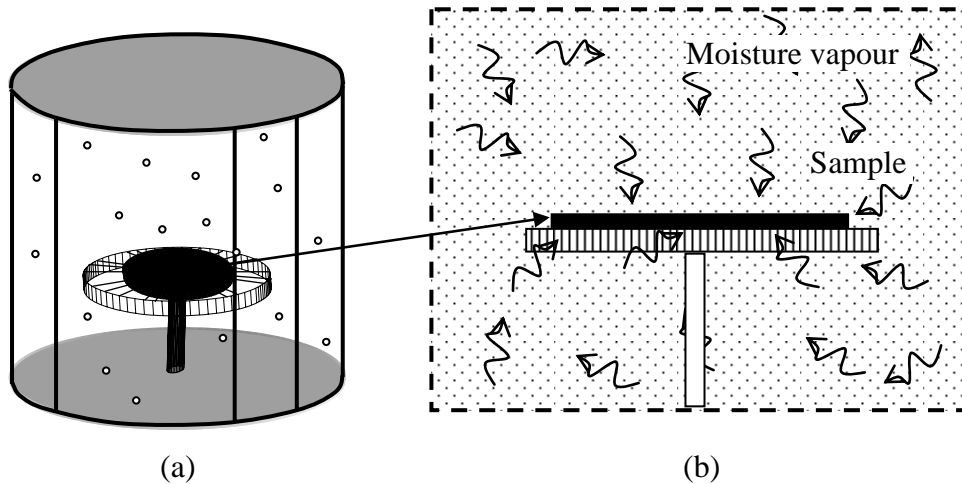


Fig. 6.3.1: Schematic of mastic/aggregate sample in a moisture chamber

In order to determine the diffusion coefficients of the materials, the samples must have a known geometry. For the following equations, the geometry of the materials should always consist of a sheet of material (i.e. length and width \gg thickness) of known thickness h

In the detailed description of the experimental procedure, the assumption is made that the diffusion process is of 'Fickian' nature.

Assuming a constant diffusion coefficient and no volume change of the samples upon moisture infiltration, the experimental procedure is to place the sample of thickness h in the conditioned chamber with a controlled vapour relative humidity $RH(1)$, maintained at a constant temperature and pressure, and to observe the rate of uptake of vapour by monitoring the increase in weight of the sample. The mastic must be initially free of vapour (dry sample).

The appropriate solution of the diffusion equation for a sheet of material may be written as [Crank 1975]

$$\frac{M_t}{M_\infty} = 1 - \frac{8}{\pi^2} \sum_{m=0}^{\infty} \frac{1}{(2m+1)^2} e^{\left(-D(2m+1)^2 \pi^2 t / h^2\right)} \quad (6.6)$$

if the uptake is considered to be a diffusion process controlled by a constant diffusion coefficient D . Here, M_t is the total amount of vapour absorbed by the sample at time t , and M_∞ is the equilibrium sorption attained when the sorption curves reaches a constant value.

The application of Eq. (6.6) is based on the assumption that the sheet of mastic is immediately placed in the vapour and that each surface attains a concentration value corresponding to the equilibrium moisture capacity M_∞ for the vapour pressure existing, and remains constant afterwards.

The experiment should be continued until the moisture sorption curve reaches its maximum moisture uptake M_∞ . Then, the time t should be determined at which the sample had reached half of this amount $M_t/M_\infty = 0.5$. This time is called the “half-time” of the sorption process and will be indicated in the following as $t_{0.5}$, Fig. 6.3.2.

The value of t/h^2 for which $M_t/M_\infty = 0.5$ is given by

$$\frac{t_{0.5}}{h^2} \approx -\frac{1}{\pi^2 D} \ln \left(\frac{\pi^2}{16} - \frac{1}{9} \left(\frac{\pi^2}{16} \right)^9 \right) \quad (6.7)$$

From this the diffusion coefficient can be found as

$$D = 0.049 \frac{1}{(t_{0.5}/h^2)} \quad (6.8)$$

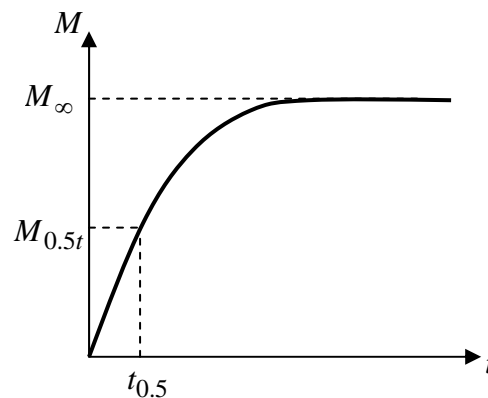


Fig. 6.3.2: Principle of half-time diffusion

This experimental procedure must be repeated for the same relative humidity $RH(1)$, for samples with various thicknesses. Table 6.3.1 gives an example of the experimental results of two (fictitious) materials with three different sample thicknesses. It can be clearly seen that different geometries of the same material should give similar diffusion coefficients.

Table 6.3.1: Schematic of diffusivity measurements for two materials with different thicknesses

Material	Mastic film	Half time	$t/(l^2)$	D
Type	thickness [mm]	[hr]	[hr/mm ²]	[mm ² /hr]
A	1	2	2	0.0245
A	2	8	2	0.0245
A	5	50	2	0.0245
B	1	10	10	0.0049
B	2	40	10	0.0049
B	5	250	10	0.0049

The experiment should now be repeated for the same materials, with a constant sample thickness but with a different relative humidity RH(2).

The different moisture vapour concentrations should give the same diffusivity coefficient for the same material samples. For the sorption curves this would mean that the value of $t_{0.5}/h^2$ should be the same for different samples of the same material, Fig. 6.3.3.

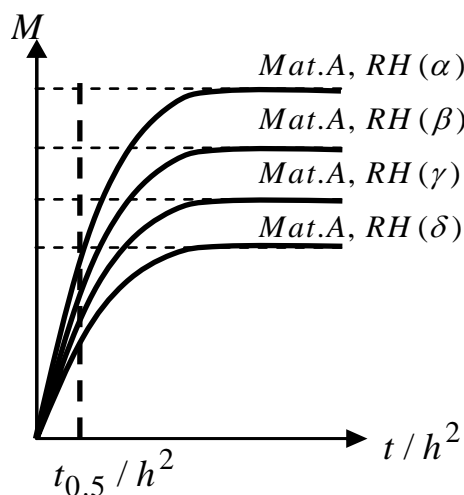


Fig. 6.3.3: Schematic of sorption curves for the same material with a constant diffusion coefficient

If, from the experiments, follows that the $t_{0.5}/h^2$ value is significantly different for samples of the same material, exposed to various moisture vapour concentrations, the assumption that the diffusion coefficient is concentration independent is not valid. Fig. 6.3.4 gives a schematic of sorption curves for a material with a concentration dependent diffusion coefficient. The curves show that for a higher maximum moisture uptake, lower values of $t_{0.5}/h^2$ are found and, therefore, the measured diffusion coefficient increases as the concentration of moisture increases.

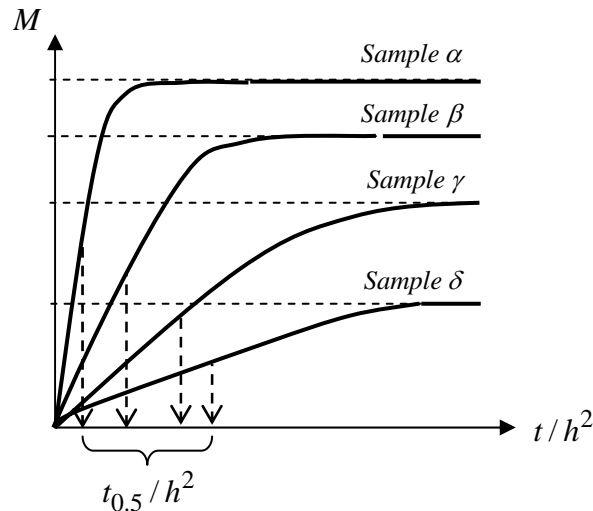


Fig. 6.3.4: Sorption curves for a material with a concentration dependent diffusion coefficient

So far, focus has been placed on determining the rate of moisture diffusion into the asphalt components. Since finding the fundamental material parameters that control the moisture susceptibility of an asphalt mix is the main purpose of this experimental effort, it is also of great importance to know how fast the moisture would leave the wet asphalt mix after being exposed to a dry environment.

Therefore, not only moisture sorption but also moisture *desorption* experiments must be performed. The experimental procedure is similar to the sorption procedure, described before. The main difference is that the desorption experiment starts on a fully 'saturated' sample (i.e. after the end of the moisture sorption experiment is reached) and the relative humidity in the chamber should be set to 'zero' RH_0 .

With this procedure, the molecular moisture diffusivity coefficient of the materials, upon 'drying' of the materials will be measured. Furthermore, the remaining weight of the sample \bar{M}_0 , after reaching a constant minimum weight in the sorption curve, must be compared to its original dry weight. This is to check if the material is immobilizing water molecules.

6.3.2 Adsorption of moisture on the outside of the film

In the above procedure it is assumed that when the material examples are exposed to a moisture concentration that is higher than the samples' initial (zero) moisture concentration, immediately a diffusion process starts. It may be true, however, that some of the diffusing molecules are immobilized at the surface of the sample by adsorbing to it. Obviously, if moisture is indeed adhering to the surface of the sample, this moisture mass M_{surface} should be subtracted from the total moisture sorption curve before determining the diffusion coefficient D . There are various ways of treating this issue, in the following a possible approach is discussed.

Two specimens of the same surface area with different thicknesses should be prepared. The sides of the specimens should be coated with a water repelling (non-moisture adhering) coating to reduce the moisture adsorption as much as possible, Fig. 6.3.5.

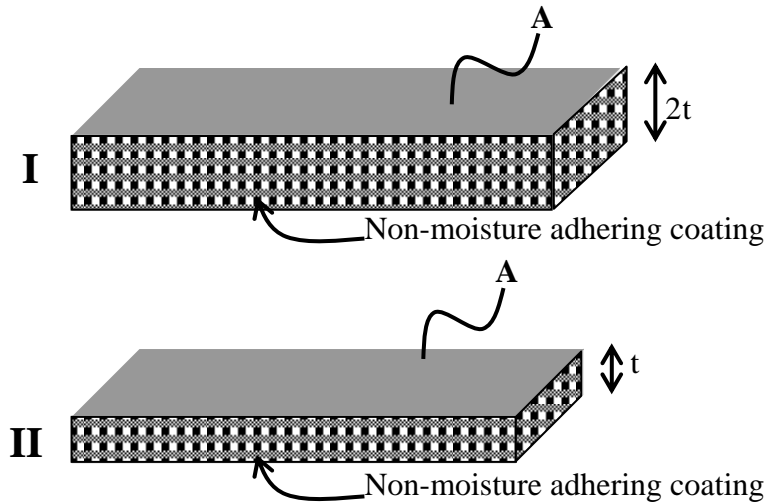


Fig. 6.3.5: Two samples to filter out adsorbed surface moisture

Both specimens should undergo the same moisture sorption experiment, as described above, with the same relative humidity RH .

Since the volume of Specimen I in Fig. 6.3.6 is twice the volume of Specimen II, the moisture absorbed via a diffusion process M_{diff} is also twice as much in Specimen I. The moisture adsorbed to the surface, however, is the same for both samples, since the surface area A is the same for both sample.

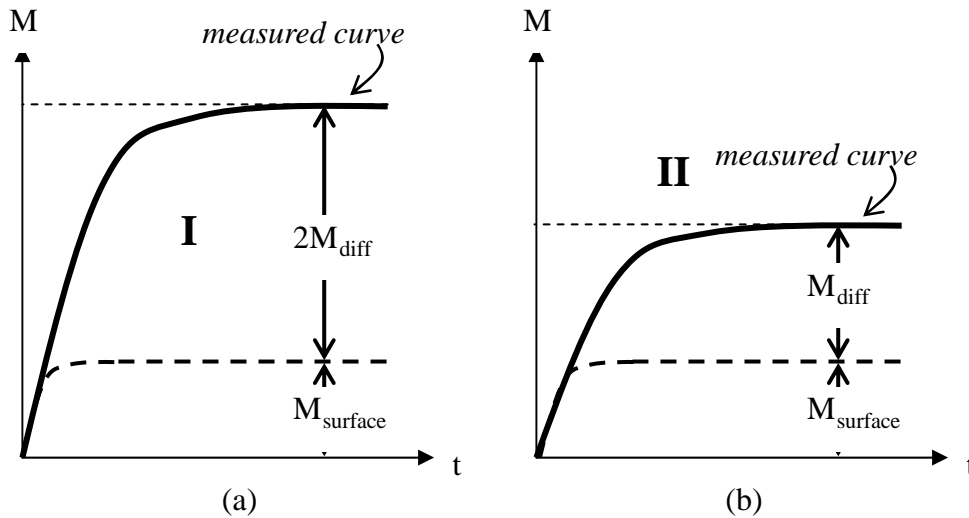


Fig. 6.3.6: Sorption curves for (a) specimen I (b) specimen II

Based on Fig. 6.3.7, the moisture sorption curves for both specimens can be expressed as

$$M_I = 2M_{diff} + M_{surface} \quad (6.9)$$

and

$$M_{II} = M_{diff} + M_{surface} \quad (6.10)$$

Therefore

$$M_I - M_{II} = M_{diff} = M_{\infty} \quad (6.11)$$

Which gives the sorption curve for both specimens:

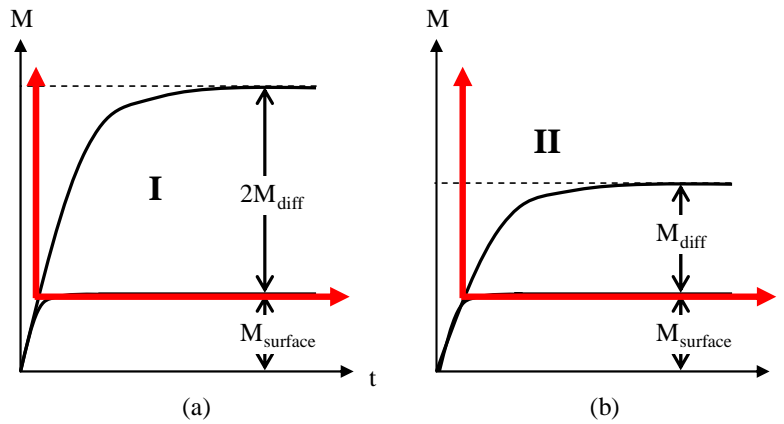


Fig. 6.3.7: Filtering out of the diffusion sorption curve

Therefore, based on the above procedure, the moisture which is possibly adhering to the outside of the sample can be filtered out from the total mass increase.

6.3.3 Experimental procedure

The sorption device that was utilized to determine the surface tension of the aggregates, is also utilized for the moisture sorption experiments. Sorption analyses according to the procedure described earlier will be performed at a consistent temperature of 25°C

Based on the above detailed description, the moisture sorption experiments can be performed. In Fig. 6.3.8: the experimental test procedure is described in steps.

STEP	Experimental procedure, Sample α	Determined parameter
1	<u>Initial geometry characterization</u> Measurement of initial weight M_0 and geometry of dry sample	M_0 [g], h [mm], V [mm ³]
2	<u>Moisture sorption experiment</u> Measurement of sorption diffusion coefficient D_s and maximum moisture uptake M_{∞} with a relative humidity RH(1)	D_s [mm ² / hr], M_{∞}
3	<u>Swelling check</u>	\bar{h} [mm]

	Measurement of sample volume \bar{V}	
4	<u>Moisture desorption experiment</u> Measurement of desorption diffusion coefficient D_d and immobilized moisture $(\bar{M}_0 - M_0)$ with a relative humidity of RH_0	D_d [mm/hr], \bar{M}_0
5	<u>Concentration dependency check</u> Repeat step 1-4 for a different relative humidity at step 2 $RH(2)$	$D_s(RH), D_d(RH)$
6	<u>Experiment consistency check</u> Repeat step 1-5 for the same material with a different geometry (1)	[-]

Fig. 6.3.8:: Experimental procedure for determination of the diffusion coefficients

6.3.4 Determination mastic diffusion coefficients

To enable realistic simulations of moisture diffusion into mastic films, it is important to know the diffusion coefficient of the mastic, which consists of pure bitumen and a granular filler.

From diffusion experiments performed at the National Institute of Standards and Technology and at the Turner Fairbanks Research Centre, moisture diffusion coefficients ranging from $1.2 \cdot 10^{-4} \text{ mm}^2/\text{hr}$ – $5.0 \cdot 10^{-5} \text{ mm}^2/\text{hr}$ have been determined [Nguyen 1992, 1996], [Wei 2007].

Unfortunately, no data is available to date with regard to moisture diffusion coefficients of asphaltic mastics. For this reason, in the following, numerical analyses are performed to determine the diffusion coefficient of mastics, as a function of granular filler content. In these analyses the ‘half-time’ diffusion methodology as described in section 6.3.1 is utilized.

A sheet of bitumen of size $500 \mu\text{m} \times 500 \mu\text{m} \times 50 \mu\text{m}$ is modelled, with elements of size $20 \mu\text{m} \times 20 \mu\text{m} \times 10 \mu\text{m}$, Fig. 6.3.9.

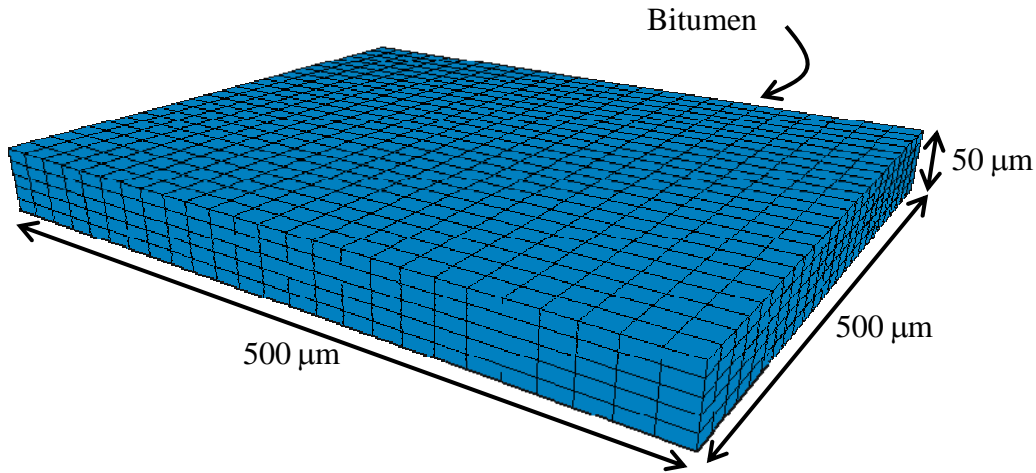


Fig. 6.3.9: Finite element discretization of a sheet of bitumen

Based on the available parameters, in the analysis a moisture diffusion coefficient of $1.0 \cdot 10^{-4} \text{ mm}^2/\text{hr}$ is utilized for the bitumen.

The half-time diffusion principle into a plane sheet of material was expressed by Eq. (6.8), and is here repeated for sake of convenience

$$D = 0.049 \left(t_{0.5} / h^2 \right)^{-1} \quad (6.12)$$

where $t_{0.5}$ is the time (“half-time”) when the material has absorbed half of its maximum capacity and h is the thickness of the sheet. Eq. (6.12) assumes moisture is only infiltrating the material from its plane faces.

Since the maximum moisture uptake concentration C_m^{max} is not known for all the mastics, nor influences the value of $t_{0.5}$ which is to be determined in the analyses, the diffusion analyses are performed for a normalized moisture concentration $\theta = C_m / C_m^{\text{max}}$, referred to as the moisture content. The moisture content values, as

calculated per gauss point, are transformed into equivalent mass values, by multiplying the moisture content values by the appropriate volumes. Finally, the total equivalent moisture mass uptake is computed by summing the moisture uptake over all the elements.

For the ‘zero filler’ diffusivity computation, as well as to show the applicability of Eq. (6.12) for the finite element mesh shown in Fig. 6.3.9, a first moisture diffusion analysis is performed with RoAM on the pure bitumen mesh, whereby exposing the plane sheet bitumen to moisture from its (top and bottom) plane faces, Fig. 6.3.10.

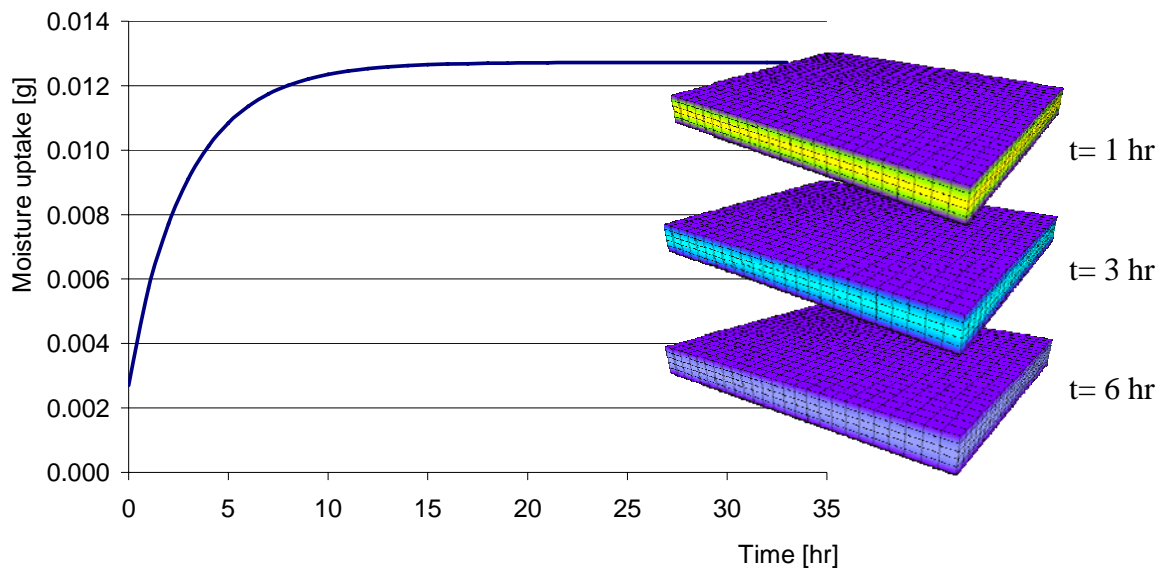


Fig. 6.3.10: Simulation of moisture uptake due to diffusion into a plane sheet of bitumen with zero filler content

From the computation of the moisture uptake, the half-time can be determined, as explained in section 6.3.1, Fig. 6.3.11.

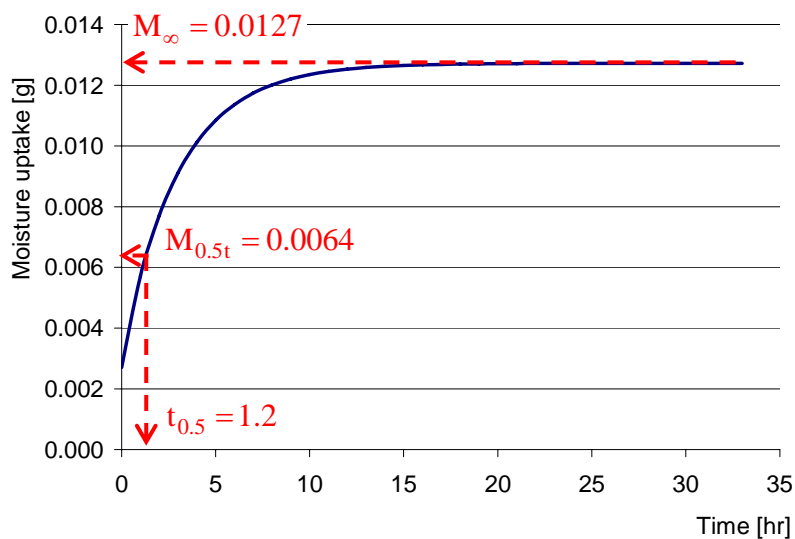


Fig. 6.3.11: Computation of half-time diffusion value for pure bitumen

For the case of the pure bitumen, a half-time value of $t_{0.5} = 1.2$ hr is determined. Substituting this value, together with the sheet thickness $h = 50 \mu\text{m}$ into Eq. (6.12), indeed gives a diffusivity D of $1.0 \cdot 10^{-4} \text{ mm}^2/\text{hr}$.

Having confirmed the suitability of the chosen geometry of the finite element mesh, random computed mastics are generated. In these mastics, square filler particles of the size $20 \mu\text{m} \times 20 \mu\text{m} \times 10 \mu\text{m}$ are added to the bitumen.

In the following, mastics are generated with a filler content of 2%, 5%, 10%, 25%, 50%, 75% and 100% by volume, respectively. The 100% filler case is obviously equal to a plane sheet of the aggregate material, and is used to show the influence of the filler content over a range of 0 – 100 %. In practise, a wide range of aggregates is used as filler material for bitumen. Therefore, in addition to the filler content, the effect of the diffusivity of the aggregates themselves is also investigated by utilizing three different fillers with diffusivity values of $1.0 \cdot 10^{-3} \text{ mm}^2/\text{hr}$, $1.0 \cdot 10^{-2} \text{ mm}^2/\text{hr}$ and $1.0 \cdot 10^{-1} \text{ mm}^2/\text{hr}$ in the analyses.

In Fig. 6.3.12 and Fig. 6.3.13 the generated finite element mastics are shown for, 2% - 10% and 25 % - 75% filler content, respectively.

Utilizing the half-time diffusion methodology, as described in the above, the mastic diffusion coefficients are computed for the various filler contents, using the three filler types, Table 6.3.2.

Table 6.3.2: Mastic diffusion coefficients D [mm^2/hr] as a function of filler content for three different filler types, with D-bitumen $1.0 \cdot 10^{-4} \text{ mm}^2/\text{hr}$

D-filler [mm^2/hr]	Percentage filler in mastic [% by volume]							
	0	2	5	10	25	50	75	100
1.0 e-03	1.0E-04	1.38E-04	1.58E-04	1.98E-04	3.76E-04	6.73E-04	9.0E-04	1.0E-03
1.0 e-02	1.0E-04	1.47E-04	2.02E-04	4.37E-04	2.78E-03	5.48E-03	7.90E-03	1.0E-02
1.0 e-01	1.0E-04	1.50E-04	2.59E-04	1.69E-03	1.48E-02	5.43E-02	7.89E-02	1.0E-01

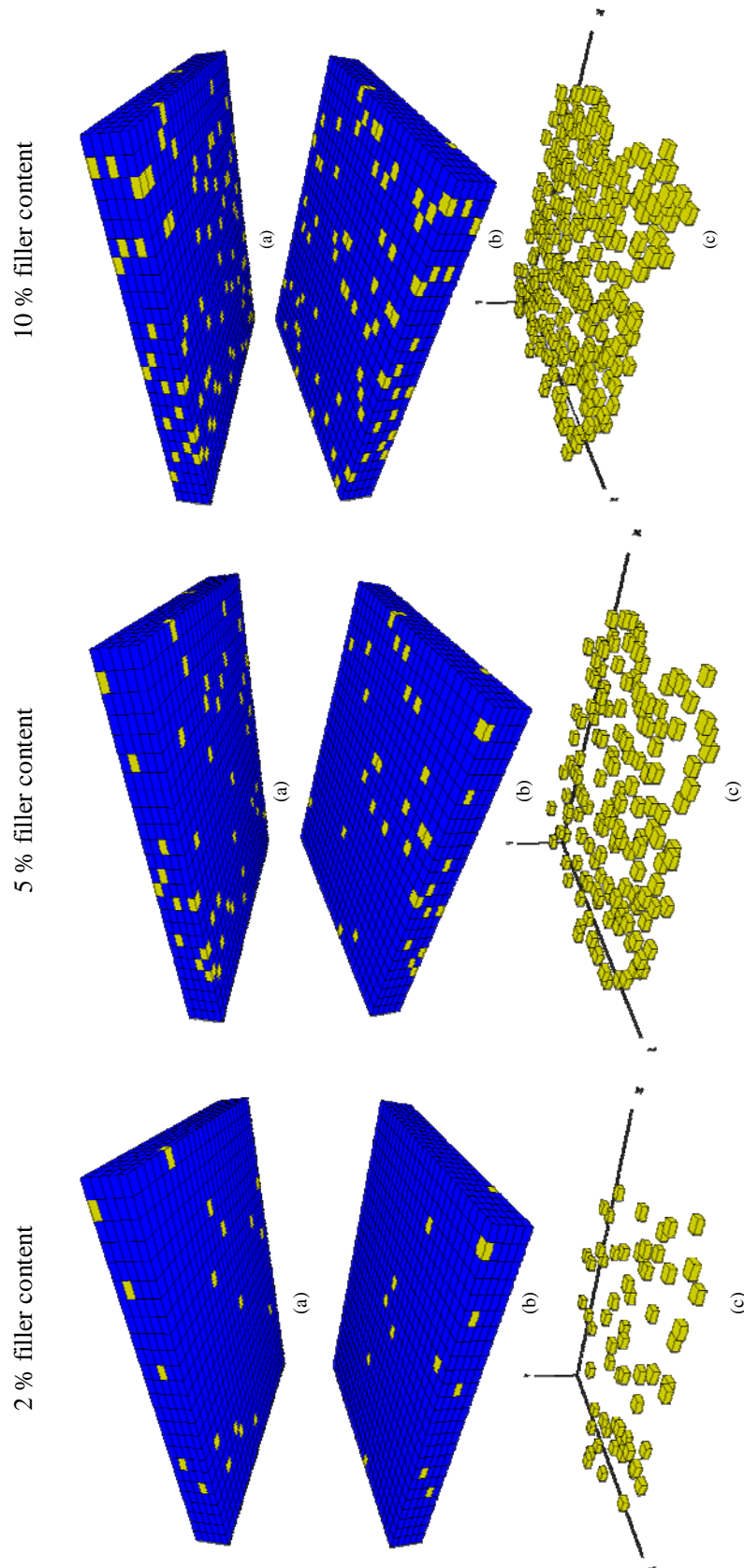


Fig. 6.3.12: Randomly generated mastic, using 2- 10% (by volume) filler particles
 (a) bottom plane view (b) top plane view (c) filler particles distribution

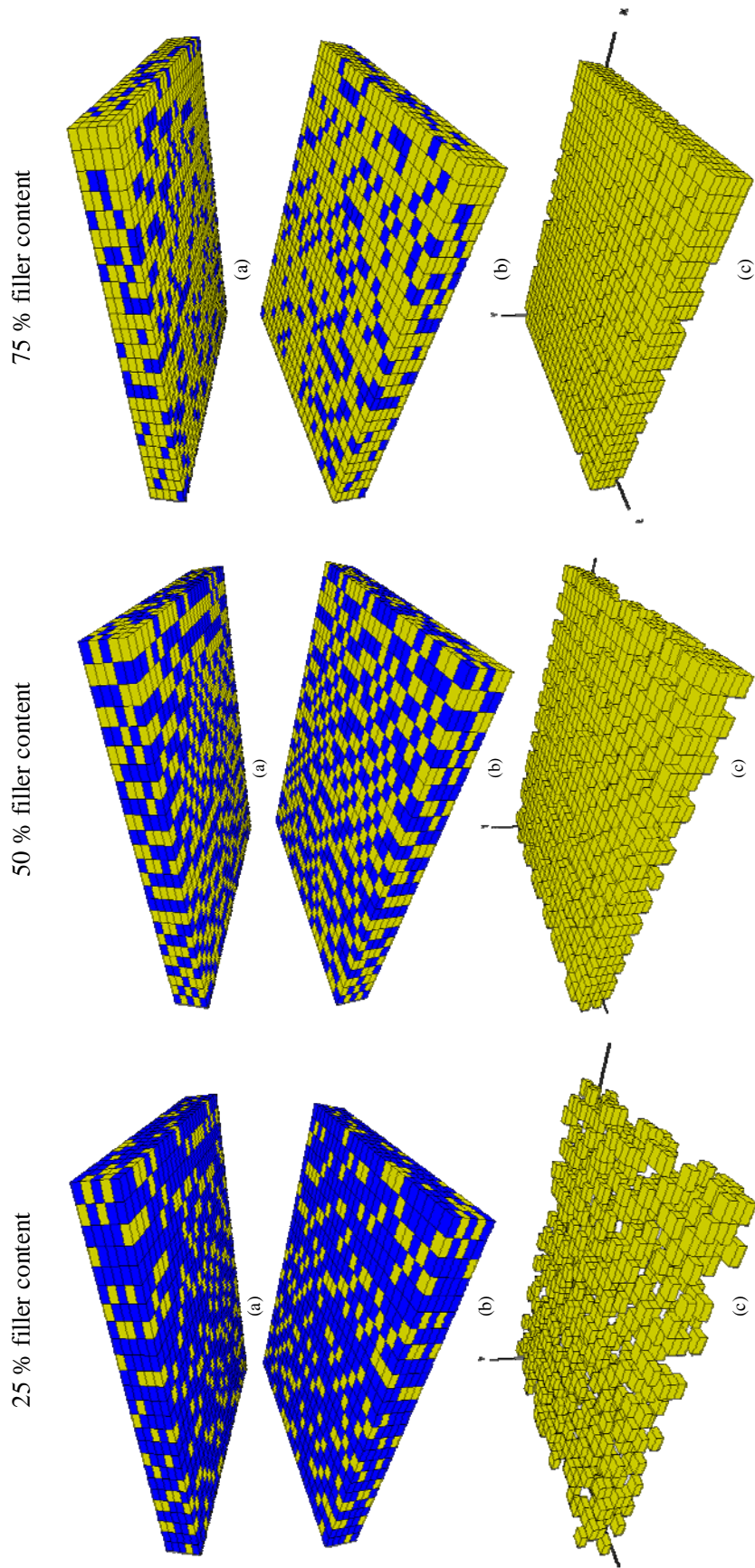


Fig. 6.3.13: Randomly generated mastic, using 25- 75% (by volume) filler particles
 (a) bottom plane view (b) top plane view (c) filler particles distribution

In Fig. 6.3.14 and Fig. 6.3.15 the computed mastic diffusion coefficients are plotted as a function of filler content.

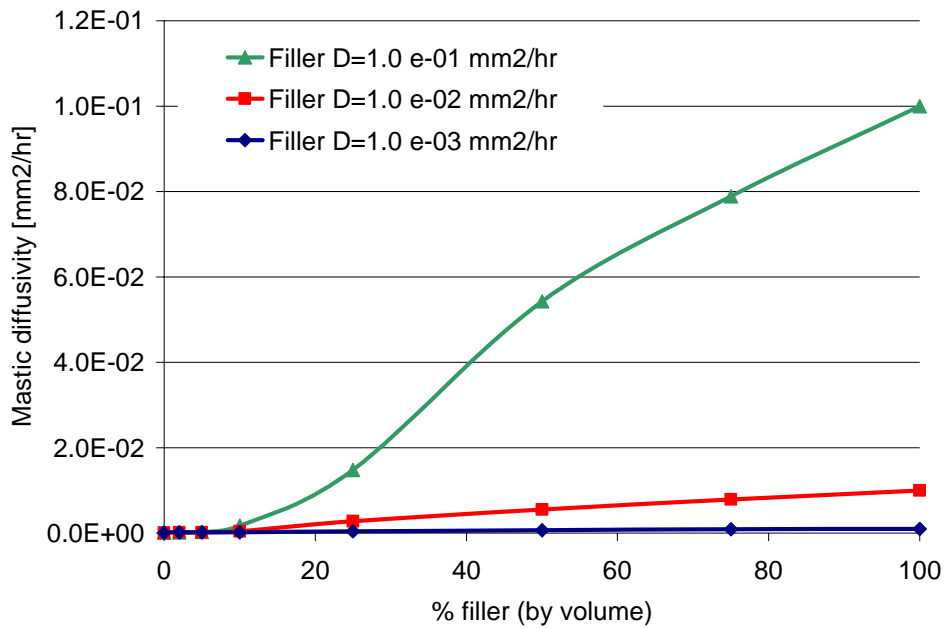


Fig. 6.3.14: Mastic diffusion coefficients distribution for 0 -100 % of filler content for three different filler types, with D-bitumen $1.0 \cdot 10^{-04} \text{ mm}^2/\text{hr}$

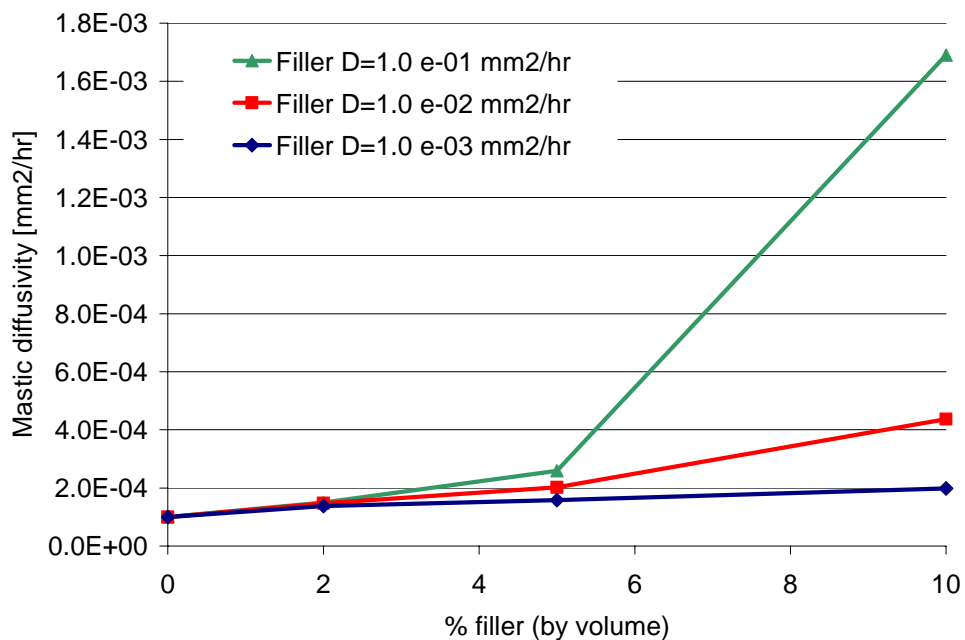


Fig. 6.3.15: Mastic diffusion coefficients distribution for 0 -10 % of filler content for three different filler types, with D-bitumen $1.0 \cdot 10^{-04} \text{ mm}^2/\text{hr}$

Fig. 6.3.16 shows the moisture diffusion into the mastic and its components for the mastic with 25% filler content.

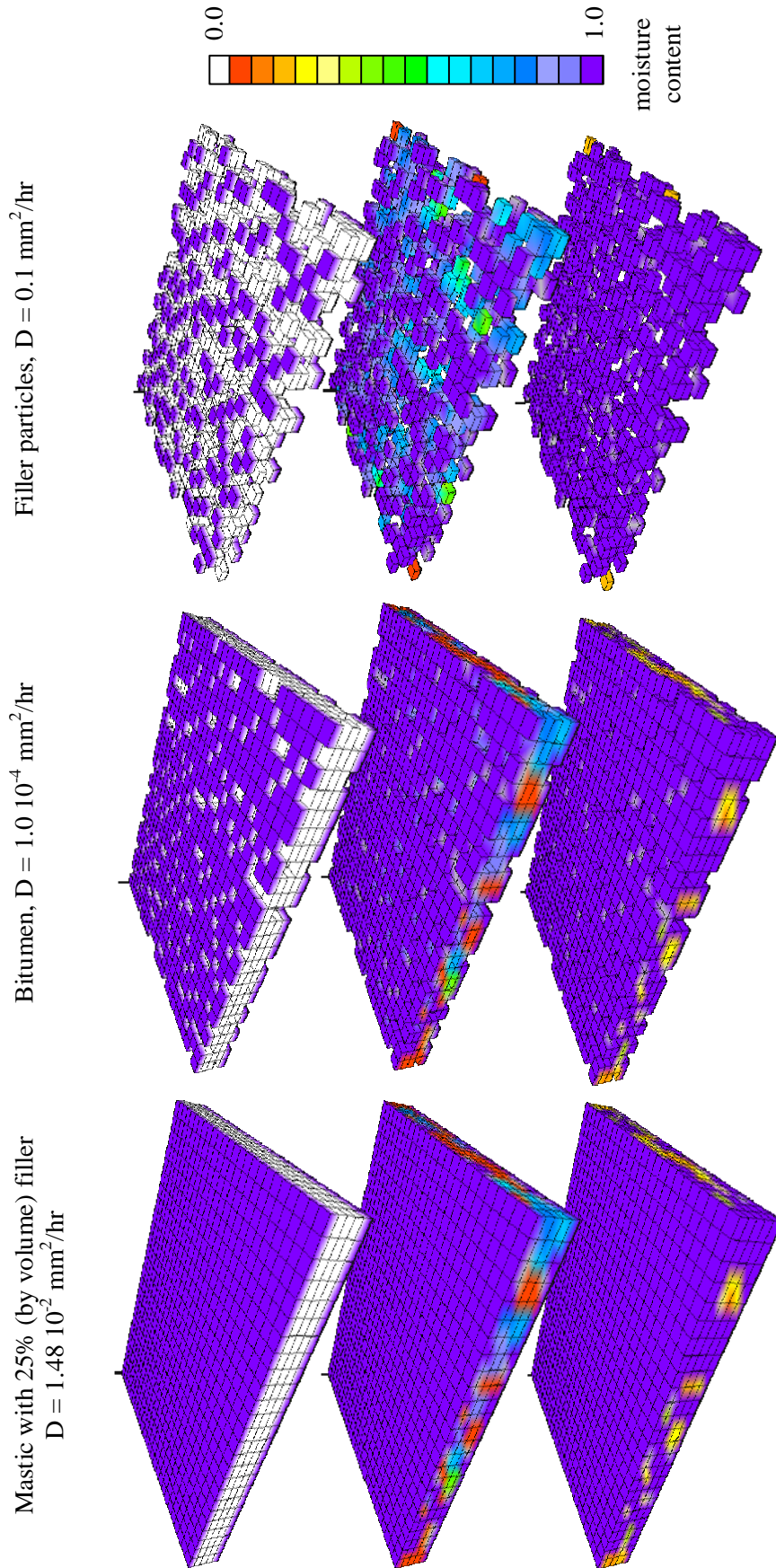


Fig. 6.3.16: Moisture diffusion into the mastic and its components

By dividing the computed moisture diffusion coefficients of the mastic with the moisture diffusion coefficients of the fillers, normalized diffusion values for the mastics are computed. The normalized values can be more easily compared and all three mastics seem to tend to an S-type shape, Fig. 6.3.17, ranging from

$$\tilde{D}_{0\%} = \frac{D_{\text{bitumen}}}{D_{\text{filler}}} \text{ for } 0\% \text{ filler content to } \tilde{D}_{100\%} = 1.0 \text{ for } 100\% \text{ filler content.}$$

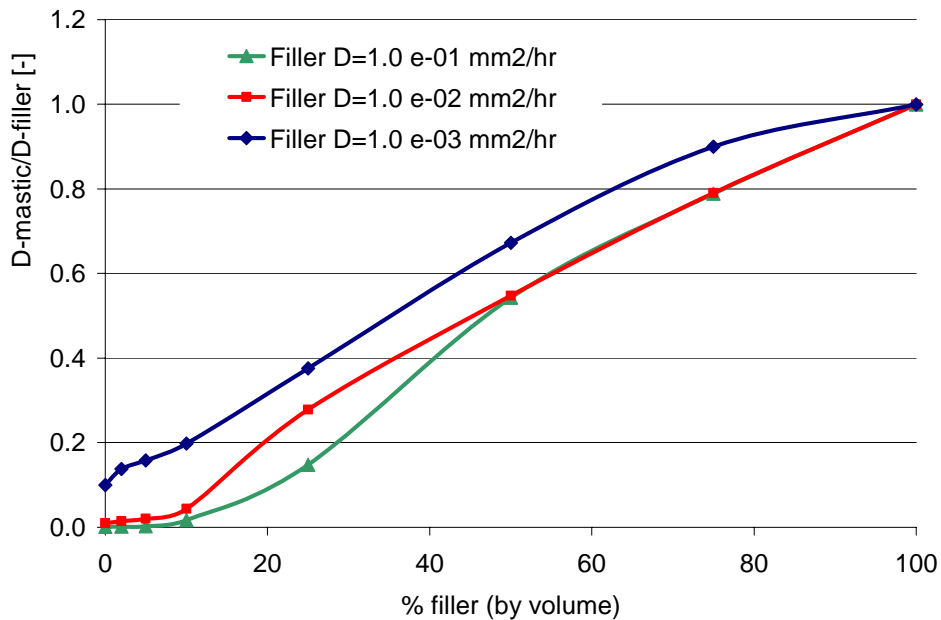


Fig. 6.3.17: Normalized diffusivity versus filler content

The inflexion points of the curves in Fig. 6.3.17, seem to be in the areas of 2-5%, 10-20% and 20-40% for the three mastics with $D_{\text{filler}} = 1.0 \cdot 10^{-3} \text{ mm}^2/\text{hr}$, $1.0 \cdot 10^{-2} \text{ mm}^2/\text{hr}$ and $1.0 \cdot 10^{-1} \text{ mm}^2/\text{hr}$, respectively.

It could therefore be postulated that the inflexion point of these curves is related to the value of $100\sqrt{D_{\text{filler}}/D_{\text{bitumen}}}$, since this roughly amounts to 3%, 10% and 32% for the three mastics.

Given the moisture diffusion coefficients of the neat bitumen and the filler material, it would therefore be possible to develop a schematic of the mastic diffusion coefficients as a function of filler content, Fig. 6.3.18.

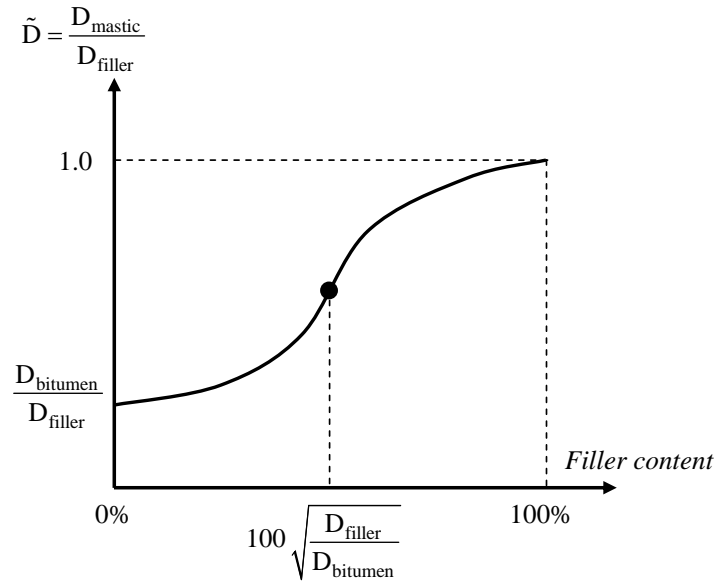


Fig. 6.3.18: Mastic diffusion coefficient as a function of filler content schematic

In the above, the percentage of filler is expressed in percentage by volume. In general, specifications are made for bitumen filler contents, based on percentage by weight. For this reason, the filler content percentages (by weight) equivalences are calculated in the following.

Utilizing a mean value for the bitumen density at 20 °C of $1.0 \cdot 10^3 \text{ kg/m}^3$, the filler content equivalences, for percentages by weight, are calculated for various aggregate filler types, Table 6.3.3.

Table 6.3.3: Filler content percentages by weight equivalences

Filler type (x 10 ³) [DWW 2006]	Percentage filler in mastic [% by weight]							
	0% by vol.	2% by vol.	5% by vol.	10% by vol.	25% by vol.	50% by vol.	75% by vol.	100% by vol.
Limestone based (3.0 kg/m ³)	0.0%	5.8%	13.6%	25.0%	50.0%	75.0%	90.0%	100 %
Granite based (2.7 kg/m ³)	0.0%	5.2%	12.4%	23.1%	47.4%	73.0%	89.0%	100 %
Production dust (2.7 kg/m ³)	0.0%	5.2%	12.4%	23.1%	47.4%	73.0%	89.0%	100 %
Morene sand based (2.6 kg/m ³)	0.0%	5.0%	12.0%	22.4%	46.4%	72.2%	88.6%	100 %
Wigro 60K filler (2.6 kg/m ³)	0.0%	5.0%	12.0%	22.4%	46.4%	72.2%	88.6%	100 %
Rhecal 60 filler (2.6 kg/m ³)	0.0%	5.0%	12.0%	22.4%	46.4%	72.2%	88.6%	100 %
Sandstone based (2.3 kg/m ³)	0.0%	4.5%	10.8%	20.4%	43.4%	69.7%	87.3%	100 %
Low density gravel (1.5 kg/m ³)	0.0%	3.0%	7.3%	14.3%	33.3%	60.0%	81.8%	100 %

In Fig. 6.3.19 and Fig. 6.3.20 the mastic diffusivity is plotted as a function of percentage filler content, by weight, for a limestone and a low density filler, respectively.

By comparing the green curves for both filler types, it can be seen that for the same percentage of filler content (e.g. 50% by weight), the mastic diffusivity can be almost 3x higher for the filler with a lower density, given the same filler diffusivity.

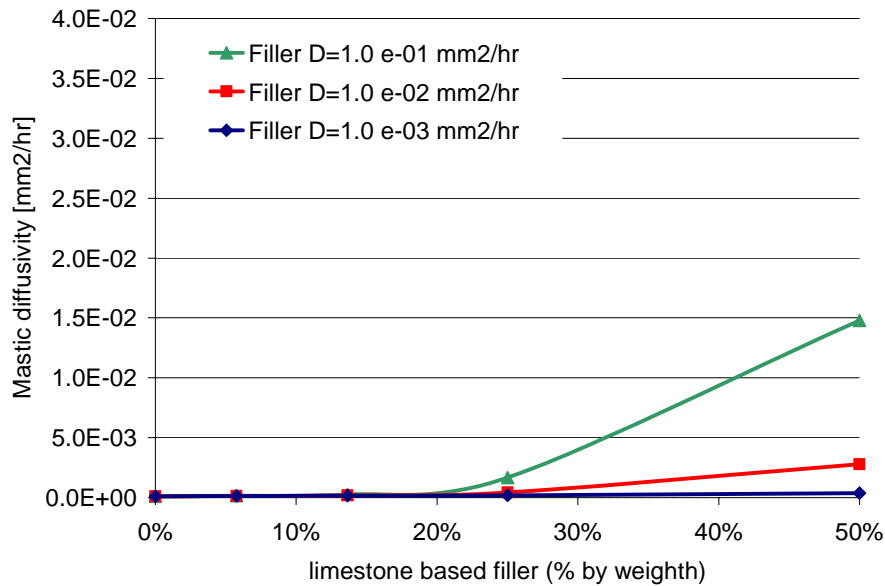


Fig. 6.3.19: Mastic diffusivity for a limestone based filler

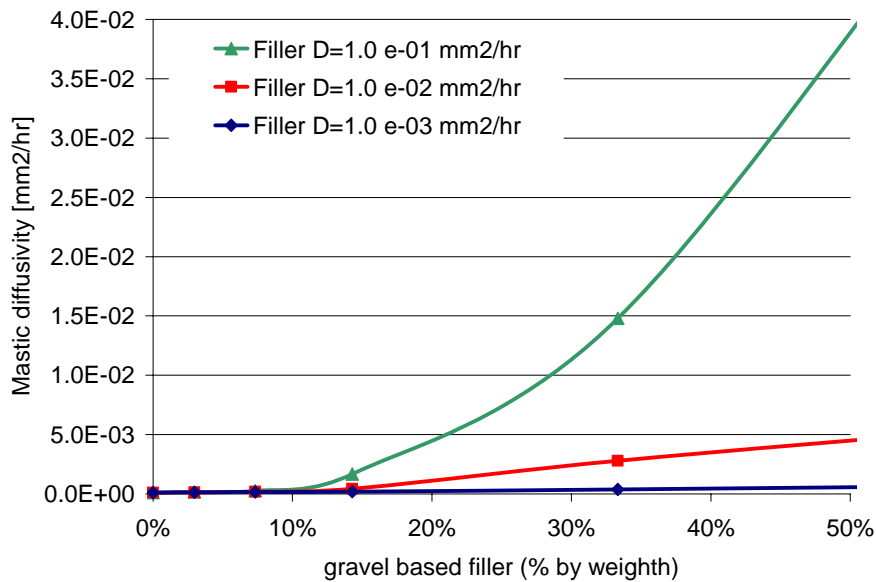


Fig. 6.3.20: Mastic diffusivity for a low density filler

Nevertheless, it is a plausible assumption that the diffusivity of a material and the density are related. Therefore, in reality, the comparison of Fig. 6.3.19 with Fig. 6.3.20 is not as straightforward as it seems.

Postulating that a denser material has less micro-pores and therefore will give a lower overall moisture diffusivity value, comparing the red curve of the lime based filler with the green curve of the low density filler, would actually indicate an even bigger influence of the filler type on the mastic diffusivity.

Filler material is in general added to bitumen to increase its stiffness and is chosen, mainly based on its availability and its past performance. In relation to reducing the moisture susceptibility of an asphaltic mix, mastic should be designed to have a low moisture diffusion coefficient. Therefore, in addition to the mechanical properties of the mastic, fillers should be selected to minimize the moisture susceptibility.

Based on the above analyses, fillers could therefore be categorized in preferred order by its effect on the mastic diffusivity. Utilizing the same filler diffusion coefficient, the fillers can be categorized based on the mastic diffusion coefficient, Fig. 6.3.21. From this graph it could be concluded that the fillers with higher densities (e.g. limestone, dust and Wigro 60K) would be preferred over the fillers with lower densities (e.g. gravel).

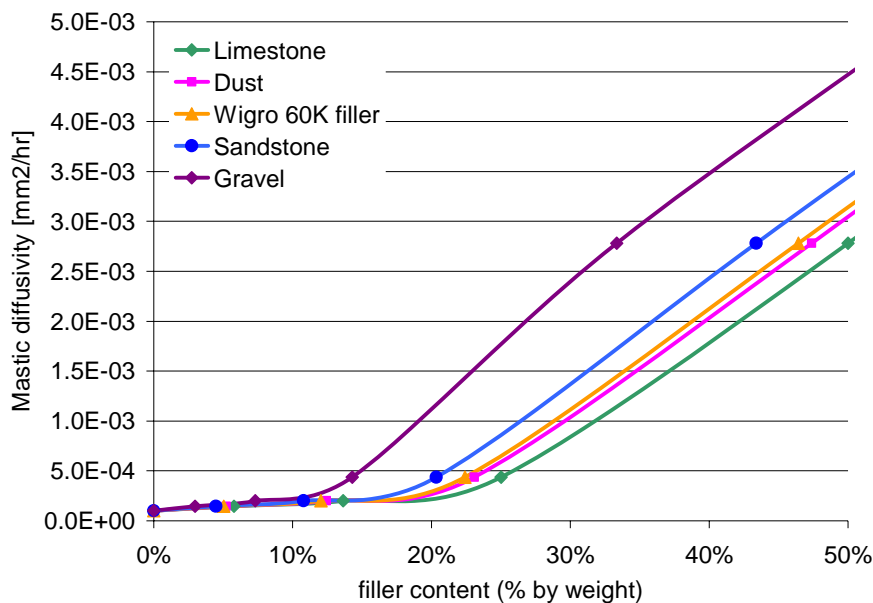


Fig. 6.3.21: Mastic diffusivity as a function of filler content for various fillers, with D-bitumen $1.0 \cdot 10^{-4} \text{ mm}^2/\text{hr}$ and D-filler $1.0 \cdot 10^{-2} \text{ mm}^2/\text{hr}$

By incorporating the relationship between high density and low diffusivity and visa-versa, the fillers could be re-plotted, Fig. 6.3.22, whereby utilizing the parametric diffusivity values of $1.0 \cdot 10^{-3} \text{ mm}^2/\text{hr}$, $1.0 \cdot 10^{-2} \text{ mm}^2/\text{hr}$ and $1.0 \cdot 10^{-1} \text{ mm}^2/\text{hr}$ for the limestone, sandstone and low density filler fillers, respectively.

From this graph, the same categorization would be made, i.e. limestone should still be preferred over gravel. The main difference between Fig. 6.3.21 and Fig. 6.3.22 is, that the effect of the mastic moisture susceptibility would be much higher, based on the second graph.

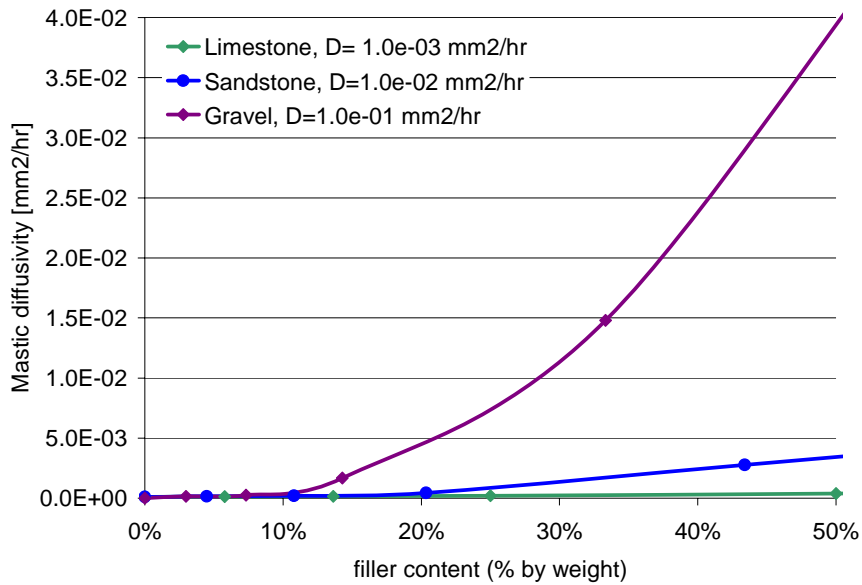


Fig. 6.3.22: Mastic diffusivity as a function of filler content for various fillers, with D-bitumen $1.0 \cdot 10^{-04} \text{ mm}^2/\text{hr}$, utilizing different filler diffusivities

Even though in the above analyses a wide range of parameters is used and the filler densities given in Table 6.3.3 can be varying, depending on the source of the fillers and their manufacturer, it can be concluded that characterization of the moisture susceptibility of the mastic components and choosing a suitable filler percentage, can have a huge impact on the moisture diffusion values of the mastic.

In section 9.6.2. of chapter 9, analyses are performed to determine the time of aggregate-mastic bond deterioration, as a function of mastic film thickness for a wide range of mastic diffusion coefficients. From these analyses the importance of the moisture diffusion coefficient of the mastic becomes clear.

6.4 Mastic desorption determination

As discussed previously, when an asphalt mix is exposed to a moisture flow field, moisture will infiltrate into the mastic film and may have an adverse effect on both the mastic film and the aggregate-mastic bond. In addition to these two phenomena, there is an additional physical process which entails the desorption of the mastic from the aggregate in the presence of moisture. This effect may be a combination of advective transport, which accounts for transport of mastic by virtue of a water flow field, and additional loss of concentration of the mastic, named dispersion, which accounts for the loss of mastic by virtue of moisture content within the material and diffusion of the mastic into the water in the macro-pores. The combined effect, the loss of mastic, is referred to as the erosion of the mastic.

To measure the erosion properties of a mastic, a mastic desorption test can be devised. The intention for such a mastic desorption test is to measure how much mastic is lost from the mix due to a water flow field. A possible methodology may be based on a standard permeability test, with added features to measure the loss of mastic.

In order to measure the loss of mastic due to a flow field, a core of mastic can be prepared through which a constant flow field is created, Fig. 6.4.1.

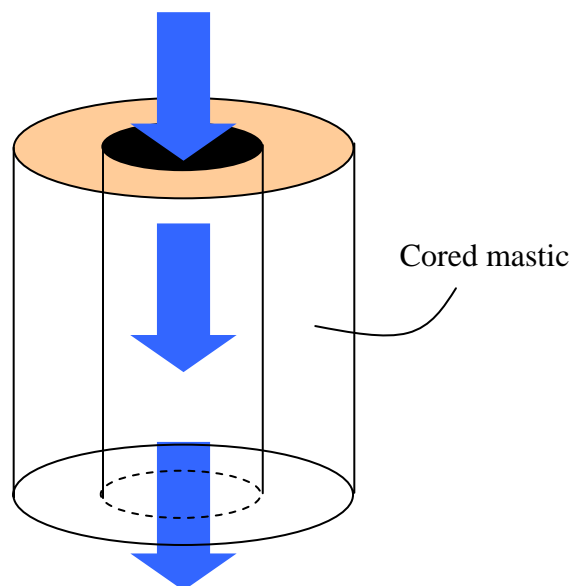


Fig. 6.4.1: Cilinder of mastic with a hole in the middle which is exposed to a constant water flow field

At regular intervals, the mastic weight should be recorded. From this procedure the desorption of mastic due to the advective transport is measured. Because the moisture content within the mastic may influence the damage of the material due to a flow field, the sample should be moisture conditioned before tested. The velocity of the flow field should be monitored and kept as high as possible, to simulate the representative water flow field in the pavement due to the pumping action of the traffic load.

In addition to measuring the weight change, the water which passed through the core should be chemically analyzed and should match with the recorded weight changes. Any discrepancy in the comparison of these two records can be explained by moisture

infiltration into the mastic, which was counteracting the monitored weight loss of the mastic.

Experimental Determination of Work of Adhesion

The surface tension γ of an asphaltic binder can be split into a dispersive or apolar component, also known as Lifshitz-van der Waals component, and a polar or acid-base component, as shown in the following

$$\gamma = \gamma^{\text{LW}} + \gamma^{\text{AB}} \quad (\text{A 6.1.1})$$

where γ^{LW} is the Lifshitz-van der Waals component and γ^{AB} is the acid-base component.

The acid-base term can be decomposed to a Lewis acidic surface parameter γ^+ and a Lewis basic surface parameter γ^- as follows:

$$\gamma^{\text{AB}} = 2\sqrt{\gamma^+\gamma^-} \quad (\text{A 6.1.2})$$

To determine these components, dynamic contact angle measurements of the asphaltic binder with different liquids can be used.

In this research, the *Dynamic Wilhelmy Plate method* is chosen to measure such contact angles. This method is based on kinetic force equilibrium when a thin plate is immersed and then withdrawn from a liquid solvent at a very slow and constant speed. The dynamic contact angle between an asphalt binder and a liquid solvent obtained during the immersing process is called “advancing contact angle”, Fig. A.6.1.1(a), while the dynamic contact angle during the withdrawal process, Fig. A.6.1.1(b) is called the “receding contact angle”. In this research, only advancing contact angle was considered for analyses, since it is difficult to measure the receding contact angle accurately.

A microbalance measures the change in force ΔF during the immersion and withdrawal process. These forces, in combination with a buoyant force correction, are used to determine the dynamic contact angle applying the kinetic equilibrium equation, as follows

$$\cos \varphi = (\Delta F + V_{\text{im}} (\rho_{\text{L}} - \rho_{\text{air}})g) / (P_t \gamma_{\text{L}}) \quad (\text{A 6.1.3})$$

where φ is the contact angle ($^\circ$), V_{im} is the immersed volume (cm^3), ρ_{L} is the density of liquid solvent (g/cm^3), ρ_{air} is the density of air (g/cm^3), P_t is the perimeter of the sample (cm), ΔF is the change in force (dyne), and γ_{L} is the surface tension of the liquid (dyne/cm).

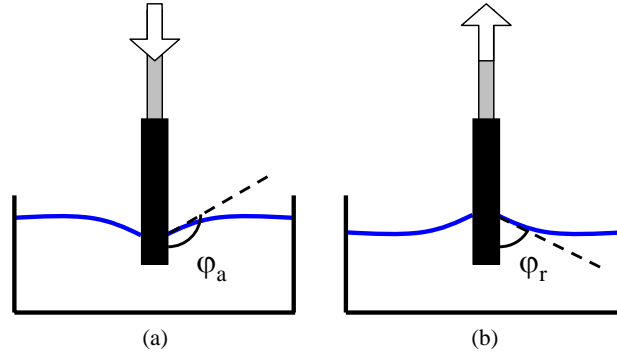


Fig. A.6.1.1: Dynamic Wilhelmy Plate Method for (a) advancing contact angle ϕ_a and (b) receding contact angle ϕ_r

Assuming that equilibrium film pressure is negligible for an asphalt binder, Young's equation and Dupré's equation can be combined with Good's postulate to obtain the so called Young-Dupré equation. The resulting Young-Dupré equation can be expressed as follows:

$$\gamma_L (1 + \cos \phi) = 2\sqrt{\gamma_S^{LW} \gamma_L^{LW}} + 2\sqrt{\gamma_S^- \gamma_L^+} + 2\sqrt{\gamma_S^+ \gamma_L^-} \quad (\text{A 6.1.4})$$

Where γ_L^{LW} , γ_L^+ and γ_L^- are the surface tension components of the liquid solvent and γ_S^{LW} , γ_S^- and γ_S^+ are the surface tension components of the asphaltic binder.

In the above equation, the surface tension components of an asphalt binder are given by the three unknowns (γ_S^{LW} , γ_S^- and γ_S^+). To obtain these unknowns, dynamic contact angles must be measured in at least three different liquid solvents. The surface tension characteristics of these liquid solvents must be known a priori.

Depending on the chemical composition of the bitumen, water, glycerin and formamide may be used as liquid solvents because of their relatively large surface tension, immiscibility with most asphalt binders, and differing surface tension components.

A Dynamic Contact Angle (DCA) analyzer, can be used for measuring advancing contact angles. Cover glasses can be partially coated with an asphalt binder. The following experimental setup and procedure was developed and utilized by the Oklahoma Transportation Centre and can be used for sample preparation and contact angle measurements.

For cleaning, cover glass plate should be placed into an oxygen flame, called flaming, horizontally along its length in a moving condition for at least three times. The flaming of a single cover glass plate does not take more than a few seconds.

For sample preparation, approximately 100 g of asphalt binder can be poured in a tin can, and the tin can must be heated in a gravity oven for 2 hours at 163°C. Each cover glass plate can then be dipped with a vertical orientation into the hot asphalt binder, to a depth of about 2 cm for approximately 5 seconds. After dipping, the sample should be held above the asphalt binder for an additional 5 seconds to allow excess asphalt binder to drop into the tin can. Samples can then be kept in a sample holder with

coated end up for 2 minutes. Sample preparation should be done inside a gravity oven with the help of forceps and a sample holder. The aforementioned method provides a uniform coating of at least 1 cm in length at the top end of the cover glass plate. Prepared samples may be kept overnight inside a desiccator before thickness measurement, **Error! Reference source not found.** The thickness of the samples can be measured using an Image Analyzer.

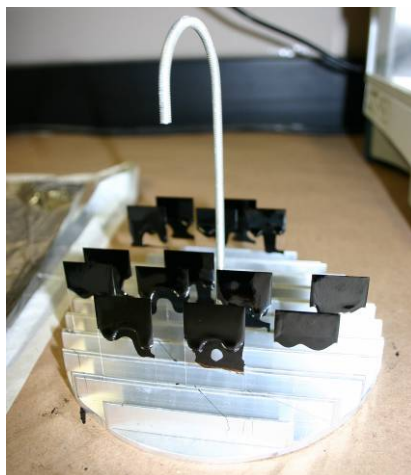


Fig. A.6.1.2: Samples in a sample holder.

For contact angle measurement, triplicate samples should be used for each of the three different solvents, namely, water, glycerin and formamide. No solvent should be reused for any two samples. Both motor and balance of the DCA analyzer should be calibrated at the beginning of each day the device was used. The sample can be placed in the microbalance with the help of a sample holder such that it remained freely hanging in a vertical orientation for the duration of measurements. Liquid solvent to be used for measuring contact angles should be poured in a clean beaker and placed under the mounted sample. The distance between the surface of the liquid solvent and the bottom of the sample should be maintained below 4 mm before the start of the test by moving the stage up and down, as desired.



Fig. A.6.1.1: Surface tension measurements

The beaker is then allowed to move vertically upward, Fig. A.6.1.1. No change in weight data should occur before the sample touches the liquid solvent. A plus symbol

inside a circle shows the ZDOI (Zero Depth of Immersion). The samples can be dipped into the liquid solvent up to 6 mm from the Zero Depth of Immersion at the same advancing rate. The sample should then be held steady for 2 min (dwelling time) before withdrawing from the liquid solvent at the same speed. The lower portion shows the weight (force) data for advancing contact angle, while the upper portion shows the same data for receding contact angle.

In summary, using the above described procedure, the surface tension values of the mastics can be determined. To determine the work of adhesion with and without moisture in the interface for the mastics and aggregates via Eq. 6.4 and Eq. 6.5, the surface tension of the aggregates also need to be determined.

For the measurement of the surface tension of the aggregates, the above procedure can not be utilized. Instead, a universal gas adsorption method may be used, which utilizes the characteristics of adsorption of a particular gas solvent onto the surface of an aggregate to indirectly determine the surface energy of the aggregate. This method can accommodate the peculiarities of the irregular shape, mineralogy and rough surface texture of the aggregate and details of the procedure can be found in [Cheng 2003].

Elasto-Visco Plastic Constitutive Model for Mastic

7.1 Introduction

In the previous chapters of this dissertation the theory and formulations were given of the physical damage processes in asphaltic mixes, when exposed to moisture. It was shown that RoAM enables the simulation of water flow, moisture diffusion and loss of a mastic concentration via a combined advective/dispersive process. However, the reason for simulating these physical processes is, to evaluate the changing physical material characteristics of the asphalt components, due to damage caused by moisture infiltration, while being subjected to mechanical (traffic) loading which, by itself, is also causing damage. Therefore, to accurately capture the material response under loading, a constitutive model for the asphalt components is needed.

As discussed earlier, asphaltic mixes are in this research considered on a component level, i.e. aggregates, mastic, aggregate-mastic interface and the macro-pores. Obviously, the macro-pores do not contribute to the mechanical properties of the mix, and as such, do not need a mechanical material model. The other components, i.e. the aggregates, the mastic and their interface, are of great importance in the mechanical properties of the mix and do need a robust constitutive formulation. Since the aggregate material response is assumed to behave in a fairly straight forward elastic-like manner, the main focus in this chapter shall lie on the more complex formulations of the mastic material model. The mastic material model, however, can also be used for simulation of the aggregate and interface response behavior.

So far, mastic has been treated in this dissertation as a homogeneous material. However, mastic normally consists of bitumen, granular particles with a diameter in the order of $\sim 0.5\text{mm}$ (sand particles) and granular particles with a diameter in the order of $< 75\mu\text{m}$ (filler particles). In other words, going one scale down from the asphalt components, mastic could also be considered as a composite material, Fig. 7.1.1..

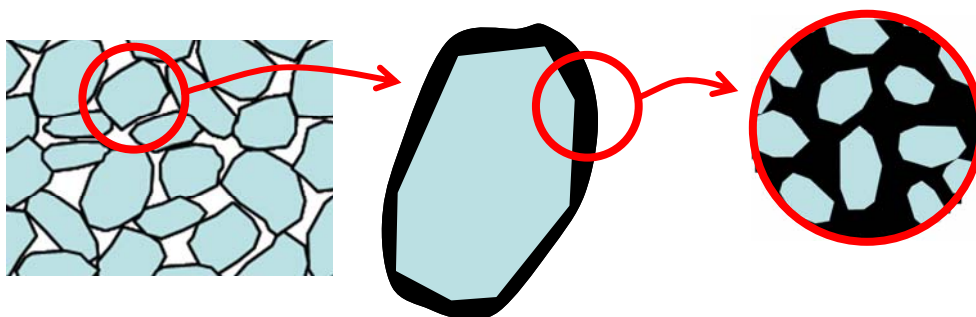


Fig. 7.1.1: Mastic as an asphaltic mix, but one scale down

Therefore, the response behavior of an asphaltic mix and that of its mastic exhibit similar characteristics which can be captured by the same material model.

In this chapter, a new generic material model for the mastic is presented. This model is developed at the Section of Structural Mechanics in the context of the ongoing asphalt modeling efforts, [Scarpas, 1997-2006], and can also be applied to the asphalt mix itself. The formulations which are given in this chapter are for the dry material response. In Chapter 8, the effect of moisture on the material model is discussed. Chapter 9 gives the combined physical-mechanical model, where the physical moisture induced damage processes, as discussed in Chapter 3-5, and the mechanical damage processes, as discussed in Chapter 7-8, are brought together.

7.2 Mastic constitutive model

7.2.1 Elasto-visco-plastic material response

In general, the deformation that an asphaltic material builds up during loading consists of elastic, visco-elastic and plastic deformation, which becomes visible after the load is removed from the material, Fig. 7.2.1. What makes asphaltic materials such challenging materials to model, however, is not just the combined elasto-visco-plastic response of the material, but its dependency on the temperature T and the rate of deformation $\dot{\epsilon}$. As Fig. 7.2.1 indicates, for higher strain rates the material behaves quite stiffer, as it also does at lower temperatures.

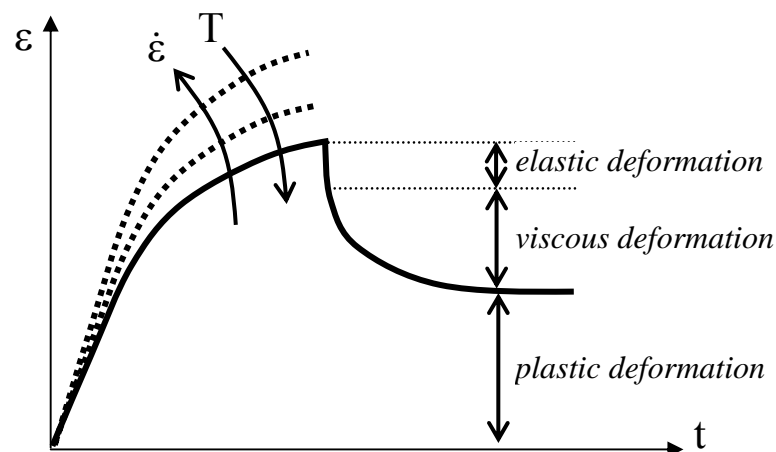


Fig. 7.2.1: General response of an asphaltic material

Constitutive models for asphaltic materials can be developed by combining the features of purely elasto-plastic and purely visco-elastic materials to create a more general category of constitutive models termed *elasto-visco-plastic*.

Fig. 7.2.2 shows a one-dimensional schematic of such a material model consisting of a single elasto-plastic component in parallel with an arbitrary number of viscoelastic ones. It would be beneficial for the modeling to be able to distinguish the individual visco-elastic and elasto-plastic material response, evaluate each of them with their own parameters and sum them up to give the overall response. Unfortunately, all of the response characteristics interact with each other in a three dimensional fashion, and make it therefore impossible to simply add up the effects in one direction. Therefore, a generic three dimensional energy based model is proposed, which operates on finite (i.e. large) strains, which has as an additional benefit that there are no restrictions regarding the range of strain in which the material can be modeled.

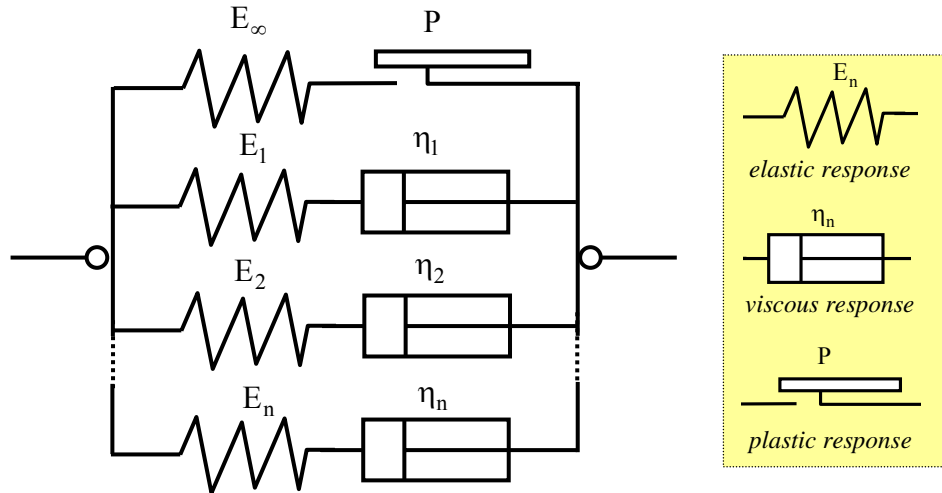


Fig. 7.2.2: Schematic of a one dimensional elasto-visco-plastic model

In the following, the deformation tensor, which determines the total deformation response of the material due to loading is formulated and the individual visco-elastic and elasto-plastic contributions and their coupling are derived.

7.2.2 Multiplicative decomposition

A vector $d\mathbf{x}$ in the deformed current configuration is related by means of the *deformation gradient* tensor \mathbf{F} to its undeformed (reference) configuration via the relation

$$d\mathbf{x} = \mathbf{F} d\mathbf{X} \quad (7.1)$$

If it is now assumed that the forces acting on the material element are removed, the initial reference configuration will only be obtained if the material is elastic. In all other cases, another configuration will be obtained in which the original vector $d\mathbf{X}$ is mapped onto vector $d\mathbf{x}_r$ with the subscript r indicating the residual nature of deformation, Fig. 7.2.3.

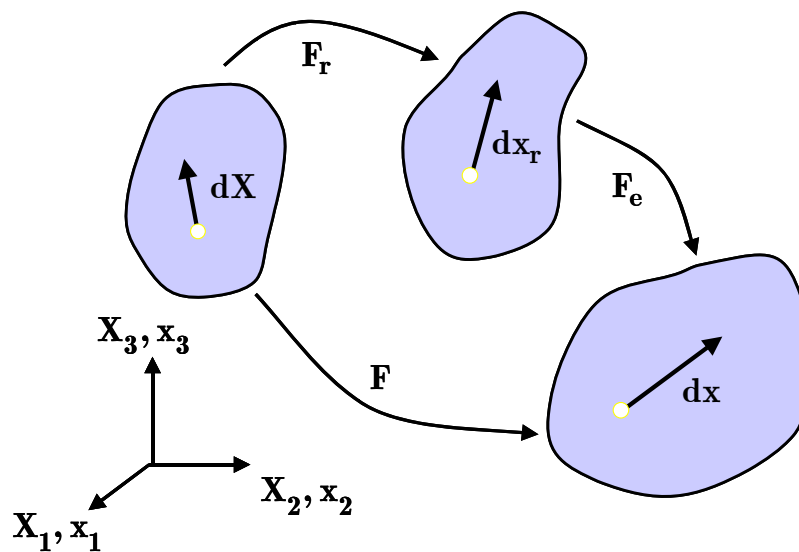


Fig. 7.2.3 Multiplicative decomposition of the deformation gradient

Let \mathbf{F}_e denote the deformation gradient relating the residual deformation configuration to the current configuration. Then, according to Eq. (7.1)

$$d\mathbf{x} = \mathbf{F}_e d\mathbf{x}_r \quad (7.2)$$

Similarly, if \mathbf{F}_r denotes the deformation gradient relating the residual deformation configuration to the reference configuration, then it also holds

$$d\mathbf{x}_r = \mathbf{F}_r d\mathbf{X} \quad (7.3)$$

so that

$$d\mathbf{x} = \mathbf{F}_e \mathbf{F}_r d\mathbf{X} \quad (7.4)$$

and therefore

$$\mathbf{F} = \mathbf{F}_e \mathbf{F}_r \quad (7.5)$$

The process represented by Eq. (7.5) is known as the “*multiplicative decomposition*” of the deformation gradient to a residual deformation component and a component signifying the elastic unloading that the material must undergo from the configuration at time t to the residual configuration.

The concept of multiplicative decomposition of the deformation gradient provides an elegant tool for description of the three dimensional response of elasto-visco-plastic material models consisting of elasto-plastic and visco-elastic components.

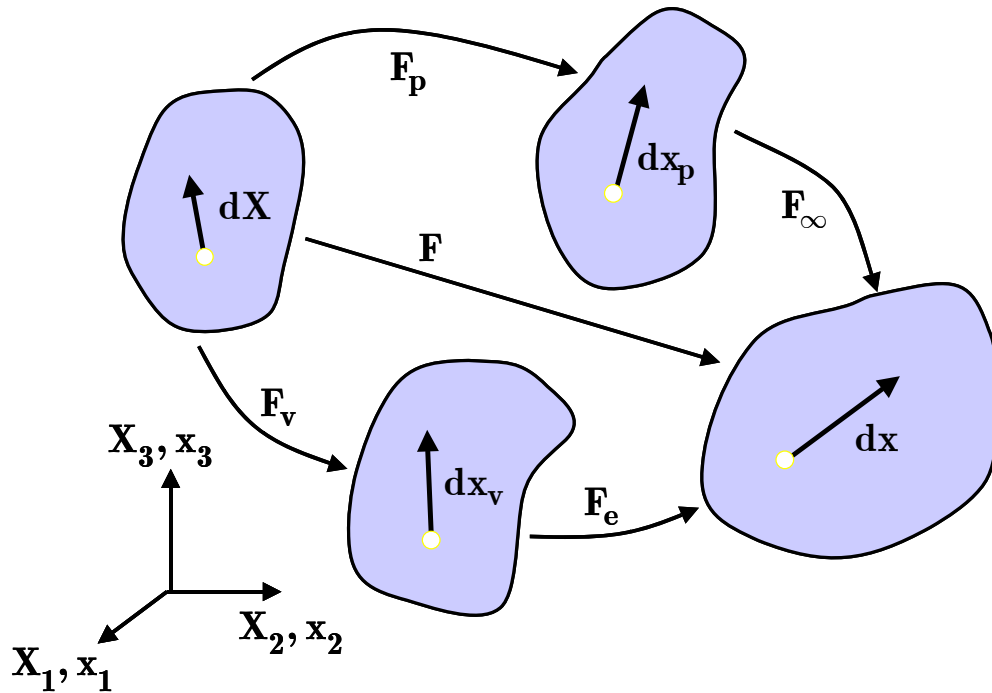


Fig. 7.2.4 Multiplicative decomposition of the deformation gradient of an elasto-visco-plastic material

As shown schematically in Fig. 7.2.4, the deformation gradient of a material in which the elasto-plastic and the viscoelastic components act in parallel can be decomposed as

$$\mathbf{F} = \mathbf{F}_\infty \mathbf{F}_p \quad ; \quad \mathbf{F} = \mathbf{F}_e \mathbf{F}_v \quad (7.6)$$

in which \mathbf{F}_∞ = the elastic component of the deformation gradient of the elasto-plastic element

\mathbf{F}_p = the plastic component of the deformation gradient of the elasto-plastic element

\mathbf{F}_e = the elastic component of the deformation gradient of the visco-elastic element

\mathbf{F}_v = the viscous component of the deformation gradient of the visco-elastic element

Furthermore the following definition hold:

$$\begin{aligned} \mathbf{C}_\infty &= \mathbf{F}_\infty^T \mathbf{F}_\infty & \mathbf{C}_e &= \mathbf{F}_e^T \mathbf{F}_e \\ \mathbf{C}_p &= \mathbf{F}_p^T \mathbf{F}_p & \mathbf{C}_v &= \mathbf{F}_v^T \mathbf{F}_v \end{aligned} \quad (7.7)$$

where \mathbf{C} is the right Cauchy-Green strain tensor, and shall be referred to from here on as the strain tensor.

Therefore, using Eq. (7.6) and Eq. (7.7), it can be shown

$$\begin{aligned} \mathbf{C} &= \mathbf{F}^T \mathbf{F} = \mathbf{F}_v^T \mathbf{C}_e \mathbf{F}_v \\ &= \mathbf{F}_p^T \mathbf{C}_\infty \mathbf{F}_p \end{aligned} \quad (7.8)$$

With this, a definition has been derived to compute the total strain tensor of the material \mathbf{C} , based on either of the elastic strain tensors and the plastic or the viscous deformation gradient, respectively.

However, what distinguishes one material from another is its stress-strain response. In this thesis, it is assumed that the constitutive behavior of the mastic can be simulated via hyper-elasticity theory. This means, that the existence of a so-called *Helmholtz free-energy function* Ψ is postulated. In the following, the stress tensor in the intermediate configuration, based the Helmholtz free-energy function, is derived.

7.2.3 Local Dissipation Model

The Helmholtz free energy function for a three dimensional model equivalent to the generalized model proposed in the above can be expressed as

$$\Psi = \Psi_v(\mathbf{C}_e) + \Psi_p(\mathbf{C}_\infty, \xi_p) \quad (7.9)$$

where ξ_p is a measure of the plastic deformation and will be explained in more detail later on.

The second law of thermodynamics states that a material can either be non-dissipative or dissipative, but it cannot produce energy as such. In writing, this is often referred to as the *Clausius-Planck local dissipation inequality* and can be formulated as

$$\mathbf{S} : \frac{1}{2} \dot{\mathbf{C}} - \left[\frac{\partial \Psi_v}{\partial \mathbf{C}_e} : \dot{\mathbf{C}}_e \right] - \left[\frac{\partial \Psi_p}{\partial \mathbf{C}_\infty} : \dot{\mathbf{C}}_\infty + \frac{\partial \Psi_p}{\partial \xi_p} \dot{\xi}_p \right] \geq 0 \quad (7.10)$$

where \mathbf{S} is the second Piola-Kirchhoff stress tensor.

It has been shown [Scarpas, 2006] that the above inequality can be reformulated as

$$\begin{aligned}
& \left[\mathbf{S} - 2 \mathbf{F}_v^{-1} \frac{\partial \Psi_v}{\partial \mathbf{C}_e} \mathbf{F}_v^{-T} - 2 \mathbf{F}_p^{-1} \frac{\partial \Psi_p}{\partial \mathbf{C}_\infty} \mathbf{F}_p^{-T} \right] : \frac{1}{2} \dot{\mathbf{C}} \\
& \quad + \left[2 \mathbf{F}_e \frac{\partial \Psi_v}{\partial \mathbf{C}_e} \mathbf{F}_e^T \mathbf{F}_e^{-T} : \mathbf{F}_e \mathbf{l}_v \right] \\
& \quad + \left[2 \mathbf{F}_\infty \frac{\partial \Psi_p}{\partial \mathbf{C}_\infty} \mathbf{F}_\infty^T \mathbf{F}_\infty^{-T} : \mathbf{F}_\infty \mathbf{l}_p - \frac{\partial \Psi_p}{\partial \xi_p} \dot{\xi}_p \right] \\
& \geq 0
\end{aligned} \tag{7.11}$$

By standard arguments, [Coleman & Gurtin 1967], on the basis of Eq. (7.11), the stress tensor \mathbf{S} can be additively decomposed into a viscoelastic \mathbf{S}_v and a plastic component \mathbf{S}_p

$$\begin{aligned}
\mathbf{S} &= 2 \mathbf{F}_v^{-1} \frac{\partial \Psi_v}{\partial \mathbf{C}_e} \mathbf{F}_v^{-T} + 2 \mathbf{F}_p^{-1} \frac{\partial \Psi_p}{\partial \mathbf{C}_\infty} \mathbf{F}_p^{-T} \\
&= \mathbf{S}_e + \mathbf{S}_\infty
\end{aligned} \tag{7.12}$$

Also the following inequalities are obtained

$$2 \mathbf{F}_e \frac{\partial \Psi_v}{\partial \mathbf{C}_e} \mathbf{F}_e^T \mathbf{F}_e^{-T} : \mathbf{F}_e \mathbf{l}_v \geq 0 \tag{7.13}$$

$$2 \mathbf{F}_\infty \frac{\partial \Psi_p}{\partial \mathbf{C}_\infty} \mathbf{F}_\infty^T \mathbf{F}_\infty^{-T} : \mathbf{F}_\infty \mathbf{l}_p - \frac{\partial \Psi_p}{\partial \xi_p} \dot{\xi}_p \geq 0 \tag{7.14}$$

Until here, the general frame-work of the large-strain, energy based, formulation has been set-up. To evaluate the response evolution, the stress and strain tensors need to be defined in the intermediate configuration. Since the visco-elastic and elasto-plastic components have their own intermediate configuration, Fig. 7.2.4, they are treated separately. In the following the formulations for the elasto-plastic component are derived.

7.2.4 Elasto-Plastic Component

To set-up the equations on the intermediate configuration, first, the Lagrange-Green strain tensor is defined in the reference configuration as

$$\mathbf{E} = \frac{1}{2} (\mathbf{F}^T \mathbf{F} - \mathbf{I}) \tag{7.15}$$

or in terms of the decomposition of Eq. (7.6)₁ as

$$\mathbf{E} = \frac{1}{2} (\mathbf{F}_p^T \mathbf{F}_\infty^T \mathbf{F}_\infty \mathbf{F}_p - \mathbf{I}) \tag{7.16}$$

By performing a *push forward* or a *pull back* operation, tensors can be mapped from the reference or the current configuration, respectively, onto the intermediate configuration. In general, tensors defined in the reference configuration are expressed in capital symbols and tensors defined in the current are noted by small symbols. In the following, tensors defined on the intermediate configuration, Fig. 7.2.4, are noted by a cap ($\hat{\bullet}$).

On the intermediate configuration, the Lagrange-Green strain tensor is defined by performing a push-forward operation, from the reference to the intermediate configuration

$$\hat{\mathbf{E}} = \mathbf{F}_p^{-T} \mathbf{E} \mathbf{F}_p^{-1} \quad (7.17)$$

which upon substitution of \mathbf{E} from Eq. (7.16) becomes

$$\begin{aligned} \hat{\mathbf{E}} &= \mathbf{F}_p^{-T} \mathbf{E} \mathbf{F}_p^{-1} = \frac{1}{2} \mathbf{F}_p^{-T} \left(\mathbf{F}_p^T \mathbf{F}_\infty^T \mathbf{F}_\infty \mathbf{F}_p - \mathbf{I} \right) \mathbf{F}_p^{-1} \\ &= \frac{1}{2} \left(\mathbf{F}_\infty^T \mathbf{F}_\infty - \mathbf{F}_p^{-T} \mathbf{F}_p^{-1} \right) \\ &= \frac{1}{2} \left(\mathbf{C}_\infty - \mathbf{I} \right) + \frac{1}{2} \left(\mathbf{I} - \mathbf{b}_p^{-1} \right) \\ &= \hat{\mathbf{E}}_\infty + \hat{\mathbf{E}}_p \end{aligned} \quad (7.18)$$

defining thus, on the intermediate configuration, the elastic Lagrange-Green strain tensor as $\hat{\mathbf{E}}_\infty = \frac{1}{2} \left(\mathbf{C}_\infty - \mathbf{I} \right)$ and the plastic Euler-Almansi strain tensor as $\hat{\mathbf{E}}_p = \frac{1}{2} \left(\mathbf{I} - \mathbf{b}_p^{-1} \right)$.

By means of the same push-forward operation as in Eq. (7.17), the rate of deformation tensor on the intermediate configuration can be expressed in terms of the Lagrange-Green strain rate tensor $\dot{\mathbf{E}}$

$$\hat{\mathbf{d}} = \mathbf{F}_p^{-T} \dot{\mathbf{E}} \mathbf{F}_p^{-1} \quad (7.19)$$

or, after substitution from Eq. (7.16), and utilizing $\dot{\mathbf{F}}_\infty = \mathbf{l}_\infty \mathbf{F}_\infty$, $\dot{\mathbf{F}}_\infty^T = \mathbf{F}_\infty^T \mathbf{l}_\infty^T$, $\dot{\mathbf{F}}_p = \mathbf{l}_p \mathbf{F}_p$ and $\dot{\mathbf{F}}_p^T = \mathbf{F}_p^T \mathbf{l}_p^T$ and $\mathbf{F}_\infty^T \mathbf{F}_\infty = \left(\mathbf{F}_\infty^T \mathbf{F}_\infty - \mathbf{I} \right) + \mathbf{I} = 2\hat{\mathbf{E}}_\infty + \mathbf{I}$

$$\begin{aligned} \hat{\mathbf{d}} &= \frac{1}{2} \left(\begin{aligned} &\mathbf{F}_p^{-T} \dot{\mathbf{F}}_p^T \mathbf{F}_\infty^T \mathbf{F}_\infty \mathbf{F}_p \mathbf{F}_p^{-1} + \mathbf{F}_p^{-T} \mathbf{F}_p^T \dot{\mathbf{F}}_\infty^T \mathbf{F}_\infty \mathbf{F}_p \mathbf{F}_p^{-1} \\ &+ \mathbf{F}_p^{-T} \mathbf{F}_p^T \mathbf{F}_\infty^T \dot{\mathbf{F}}_\infty \mathbf{F}_p \mathbf{F}_p^{-1} + \mathbf{F}_p^{-T} \mathbf{F}_p^T \mathbf{F}_\infty^T \mathbf{F}_\infty \dot{\mathbf{F}}_p \mathbf{F}_p^{-1} \end{aligned} \right) \\ &= \frac{1}{2} \left(\mathbf{F}_p^{-T} \dot{\mathbf{F}}_p^T \mathbf{F}_\infty^T \mathbf{F}_\infty + \dot{\mathbf{F}}_\infty^T \mathbf{F}_\infty \mathbf{F}_p \mathbf{F}_p^{-1} + \mathbf{F}_\infty^T \dot{\mathbf{F}}_\infty + \mathbf{F}_\infty^T \mathbf{F}_\infty \dot{\mathbf{F}}_p \mathbf{F}_p^{-1} \right) \\ &= \frac{1}{2} \left(\mathbf{l}_p^T \mathbf{F}_\infty^T \mathbf{F}_\infty + \mathbf{F}_\infty^T \mathbf{F}_\infty \mathbf{l}_p + \mathbf{F}_\infty^T \mathbf{l}_\infty^T \mathbf{F}_\infty + \mathbf{F}_\infty^T \mathbf{l}_\infty \mathbf{F}_\infty \right) \\ &= \frac{1}{2} \left(\mathbf{l}_p^T \left(2\hat{\mathbf{E}}_\infty + \mathbf{I} \right) + \left(2\hat{\mathbf{E}}_\infty + \mathbf{I} \right) \mathbf{l}_p + \mathbf{F}_\infty^T \left(\mathbf{l}_\infty^T + \mathbf{l}_\infty \right) \mathbf{F}_\infty \right) \\ &= \mathbf{l}_p^T \hat{\mathbf{E}}_\infty + \hat{\mathbf{E}}_\infty \mathbf{l}_p + \frac{1}{2} \left(\mathbf{l}_p^T + \mathbf{l}_p \right) + \mathbf{F}_\infty^T \frac{1}{2} \left(\mathbf{l}_\infty^T + \mathbf{l}_\infty \right) \mathbf{F}_\infty \\ &= \mathbf{l}_p^T \hat{\mathbf{E}}_\infty + \hat{\mathbf{E}}_\infty \mathbf{l}_p + \mathbf{F}_\infty^T \hat{\mathbf{d}}_\infty \mathbf{F}_\infty + \hat{\mathbf{d}}_p \\ &= \mathbf{l}_p^T \hat{\mathbf{E}}_\infty + \hat{\mathbf{E}}_\infty \mathbf{l}_p + \hat{\mathbf{E}}_\infty + \hat{\mathbf{d}}_p \\ &= \hat{\mathbf{d}}_\infty + \hat{\mathbf{d}}_p \end{aligned} \quad (7.20)$$

Where it can be shown that

$$\begin{aligned}\hat{\mathbf{d}}_\infty &= \dot{\hat{\mathbf{E}}}_\infty + \mathbf{l}_p^T \hat{\mathbf{E}}_\infty + \hat{\mathbf{E}}_\infty \mathbf{l}_p = \frac{1}{2}(\mathbf{l}_\infty^T + \mathbf{l}_\infty) \\ \hat{\mathbf{d}}_p &= \dot{\hat{\mathbf{E}}}_p + \mathbf{l}_p^T \hat{\mathbf{E}}_p + \hat{\mathbf{E}}_p \mathbf{l}_p = \frac{1}{2}(\mathbf{l}_p^T + \mathbf{l}_p)\end{aligned}\quad (7.21)$$

defining thus, on the intermediate configuration, two Oldroyd type rates of the strain $\hat{\mathbf{E}}$. An elastic one $\hat{\mathbf{d}}_\infty$ and a plastic one $\hat{\mathbf{d}}_p$.

The second Piola-Kirchhoff stress can be also pushed forward to the intermediate configuration.

$$\mathbf{S}_\infty = \mathbf{F}_p \mathbf{S} \mathbf{F}_p^T \quad (7.22)$$

The inner product of a stress tensor and its associated rate of deformation tensor describe the rate of internal mechanical work (or stress power). From this, it is said that the stress tensor is *work conjugate* to its strain tensor. Therefore, \mathbf{S} , \mathbf{S}_∞ and $\dot{\mathbf{E}}$, $\hat{\mathbf{d}}$ are work conjugate, respectively. Meaning that

$$\mathbf{S} : \dot{\mathbf{E}} = \mathbf{S}_\infty : \hat{\mathbf{d}} \quad (7.23)$$

Substituting in the above the components of $\hat{\mathbf{d}}$ it holds

$$\begin{aligned}\mathbf{S} : \dot{\mathbf{E}} &= \mathbf{S}_\infty : \hat{\mathbf{d}} \\ &= \mathbf{S}_\infty : \hat{\mathbf{d}}_e + \mathbf{S}_\infty : \hat{\mathbf{d}}_p \\ &= \mathbf{S}_\infty : \left[\left(\dot{\hat{\mathbf{E}}}_e + \mathbf{l}_p^T \hat{\mathbf{E}}_e + \hat{\mathbf{E}}_e \mathbf{l}_p \right) + \left(\dot{\hat{\mathbf{E}}}_p + \mathbf{l}_p^T \hat{\mathbf{E}}_p + \hat{\mathbf{E}}_p \mathbf{l}_p \right) \right] \\ &= \mathbf{S}_\infty : \dot{\hat{\mathbf{E}}}_e + \mathbf{S}_\infty : \left[\dot{\hat{\mathbf{E}}}_p + \mathbf{l}_p^T \hat{\mathbf{E}}_p + \hat{\mathbf{E}}_p \mathbf{l}_p + \mathbf{l}_p^T \hat{\mathbf{E}}_e + \hat{\mathbf{E}}_e \mathbf{l}_p \right] \\ &= \mathbf{S}_\infty : \dot{\hat{\mathbf{E}}}_e + \mathbf{S}_\infty : \left[\frac{1}{2}(\mathbf{l}_p + \mathbf{l}_p^T) + \mathbf{l}_p^T \hat{\mathbf{E}}_e + \hat{\mathbf{E}}_e \mathbf{l}_p \right] \\ &= \mathbf{S}_\infty : \dot{\hat{\mathbf{E}}}_e + \mathbf{S}_\infty : \left[\mathbf{l}_p + 2\hat{\mathbf{E}}_e \mathbf{l}_p \right] \\ &= \mathbf{S}_\infty : \dot{\hat{\mathbf{E}}}_e + \mathbf{S}_\infty : \left(\mathbf{I} + 2\hat{\mathbf{E}}_e \right) \mathbf{l}_p \\ &= \mathbf{S}_\infty : \dot{\hat{\mathbf{E}}}_e + \mathbf{S}_\infty : \mathbf{C}_\infty \mathbf{l}_p \quad \left\{ \mathbf{A} : \mathbf{BC} \equiv \mathbf{B}^T \mathbf{A} : \mathbf{C} \right\} \\ &= \mathbf{S}_\infty : \dot{\hat{\mathbf{E}}}_e + \mathbf{C}_\infty \mathbf{S}_\infty : \mathbf{l}_p\end{aligned}\quad (7.24)$$

In the intermediate configuration, for the elasto-plastic component of the model, the Helmholtz free energy can be set up as

$$\Psi = \Psi(\mathbf{C}_\infty, \xi) \quad (7.25)$$

$$\dot{\Psi} = \frac{\partial \Psi}{\partial \mathbf{C}_\infty} : \dot{\mathbf{C}}_\infty + \frac{\partial \Psi}{\partial \xi} : \dot{\xi} \quad (7.26)$$

Eq. (7.26) can be further elaborated as

$$\begin{aligned}
\dot{\Psi} &= 2 \frac{\partial \Psi}{\partial \mathbf{C}_\infty} : \mathbf{F}_\infty^T \dot{\mathbf{F}}_\infty + \frac{\partial \Psi}{\partial \xi} : \dot{\xi} = 2 \mathbf{F}_\infty \frac{\partial \Psi}{\partial \mathbf{C}_\infty} : \dot{\mathbf{F}}_\infty + \frac{\partial \Psi}{\partial \xi} : \dot{\xi} \\
&= 2 \mathbf{F}_\infty \frac{\partial \Psi}{\partial \mathbf{C}_\infty} : \left(\dot{\mathbf{F}} \mathbf{F}_p^{-1} + \mathbf{F} \dot{\mathbf{F}}_p^{-1} \right) + \frac{\partial \Psi}{\partial \xi} : \dot{\xi} \\
&= 2 \mathbf{F}_\infty \frac{\partial \Psi}{\partial \mathbf{C}_\infty} : \dot{\mathbf{F}} \mathbf{F}_p^{-1} + 2 \mathbf{F}_\infty \frac{\partial \Psi}{\partial \mathbf{C}_\infty} : \mathbf{F} \dot{\mathbf{F}}_p^{-1} + \frac{\partial \Psi}{\partial \xi} : \dot{\xi}
\end{aligned} \tag{7.27}$$

Utilizing the tensor identity $\mathbf{A} : \mathbf{BC} = \mathbf{AC}^T : \mathbf{B}$ it results

$$2 \mathbf{F}_\infty \frac{\partial \Psi}{\partial \mathbf{C}_\infty} : \dot{\mathbf{F}} \mathbf{F}_p^{-1} = 2 \mathbf{F}_\infty \frac{\partial \Psi}{\partial \mathbf{C}_\infty} \mathbf{F}_p^{-T} : \dot{\mathbf{F}} \tag{7.28}$$

By means of the identity $\dot{\mathbf{F}}_p^{-1} = -\mathbf{F}_p^{-1} \dot{\mathbf{F}}_p \mathbf{F}_p^{-1}$ and the identity $\mathbf{F}_\infty = \mathbf{F} \mathbf{F}_p^{-1}$ it holds

$$2 \mathbf{F}_\infty \frac{\partial \Psi}{\partial \mathbf{C}_\infty} : \mathbf{F} \dot{\mathbf{F}}_p^{-1} = -2 \mathbf{F}_\infty \frac{\partial \Psi}{\partial \mathbf{C}_\infty} : \mathbf{F} \left(\mathbf{F}_p^{-1} \dot{\mathbf{F}}_p \mathbf{F}_p^{-1} \right) = -2 \mathbf{F}_\infty \frac{\partial \Psi}{\partial \mathbf{C}_\infty} : \mathbf{F}_\infty \dot{\mathbf{F}}_p \mathbf{F}_p^{-1} \tag{7.29}$$

Utilizing the tensor identity $\mathbf{A} : \mathbf{BC} = \mathbf{B}^T \mathbf{A} : \mathbf{C}$ it results

$$-2 \left(\mathbf{F}_\infty \frac{\partial \Psi}{\partial \mathbf{C}_\infty} \right) : \mathbf{F}_\infty \dot{\mathbf{F}}_p \mathbf{F}_p^{-1} = -2 \mathbf{F}_\infty^T \left(\mathbf{F}_\infty \frac{\partial \Psi}{\partial \mathbf{C}_\infty} \right) : \dot{\mathbf{F}}_p \mathbf{F}_p^{-1} = -2 \mathbf{C}_\infty \frac{\partial \Psi}{\partial \mathbf{C}_\infty} : \dot{\mathbf{F}}_p \mathbf{F}_p^{-1} \tag{7.30}$$

which can be further simplified by means of the identity $\mathbf{A} : \mathbf{BC} = \mathbf{AC}^T : \mathbf{B}$

$$-2 \mathbf{C}_\infty \frac{\partial \Psi}{\partial \mathbf{C}_\infty} : \dot{\mathbf{F}}_p \mathbf{F}_p^{-1} = -2 \mathbf{C}_\infty \frac{\partial \Psi}{\partial \mathbf{C}_\infty} \mathbf{F}_p^{-T} : \dot{\mathbf{F}}_p \tag{7.31}$$

Substituting Eq. (7.28) and Eq. (7.31) into Eq. (7.27)

$$\dot{\Psi} = 2 \mathbf{F}_\infty \frac{\partial \Psi}{\partial \mathbf{C}_\infty} \mathbf{F}_p^{-T} : \dot{\mathbf{F}} - 2 \mathbf{C}_\infty \frac{\partial \Psi}{\partial \mathbf{C}_\infty} \mathbf{F}_p^{-T} : \dot{\mathbf{F}}_p + \frac{\partial \Psi}{\partial \xi} : \dot{\xi} \tag{7.32}$$

so that the Clausius-Planck local dissipation inequality reads

$$\begin{aligned}
\mathcal{D} &= \mathbf{P} : \dot{\mathbf{F}} - \dot{\Psi} \\
&= \mathbf{P} : \dot{\mathbf{F}} - 2 \mathbf{F}_\infty \frac{\partial \Psi}{\partial \mathbf{C}_\infty} \mathbf{F}_p^{-T} : \dot{\mathbf{F}} + 2 \mathbf{C}_\infty \frac{\partial \Psi}{\partial \mathbf{C}_\infty} \mathbf{F}_p^{-T} : \dot{\mathbf{F}}_p - \frac{\partial \Psi}{\partial \xi} : \dot{\xi} \\
&= \left[\mathbf{P} - 2 \mathbf{F}_\infty \frac{\partial \Psi}{\partial \mathbf{C}_\infty} \mathbf{F}_p^{-T} \right] : \dot{\mathbf{F}} + 2 \mathbf{C}_\infty \frac{\partial \Psi}{\partial \mathbf{C}_\infty} : l_p + q \dot{\xi} \geq 0
\end{aligned} \tag{7.33}$$

from which by standard argumentation the first Piola-Kirchhoff stress tensor is obtained as

$$\mathbf{P} = 2 \mathbf{F}_\infty \frac{\partial \Psi}{\partial \mathbf{C}_\infty} \mathbf{F}_p^{-T} \tag{7.34}$$

and the dissipation inequality

$$2\mathbf{C}_\infty \frac{\partial \Psi}{\partial \mathbf{C}_\infty} : \mathbf{l}_p + q \dot{\xi} \geq 0 \quad (7.35)$$

or, after defining the Mandel stress tensor as

$$\boldsymbol{\Sigma} = 2\mathbf{C}_\infty \frac{\partial \Psi}{\partial \mathbf{C}_\infty} = \mathbf{C}_\infty \mathbf{S}_\infty \quad (7.36)$$

with \mathbf{S}_∞ the second Piola-Kirchhoff stress tensor defined in the intermediate configuration, inequality (7.35) can be expressed as

$$\boldsymbol{\Sigma} : \mathbf{l}_p + q \dot{\xi} \geq 0 \quad (7.37)$$

For completeness the push-forward operation of \mathbf{S}_∞ is reiterated

$$\boldsymbol{\tau} = \mathbf{J} \boldsymbol{\sigma} = \mathbf{F}_\infty \mathbf{S}_\infty \mathbf{F}_\infty^T \quad (7.38)$$

On the basis of inequality (7.37) the following constrained minimization statement can be set up

$$\begin{aligned} & \text{minimize} && -\left(\boldsymbol{\Sigma} : \mathbf{l}_p + q \dot{\xi} \right) \\ & \text{subject to} && f(\boldsymbol{\Sigma}, q) \leq 0 \end{aligned} \quad (7.39)$$

which is equivalent to the following set of plastic evolution equations

$$\begin{aligned} \mathbf{l}_p &= \dot{\mathbf{F}}_p \mathbf{F}_p^{-1} = \lambda \mathbf{N} \\ \dot{\xi} &= \lambda \left(\frac{\partial f}{\partial q} \right) \\ \lambda &\geq 0 \quad ; \quad f(\boldsymbol{\Sigma}, q) \leq 0 \quad ; \quad \lambda f(\boldsymbol{\Sigma}, q) = 0 \end{aligned} \quad (7.40)$$

in which λ is the plastic consistency parameter, $\mathbf{N} = \partial f / \partial \boldsymbol{\Sigma}$ and $f(\boldsymbol{\Sigma}, q)$ is the Drucker Prager yield surface and is discussed in Appendix 7.2.

The flow rule expressed by Eq. (7.40)₁ can be written as

$$\frac{\partial \mathbf{F}_p}{\partial t} = \lambda \mathbf{N} \mathbf{F}_p \quad (7.41)$$

7.2.5 Elasto-Plastic stress Reduction Procedure

7.2.5.1 Elasto-Plastic Trial Elastic State

To solve the above equations, using a finite element method, they need to be discretized in time (and space). Therefore, from Eq. (7.6)₁ the elastic deformation gradient \mathbf{F}_∞ can be expressed as

$${}^{t+\Delta t} \mathbf{F}_\infty = {}^{t+\Delta t} \mathbf{F} {}^{t+\Delta t} \mathbf{F}_p^{-1} \quad (7.42)$$

If it is temporarily assumed that during the motion in the time interval $[t, t+\Delta t]$ no further plastic deformation takes place, i.e. if it is temporarily set

$${}^{t+\Delta t}\mathbf{F}_p = {}^t\mathbf{F}_p \quad ; \quad {}^{t+\Delta t}\xi = {}^t\xi \quad (7.43)$$

then, an approximate elastic deformation gradient can be computed as

$${}_{\text{trial}}^{t+\Delta t}\mathbf{F}_\infty = {}^{t+\Delta t}\mathbf{F} {}^t\mathbf{F}_p^{-1} \quad (7.44)$$

7.2.5.2 Elasto-Plastic Flow Rule Discretization

The evolution problem defined by Eq. (7.41) can be solved in the time interval $[t, t+\Delta t]$ to give a first order accurate estimate for ${}^{t+\Delta t}\mathbf{F}_p$

$${}^{t+\Delta t}\mathbf{F}_p = \exp^{t+\Delta t}[\Delta\lambda \mathbf{N}] {}^t\mathbf{F}_p \quad (7.45)$$

in which $\Delta\lambda = \lambda \Delta t$.

Substituting the above in Eq. (7.42)

$$\begin{aligned} {}^{t+\Delta t}\mathbf{F}_\infty &= {}^{t+\Delta t}\mathbf{F} {}^t\mathbf{F}_p^{-1} \exp^{t+\Delta t}[-\Delta\lambda \mathbf{N}] \\ &= {}_{\text{trial}}^{t+\Delta t}\mathbf{F}_\infty \exp^{t+\Delta t}[-\Delta\lambda \mathbf{N}] \end{aligned} \quad (7.46)$$

The corresponding elastic right Cauchy-Green tensor is therefore

$$\begin{aligned} {}^{t+\Delta t}\mathbf{C}_\infty &= {}^{t+\Delta t}\mathbf{F}_\infty^T {}^{t+\Delta t}\mathbf{F}_\infty \\ &= {}^{t+\Delta t} \left| \exp[-\Delta\lambda \mathbf{N}^T] \right|_{\text{trial}} \mathbf{F}_\infty^T \left| \text{trial} \mathbf{F}_\infty \right| \exp[-\Delta\lambda \mathbf{N}] \\ &= {}^{t+\Delta t} \left| \exp[-\Delta\lambda \mathbf{N}] \right|_{\text{trial}} \mathbf{C}_\infty \exp[-\Delta\lambda \mathbf{N}] \end{aligned} \quad (7.47)$$

The exponential of a tensor \mathbf{A} can be expressed in terms of a Taylor series as

$$\exp[\mathbf{A}] = \sum_{n=1}^{\infty} \frac{1}{n!} \mathbf{A}^n = \mathbf{I} + \mathbf{A} + \frac{1}{2!} \mathbf{A}^2 + \frac{1}{3!} \mathbf{A}^3 \quad (7.48)$$

hence
$$\exp[-\Delta\lambda \mathbf{N}] = \mathbf{I} - \Delta\lambda \mathbf{N} + \frac{\Delta\lambda^2}{2} \mathbf{N}^2 \dots \quad (7.49)$$

Utilizing a first order expansion of the above into Eq. (7.47)

$$\begin{aligned} {}^{t+\Delta t}\mathbf{C}_\infty &= {}^{t+\Delta t} \left| \exp[-\Delta\lambda \mathbf{N}] \right|_{\text{trial}} \mathbf{C}_\infty \exp[-\Delta\lambda \mathbf{N}] \\ &= {}^{t+\Delta t} \left| (\mathbf{I} - \Delta\lambda \mathbf{N}) \right|_{\text{trial}} \mathbf{C}_\infty (\mathbf{I} - \Delta\lambda \mathbf{N}) \\ &= {}^{t+\Delta t} \left| \text{trial} \mathbf{C}_\infty - \Delta\lambda (\mathbf{N} \text{trial} \mathbf{C}_\infty + \text{trial} \mathbf{C}_\infty \mathbf{N}) + \Delta\lambda^2 \mathbf{N} \text{trial} \mathbf{C}_\infty \mathbf{N} \right| \end{aligned} \quad (7.50)$$

Ignoring the second order term

$${}^{t+\Delta t}\mathbf{C}_\infty = {}^{t+\Delta t} \left| \text{trial} \mathbf{C}_\infty - \Delta\lambda (\mathbf{N} \text{trial} \mathbf{C}_\infty + \text{trial} \mathbf{C}_\infty \mathbf{N}) \right| \quad (7.51)$$

constitutes an elastic predictor – plastic corrector solution for the elastic right Cauchy-Green tensor.

Also on the basis of Eq. (7.40)₂, a backward Euler integration scheme results to the following algorithmic scheme for the hardening rule

$${}^{t+\Delta t}\xi = {}^t\xi + \left. \Delta\lambda \left(\frac{\partial f}{\partial q} \right) \right|^{t+\Delta t} \quad (7.52)$$

7.2.5.3 Elasto-Plastic Return Mapping Procedure

On the basis of the above an incremental problem can be defined. Eq. (7.51) can be expressed as

$${}^{t+\Delta t}\mathbf{C}_\infty = \left. {}^{t+\Delta t}\mathbf{C}_\infty - \Delta\lambda \mathbf{W} \right|_{\text{trial}} \quad (7.53)$$

in which

$$\begin{aligned} \left. {}^{t+\Delta t}\mathbf{C}_\infty \right|_{\text{trial}} &= \left. {}^{t+\Delta t}\mathbf{F}_\infty^T \right|_{\text{trial}} \left. {}^{t+\Delta t}\mathbf{F}_\infty \right|_{\text{trial}} \\ &= \left(\left. {}^{t+\Delta t}\mathbf{F} \right|_{\text{trial}} \left. {}^t\mathbf{F}_p^{-1} \right|_{\text{trial}} \right)^T \left(\left. {}^{t+\Delta t}\mathbf{F} \right|_{\text{trial}} \left. {}^t\mathbf{F}_p^{-1} \right|_{\text{trial}} \right) \end{aligned} \quad (7.54)$$

and

$$\left. {}^{t+\Delta t}\mathbf{W} \right|_{\text{trial}} = \left. \mathbf{N} \left(\left. {}^{t+\Delta t}\mathbf{C}_\infty \right|_{\text{trial}} \right) + \left(\left. {}^t\mathbf{C}_\infty \right|_{\text{trial}} \right) \mathbf{N} \quad (7.55)$$

As a starting point for the set up of a Newton Raphson procedure, a tensor of residuals for the elastic right Cauchy-Green tensor is defined as

$$\mathbf{R}_{\mathbf{C}_\infty} = {}^{t+\Delta t}\mathbf{C}_\infty - \left. {}^{t+\Delta t}\mathbf{C}_\infty \right|_{\text{trial}} + \Delta\lambda \left. {}^{t+\Delta t}\mathbf{W} \right|_{\text{trial}} \quad (7.56)$$

or in index notation, where for the sake of notation simplification, the superscript $t + \Delta t$ is omitted,

$$\left(\mathbf{R}_{\mathbf{C}_\infty} \right)_{ij} = \left(\mathbf{C}_\infty \right)_{ij} - \left(\left. \mathbf{C}_\infty \right|_{\text{trial}} \right)_{ij} + \Delta\lambda \mathbf{W}_{ij} \quad (7.57)$$

The derivative of this w.r.t. $\left(\mathbf{C}_\infty \right)_{mn}$ gives

$$\begin{aligned} \frac{\partial \left(\mathbf{R}_{\mathbf{C}_\infty} \right)_{ij}}{\partial \left(\mathbf{C}_\infty \right)_{mn}} &= \frac{\partial \left(\mathbf{C}_\infty \right)_{ij}}{\partial \left(\mathbf{C}_\infty \right)_{mn}} + \Delta\lambda \frac{\partial \mathbf{W}_{ij}}{\partial \left(\mathbf{C}_\infty \right)_{mn}} \\ &= \delta_{im} \delta_{jn} + \Delta\lambda \frac{\partial \mathbf{W}_{ij}}{\partial \left(\mathbf{C}_\infty \right)_{mn}} \end{aligned} \quad (7.58)$$

$$\text{In which } \frac{\partial \mathbf{W}_{ij}}{\partial \left(\mathbf{C}_\infty \right)_{mn}} = \frac{\partial^2 f}{\partial \bar{\Sigma}_{ik} \partial \left(\mathbf{C}_\infty \right)_{mn}} \left(\left. \mathbf{C}_\infty \right|_{\text{trial}} \right)_{kj} + \left(\left. \mathbf{C}_\infty \right|_{\text{trial}} \right)_{il} \frac{\partial^2 f}{\partial \bar{\Sigma}_{lj} \partial \left(\mathbf{C}_\infty \right)_{mn}} \quad (7.59)$$

Using a Von Mises yield surface, the derivatives of Eq. (7.59) can be found as

$$\frac{\partial^2 f}{\partial \bar{\Sigma}_{ik} \partial \left(\mathbf{C}_\infty \right)_{mn}} = \frac{\partial^2 f}{\partial \bar{\Sigma}_{ik} \partial \bar{\Sigma}_{pq}} \left(\mu \delta_{pm} \delta_{nq} + \frac{1}{2} \lambda I_3^{-\alpha} \left(\mathbf{C}_\infty \right)_{mn}^{-1} \delta_{pq} \right) \quad (7.60)$$

And

$$\frac{\partial f(\bar{\Sigma}, q)}{\partial \bar{\Sigma}_{pq} \partial \bar{\Sigma}_{mn}} = \sqrt{\frac{3}{2}} \frac{1}{\|\bar{s}_{ij}\|} \left[\left(\delta_{pm} \delta_{qn} - \frac{1}{3} \delta_{mn} \delta_{pq} \right) - \frac{\bar{s}_{mn} \bar{s}_{pq}}{\bar{s}_{ij} \bar{s}_{ij}} \right] \quad (7.61)$$

In Appendix 7.1 all necessary derivatives related to the Von Mises and the Drucker Prager yield surfaces are derived, respectively.

The derivative of Eq. (7.57) w.r.t. $\Delta\lambda$ gives

$$\frac{\partial (R_{C_\infty})_{ij}}{\partial \Delta\lambda} = W_{ij} + \Delta\lambda \frac{\partial W_{ij}}{\partial \Delta\lambda} \quad (7.62)$$

With

$$\frac{\partial W_{ij}}{\partial \Delta\lambda} = \frac{\partial^2 f}{\partial \bar{\Sigma}_{ik} \partial q} \left(-\frac{\partial^2 \psi}{\partial \xi^2} \cdot \frac{\partial f}{\partial q} \right) ({}^{\text{trial}}C_\infty)_{kj} + ({}^{\text{trial}}C_\infty)_{il} \frac{\partial^2 f}{\partial \bar{\Sigma}_{lj} \partial q} \left(-\frac{\partial^2 \psi}{\partial \xi^2} \cdot \frac{\partial f}{\partial q} \right) \quad (7.63)$$

Since in this case $\frac{\partial W_{ij}}{\partial \Delta\lambda} = 0$; Eq. (7.62) becomes

$$\frac{\partial (R_{C_\infty})_{ij}}{\partial \Delta\lambda} = W_{ij} \quad (7.64)$$

The residual for the yield surface is

$$R_f = {}^{t+\Delta t}f(\bar{\Sigma}, q) \quad (7.65)$$

In the following, for the sake of notation simplification, the superscript $t + \Delta t$ is omitted.

The partial derivative of R_f w.r.t. $(C_\infty)_{mn}$ can be found in the following.

$$\frac{\partial R_f}{\partial (C_\infty)_{mn}} = \frac{\partial f}{\partial \bar{\Sigma}_{pq}} \frac{\partial \bar{\Sigma}_{pq}}{\partial (C_\infty)_{mn}} \quad (7.66)$$

Where, for a Von Mises yield surface

$$\frac{\partial f(\bar{\Sigma}, q)}{\partial \bar{\Sigma}_{pq}} = \sqrt{\frac{3}{2}} \frac{\bar{s}_{pq}}{\|\bar{s}_{ij}\|} \quad (7.67)$$

And for a Drucker Prager yield surface

$$\frac{\partial f(\bar{\Sigma}, q)}{\partial \bar{\Sigma}_{pq}} = \sqrt{\frac{1}{2}} \frac{\bar{s}_{pq}}{\|\bar{s}_{ij}\|} + \alpha \delta_{pq} \quad (7.68)$$

Furthermore,

$$\frac{\partial \bar{\Sigma}_{pq}}{\partial (C_\infty)_{mn}} = \mu \delta_{pm} \delta_{nq} + \frac{1}{2} \lambda I_3^{-\alpha} (C_\infty)_{mn}^{-1} \delta_{pq} \quad (7.69)$$

The partial derivative of R_f w.r.t. $\Delta\lambda$ can be found in the following.

$$\frac{\partial \mathbf{R}_f}{\partial \Delta \lambda} = \frac{\partial f}{\partial \mathbf{q}} \frac{\partial \mathbf{q}}{\partial \xi} \frac{\partial \xi}{\partial \Delta \lambda} \quad (7.70)$$

Since
$$\xi = \Delta \lambda \left(\frac{\partial f}{\partial \mathbf{q}} \right) ; \quad \frac{\partial \xi}{\partial \Delta \lambda} = \frac{\partial f}{\partial \mathbf{q}} \quad (7.71)$$

Furthermore
$$\mathbf{q} = -\frac{\partial \psi}{\partial \xi} ; \quad \frac{\partial \mathbf{q}}{\partial \xi} = -\frac{\partial^2 \psi}{\partial \xi^2} \quad (7.72)$$

$$\frac{\partial \mathbf{R}_f}{\partial \Delta \lambda} = \left(\frac{\partial f}{\partial \mathbf{q}} \right)^2 \left(-\frac{\partial^2 \psi}{\partial \xi^2} \right) \quad (7.73)$$

Define

$$\begin{Bmatrix} d\mathbf{C}_\infty \\ d\Delta \lambda \end{Bmatrix} = {}^{t+\Delta t} \mathbf{r} [-\mathbf{J}]^{-1} \begin{Bmatrix} \mathbf{R}_{\mathbf{C}_\infty} \\ \mathbf{R}_f \end{Bmatrix} \quad (7.74)$$

with

$${}^{t+\Delta t} \mathbf{r} [-\mathbf{J}] = - \begin{bmatrix} \frac{\partial (\mathbf{R}_{\mathbf{C}_\infty})_{11}}{\partial (\mathbf{C}_\infty)_{11}} & \frac{\partial (\mathbf{R}_{\mathbf{C}_\infty})_{11}}{\partial (\mathbf{C}_\infty)_{12}} & \dots & \frac{\partial (\mathbf{R}_{\mathbf{C}_\infty})_{11}}{\partial (\mathbf{C}_\infty)_{33}} & \frac{\partial (\mathbf{R}_{\mathbf{C}_\infty})_{11}}{\partial (\Delta \lambda)} \\ \frac{\partial (\mathbf{R}_{\mathbf{C}_\infty})_{12}}{\partial (\mathbf{C}_\infty)_{11}} & \frac{\partial (\mathbf{R}_{\mathbf{C}_\infty})_{12}}{\partial (\mathbf{C}_\infty)_{12}} & \dots & \frac{\partial (\mathbf{R}_{\mathbf{C}_\infty})_{12}}{\partial (\mathbf{C}_\infty)_{33}} & \frac{\partial (\mathbf{R}_{\mathbf{C}_\infty})_{12}}{\partial (\Delta \lambda)} \\ \vdots & \vdots & \ddots & \vdots & \vdots \\ \frac{\partial (\mathbf{R}_{\mathbf{C}_\infty})_{33}}{\partial (\mathbf{C}_\infty)_{11}} & \frac{\partial (\mathbf{R}_{\mathbf{C}_\infty})_{33}}{\partial (\mathbf{C}_\infty)_{12}} & \dots & \frac{\partial (\mathbf{R}_{\mathbf{C}_\infty})_{33}}{\partial (\mathbf{C}_\infty)_{33}} & \frac{\partial (\mathbf{R}_{\mathbf{C}_\infty})_{33}}{\partial (\Delta \lambda)} \\ \frac{\partial (\mathbf{R}_f)}{\partial (\mathbf{C}_\infty)_{11}} & \frac{\partial (\mathbf{R}_f)}{\partial (\mathbf{C}_\infty)_{12}} & \dots & \frac{\partial (\mathbf{R}_f)}{\partial (\mathbf{C}_\infty)_{33}} & \frac{\partial (\mathbf{R}_f)}{\partial (\Delta \lambda)} \end{bmatrix} \quad (7.75)$$

7.2.6 Visco-Elastic Component

Similar to the elasto-plastic component, the formulations for the visco-elastic component in the intermediate configurations need to be set-up. In the intermediate configuration, for the visco-elastic component of the model, the Helmholtz free energy can be set up as

$$\Psi = \Psi (\mathbf{C}_e) \quad (7.76)$$

Since the Helmholtz free energy function of the visco-elastic component only depends on the strain tensor, it can also be referred to as a Strain Energy function. Its time derivative can therefore be found as

$$\dot{\Psi} = \frac{\partial \Psi}{\partial \mathbf{C}_e} : \dot{\mathbf{C}}_e \quad (7.77)$$

On the basis of Eq. 3.8, Eq. (7.25) can be further elaborated as

$$\begin{aligned}
\dot{\Psi} &= 2 \frac{\partial \Psi}{\partial \mathbf{C}_e} : \mathbf{F}_e^T \dot{\mathbf{F}}_e = 2 \mathbf{F}_e \frac{\partial \Psi}{\partial \mathbf{C}_e} : \dot{\mathbf{F}}_e \\
&= 2 \mathbf{F}_e \frac{\partial \Psi}{\partial \mathbf{C}_e} : \left(\dot{\mathbf{F}} \mathbf{F}_v^{-1} + \mathbf{F} \dot{\mathbf{F}}_v^{-1} \right) \\
&= 2 \mathbf{F}_e \frac{\partial \Psi}{\partial \mathbf{C}_e} : \dot{\mathbf{F}} \mathbf{F}_v^{-1} + 2 \mathbf{F}_e \frac{\partial \Psi}{\partial \mathbf{C}_e} : \mathbf{F} \dot{\mathbf{F}}_v^{-1}
\end{aligned} \tag{7.78}$$

Utilizing the tensor identity $\mathbf{A} : \mathbf{BC} = \mathbf{AC}^T : \mathbf{B}$ it results

$$2 \mathbf{F}_e \frac{\partial \Psi}{\partial \mathbf{C}_e} : \dot{\mathbf{F}} \mathbf{F}_v^{-1} = 2 \mathbf{F}_e \frac{\partial \Psi}{\partial \mathbf{C}_e} \mathbf{F}_v^{-T} : \dot{\mathbf{F}} \tag{7.79}$$

By means of the identity $\dot{\mathbf{F}}_v^{-1} = -\mathbf{F}_v^{-1} \dot{\mathbf{F}}_v \mathbf{F}_v^{-1}$ and the identity $\mathbf{F}_e = \mathbf{F} \mathbf{F}_v^{-1}$ it holds

$$2 \mathbf{F}_e \frac{\partial \Psi}{\partial \mathbf{C}_e} : \mathbf{F} \dot{\mathbf{F}}_v^{-1} = -2 \mathbf{F}_e \frac{\partial \Psi}{\partial \mathbf{C}_e} : \mathbf{F} \left(\mathbf{F}_v^{-1} \dot{\mathbf{F}}_v \mathbf{F}_v^{-1} \right) = -2 \mathbf{F}_e \frac{\partial \Psi}{\partial \mathbf{C}_e} : \mathbf{F}_e \dot{\mathbf{F}}_v \mathbf{F}_v^{-1} \tag{7.80}$$

Utilizing the tensor identity $\mathbf{A} : \mathbf{BC} = \mathbf{B}^T \mathbf{A} : \mathbf{C}$ it results

$$-2 \left(\mathbf{F}_e \frac{\partial \Psi}{\partial \mathbf{C}_e} \right) : \mathbf{F}_e \dot{\mathbf{F}}_v \mathbf{F}_v^{-1} = -2 \mathbf{F}_e^T \left(\mathbf{F}_e \frac{\partial \Psi}{\partial \mathbf{C}_e} \right) : \dot{\mathbf{F}}_v \mathbf{F}_v^{-1} = -2 \mathbf{C}_e \frac{\partial \Psi}{\partial \mathbf{C}_e} : \dot{\mathbf{F}}_v \mathbf{F}_v^{-1} \tag{7.81}$$

which can be further simplified by means of the identity $\mathbf{A} : \mathbf{BC} = \mathbf{AC}^T : \mathbf{B}$

$$-2 \mathbf{C}_e \frac{\partial \Psi}{\partial \mathbf{C}_e} : \dot{\mathbf{F}}_v \mathbf{F}_v^{-1} = -2 \mathbf{C}_e \frac{\partial \Psi}{\partial \mathbf{C}_e} \mathbf{F}_v^{-T} : \dot{\mathbf{F}}_v \tag{7.82}$$

Substituting Eq. (7.28) and Eq. (7.31) into Eq. (7.27)

$$\dot{\Psi} = 2 \mathbf{F}_e \frac{\partial \Psi}{\partial \mathbf{C}_e} \mathbf{F}_v^{-T} : \dot{\mathbf{F}} - 2 \mathbf{C}_e \frac{\partial \Psi}{\partial \mathbf{C}_e} \mathbf{F}_v^{-T} : \dot{\mathbf{F}}_v \tag{7.83}$$

so that the Clausius-Planck local dissipation inequality reads

$$\begin{aligned}
\mathcal{D} &= \mathbf{P} : \dot{\mathbf{F}} - \dot{\Psi} \\
&= \mathbf{P} : \dot{\mathbf{F}} - 2 \mathbf{F}_e \frac{\partial \Psi}{\partial \mathbf{C}_e} \mathbf{F}_v^{-T} : \dot{\mathbf{F}} + 2 \mathbf{C}_e \frac{\partial \Psi}{\partial \mathbf{C}_e} \mathbf{F}_v^{-T} : \dot{\mathbf{F}}_v \\
&= \left[\mathbf{P} - 2 \mathbf{F}_e \frac{\partial \Psi}{\partial \mathbf{C}_e} \mathbf{F}_v^{-T} \right] : \dot{\mathbf{F}} + 2 \mathbf{C}_e \frac{\partial \Psi}{\partial \mathbf{C}_e} : \dot{\mathbf{F}}_v \mathbf{F}_v^{-1} \\
&= \left[\mathbf{P} - 2 \mathbf{F}_e \frac{\partial \Psi}{\partial \mathbf{C}_e} \mathbf{F}_v^{-T} \right] : \dot{\mathbf{F}} + 2 \mathbf{C}_e \frac{\partial \Psi}{\partial \mathbf{C}_e} : \mathbf{l}_v \geq 0
\end{aligned} \tag{7.84}$$

from which by standard argumentation the first Piola-Kirchhoff stress tensor is obtained as

$$\mathbf{P} = 2 \mathbf{F}_e \frac{\partial \Psi}{\partial \mathbf{C}_e} \mathbf{F}_v^{-T} \tag{7.85}$$

and the dissipation inequality

$$2\mathbf{C}_e \frac{\partial \Psi}{\partial \mathbf{C}_e} : \mathbf{l}_v \geq 0 \quad (7.86)$$

or, after defining the Mandel stress tensor

$$\boldsymbol{\Sigma} = 2\mathbf{C}_e \frac{\partial \Psi}{\partial \mathbf{C}_e} = \mathbf{C}_e \mathbf{S}_e \quad (7.87)$$

with \mathbf{S}_e the second Piola-Kirchhoff stress tensor defined in the intermediate configuration, inequality (7.35) can be expressed as

$$\boldsymbol{\Sigma} : \mathbf{l}_v \geq 0 \quad (7.88)$$

The following evolution law can be found

$$\mathbf{l}_v = \mathbb{C}_v^{-1} : \boldsymbol{\Sigma} \quad (7.89)$$

with

$$\mathbb{C}_v^{-1} = \frac{1}{2\eta_D} \left(\mathbb{I} - \frac{1}{3} \mathbf{I} \otimes \mathbf{I} \right) + \frac{1}{9\eta_V} \mathbf{I} \otimes \mathbf{I} \quad (7.90)$$

while η_D and η_V are the deviatoric and volumetric viscosities which may be deformation dependent

$$\eta_D = \eta_D(\boldsymbol{\Sigma}) > 0 \quad ; \quad \eta_V = \eta_V(\boldsymbol{\Sigma}) > 0 \quad (7.91)$$

Therefore

$$\mathbf{l}_v = \dot{\mathbf{F}}_v \mathbf{F}_v^{-1} = \mathbb{C}_v^{-1} : \boldsymbol{\Sigma} \quad (7.92)$$

Which can be written as

$$\frac{\partial \mathbf{F}_v}{\partial t} = \left(\mathbb{C}_v^{-1} : \boldsymbol{\Sigma} \right) \mathbf{F}_v \quad (7.93)$$

7.2.7 Visco-Elastic Stress Reduction Procedure

7.2.7.1 Visco-Elastic Trial Elastic State

The elastic deformation gradient \mathbf{F}_e can be expressed as

$${}^{t+\Delta t} \mathbf{F}_e = {}^{t+\Delta t} \mathbf{F} {}^{t+\Delta t} \mathbf{F}_v^{-1} \quad (7.94)$$

If it is temporarily assumed that during the motion in the time interval $[t, t+\Delta t]$ no further viscous deformation takes place, i.e. if it is temporarily set

$${}^{t+\Delta t} \mathbf{F}_v = {}^t \mathbf{F}_v \quad (7.95)$$

then, an approximate elastic deformation gradient can be computed as

$${}_{\text{trial}}^{t+\Delta t} \mathbf{F}_e = {}^{t+\Delta t} \mathbf{F} {}^t \mathbf{F}_v^{-1} \quad (7.96)$$

7.2.7.2 Visco-Elastic Flow Rule Discretization

The evolution problem defined by Eq. (7.93) can be solved in the time interval $[t, t + \Delta t]$ to give a first order accurate estimate for ${}^{t+\Delta t}\mathbf{F}_v^{-1}$

$${}^{t+\Delta t}\mathbf{F}_v^{-1} = {}^t\mathbf{F}_v^{-1} \exp {}^{t+\Delta t} \left[-\Delta\mathbf{C}_v^{-1} : \boldsymbol{\Sigma} \right] \quad (7.97)$$

in which $\Delta\mathbf{C}_v^{-1} = \mathbf{C}_v^{-1}\Delta t$.

Substituting the above in Eq. (7.94)

$$\begin{aligned} {}^{t+\Delta t}\mathbf{F}_e &= {}^{t+\Delta t}\mathbf{F} {}^t\mathbf{F}_v^{-1} \exp {}^{t+\Delta t} \left[-\Delta\mathbf{C}_v^{-1} : \boldsymbol{\Sigma} \right] \\ &= {}_{\text{trial}}^{t+\Delta t}\mathbf{F}_e \exp {}^{t+\Delta t} \left[-\Delta\mathbf{C}_v^{-1} : \boldsymbol{\Sigma} \right] \end{aligned} \quad (7.98)$$

The corresponding elastic right Cauchy-Green tensor is therefore

$$\begin{aligned} {}^{t+\Delta t}\mathbf{C}_e &= {}^{t+\Delta t}\mathbf{F}_e^T {}^{t+\Delta t}\mathbf{F}_e \\ &= {}^{t+\Delta t} \left| \exp \left[-\Delta\mathbf{C}_v^{-1} : \boldsymbol{\Sigma}^T \right] {}_{\text{trial}}\mathbf{F}_e^T {}_{\text{trial}}\mathbf{F}_e \exp \left[-\Delta\mathbf{C}_v^{-1} : \boldsymbol{\Sigma} \right] \right. \\ &= {}^{t+\Delta t} \left| \exp \left[-\Delta\mathbf{C}_v^{-1} : \boldsymbol{\Sigma} \right] {}_{\text{trial}}\mathbf{C}_e \exp \left[-\Delta\mathbf{C}_v^{-1} : \boldsymbol{\Sigma} \right] \right. \end{aligned} \quad (7.99)$$

Hence
$$\exp \left[-\Delta\mathbf{C}_v^{-1} : \boldsymbol{\Sigma} \right] = \mathbf{I} - \Delta\mathbf{C}_v^{-1} : \boldsymbol{\Sigma} + \frac{(\Delta\mathbf{C}_v^{-1})^2}{2} \boldsymbol{\Sigma}^2 \dots \quad (7.100)$$

Utilizing a first order expansion of the above into Eq. (7.99)

$$\begin{aligned} {}^{t+\Delta t}\mathbf{C}_e &= {}^{t+\Delta t} \left| \exp \left[-\Delta\mathbf{C}_v^{-1} : \boldsymbol{\Sigma} \right] {}_{\text{trial}}\mathbf{C}_e \exp \left[-\Delta\mathbf{C}_v^{-1} : \boldsymbol{\Sigma} \right] \right. \\ &= {}^{t+\Delta t} \left(\mathbf{I} - \Delta\mathbf{C}_v^{-1} : \boldsymbol{\Sigma} \right) {}_{\text{trial}}\mathbf{C}_e \left(\mathbf{I} - \Delta\mathbf{C}_v^{-1} : \boldsymbol{\Sigma} \right) \\ &= {}^{t+\Delta t} \left| {}_{\text{trial}}\mathbf{C}_e - \Delta\mathbf{C}_v^{-1} : \left(\boldsymbol{\Sigma} {}_{\text{trial}}\mathbf{C}_e + {}_{\text{trial}}\mathbf{C}_e \boldsymbol{\Sigma} \right) + (\Delta\mathbf{C}_v^{-1})^2 \boldsymbol{\Sigma} {}_{\text{trial}}\mathbf{C}_e \boldsymbol{\Sigma} \right. \end{aligned} \quad (7.101)$$

Ignoring the second order term

$${}^{t+\Delta t}\mathbf{C}_e = {}^{t+\Delta t} \left| {}_{\text{trial}}\mathbf{C}_e - \Delta\mathbf{C}_v^{-1} : \left(\boldsymbol{\Sigma} {}_{\text{trial}}\mathbf{C}_e + {}_{\text{trial}}\mathbf{C}_e \boldsymbol{\Sigma} \right) \right. \quad (7.102)$$

constitutes an elastic predictor – viscous corrector solution for the elastic right Cauchy-Green tensor.

7.2.7.3 Visco-Elastic Return Mapping Procedure

On the basis of the above an incremental problem can be defined. Eq. (7.102) can be expressed as

$${}^{t+\Delta t}\mathbf{C}_e = {}^{t+\Delta t} \left| {}_{\text{trial}}\mathbf{C}_e - \Delta\mathbf{C}_v^{-1} : \mathbf{W} \right. \quad (7.103)$$

in which

$$\begin{aligned} {}^{t+\Delta t} \mathbf{C}_e &= {}^{t+\Delta t} \mathbf{F}_e^T {}^{t+\Delta t} \mathbf{F}_e \\ &= \left({}^{t+\Delta t} \mathbf{F} {}^t \mathbf{F}_v^{-1} \right)^T \left({}^{t+\Delta t} \mathbf{F} {}^t \mathbf{F}_v^{-1} \right) \end{aligned} \quad (7.104)$$

and

$${}^{t+\Delta t} \mathbf{W} = {}^{t+\Delta t} \left| \Sigma \right| {}^{\text{trial}} \mathbf{C}_e + {}^{\text{trial}} \mathbf{C}_e \Sigma \quad (7.105)$$

As a starting point for the set up of a Newton Raphson procedure, a tensor of residuals for the elastic right Cauchy-Green tensor is defined as

$$\mathbf{R}_{C_e} = {}^{t+\Delta t} \mathbf{C}_e - {}^{\text{trial}} \mathbf{C}_e + \Delta \mathbf{C}_v^{-1} : {}^{t+\Delta t} \mathbf{W} \quad (7.106)$$

or in index notation, where for the sake of notation simplification, the superscript $t + \Delta t$ is omitted,

$$\left(\mathbf{R}_{C_e} \right)_{ij} = \left(C_e \right)_{ij} - \left({}^{\text{trial}} C_e \right)_{ij} + \left(\Delta C_v^{-1} \right)_{ijkl} W_{kl} \quad (7.107)$$

The derivative of this w.r.t. $(C_e)_{mn}$ gives

$$\begin{aligned} \frac{\partial \left(\mathbf{R}_{C_e} \right)_{ij}}{\partial (C_e)_{mn}} &= \frac{\partial (C_e)_{ij}}{\partial (C_e)_{mn}} + \left(\Delta C_v^{-1} \right)_{ijkl} \frac{\partial W_{kl}}{\partial (C_e)_{mn}} \\ &= \delta_{im} \delta_{jn} + \left(\Delta C_v^{-1} \right)_{ijkl} \frac{\partial W_{kl}}{\partial (C_e)_{mn}} \end{aligned} \quad (7.108)$$

Since

$$W_{kl} = \Sigma_{km} \left({}^{\text{trial}} C_e \right)_{ml} + \left({}^{\text{trial}} C_e \right)_{kp} \Sigma_{pl} \quad (7.109)$$

Therefore

$$\frac{\partial W_{kl}}{\partial (C_e)_{mn}} = \frac{\partial \Sigma_{km}}{\partial (C_e)_{mn}} \left({}^{\text{trial}} C_e \right)_{ml} + \left({}^{\text{trial}} C_e \right)_{kp} \frac{\partial \Sigma_{pl}}{\partial (C_e)_{mn}} \quad (7.110)$$

And

$$\frac{\partial \Sigma_{pl}}{\partial (C_e)_{mn}} = \mu \delta_{pm} \delta_{nl} + \frac{1}{2} \lambda I_3^{-\alpha} (C_e)_{mn}^{-1} \delta_{pl} \quad \text{A.6.(7.111)}$$

Define

$$\{dC_e\} = {}^{t+\Delta t} \left[-J \right]^{-1} {}^{t+\Delta t} \left\{ \mathbf{R}_{C_e} \right\} \quad (7.112)$$

with

$${}^{t+\Delta t} \mathbf{r} [-\mathbf{J}] = - {}^{t+\Delta t} \begin{bmatrix} \frac{\partial(\mathbf{R}_{C_e})_{11}}{\partial(C_e)_{11}} & \frac{\partial(\mathbf{R}_{C_e})_{11}}{\partial(C_e)_{12}} & \dots & \frac{\partial(\mathbf{R}_{C_e})_{11}}{\partial(C_e)_{33}} \\ \frac{\partial(\mathbf{R}_{C_e})_{12}}{\partial(C_e)_{11}} & \frac{\partial(\mathbf{R}_{C_e})_{12}}{\partial(C_e)_{12}} & \dots & \frac{\partial(\mathbf{R}_{C_e})_{12}}{\partial(C_e)_{33}} \\ \vdots & \vdots & \ddots & \vdots \\ \frac{\partial(\mathbf{R}_{C_e})_{33}}{\partial(C_e)_{11}} & \frac{\partial(\mathbf{R}_{C_e})_{33}}{\partial(C_e)_{12}} & \dots & \frac{\partial(\mathbf{R}_{C_e})_{33}}{\partial(C_e)_{33}} \end{bmatrix} \quad (7.113)$$

7.3 Parameter Determination

7.3.1 Procedure

In the following, a new methodology for determination of the parameters of the above presented model is developed. For sake of convenience, in Fig. 7.3.1 the schematic of the one-dimensional model is repeated.

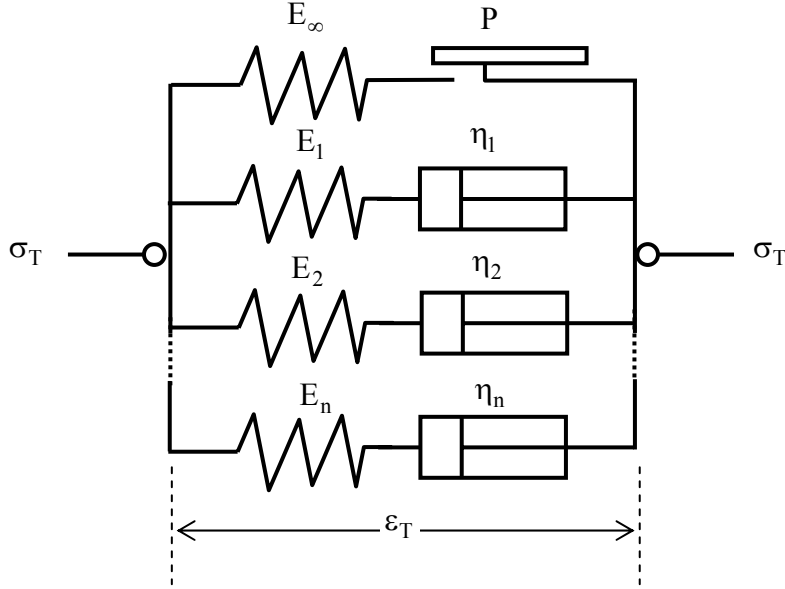


Fig. 7.3.1: Schematic of one-dimensional model

In the following the subscripts s_i and d_i indicate the spring and dashpot element of the i -th visco-elastic element, with $i = 1, n$.

Because of the parallel set-up of the components w.r.t. each other, the total strain in the elasto-plastic (EP) and in each visco-elastic (VE) component must be the same:

$$\varepsilon_T = \varepsilon_\infty + \varepsilon_p = \varepsilon_{s_i} + \varepsilon_{d_i} \quad (7.114)$$

Therefore

$$\varepsilon_\infty = \varepsilon_T - \varepsilon_p ; \varepsilon_{s_i} = \varepsilon_T - \varepsilon_{d_i} \quad (7.115)$$

Within each EP and VE component, the stress must be equal in the elements, therefore

$$\sigma_\infty = \sigma_p ; \sigma_{s_i} = \sigma_{d_i} = \sigma_i \quad (7.116)$$

The total stress is thus a summation of the stresses in the EP and VE components:

$$\sigma_T = \sigma_\infty + \sum_{i=1}^n \sigma_i \quad (7.117)$$

Which is the one dimensional equivalence of Eq. (7.12).

The stress in each spring is

$$\sigma_\infty = E_\infty \varepsilon_\infty ; \sigma_i = E_i \varepsilon_{s_i} \quad (7.118)$$

and in each dashpot

$$\sigma_{d_i} = \eta_i \dot{\varepsilon}_{d_i} \quad (7.119)$$

Substituting Eq. (7.118) into Eq. (7.117)

$$\sigma_T = E_\infty \varepsilon_\infty + \sum_{i=1}^n E_i \varepsilon_{s_i} \quad (7.120)$$

If it is assumed that $E_\infty = E_i$ then

$$\sigma_T = E \left(\varepsilon_\infty + \sum_{i=1, n} \varepsilon_{s_i} \right) \quad (7.121)$$

And

$$\sigma_\infty = \sigma_p = E \varepsilon_{s_i} \quad ; \quad \sigma_i = E \varepsilon_{s_i} \quad (7.122)$$

The stress in the plastic spring can be found as

$$\sigma_\infty = E \varepsilon_\infty = E (\varepsilon_T - \varepsilon_p) \quad (7.123)$$

With Eq. (7.117)

$$\begin{aligned} \sigma_i &= \sigma_T - \sigma_\infty - \sum_{j=1}^{n-1} \sigma_j \\ &= \sigma_T - E (\varepsilon_T - \varepsilon_p) - \sum_{j=1}^{n-1} \sigma_j \end{aligned} \quad (7.124)$$

Since, from Eq. (7.116), the stress in the viscous spring and the dashpot are equal, and using Eq. (7.119) it follows

$$\eta_i \dot{\varepsilon}_{d_i} = \sigma_T - E (\varepsilon_T - \varepsilon_p) - \sum_{j=1}^{n-1} \sigma_j \quad (7.125)$$

The strain rate in the dashpot can be written as

$$\dot{\varepsilon}_{d_i} = \frac{d}{dt} (\varepsilon_{d_i}) \quad (7.126)$$

Since this strain rate can be written as

$$\begin{aligned} \varepsilon_{d_i} &= \varepsilon_T - \varepsilon_{s_i} = \varepsilon_T - \frac{\sigma_i}{E} \\ &= \varepsilon_T - \left(\sigma_T / E - (\varepsilon_T - \varepsilon_p) - \sum_{j=1}^{n-1} \sigma_j / E \right) \end{aligned} \quad (7.127)$$

Therefore

$$\begin{aligned}
\dot{\varepsilon}_{d_i} &= \frac{d}{dt} \left(\varepsilon_T - \left(\sigma_T / E - (\varepsilon_T - \varepsilon_p) - \sum_{j=1}^{n-1} \sigma_j / E \right) \right) \\
&= \dot{\varepsilon}_T - \left(\dot{\sigma}_T / E - (\dot{\varepsilon}_T - \dot{\varepsilon}_p) - \sum_{j=1}^{n-1} \dot{\sigma}_j / E \right) \\
&= (2\dot{\varepsilon}_T - \dot{\varepsilon}_p) + \frac{1}{E} \left(\sum_{j=1}^{n-1} \dot{\sigma}_j - \dot{\sigma}_T \right)
\end{aligned} \tag{7.128}$$

Substituting Eq. (7.128) into Eq. (7.125)

$$\eta_i (2\dot{\varepsilon}_T - \dot{\varepsilon}_p) + \frac{\eta_i}{E} \left(\sum_{j=1}^{n-1} \dot{\sigma}_j - \dot{\sigma}_T \right) + E(\varepsilon_T - \varepsilon_p) = \sigma_T - \sum_{j=1}^{n-1} \sigma_j \tag{7.129}$$

For $n = 1$, Eq. (7.129) becomes

$$\eta (2\dot{\varepsilon}_T - \dot{\varepsilon}_p - \dot{\sigma}_T / E) + E(\varepsilon_T - \varepsilon_p) = \sigma_T \tag{7.130}$$

If the material is loaded in a creep test, the total load σ_T that is applied is constant, hence the total stress rate $\dot{\sigma}_T$ is zero, which simplifies Eq. (7.130) to

$$\eta (2\dot{\varepsilon}_T - \dot{\varepsilon}_p) + E(\varepsilon_T - \varepsilon_p) = \sigma_T \tag{7.131}$$

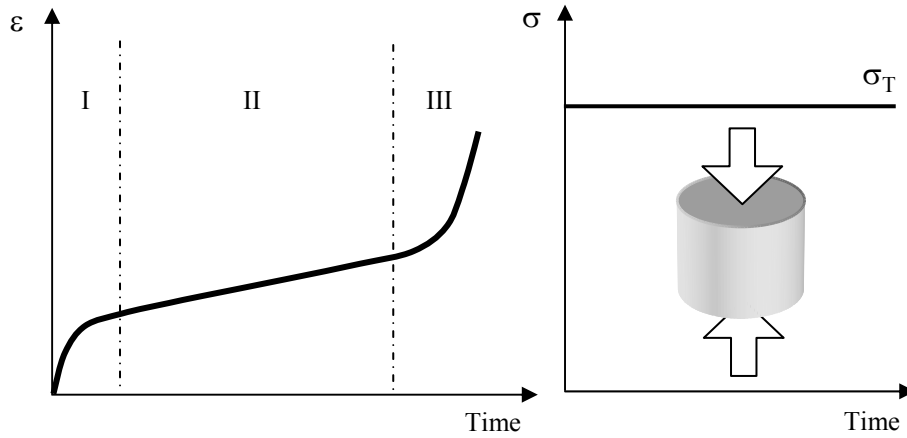


Fig. 7.3.2: A constant compression creep test

In a creep-recovery experiment, by exposing an asphaltic material to a constant compression load σ_T , the total strain response ε_T is measured in all three directions. Then, at time t the load is removed and the material can recover. From this recovery, the permanent plastic deformation ε_p of the material can be measured. By repeating this procedure for the same material, with different unloading times, the total and the plastic strain response of the material are determined in time, Fig. 7.3.3. From this, the total and the plastic strain rate response, which are needed to solve Eq. (7.131), can also be computed from the slope of the respective curves.

Postulating a Drucker Prager yield surface, see also Appendix 7.2 for more details,

$$f(\sigma, \xi) = \sqrt{J_2} + \alpha I_1 = k_y \quad (7.137)$$

where α depends on the friction angle ϕ via

$$\alpha = \frac{2 \sin \phi}{\sqrt{3}(3 - \sin \phi)} \quad (7.138)$$

and where k_y is the hardening of the yield surface, described by

$$k_y = k_{y_0} + \frac{\partial \Psi}{\partial \xi} = k_{y_\infty} + (k_{y_0} - k_{y_\infty}) e^{-\delta \xi} \quad (7.139)$$

Where

$$\xi = \int \lambda \left(\frac{\partial f}{\partial q} \right) dt \quad (7.140)$$

Since

$$\begin{aligned} \sqrt{J_2} &= \sqrt{\frac{1}{6} \left[(\sigma_x^p - \sigma_y^p)^2 + (\sigma_y^p - \sigma_z^p)^2 + (\sigma_z^p - \sigma_x^p)^2 \right] + (\sigma_{xy}^p)^2 + (\sigma_{yz}^p)^2 + (\sigma_{zx}^p)^2} \\ &= \sqrt{\frac{1}{6} \left[2(\sigma_x^p - \sigma_y^p)^2 \right]} \\ &= \frac{1}{\sqrt{3}} |\sigma_x^p - \sigma_y^p| \end{aligned} \quad (7.141)$$

and

$$I_1 = \sigma_x^p + \sigma_y^p + \sigma_z^p = 2\sigma_x^p + \sigma_y^p \quad (7.142)$$

Therefore, the parameters of the yield surface can now be computed.

In the following a demonstration is given of the above described parameter determination procedure, using experimental data from the Nottingham Centre for Pavement Engineering [Takerhani, 2006].

7.3.2 Creep recovery example

In Fig. 7.3.4 the compressive creep-recovery response of an asphaltic material, under constant temperature of 20° , is shown, for a constant load of 1 MPa in the axial (y) direction.

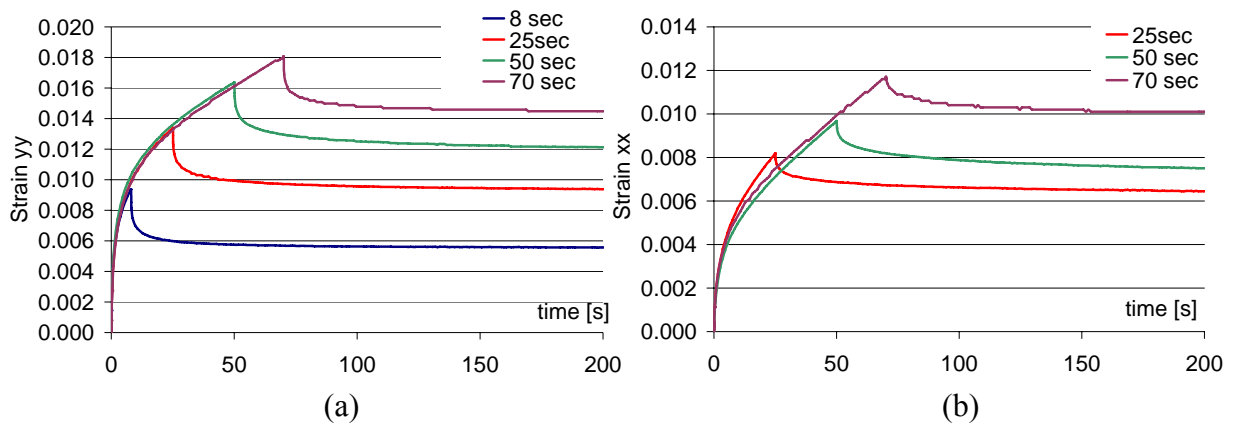


Fig. 7.3.4: Experimental creep-recovery data, 1MPa compressive loading
(a) Axial strain response (b) radial strain response

As can be seen from the graphs, the radial response is practically of the same order as the axial (loading direction) response. This is quite typical for asphaltic materials, and it illustrates the importance of a three dimensional material model.

In order to obtain the total, elastic and plastic strain response of this material, the procedure, as described in Fig. 7.3.3 is applied to the data. In order to reduce the scatter in the data, a regression analysis is applied, to get a best possible approximation of the response, see Fig. 7.3.5.

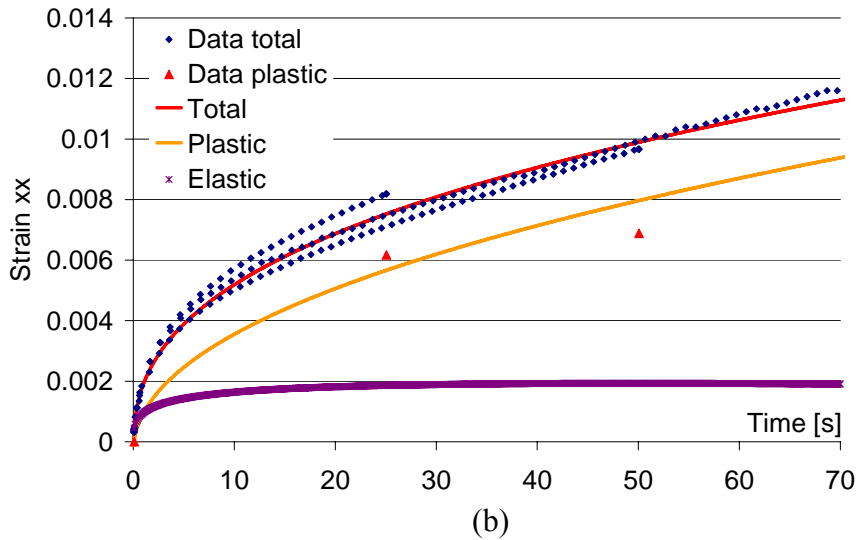
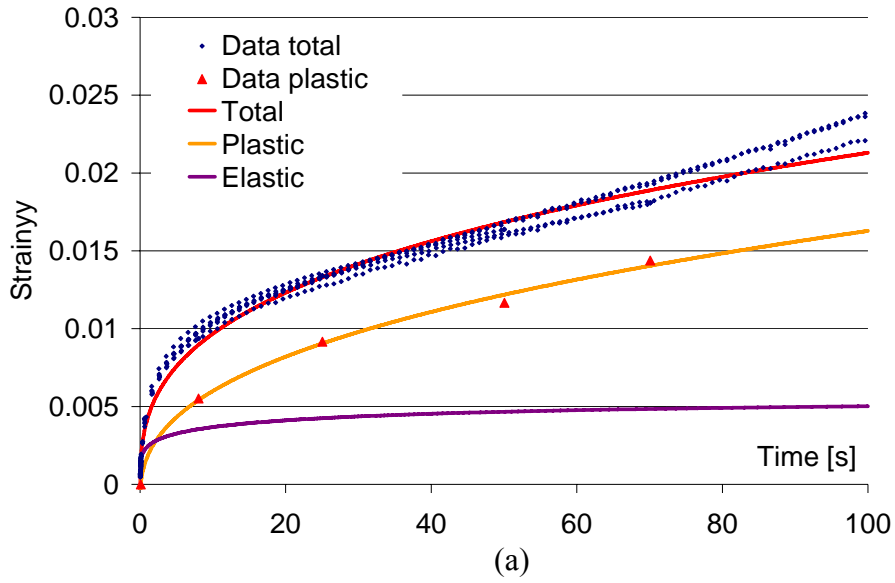


Fig. 7.3.5: Reduction of the experimental data via a regression analysis

From these graphs, the values of the E and η can be determined, using the above described procedure. From the Least Squares procedure, the parameters are determined as $E = 176 \text{ MPa}$ and $\eta = 317 \text{ MPa} \cdot \text{s}$.

Because of the three dimensionality, the viscosity parameter in the model, is separated into a volumetric and a deviatoric component via Eq. (7.135). Choosing a value for the volumetric viscous behavior of $\eta_v = 1000 \text{ MPa} \cdot \text{s}$, the deviatoric viscosity is determined as $\eta_d = 110 \text{ MPa} \cdot \text{s}$.

From the definitions of the Drucker-Prager yield surface, the hardening function k_y can now be plotted from the experimental data. Hereby the approximation of the equivalent plastic strain ξ is made via

$$\xi = \beta \sqrt{2(\varepsilon_x^p)^2 + (\varepsilon_y^p)^2} \quad (7.143)$$

where $\beta = 1.3$ is utilized.

Using Eq. (7.137), the plastic hardening function can thus be determined from the experimental data, Fig. 7.3.6: Plastic hardening function, determined from the experimental data.

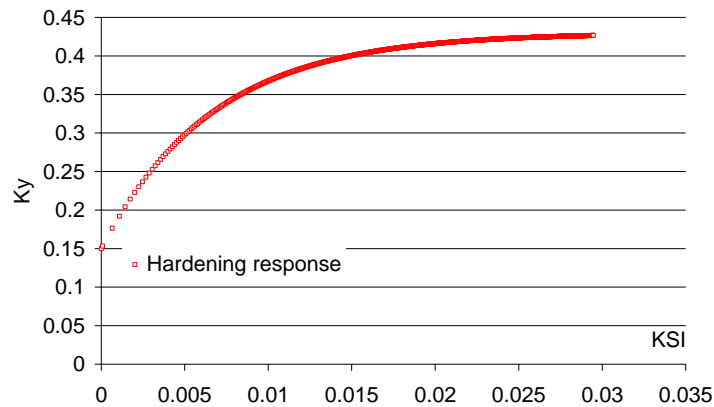


Fig. 7.3.6: Plastic hardening function, determined from the experimental data

From this, the values of the hardening function, as given in Eq. (7.139) can be determined as $k_{y_0} = 0.15$ MPa, $k_{y_\infty} = 0.43$ MPa and $\delta = 90$, whereby using a $\phi = 0.25$ rad ($\sim 14^\circ$). These values correspond to the cohesion values of $c_{y_0} = 0.12$ MPa and $c_{y_\infty} = 0.35$ MPa, see Appendix 7.2 for more details on the formulations.

In Fig. 7.3.7 a comparison is given between the model prediction, using the above determined parameters, and the experimental data.

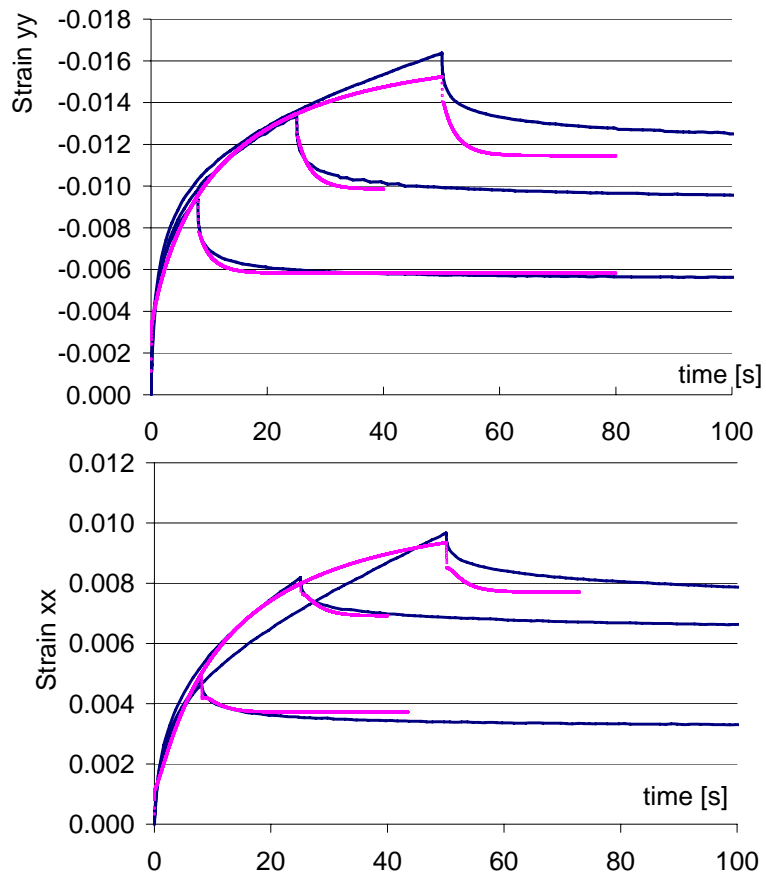


Fig. 7.3.7: Comparison model prediction in axial and radial direction with experimental data

Derivations for the yield response

In the following, the derivatives of the plastic response surfaces, which are used in chapter 7, are derived.

For a Von-Mises yield function

$$\boxed{f(\bar{\Sigma}, q) \rightarrow}$$

$$f(\bar{\Sigma}, q) = \sqrt{3J_2(\bar{\Sigma})} - k(q) \quad (\text{A 7.1.1})$$

$$J_2 = \frac{1}{2} \bar{s}_{ij} \bar{s}_{ij} \quad (\text{A 7.1.2})$$

With
$$\bar{s}_{ij} = \bar{\Sigma}_{ij} - \bar{p} \delta_{ij} \quad ; \quad \bar{p} = \frac{1}{3} (\bar{\Sigma}_{ii}) \quad (\text{A 7.1.3})$$

$$f(\bar{\Sigma}, q) = \sqrt{\frac{3}{2}} \sqrt{(\bar{\Sigma}_{ij} - \bar{p} \delta_{ij})(\bar{\Sigma}_{ij} - \bar{p} \delta_{ij})} - k(q) \quad (\text{A 7.1.4})$$

Alternatively, using the Cauchy stress tensor

$$\sigma_{ij} = J^{-1} (F_{\infty})_{ik} \bar{S}_{kn} (F_{\infty})_{nj}^T \quad (\text{A 7.1.5})$$

$$\bar{S}_{ij} = 2 \frac{\partial \bar{\psi}}{\partial (C_{\infty})_{ij}} \quad (\text{A 7.1.6})$$

Since
$$\bar{\Sigma}_{mn} = (C_{\infty})_{mk} \bar{S}_{kn} \quad (\text{A 7.1.7})$$

Therefore
$$\bar{S}_{kn} = (C_{\infty})_{km}^{-1} \bar{\Sigma}_{mn} \quad (\text{A 7.1.8})$$

Substituting this into the Cauchy stress tensor

$$\sigma_{ij} = J^{-1} (F_{\infty})_{ik}^{-1} (C_{\infty})_{km}^{-1} \bar{\Sigma}_{mn} (F_{\infty})_{nj}^T \quad (\text{A 7.1.9})$$

$$J_2 = \frac{1}{2} s_{ij} s_{ij} \quad (\text{A 7.1.10})$$

With
$$s_{ij} = \sigma_{ij} - p \delta_{ij} \quad ; \quad p = \frac{1}{3} (\sigma_{ii}) \quad (\text{A 7.1.11})$$

$$p = \frac{1}{3} J^{-1} (F_{\infty})_{ik}^{-1} (C_{\infty})_{km}^{-1} \bar{\Sigma}_{mn} (F_{\infty})_{ni}^T \quad (\text{A 7.1.12})$$

$$s_{ij} = \mathbf{J}^{-1} (\mathbf{F}_\infty)_{ik}^{-1} (\mathbf{C}_\infty)_{km}^{-1} \bar{\Sigma}_{mn} (\mathbf{F}_\infty)_{nj}^T - \mathbf{p}\delta_{ij} \quad (\text{A 7.1.13})$$

$$f(\bar{\Sigma}, \mathbf{q})$$

$$= \sqrt{\frac{3}{2}} \left[\left(\mathbf{J}^{-1} (\mathbf{F}_\infty)_{ik}^{-1} (\mathbf{C}_\infty)_{km}^{-1} \bar{\Sigma}_{mn} (\mathbf{F}_\infty)_{nj}^T - \mathbf{p}\delta_{ij} \right) \left(\mathbf{J}^{-1} (\mathbf{F}_\infty)_{ik}^{-1} (\mathbf{C}_\infty)_{km}^{-1} \bar{\Sigma}_{mn} (\mathbf{F}_\infty)_{nj}^T - \mathbf{p}\delta_{ij} \right) \right]^{\frac{1}{2}} - \mathbf{k}(\mathbf{q}) \quad (\text{A 7.1.14})$$

$$\boxed{\frac{\partial f}{\partial \bar{\Sigma}_{pq}} \rightarrow}$$

Using the formulation of Eq. (A 7.1.4)

$$f(\bar{\Sigma}, \mathbf{q}) = \sqrt{\frac{3}{2}} \sqrt{(\bar{\Sigma}_{ij} - \bar{\mathbf{p}}\delta_{ij})(\bar{\Sigma}_{ij} - \bar{\mathbf{p}}\delta_{ij})} - \mathbf{k}(\mathbf{q}) \quad (\text{A 7.1.15})$$

$$\frac{\partial f(\bar{\Sigma}, \mathbf{q})}{\partial \bar{\Sigma}_{pq}} = \frac{1}{2} \sqrt{\frac{3}{2}} \left[(\bar{\Sigma}_{ij} - \bar{\mathbf{p}}\delta_{ij})(\bar{\Sigma}_{ij} - \bar{\mathbf{p}}\delta_{ij}) \right]^{\frac{1}{2}} \frac{\partial}{\partial \bar{\Sigma}_{pq}} \left[(\bar{\Sigma}_{ij} - \bar{\mathbf{p}}\delta_{ij})(\bar{\Sigma}_{ij} - \bar{\mathbf{p}}\delta_{ij}) \right] \quad (\text{A 7.1.16})$$

Since

$$\begin{aligned} & \frac{\partial}{\partial \bar{\Sigma}_{pq}} \left[(\bar{\Sigma}_{ij} - \bar{\mathbf{p}}\delta_{ij})(\bar{\Sigma}_{ij} - \bar{\mathbf{p}}\delta_{ij}) \right] \\ &= 2 \left(\frac{\partial \bar{\Sigma}_{ij}}{\partial \bar{\Sigma}_{pq}} - \frac{\partial \bar{\mathbf{p}}}{\partial \bar{\Sigma}_{pq}} \delta_{ij} \right) (\bar{\Sigma}_{ij} - \bar{\mathbf{p}}\delta_{ij}) \\ &= 2 \left(\delta_{ip} \delta_{jq} - \frac{1}{3} \delta_{pq} \delta_{ij} \right) (\bar{\Sigma}_{ij} - \bar{\mathbf{p}}\delta_{ij}) \\ &= 2 \left(\delta_{ip} \delta_{jq} \bar{\Sigma}_{ij} - \delta_{ip} \delta_{jq} \bar{\mathbf{p}}\delta_{ij} - \frac{1}{3} \delta_{pq} \delta_{ij} \bar{\Sigma}_{ij} + \frac{1}{3} \delta_{pq} \delta_{ij} \bar{\mathbf{p}}\delta_{ij} \right) \\ &= 2 \left(\bar{\Sigma}_{pq} - \bar{\mathbf{p}}\delta_{pq} - \bar{\mathbf{p}}\delta_{pq} + \bar{\mathbf{p}}\delta_{pq} \right) \\ &= 2 \left(\bar{\Sigma}_{pq} - \bar{\mathbf{p}}\delta_{pq} \right) \\ &= 2 \bar{s}_{pq} \end{aligned} \quad (\text{A 7.1.17})$$

And

$$\begin{aligned} \left[(\bar{\Sigma}_{ij} - \bar{\mathbf{p}}\delta_{ij})(\bar{\Sigma}_{ij} - \bar{\mathbf{p}}\delta_{ij}) \right]^{\frac{1}{2}} &= \frac{1}{\sqrt{\bar{s}_{ij} \bar{s}_{ij}}} \\ &= \frac{1}{\|\bar{s}_{ij}\|} \end{aligned} \quad (\text{A 7.1.18})$$

Substituting Eq. (A 7.1.17) and Eq. (A 7.1.18) into Eq. (A 7.1.16)

$$\frac{\partial f(\bar{\Sigma}, \mathbf{q})}{\partial \bar{\Sigma}_{pq}} = \sqrt{\frac{3}{2}} \frac{\bar{s}_{pq}}{\|\bar{s}_{ij}\|} \quad (\text{A 7.1.19})$$

$$\boxed{\frac{\partial^2 f}{\partial \bar{\Sigma}_{pq} \partial \bar{\Sigma}_{mn}} \rightarrow}$$

Since

$$\frac{\partial f(\bar{\Sigma}, \mathbf{q})}{\partial \bar{\Sigma}_{pq}} = \sqrt{\frac{3}{2}} \left[(\bar{\Sigma}_{ij} - \bar{p}\delta_{ij})(\bar{\Sigma}_{ij} - \bar{p}\delta_{ij}) \right]^{-\frac{1}{2}} (\bar{\Sigma}_{pq} - \bar{p}\delta_{pq}) \quad (\text{A 7.1.20})$$

$$\begin{aligned} \frac{\partial f(\bar{\Sigma}, \mathbf{q})}{\partial \bar{\Sigma}_{pq} \partial \bar{\Sigma}_{mn}} &= \sqrt{\frac{3}{2}} \frac{\partial \left[(\bar{\Sigma}_{ij} - \bar{p}\delta_{ij})(\bar{\Sigma}_{ij} - \bar{p}\delta_{ij}) \right]^{-\frac{1}{2}}}{\partial \bar{\Sigma}_{mn}} (\bar{\Sigma}_{pq} - \bar{p}\delta_{pq}) \\ &\quad + \sqrt{\frac{3}{2}} \left[(\bar{\Sigma}_{ij} - \bar{p}\delta_{ij})(\bar{\Sigma}_{ij} - \bar{p}\delta_{ij}) \right]^{-\frac{1}{2}} \frac{\partial (\bar{\Sigma}_{pq} - \bar{p}\delta_{pq})}{\partial \bar{\Sigma}_{mn}} \end{aligned} \quad (\text{A 7.1.21})$$

With

$$\begin{aligned} &\frac{\partial \left[(\bar{\Sigma}_{ij} - \bar{p}\delta_{ij})(\bar{\Sigma}_{ij} - \bar{p}\delta_{ij}) \right]^{-\frac{1}{2}}}{\partial \bar{\Sigma}_{mn}} \\ &= -\frac{1}{2} \left[(\bar{\Sigma}_{ij} - \bar{p}\delta_{ij})(\bar{\Sigma}_{ij} - \bar{p}\delta_{ij}) \right]^{-\frac{1}{2}} \frac{\partial}{\partial \bar{\Sigma}_{mn}} \left[(\bar{\Sigma}_{ij} - \bar{p}\delta_{ij})(\bar{\Sigma}_{ij} - \bar{p}\delta_{ij}) \right] \\ &= -\left[(\bar{\Sigma}_{ij} - \bar{p}\delta_{ij})(\bar{\Sigma}_{ij} - \bar{p}\delta_{ij}) \right]^{-\frac{1}{2}} (\bar{\Sigma}_{mn} - \bar{p}\delta_{mn}) \end{aligned} \quad (\text{A 7.1.22})$$

And

$$\begin{aligned} \frac{\partial (\bar{\Sigma}_{pq} - \bar{p}\delta_{pq})}{\partial \bar{\Sigma}_{mn}} &= \left(\frac{\partial \bar{\Sigma}_{pq}}{\partial \bar{\Sigma}_{mn}} - \frac{\partial \bar{p}}{\partial \bar{\Sigma}_{mn}} \delta_{pq} \right) \\ &= \delta_{pm} \delta_{qn} - \frac{1}{3} \delta_{mn} \delta_{pq} \end{aligned} \quad (\text{A 7.1.23})$$

Substituting Eq. (A 7.1.22) and Eq. (A 7.1.23) into Eq. (A 7.1.21)

$$\begin{aligned}
& \frac{\partial f(\bar{\Sigma}, \mathbf{q})}{\partial \bar{\Sigma}_{pq} \partial \bar{\Sigma}_{mn}} \\
&= -\sqrt{\frac{3}{2}} \left[(\bar{\Sigma}_{ij} - \bar{p} \delta_{ij}) (\bar{\Sigma}_{ij} - \bar{p} \delta_{ij}) \right]^{-\frac{1}{2}} (\bar{\Sigma}_{mn} - \bar{p} \delta_{mn}) (\bar{\Sigma}_{pq} - \bar{p} \delta_{pq}) \\
&\quad + \sqrt{\frac{3}{2}} \left[(\bar{\Sigma}_{ij} - \bar{p} \delta_{ij}) (\bar{\Sigma}_{ij} - \bar{p} \delta_{ij}) \right]^{-\frac{1}{2}} \left(\delta_{pm} \delta_{qn} - \frac{1}{3} \delta_{mn} \delta_{pq} \right) \\
&= -\sqrt{\frac{3}{2}} \left[\bar{s}_{ij} \bar{s}_{ij} \right]^{-\frac{1}{2}} \bar{s}_{mn} \bar{s}_{pq} + \sqrt{\frac{3}{2}} \left[\bar{s}_{ij} \bar{s}_{ij} \right]^{-\frac{1}{2}} \left(\delta_{pm} \delta_{qn} - \frac{1}{3} \delta_{mn} \delta_{pq} \right) \\
&= \sqrt{\frac{3}{2}} \frac{1}{\|\bar{s}_{ij}\|} \left[\left(\delta_{pm} \delta_{qn} - \frac{1}{3} \delta_{mn} \delta_{pq} \right) - \frac{\bar{s}_{mn} \bar{s}_{pq}}{\bar{s}_{ij} \bar{s}_{ij}} \right]
\end{aligned} \tag{A 7.1.24}$$

$$\boxed{\frac{\partial^2 f}{\partial \bar{\Sigma}_{pq} \partial \mathbf{q}} \rightarrow}$$

$$\frac{\partial^2 f}{\partial \bar{\Sigma}_{pq} \partial \mathbf{q}} = 0 \tag{A 7.1.25}$$

$$\boxed{\frac{\partial^2 f}{\partial \bar{\Sigma}_{ik} \partial (C_\infty)_{mn}} \rightarrow}$$

$$\frac{\partial^2 f}{\partial \bar{\Sigma}_{ik} \partial (C_\infty)_{mn}} = \frac{\partial^2 f}{\partial \bar{\Sigma}_{ik} \partial \bar{\Sigma}_{pq}} \frac{\partial \bar{\Sigma}_{pq}}{\partial (C_\infty)_{mn}} \tag{A 7.1.26}$$

Since
$$\bar{\Sigma}_{pq} = (C_\infty)_{pr} \bar{S}_{rq} \tag{A 7.1.27}$$

Using the Neo-Hookean formulation

$$\bar{S}_{rq} = \mu \delta_{rq} - \mu I_3^{-\alpha} (C_\infty)_{rq}^{-1} \tag{A 7.1.28}$$

Substituting Eq. (A 7.1.28) into Eq. (A 7.1.27)

$$\bar{\Sigma}_{pq} = (C_\infty)_{pr} \mu \delta_{rq} - \mu I_3^{-\alpha} \delta_{pq} \tag{A 7.1.29}$$

Therefore

$$\begin{aligned}
\frac{\partial \bar{\Sigma}_{pq}}{\partial (C_\infty)_{mn}} &= \frac{\partial}{\partial (C_\infty)_{mn}} \left((C_\infty)_{pr} \mu \delta_{rq} - \mu I_3^{-\alpha} \delta_{pq} \right) \\
&= \frac{\partial (C_\infty)_{pr}}{\partial (C_\infty)_{mn}} \mu \delta_{rq} - \mu \frac{\partial I_3^{-\alpha}}{\partial (C_\infty)_{mn}} \delta_{pq} \\
&= \mu \delta_{pm} \delta_{nq} - \mu \frac{\partial I_3^{-\alpha}}{\partial (C_\infty)_{mn}} \delta_{pq}
\end{aligned} \tag{A 7.1.30}$$

Since
$$\mathbf{I}_3(\mathbf{C}_\infty) = \det \mathbf{C}_\infty \quad ; \quad \frac{\partial(\det \mathbf{C}_\infty)}{\partial \mathbf{C}_\infty} = \mathbf{I}_3(\mathbf{C}_\infty) \mathbf{C}_\infty^{-1} \quad (\text{A 7.1.31})$$

$$\begin{aligned} \frac{\partial \mathbf{I}_3^{-\alpha}}{\partial (\mathbf{C}_\infty)_{mn}} &= -\alpha \mathbf{I}_3^{-\alpha-1} \frac{\partial \mathbf{I}_3}{\partial (\mathbf{C}_\infty)_{mn}} \\ &= -\alpha \mathbf{I}_3^{-\alpha-1} \mathbf{I}_3 (\mathbf{C}_\infty)_{mn}^{-1} \\ &= -\alpha \mathbf{I}_3^{-\alpha} (\mathbf{C}_\infty)_{mn}^{-1} \end{aligned} \quad (\text{A 7.1.32})$$

Substituting Eq. (A 7.1.32) into Eq. (A 7.1.30)

$$\frac{\partial \bar{\Sigma}_{pq}}{\partial (\mathbf{C}_\infty)_{mn}} = \mu \delta_{pm} \delta_{nq} + \mu \alpha \mathbf{I}_3^{-\alpha} (\mathbf{C}_\infty)_{mn}^{-1} \delta_{pq} \quad (\text{A 7.1.33})$$

Since
$$\alpha = \frac{\lambda}{2\mu} \quad (\text{A 7.1.34})$$

$$\boxed{\frac{\partial \bar{\Sigma}_{pq}}{\partial (\mathbf{C}_\infty)_{mn}}} = \mu \delta_{pm} \delta_{nq} + \frac{1}{2} \lambda \mathbf{I}_3^{-\alpha} (\mathbf{C}_\infty)_{mn}^{-1} \delta_{pq} \quad (\text{A 7.1.35})$$

Substituting this back into Eq. (A 7.1.26)

$$\frac{\partial^2 f}{\partial \bar{\Sigma}_{ik} \partial (\mathbf{C}_\infty)_{mn}} = \frac{\partial^2 f}{\partial \bar{\Sigma}_{ik} \partial \bar{\Sigma}_{pq}} \left(\mu \delta_{pm} \delta_{nq} + \frac{1}{2} \lambda \mathbf{I}_3^{-\alpha} (\mathbf{C}_\infty)_{mn}^{-1} \delta_{pq} \right) \quad (\text{A 7.1.36})$$

$$\boxed{\frac{\partial \mathbf{W}_{ij}}{\partial \bar{\Sigma}_{mn}}} \rightarrow$$

Since
$${}^{t+\Delta t} \mathbf{W} = {}^{t+\Delta t} \mathbf{N} \left({}^{\text{trial}} \mathbf{C}_\infty \right) + \left({}^{\text{trial}} \mathbf{C}_\infty \right) \mathbf{N} \quad (\text{A 7.1.37})$$

$$\frac{\partial \mathbf{W}_{ij}}{\partial \bar{\Sigma}_{mn}} = \frac{\partial}{\partial \bar{\Sigma}_{mn}} \left[\mathbf{N}_{ik} \left({}^{\text{trial}} \mathbf{C}_\infty \right)_{kj} + \left({}^{\text{trial}} \mathbf{C}_\infty \right)_{il} \mathbf{N}_{lj} \right] \quad (\text{A 7.1.38})$$

Since
$$\left(\frac{\partial \left({}^{\text{trial}} \mathbf{C}_\infty \right)_{kj}}{\partial \bar{\Sigma}_{mn}} \right) = 0 \quad (\text{A 7.1.39})$$

$$\frac{\partial \mathbf{W}_{ij}}{\partial \bar{\Sigma}_{mn}} = \frac{\partial \mathbf{N}_{ik}}{\partial \bar{\Sigma}_{mn}} \left({}^{\text{trial}} \mathbf{C}_\infty \right)_{kj} + \left({}^{\text{trial}} \mathbf{C}_\infty \right)_{il} \frac{\partial \mathbf{N}_{lj}}{\partial \bar{\Sigma}_{mn}} \quad (\text{A 7.1.40})$$

Since
$$\mathbf{N}_{ik} = \frac{\partial f}{\partial \bar{\Sigma}_{ik}} \quad (\text{A 7.1.41})$$

$$\frac{\partial \mathbf{N}_{ik}}{\partial \bar{\Sigma}_{mn}} = \frac{\partial^2 f}{\partial \bar{\Sigma}_{ik} \partial \bar{\Sigma}_{mn}} \quad (\text{A 7.1.42})$$

$$\frac{\partial W_{ij}}{\partial \bar{\Sigma}_{mn}} = \frac{\partial^2 f}{\partial \bar{\Sigma}_{mn} \partial \bar{\Sigma}_{ik}} (\text{trial } C_{\infty})_{kj} + (\text{trial } C_{\infty})_{il} \frac{\partial^2 f}{\partial \bar{\Sigma}_{lj} \partial \bar{\Sigma}_{mn}} \quad (\text{A 7.1.43})$$

$$\boxed{\frac{\partial W_{ij}}{\partial (C_{\infty})_{mn}} \rightarrow}$$

Since
$$W_{ij} = N_{ik} (\text{trial } C_{\infty})_{kj} + (\text{trial } C_{\infty})_{il} N_{lj} \quad (\text{A 7.1.44})$$

$$\frac{\partial W_{ij}}{\partial (C_{\infty})_{mn}} = \frac{\partial}{\partial (C_{\infty})_{mn}} \left[N_{ik} (\text{trial } C_{\infty})_{kj} + (\text{trial } C_{\infty})_{il} N_{lj} \right] \quad (\text{A 7.1.45})$$

Since
$$\left(\frac{\partial (\text{trial } C_{\infty})_{kj}}{\partial (C_{\infty})_{mn}} \right) = 0 \quad (\text{A 7.1.46})$$

$$\frac{\partial W_{ij}}{\partial (C_{\infty})_{mn}} = \frac{\partial N_{ik}}{\partial (C_{\infty})_{mn}} (\text{trial } C_{\infty})_{kj} + (\text{trial } C_{\infty})_{il} \frac{\partial N_{lj}}{\partial (C_{\infty})_{mn}} \quad (\text{A 7.1.47})$$

Since
$$N_{ik} = \frac{\partial f}{\partial \bar{\Sigma}_{ik}} \quad (\text{A 7.1.48})$$

$$\frac{\partial N_{ik}}{\partial (C_{\infty})_{mn}} = \frac{\partial^2 f}{\partial \bar{\Sigma}_{ik} \partial (C_{\infty})_{mn}} \quad (\text{A 7.1.49})$$

$$\frac{\partial W_{ij}}{\partial (C_{\infty})_{mn}} = \frac{\partial^2 f}{\partial \bar{\Sigma}_{ik} \partial (C_{\infty})_{mn}} (\text{trial } C_{\infty})_{kj} + (\text{trial } C_{\infty})_{il} \frac{\partial^2 f}{\partial \bar{\Sigma}_{lj} \partial (C_{\infty})_{mn}} \quad (\text{A 7.1.50})$$

$$\boxed{\frac{\partial W_{ij}}{\partial \Delta \lambda} \rightarrow}$$

Since
$$W_{ij} = N_{ik} (\text{trial } C_{\infty})_{kj} + (\text{trial } C_{\infty})_{il} N_{lj} \quad (\text{A 7.1.51})$$

$$\frac{\partial W_{ij}}{\partial \Delta \lambda} = \frac{\partial N_{ik}}{\partial \Delta \lambda} (\text{trial } C_{\infty})_{kj} + (\text{trial } C_{\infty})_{il} \frac{\partial N_{lj}}{\partial \Delta \lambda} \quad (\text{A 7.1.52})$$

Since
$$N_{ik} = \frac{\partial f}{\partial \bar{\Sigma}_{ik}} \quad (\text{A 7.1.53})$$

$$\begin{aligned}
\frac{\partial N_{ik}}{\partial \Delta\lambda} &= \frac{\partial}{\partial \Delta\lambda} \left(\frac{\partial f}{\partial \bar{\Sigma}_{ik}} \right) \\
&= \frac{\partial}{\partial \bar{\Sigma}_{ik}} \left(\frac{\partial f}{\partial \Delta\lambda} \right) \\
&= \frac{\partial}{\partial \bar{\Sigma}_{ik}} \left(\frac{\partial f}{\partial q} \frac{\partial q}{\partial \xi} \frac{\partial \xi}{\partial \Delta\lambda} \right) \\
&= \frac{\partial^2 f}{\partial \bar{\Sigma}_{ik} \partial q} \left(\frac{\partial q}{\partial \xi} \frac{\partial \xi}{\partial \Delta\lambda} \right)
\end{aligned} \tag{A 7.1.54}$$

Since $\xi = \Delta\lambda \left(\frac{\partial f}{\partial q} \right) ; \quad \frac{\partial \xi}{\partial \Delta\lambda} = \frac{\partial f}{\partial q}$ (A 7.1.55)

Furthermore $q = -\frac{\partial \psi}{\partial \xi} ; \quad \frac{\partial q}{\partial \xi} = -\frac{\partial^2 \psi}{\partial \xi^2}$ (A 7.1.56)

Therefore $\frac{\partial N_{ik}}{\partial \Delta\lambda} = \frac{\partial^2 f}{\partial \bar{\Sigma}_{ik} \partial q} \left(-\frac{\partial^2 \psi}{\partial \xi^2} \cdot \frac{\partial f}{\partial q} \right)$ (A 7.1.57)

Substituting Eq. (A 7.1.57) into Eq. (A 7.1.52) gives

$$\frac{\partial W_{ij}}{\partial \Delta\lambda} = \frac{\partial^2 f}{\partial \bar{\Sigma}_{ik} \partial q} \left(-\frac{\partial^2 \psi}{\partial \xi^2} \cdot \frac{\partial f}{\partial q} \right) ({}_{\text{trial}}C_{\infty})_{kj} + ({}_{\text{trial}}C_{\infty})_{il} \frac{\partial^2 f}{\partial \bar{\Sigma}_{lj} \partial q} \left(-\frac{\partial^2 \psi}{\partial \xi^2} \cdot \frac{\partial f}{\partial q} \right) \tag{A 7.1.58}$$

Since in this case $\frac{\partial^2 f}{\partial \bar{\Sigma}_{ik} \partial q} = 0$, Eq. (A 7.1.58) becomes zero.

$$\boxed{\frac{\partial W_{ij}}{\partial q} \rightarrow}$$

$$\frac{\partial W_{ij}}{\partial q} = \frac{\partial}{\partial q} \left[N_{ik} ({}_{\text{trial}}C_{\infty})_{kj} + ({}_{\text{trial}}C_{\infty})_{il} N_{lj} \right] \tag{A 7.1.59}$$

$$\frac{\partial W_{ij}}{\partial q} = \frac{\partial N_{ik}}{\partial q} ({}_{\text{trial}}C_{\infty})_{kj} + ({}_{\text{trial}}C_{\infty})_{il} \frac{\partial N_{lj}}{\partial q} \tag{A 7.1.60}$$

Since $N_{ik} = \frac{\partial f(\bar{\Sigma}, q)}{\partial \bar{\Sigma}_{ik}}$ (A 7.1.61)

$$\frac{\partial N_{ik}}{\partial q} = \frac{\partial^2 f}{\partial \bar{\Sigma}_{ik} \partial q} \tag{A 7.1.62}$$

Therefore $\frac{\partial W_{ij}}{\partial q} = \frac{\partial^2 f}{\partial \bar{\Sigma}_{ik} \partial q} ({}_{\text{trial}}C_{\infty})_{kj} + ({}_{\text{trial}}C_{\infty})_{il} \frac{\partial^2 f}{\partial \bar{\Sigma}_{lj} \partial q}$ (A 7.1.63)

Since in this case $\frac{\partial^2 f}{\partial \bar{\Sigma}_{ik} \partial q} = 0$,

$$\frac{\partial W_{ij}}{\partial q} = 0 \quad (\text{A 7.1.64})$$

For a Drucker Prager yield function

$$\boxed{f(\bar{\Sigma}, q) \rightarrow}$$

$$f(\bar{\Sigma}, q) = \sqrt{J_2(\bar{\Sigma})} + \alpha I_1 - k_y \quad (\text{A 7.1.65})$$

$$J_2 = \frac{1}{2} \bar{s}_{ij} \bar{s}_{ij} \quad (\text{A 7.1.66})$$

With $\bar{s}_{ij} = \bar{\Sigma}_{ij} - \bar{p} \delta_{ij} \quad ; \quad \bar{p} = \frac{1}{3} (\bar{\Sigma}_{ii})$ (A 7.1.67)

$$I_2 = \bar{\Sigma}_{ii} \quad (\text{A 7.1.68})$$

$$f(\bar{\Sigma}, q) = \sqrt{J_2} = \sqrt{\frac{1}{2} \sqrt{(\bar{\Sigma}_{ij} - \bar{p} \delta_{ij})(\bar{\Sigma}_{ij} - \bar{p} \delta_{ij})}} - \alpha \bar{\Sigma}_{ii} - k_y(q) \quad (\text{A 7.1.69})$$

$$\boxed{\frac{\partial f}{\partial \bar{\Sigma}_{pq}} \rightarrow}$$

$$\frac{\partial f(\bar{\Sigma}, q)}{\partial \bar{\Sigma}_{pq}} = \frac{1}{2} \sqrt{\frac{1}{2}} \left[(\bar{\Sigma}_{ij} - \bar{p} \delta_{ij})(\bar{\Sigma}_{ij} - \bar{p} \delta_{ij}) \right]^{-\frac{1}{2}} \frac{\partial}{\partial \bar{\Sigma}_{pq}} \left[(\bar{\Sigma}_{ij} - \bar{p} \delta_{ij})(\bar{\Sigma}_{ij} - \bar{p} \delta_{ij}) \right] - \alpha \frac{\partial \bar{\Sigma}_{ii}}{\partial \bar{\Sigma}_{pq}} \quad (\text{A 7.1.70})$$

Where $\alpha \frac{\partial \bar{\Sigma}_{ii}}{\partial \bar{\Sigma}_{pq}} = \alpha \delta_{ip} \delta_{iq} = \alpha \delta_{pq}$ (A 7.1.71)

Since

$$\begin{aligned}
& \frac{\partial}{\partial \bar{\Sigma}_{pq}} \left[(\bar{\Sigma}_{ij} - \bar{p}\delta_{ij})(\bar{\Sigma}_{ij} - \bar{p}\delta_{ij}) \right] \\
&= 2 \left(\frac{\partial \bar{\Sigma}_{ij}}{\partial \bar{\Sigma}_{pq}} - \frac{\partial \bar{p}}{\partial \bar{\Sigma}_{pq}} \delta_{ij} \right) (\bar{\Sigma}_{ij} - \bar{p}\delta_{ij}) \\
&= 2 \left(\delta_{ip} \delta_{jq} - \frac{1}{3} \delta_{pq} \delta_{ij} \right) (\bar{\Sigma}_{ij} - \bar{p}\delta_{ij}) \\
&= 2 \left(\delta_{ip} \delta_{jq} \bar{\Sigma}_{ij} - \delta_{ip} \delta_{jq} \bar{p}\delta_{ij} - \frac{1}{3} \delta_{pq} \delta_{ij} \bar{\Sigma}_{ij} + \frac{1}{3} \delta_{pq} \delta_{ij} \bar{p}\delta_{ij} \right) \\
&= 2 (\bar{\Sigma}_{pq} - \bar{p}\delta_{pq} - \bar{p}\delta_{pq} + \bar{p}\delta_{pq}) \\
&= 2 (\bar{\Sigma}_{pq} - \bar{p}\delta_{pq}) \\
&= 2 \bar{s}_{pq}
\end{aligned} \tag{A 7.1.72}$$

And

$$\begin{aligned}
\left[(\bar{\Sigma}_{ij} - \bar{p}\delta_{ij})(\bar{\Sigma}_{ij} - \bar{p}\delta_{ij}) \right]^{\frac{1}{2}} &= \frac{1}{\sqrt{\bar{s}_{ij} \bar{s}_{ij}}} \\
&= \frac{1}{\|\bar{s}_{ij}\|}
\end{aligned} \tag{A 7.1.73}$$

$$\frac{\partial f(\bar{\Sigma}, q)}{\partial \bar{\Sigma}_{pq}} = \sqrt{\frac{1}{2}} \frac{\bar{s}_{pq}}{\|\bar{s}_{ij}\|} + \alpha \delta_{pq} \tag{A 7.1.74}$$

$$\boxed{\frac{\partial^2 f}{\partial \bar{\Sigma}_{pq} \partial \bar{\Sigma}_{mn}} \rightarrow}$$

Since

$$\frac{\partial f(\bar{\Sigma}, q)}{\partial \bar{\Sigma}_{pq}} = \sqrt{\frac{1}{2}} \left[(\bar{\Sigma}_{ij} - \bar{p}\delta_{ij})(\bar{\Sigma}_{ij} - \bar{p}\delta_{ij}) \right]^{\frac{1}{2}} (\bar{\Sigma}_{pq} - \bar{p}\delta_{pq}) + \alpha \delta_{pq} \tag{A 7.1.75}$$

$$\begin{aligned}
\frac{\partial f(\bar{\Sigma}, q)}{\partial \bar{\Sigma}_{pq} \partial \bar{\Sigma}_{mn}} &= \sqrt{\frac{1}{2}} \frac{\partial \left[(\bar{\Sigma}_{ij} - \bar{p}\delta_{ij})(\bar{\Sigma}_{ij} - \bar{p}\delta_{ij}) \right]^{\frac{1}{2}}}{\partial \bar{\Sigma}_{mn}} (\bar{\Sigma}_{pq} - \bar{p}\delta_{pq}) \\
&\quad + \sqrt{\frac{1}{2}} \left[(\bar{\Sigma}_{ij} - \bar{p}\delta_{ij})(\bar{\Sigma}_{ij} - \bar{p}\delta_{ij}) \right]^{\frac{1}{2}} \frac{\partial}{\partial \bar{\Sigma}_{mn}} (\bar{\Sigma}_{pq} - \bar{p}\delta_{pq})
\end{aligned} \tag{A 7.1.76}$$

With

$$\begin{aligned}
& \frac{\partial \left[(\bar{\Sigma}_{ij} - \bar{p}\delta_{ij})(\bar{\Sigma}_{ij} - \bar{p}\delta_{ij}) \right]^{-\frac{1}{2}}}{\partial \bar{\Sigma}_{mn}} \\
&= -\frac{1}{2} \left[(\bar{\Sigma}_{ij} - \bar{p}\delta_{ij})(\bar{\Sigma}_{ij} - \bar{p}\delta_{ij}) \right]^{-\frac{1}{2}} \frac{\partial}{\partial \bar{\Sigma}_{mn}} \left[(\bar{\Sigma}_{ij} - \bar{p}\delta_{ij})(\bar{\Sigma}_{ij} - \bar{p}\delta_{ij}) \right] \\
&= - \left[(\bar{\Sigma}_{ij} - \bar{p}\delta_{ij})(\bar{\Sigma}_{ij} - \bar{p}\delta_{ij}) \right]^{-\frac{1}{2}} (\bar{\Sigma}_{mn} - \bar{p}\delta_{mn})
\end{aligned} \tag{A 7.1.77}$$

And

$$\begin{aligned}
\frac{\partial (\bar{\Sigma}_{pq} - \bar{p}\delta_{pq})}{\partial \bar{\Sigma}_{mn}} &= \left(\frac{\partial \bar{\Sigma}_{pq}}{\partial \bar{\Sigma}_{mn}} - \frac{\partial \bar{p}}{\partial \bar{\Sigma}_{mn}} \delta_{pq} \right) \\
&= \delta_{pm} \delta_{qn} - \frac{1}{3} \delta_{mn} \delta_{pq}
\end{aligned} \tag{A 7.1.78}$$

Therefore

$$\begin{aligned}
& \frac{\partial f(\bar{\Sigma}, \mathbf{q})}{\partial \bar{\Sigma}_{pq} \partial \bar{\Sigma}_{mn}} \\
&= -\sqrt{\frac{1}{2}} \left[(\bar{\Sigma}_{ij} - \bar{p}\delta_{ij})(\bar{\Sigma}_{ij} - \bar{p}\delta_{ij}) \right]^{-\frac{1}{2}} (\bar{\Sigma}_{mn} - \bar{p}\delta_{mn})(\bar{\Sigma}_{pq} - \bar{p}\delta_{pq}) \\
&\quad + \sqrt{\frac{1}{2}} \left[(\bar{\Sigma}_{ij} - \bar{p}\delta_{ij})(\bar{\Sigma}_{ij} - \bar{p}\delta_{ij}) \right]^{-\frac{1}{2}} \left(\delta_{pm} \delta_{qn} - \frac{1}{3} \delta_{mn} \delta_{pq} \right) \\
&= -\sqrt{\frac{1}{2}} \left[\bar{s}_{ij} \bar{s}_{ij} \right]^{-\frac{1}{2}} \bar{s}_{mn} \bar{s}_{pq} + \sqrt{\frac{1}{2}} \left[\bar{s}_{ij} \bar{s}_{ij} \right]^{-\frac{1}{2}} \left(\delta_{pm} \delta_{qn} - \frac{1}{3} \delta_{mn} \delta_{pq} \right) \\
&= \sqrt{\frac{1}{2}} \frac{1}{\|\bar{s}_{ij}\|} \left[\left(\delta_{pm} \delta_{qn} - \frac{1}{3} \delta_{mn} \delta_{pq} \right) - \frac{\bar{s}_{mn} \bar{s}_{pq}}{\bar{s}_{ij} \bar{s}_{ij}} \right]
\end{aligned} \tag{A 7.1.79}$$

Yield Surface Characteristics

In the following the formulations for a Von-Mises and a Drucker-Prager plastic yield function are discussed.

The Von-Mises Response Surface

The Von-Mises response surface is defined by

$$f(\boldsymbol{\tau}_{\infty,i}, q) = \sqrt{\frac{3}{2}} \|\mathbf{s}_{\infty,i}\| = \tau_y(q) \quad (\text{A 7.2.1})$$

in which the vector of principal deviatoric Kirchhoff stresses $\mathbf{s}_{\infty,i}$ is given by

$$\mathbf{s}_{\infty,i} = \text{dev}(\boldsymbol{\tau}_{\infty,i}) = \left(\mathbb{I} - \frac{1}{3} \mathbf{I} \otimes \mathbf{I} \right) : \boldsymbol{\tau}_{\infty,i} = \boldsymbol{\tau}_{\infty,i} - \frac{1}{3} \sum_{j=1}^3 \tau_{\infty,j} \mathbf{e}_j \mathbf{e}_j \quad (\text{A 7.2.2})$$

and

$$\|\mathbf{s}_{\infty,i}\| = \left(\mathbf{s}_{\infty,i} \cdot \mathbf{s}_{\infty,i} \right)^{1/2} = \left[\sum_{i=1}^3 \left(\tau_{\infty,i} - \frac{1}{3} \sum_{j=1}^3 \tau_{\infty,j} \right)^2 \right]^{1/2} \quad (\text{A 7.2.3})$$

so that

$$\begin{aligned} \partial_{\tau_{\infty,i}} f &= \frac{\partial f}{\partial s_{\infty,1}} \frac{\partial s_{\infty,1}}{\partial \tau_{\infty,i}} + \frac{\partial f}{\partial s_{\infty,2}} \frac{\partial s_{\infty,2}}{\partial \tau_{\infty,i}} + \frac{\partial f}{\partial s_{\infty,3}} \frac{\partial s_{\infty,3}}{\partial \tau_{\infty,i}} \\ &= \sqrt{\frac{3}{2}} \frac{1}{2} \left(\sqrt{s_{\infty,1}^2 + s_{\infty,2}^2 + s_{\infty,3}^2} \right)^{-1} \left(2s_{\infty,1} \frac{\partial s_{\infty,1}}{\partial \tau_{\infty,i}} + 2s_{\infty,2} \frac{\partial s_{\infty,2}}{\partial \tau_{\infty,i}} + 2s_{\infty,3} \frac{\partial s_{\infty,3}}{\partial \tau_{\infty,i}} \right) \end{aligned} \quad (\text{A 7.2.4})$$

Considering that

$$\frac{\partial s_{\infty,i}}{\partial \tau_{\infty,j}} = \delta_{ij} - \frac{1}{3} \quad (\text{A 7.2.5})$$

$$\partial_{\tau_{\infty,i}} f = \sqrt{\frac{3}{2}} \frac{s_{\infty,i}}{\sqrt{s_{\infty,1}^2 + s_{\infty,2}^2 + s_{\infty,3}^2}} \quad (\text{A 7.2.6})$$

$$\begin{aligned}
\frac{\partial^2}{\partial \tau_{\infty,i} \partial \tau_{\infty,j}} f &= \frac{\partial \left(\frac{\partial f}{\partial \tau_{\infty,i}} \right)}{\partial \tau_{\infty,j}} \\
&= \frac{\partial}{\partial \tau_{\infty,j}} \left(\sqrt{\frac{3}{2}} \frac{s_{\infty,i}}{\left(s_{\infty,1}^2 + s_{\infty,2}^2 + s_{\infty,3}^2 \right)^{1/2}} \right) \\
&= \sqrt{\frac{3}{2}} \left(\frac{-s_i s_j}{\left(s_{\infty,1}^2 + s_{\infty,2}^2 + s_{\infty,3}^2 \right)^{3/2}} + \frac{1}{\left(s_{\infty,1}^2 + s_{\infty,2}^2 + s_{\infty,3}^2 \right)^{1/2}} \frac{\partial s_i}{\partial \tau_j} \right)
\end{aligned} \tag{A 7.2.7}$$

The yield response in the Von Mises surface is controlled by the yield limit $\tau_y(q)$, Eq. (A 7.2.1), For a perfectly plastic material model, $q = 0$, the yield limit is equal to a constant yield stress τ_{y0}

$$f(\tau_{\infty,i}, 0) = \tau_{y0} \tag{A 7.2.8}$$

For a material model that enables the simulation of the hardening response of the material after the yield stress τ_{y0} has been reached, τ_y becomes a variable function which, in principle, can reach a limit yield value $\tau_{y\infty}$, Fig.A. 7.1.1. Where ξ is defined as a variable that controls the hardening/softening of the model.

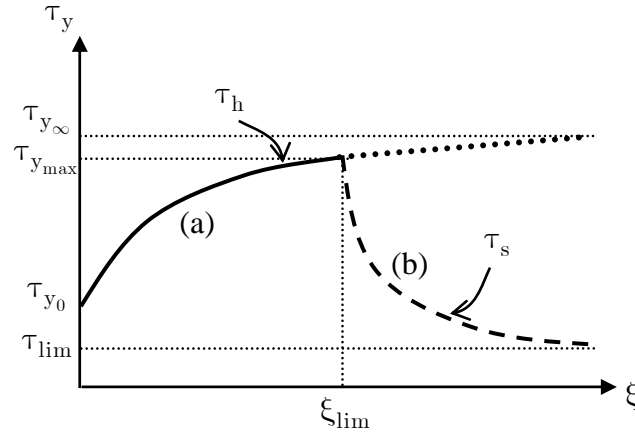


Fig.A. 7.1.1: Hardening/Softening response

When the material reaches a maximum yield stress $\tau_{y_{max}}$ at $\xi = \xi_{lim}$, the material will soften. This can be modeled by a reduction of τ_y , Fig.(b).

The maximum value of the yield surface can therefore be expressed as

$$\tau_y = \begin{cases} \tau_h & 0 \leq \xi \leq \xi_{lim} \\ \tau_s & \xi > \xi_{lim} \end{cases} \tag{A 7.2.9}$$

For the hardening part, τ_h can be found as

$$\tau_h = \tau_{y_\infty} + (\tau_{y_0} - \tau_{y_\infty})e^{-\delta\xi} \quad 0 \leq \xi \leq \xi_{\text{lim}} \quad (\text{A 7.2.10})$$

where δ determines the rate of hardening. For $\delta = 0$ and/or $\xi = 0$ the function reduces to a perfect plasticity model, with $\tau_h = \tau_{y_0}$.

For the softening response, τ_s can be expressed as

$$\tau_s = \tau_{\text{lim}} + (\tau_{y_{\text{max}}} - \tau_{\text{lim}})e^{-\delta_1(\xi - \xi_{\text{lim}})} \quad \xi > \xi_{\text{lim}} \quad (\text{A 7.2.11})$$

where δ_1 determines the rate of softening and τ_{lim} determines the maximum yielding response, or the lowest yield value.

The $\tau_{y_{\text{max}}}$ is determined from the value of τ_h at $\xi = \xi_{\text{lim}}$

$$\tau_{y_{\text{max}}} = \tau_{y_\infty} + (\tau_{y_0} - \tau_{y_\infty})e^{-\delta\xi_{\text{lim}}} \quad (\text{A 7.2.12})$$

After substitution of Eq. (A 7.2.12) into Eq. (A 7.2.11) and slightly rearranging, the softening response is given by

$$\tau_s = \tau_{\text{lim}} \left(1 - e^{-\delta_1(\xi - \xi_{\text{lim}})}\right) + \left(\tau_{y_\infty} + (\tau_{y_0} - \tau_{y_\infty})e^{-\delta\xi_{\text{lim}}}\right)e^{-\delta_1(\xi - \xi_{\text{lim}})} \quad \xi > \xi_{\text{lim}} \quad (\text{A 7.2.13})$$

The hardening/softening response of the material is therefore covered by

$$\tau_y = \begin{cases} \tau_{y_\infty} + (\tau_{y_0} - \tau_{y_\infty})e^{-\delta\xi} & \xi \leq \xi_{\text{lim}} \\ \tau_{\text{lim}} \left(1 - e^{-\delta_1(\xi - \xi_{\text{lim}})}\right) + \left(\tau_{y_\infty} + (\tau_{y_0} - \tau_{y_\infty})e^{-\delta\xi_{\text{lim}}}\right)e^{-\delta_1(\xi - \xi_{\text{lim}})} & \xi > \xi_{\text{lim}} \end{cases} \quad (\text{A 7.2.14})$$

Since the hardening response of the material is expressed by a uniform increase of the yield surface, and the softening as a uniform decrease of the yield surface, the yield limit can also be formulated as

$$\tau_y = \begin{cases} \tau_{y_0} - q_h & \xi \leq \xi_{\text{lim}} \\ \tau_{y_{\text{max}}} - q_s & \xi > \xi_{\text{lim}} \end{cases} \quad (\text{A 7.2.15})$$

Since $q_h = -\partial_\xi \psi_{\text{ph}}$ (A 7.2.16)

and $q_s = \partial_\xi \psi_{\text{ps}}$ (A 7.2.17)

Therefore

$$\tau_y = \begin{cases} \tau_{y_0} + \partial_\xi \psi_{\text{ph}} & \xi \leq \xi_{\text{lim}} \\ \tau_{y_{\text{max}}} - \partial_\xi \psi_{\text{ps}} & \xi > \xi_{\text{lim}} \end{cases} \quad (\text{A 7.2.18})$$

where ψ_{ps} and ψ_{ph} are the plastic strain energy functions for the hardening and the softening phase, respectively. Therefore

$$\begin{aligned} \partial_\xi \psi_{\text{ph}} &= \tau_h - \tau_{y_0} \\ -\partial_\xi \psi_{\text{ps}} &= \tau_s - \tau_{y_{\text{max}}} \end{aligned} \quad (\text{A 7.2.19})$$

By substituting Eq. (A 7.2.10) and Eq. (A 7.2.11) into Eq. (A 7.2.19)_{1,2}, respectively

$$\partial_{\xi} \psi_{\text{ph}} = (\tau_{y_{\infty}} - \tau_{y_0}) (1 - e^{-\delta \xi}) \quad (\text{A 7.2.20})$$

and

$$\partial_{\xi} \psi_{\text{ps}} = (\tau_{y_{\text{max}}} - \tau_{\text{lim}}) (1 - e^{-\delta_1 (\xi - \xi_{\text{lim}})}) \quad (\text{A 7.2.21})$$

From these, the strain energy function differentiated twice to ξ can be found as

$$\partial_{\xi\xi}^2 \psi_{\text{ph}} = \delta (\tau_{y_{\infty}} - \tau_{y_0}) e^{-\delta \xi} \quad (\text{A 7.2.22})$$

and

$$\partial_{\xi\xi}^2 \psi_{\text{ps}} = \delta_1 (\tau_{y_{\text{max}}} - \tau_{\text{lim}}) e^{-\delta_1 (\xi - \xi_{\text{lim}})} \quad (\text{A 7.2.23})$$

By integrating Eq. (A 7.2.20) over ξ , the plastic strain energy function for the hardening phase is found as

$$\psi_{\text{ph}} = (\tau_{y_{\infty}} - \tau_{y_0}) \left(\xi + \frac{1}{\delta} e^{-\delta \xi} \right) + C \quad (\text{A 7.2.24})$$

Since for $\xi = 0$; $\psi_{\text{ph}} = 0$, the integration constant C can be found as

$$C = \frac{1}{\delta} (\tau_{y_0} - \tau_{y_{\infty}}) \quad (\text{A 7.2.25})$$

Substituting the C into Eq. (A 7.2.24), gives the plastic strain energy function for the hardening phase

$$\psi_{\text{ph}} = (\tau_{y_{\infty}} - \tau_{y_0}) \left(\xi + \frac{1}{\delta} (e^{-\delta \xi} - 1) \right) \quad (\text{A 7.2.26})$$

Similarly, the plastic strain energy function for the softening phase can be found from Eq. (A 7.2.21) as

$$\psi_{\text{ps}} = (\tau_{y_{\text{max}}} - \tau_{\text{lim}}) \left(\xi + \frac{1}{\delta_1} e^{-\delta_1 (\xi - \xi_{\text{lim}})} \right) + C \quad (\text{A 7.2.27})$$

Since for $\xi = \xi_{\text{lim}}$; $\psi_{\text{ps}} = \psi_{\text{ph}}$, the integration constant C can be found as

$$C = (\tau_{y_{\infty}} - \tau_{y_0}) \left(\xi_{\text{lim}} + \frac{1}{\delta} (e^{-\delta \xi_{\text{lim}}} - 1) \right) - (\tau_{y_{\text{max}}} - \tau_{\text{lim}}) \left(\xi_{\text{lim}} + \frac{1}{\delta_1} \right) \quad (\text{A 7.2.28})$$

Substituting the C into Eq. (A 7.2.27), gives the plastic strain energy function for the softening phase as

$$\psi_{\text{ps}} = (\tau_{y_{\text{max}}} - \tau_{\text{lim}}) \left(\xi - \xi_{\text{lim}} + \frac{1}{\delta_1} (e^{-\delta_1 (\xi - \xi_{\text{lim}})} - 1) \right) + (\tau_{y_{\infty}} - \tau_{y_0}) \left(\xi_{\text{lim}} + \frac{1}{\delta} (e^{-\delta \xi_{\text{lim}}} - 1) \right) \quad (\text{A 7.2.29})$$

Some other useful derivatives are

$$\partial_{\mathbf{q}} f = 1 \quad (\text{A 7.2.30})$$

$$\partial_{\mathbf{q}\mathbf{q}}^2 f = \frac{\partial(\partial_{\mathbf{q}} f)}{\partial \mathbf{q}} = 0 \quad (\text{A 7.2.31})$$

$$\partial_{\tau_{\infty,i}\mathbf{q}}^2 f = \frac{\partial}{\partial \tau_{\infty,i}} \left(\frac{\partial f}{\partial \mathbf{q}} \right) = 0 \quad (\text{A 7.2.32})$$

In the above only the plastic part of the strain energy function is discussed. In reality, the strain energy function consists of both an elastic and a plastic part

$$\psi(\varepsilon_{\infty,i}, \xi) = \psi_e(\varepsilon_{\infty,i}) + \psi_p(\xi) \quad (\text{A 7.2.33})$$

The elastic part consists of

$$\psi_e(\varepsilon_{\infty,i}) = \frac{\kappa}{2} \left(\sum_{i=1}^3 \varepsilon_{\infty,i} \right)^2 + \mu \left(\sum_{i=1}^3 \varepsilon_{\infty,i}^2 \right) \quad (\text{A 7.2.34})$$

where κ and λ are Lamé's constants.

So that

$$\partial_{\varepsilon_{\infty,i}} \psi = \kappa \sum_{i=1}^3 \varepsilon_{\infty,i} + 2\mu \varepsilon_{\infty,i} \quad (\text{A 7.2.35})$$

$$\partial_{\varepsilon_{\infty,i} \varepsilon_{\infty,j}}^2 \psi = \kappa + 2\mu \delta_{ij} \quad (\text{A 7.2.36})$$

$$\partial_{\varepsilon_{\infty,i} \xi}^2 \psi = \frac{\partial}{\partial \varepsilon_{\infty,i}} \left(\frac{\partial \psi}{\partial \xi} \right) = 0 \quad (\text{A 7.2.37})$$

The Drucker-Prager Response Surface

The Drucker-Prager response surface is defined by

$$f(\sigma_{\infty}, \mathbf{q}) = \sqrt{J_2} + \alpha I_1 = k_y \quad (\text{A 7.2.38})$$

With

$$I_1 = \sigma_{\infty,ii} \quad (\text{A 7.2.39})$$

$$J_2 = \frac{1}{2} s_{\infty,ij} s_{\infty,ij}$$

and

$$= \frac{1}{6} \left[(\sigma_{\infty,11} - \sigma_{\infty,22})^2 + (\sigma_{\infty,22} - \sigma_{\infty,33})^2 + (\sigma_{\infty,33} - \sigma_{\infty,11})^2 \right] \quad (\text{A 7.2.40})$$

$$+ \sigma_{\infty,12}^2 + \sigma_{\infty,23}^2 + \sigma_{\infty,31}^2$$

And in which α is a material constant which depends on the friction angle ϕ

$$\alpha = \frac{2 \sin \phi}{\sqrt{3}(3 - \sin \phi)} \quad (\text{A 7.2.41})$$

The value of k_y depends on q , k_{y_0} and k_{y_∞} and will be discussed in the following. The material constants k_{y_0} and k_{y_∞} depend on the friction angle ϕ and the cohesion values c_{y_0} and c_{y_∞} respectively

$$k_{y_0} = 6c_{y_0} \frac{\cos \phi}{\sqrt{3}(3 - \sin \phi)} \quad ; \quad k_{y_\infty} = 6c_{y_\infty} \frac{\cos \phi}{\sqrt{3}(3 - \sin \phi)} \quad (\text{A } 7.2.42)$$

To introduce k_y as the hardening and softening of the yield surface, one can either change the cohesion or the friction angle, Fig.A. 7.1.2(a) and (b) respectively. It was chosen to implement the cohesion hardening in CAPA-3D.

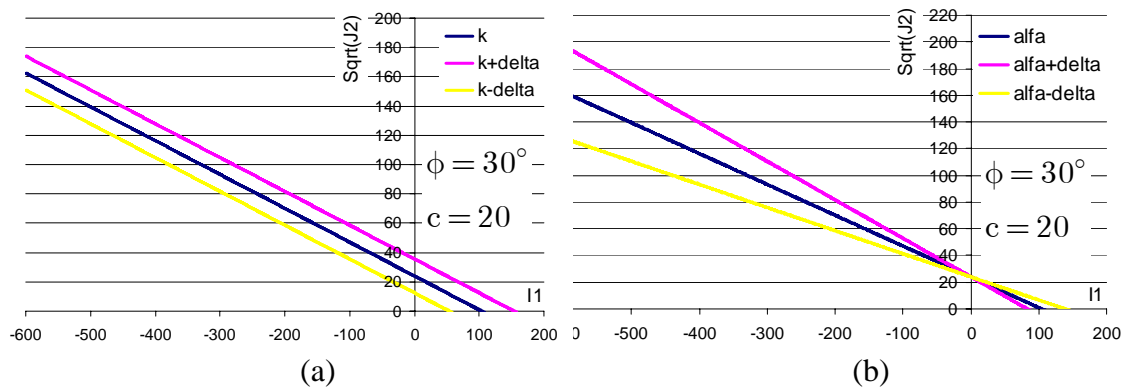


Fig.A. 7.1.2: Hardening/Softening of the Drucker-Prager yield surface
(a) k -hardening (b) α -hardening

In analogy with the Von Mises surface, a variable ξ is defined that controls the hardening/softening of the model and k_y determines the variable yield behavior. This time, the yield initiation is determined by k_{y_0} .

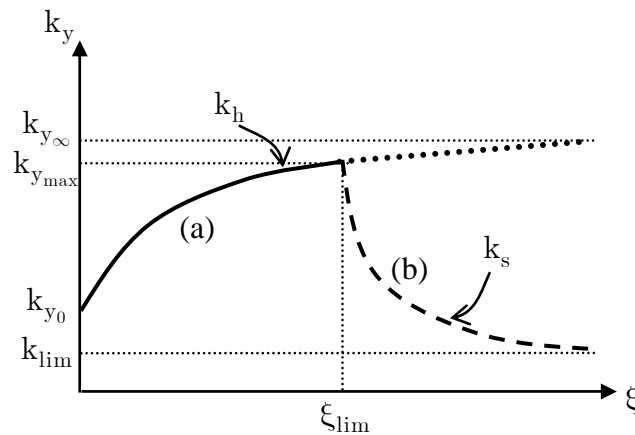


Fig.A. 7.1.3: Hardening/Softening response

When the material reaches a maximum yield stress $k_{y_{\max}}$, at $\xi = \xi_{\text{lim}}$, the material will soften. This can be expressed by a reduction of k_y , Fig.A. 7.1.3.

The maximum value of the yield surface can therefore be expressed as

$$k_y = \begin{cases} k_h & 0 \leq \xi \leq \xi_{lim} \\ k_s & \xi > \xi_{lim} \end{cases} \quad (A 7.2.43)$$

For the hardening part, k_h can be found as

$$k_h = k_{y_\infty} + (k_{y_0} - k_{y_\infty}) e^{-\delta \xi} \quad 0 \leq \xi \leq \xi_{lim} \quad (A 7.2.44)$$

where δ determines the rate of hardening. For $\delta = 0$ and/or $\xi = 0$ the function reduces to a perfect plasticity model, with $k_h = k_{y_0}$.

For the softening response, k_s can be expressed as

$$k_s = k_{lim} + (k_{y_{max}} - k_{lim}) e^{-\delta_1(\xi - \xi_{lim})} \quad \xi > \xi_{lim} \quad (A 7.2.45)$$

where δ_1 determines the rate of softening and τ_{lim} determines the maximum yielding response, or the lowest yield value.

The $k_{y_{max}}$ is determined from the value of k_h at $\xi = \xi_{lim}$

$$k_{y_{max}} = k_{y_\infty} + (k_{y_0} - k_{y_\infty}) e^{-\delta \xi_{lim}} \quad (A 7.2.46)$$

After substitution of Eq. (A 7.2.46) into Eq. (A 7.2.45) and slightly rearranging, the softening response is given by

$$k_s = k_{lim} \left(1 - e^{-\delta_1(\xi - \xi_{lim})} \right) + \left(k_{y_\infty} + (k_{y_0} - k_{y_\infty}) e^{-\delta \xi_{lim}} \right) e^{-\delta_1(\xi - \xi_{lim})} \quad \xi > \xi_{lim} \quad (A 7.2.47)$$

The hardening/softening response of the material is therefore covered by

$$k_y = \begin{cases} k_{y_\infty} + (k_{y_0} - k_{y_\infty}) e^{-\delta \xi} & \xi \leq \xi_{lim} \\ k_{lim} \left(1 - e^{-\delta_1(\xi - \xi_{lim})} \right) + \left(k_{y_\infty} + (k_{y_0} - k_{y_\infty}) e^{-\delta \xi_{lim}} \right) e^{-\delta_1(\xi - \xi_{lim})} & \xi > \xi_{lim} \end{cases} \quad (A 7.2.48)$$

Since the hardening response of the material is expressed by a uniform increase of the yield surface, and the softening as a uniform decrease of the yield surface, the yield limit can also be formulated as

$$k_y = \begin{cases} k_{y_0} - q_h & \xi \leq \xi_{lim} \\ k_{y_{max}} - q_s & \xi > \xi_{lim} \end{cases} \quad (A 7.2.49)$$

Since

$$\begin{aligned} q_h &= -\partial_\xi \Psi_{ph} \\ q_s &= \partial_\xi \Psi_{ps} \end{aligned} \quad (A 7.2.50)$$

Therefore

$$k_y = \begin{cases} k_{y_0} + \partial_\xi \Psi_{ph} & \xi \leq \xi_{lim} \\ k_{y_{max}} - \partial_\xi \Psi_{ps} & \xi > \xi_{lim} \end{cases} \quad (A 7.2.51)$$

where ψ_{ps} and ψ_{ph} are the plastic strain energy functions for the hardening and the softening phase, respectively. Therefore

$$\begin{aligned}\partial_{\xi}\Psi_{ph} &= k_h - k_{y_0} \\ -\partial_{\xi}\Psi_{ps} &= k_s - k_{y_{\max}}\end{aligned}\quad (\text{A 7.2.52})$$

By substituting Eq.(A 7.2.10) and Eq.(A 7.2.11) into Eq.(A 7.2.19)_{1,2}, respectively

$$\partial_{\xi}\Psi_{ph} = (k_{y_{\infty}} - k_{y_0})\left(1 - e^{-\delta\xi}\right) \quad (\text{A 7.2.53})$$

and

$$\partial_{\xi}\Psi_{ps} = (k_{y_{\max}} - k_{\text{lim}})\left(1 - e^{-\delta_1(\xi - \xi_{\text{lim}})}\right) \quad (\text{A 7.2.54})$$

From these, the strain energy function differentiated twice to ξ can be found as

$$\partial_{\xi\xi}^2\Psi_{ph} = \delta(k_{y_{\infty}} - k_{y_0})e^{-\delta\xi} \quad (\text{A 7.2.55})$$

and

$$\partial_{\xi\xi}^2\Psi_{ps} = \delta_1(k_{y_{\max}} - k_{\text{lim}})e^{-\delta_1(\xi - \xi_{\text{lim}})} \quad (\text{A 7.2.56})$$

By integrating Eq.(A 7.2.20) over ξ , the plastic strain energy function for the hardening phase is found as

$$\Psi_{ph} = (k_{y_{\infty}} - k_{y_0})\left(\xi + \frac{1}{\delta}e^{-\delta\xi}\right) + C \quad (\text{A 7.2.57})$$

Since for $\xi = 0$; $\Psi_{ph} = 0$, the integration constant C can be found as

$$C = \frac{1}{\delta}(k_{y_0} - k_{y_{\infty}}) \quad (\text{A 7.2.58})$$

Substituting the C into Eq. (A 7.2.24), gives the plastic strain energy function for the hardening phase

$$\Psi_{ph} = (k_{y_{\infty}} - k_{y_0})\left(\xi + \frac{1}{\delta}(e^{-\delta\xi} - 1)\right) \quad (\text{A 7.2.59})$$

Similarly, the plastic strain energy function for the softening phase can be found from Eq. (A 7.2.21) as

$$\Psi_{ps} = (k_{y_{\max}} - k_{\text{lim}})\left(\xi + \frac{1}{\delta_1}e^{-\delta_1(\xi - \xi_{\text{lim}})}\right) + C \quad (\text{A 7.2.60})$$

Since for $\xi = \xi_{\text{lim}}$; $\Psi_{ps} = \Psi_{ph}$, the integration constant C can be found as

$$C = (k_{y_{\infty}} - k_{y_0})\left(\xi_{\text{lim}} + \frac{1}{\delta}(e^{-\delta\xi_{\text{lim}}} - 1)\right) - (k_{y_{\max}} - k_{\text{lim}})\left(\xi_{\text{lim}} + \frac{1}{\delta_1}\right) \quad (\text{A 7.2.61})$$

Substituting the C into Eq. (A 7.2.27), gives the plastic strain energy function for the softening phase as

$$\begin{aligned} \psi_{ps} = & (k_{y_{\max}} - k_{\text{lim}}) \left(\xi - \xi_{\text{lim}} + \frac{1}{\delta_1} \left(e^{-\delta_1(\xi - \xi_{\text{lim}})} - 1 \right) \right) \\ & + (k_{y_{\infty}} - k_{y_0}) \left(\xi_{\text{lim}} + \frac{1}{\delta} \left(e^{-\delta \xi_{\text{lim}}} - 1 \right) \right) \end{aligned} \quad (\text{A 7.2.62})$$

Some other useful derivatives are

$$\partial_q f = 1 \quad (\text{A 7.2.63})$$

$$\partial_{qq}^2 f = \frac{\partial(\partial_q f)}{\partial q} = 0 \quad (\text{A 7.2.64})$$

$$\partial_{\tau_{\infty,i} q}^2 f = \frac{\partial}{\partial \tau_{\infty,i}} \left(\frac{\partial f}{\partial q} \right) = 0 \quad (\text{A 7.2.65})$$

In the above only the plastic part of the strain energy function is discussed. In reality, the strain energy function consists of both an elastic and a plastic part

$$\psi(\boldsymbol{\varepsilon}_{\infty,i}, \xi) = \psi_e(\boldsymbol{\varepsilon}_{\infty,i}) + \psi_p(\xi) \quad (\text{A 7.2.66})$$

The elastic part consists of

$$\psi_e(\boldsymbol{\varepsilon}_{\infty,i}) = \frac{\kappa}{2} \left(\sum_{i=1}^3 \varepsilon_{\infty,i} \right)^2 + \mu \left(\sum_{i=1}^3 \varepsilon_{\infty,i}^2 \right) \quad (\text{A 7.2.67})$$

where κ and λ are Lamé's constants.

$$\text{So that} \quad \partial_{\varepsilon_{\infty,i}} \psi = \kappa \sum_{i=1}^3 \varepsilon_{\infty,i} + 2\mu \varepsilon_{\infty,i} \quad (\text{A 7.2.68})$$

$$\partial_{\varepsilon_{\infty,i} \varepsilon_{\infty,j}}^2 \psi = \kappa + 2\mu \delta_{ij} \quad (\text{A 7.2.69})$$

$$\partial_{\varepsilon_{\infty,i} \xi}^2 \psi = \frac{\partial}{\partial \varepsilon_{\infty,i}} \left(\frac{\partial \psi}{\partial \xi} \right) = 0 \quad (\text{A 7.2.70})$$

For computational efficiency, the above derivations are slightly rewritten as follows.

The hardening/softening function can be generalized into

$$k_y = k_{y_0} - q = k_{y_0} + \frac{\partial \psi}{\partial \xi} \quad (\text{A 7.2.71})$$

Furthermore, it can be found that

$$\frac{\partial \psi_h}{\partial \xi} = (k_{y_{\infty}} - k_{y_0}) (1 - e^{-\delta \xi}) \quad (\text{A 7.2.72})$$

and

$$\frac{\partial \psi_s}{\partial \xi} = (k_{y_{\max}} - k_{\lim}) e^{-\delta_1(\xi - \xi_{\lim})} - k_{y_0} + k_{\lim} \quad (\text{A 7.2.73})$$

With

$$k_{y_{\max}} = k_{y_0} + \left. \frac{\partial \psi_h}{\partial \xi} \right|_{\xi = \xi_{\lim}} \quad (\text{A 7.2.74})$$

To show that these formulations are equal to the earlier derived formulations Eq. (A 7.2.72) and Eq. (A 7.2.73) are substituted into Eq. (A 7.2.71) respectively.

Which gives

$$\begin{aligned} k_{y_{\max}} &= k_{y_0} + (k_{y_\infty} - k_{y_0}) (1 - e^{-\delta \xi_{\lim}}) \\ &= k_{y_\infty} + (k_{y_0} - k_{y_\infty}) e^{-\delta \xi_{\lim}} \end{aligned} \quad (\text{A 7.2.75})$$

Which is equal to Eq. (A 7.2.46)

$$\begin{aligned} k_h &= k_{y_0} + \frac{\partial \psi_h}{\partial \xi} \\ &= k_{y_0} + (k_{y_\infty} - k_{y_0}) (1 - e^{-\delta \xi}) \\ &= k_{y_\infty} + (k_{y_0} - k_{y_\infty}) e^{-\delta \xi} \end{aligned} \quad (\text{A 7.2.76})$$

Which is equal to Eq. (A 7.2.44)

$$\begin{aligned} k_s &= k_{y_0} + \frac{\partial \psi_s}{\partial \xi} \\ &= (k_{y_{\max}} - k_{\lim}) e^{-\delta_1(\xi - \xi_{\lim})} + k_{\lim} \end{aligned} \quad (\text{A 7.2.77})$$

Which is equal to Eq. (A 7.2.45)

Effect of moisture on the aggregate-mastic bond

8.1 Introduction

As was discussed in previous chapters, the aggregate-mastic bond is of crucial importance for the asphaltic mix response and its moisture induced damage susceptibility. However, in reality, very little is known about what constitutes the bond between the mastic and the aggregate and what effect moisture may have on it. For this reason, in this research, a new methodology was developed, which allows for the determination of the aggregate-mastic bond strength degradation as a function of the amount of moisture present in the interface. This is a relationship which can be directly implemented within the interface material model. In chapter 9 a detailed discussion is given of the coupling between physical and mechanical moisture induced damage.

In the following, the developed methodology for determination of aggregate-mastic bond strength as a function of moisture is discussed.

8.2 Methodology

To determine the bond strength between a mastic and an aggregate type, a thin film of mastic is adhered to a block of aggregate. To prepare the sample, a small amount of heated mastic is deposited on the flat surface of a loading fixture, Fig. 8.2.1(a)-(b), and is pressed perpendicularly on the surface of the prepared aggregate sample, Fig. 8.2.1(c), thus creating a thin film of mastic adhered to the aggregate surface.

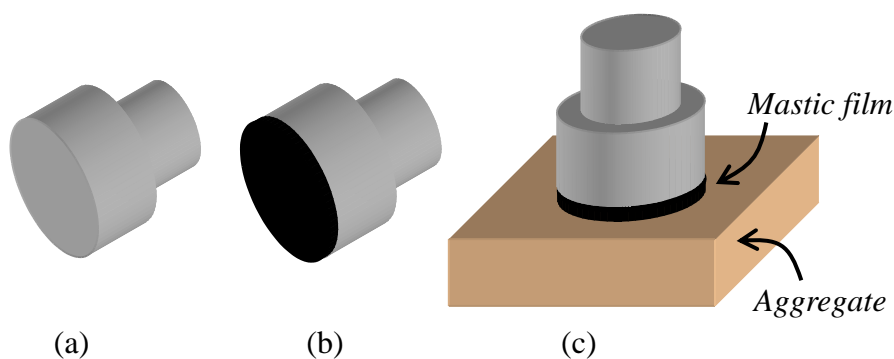


Fig. 8.2.1: (a) Steel stub (b) Steel stub coated with a mastic film
(c) aggregate-mastic bond test set-up

After a relevant time of ‘curing’ of the sample, a mastic-aggregate interface is created, which is comparable to an interface within an asphaltic mix. The film thickness is pre-determined and carefully monitored.

After preparing the aggregate-mastic samples, first the bond strength of a few dry specimens is measured with a direct tension test. The experiment aims at measuring the aggregate-mastic bond strength, and therefore relies on an adhesive failure of the specimen, Fig. 8.2.2(a). Specimens which fail within the mastic itself, Fig. 8.2.2(b) are therefore disregarded and not used in subsequent analyses.

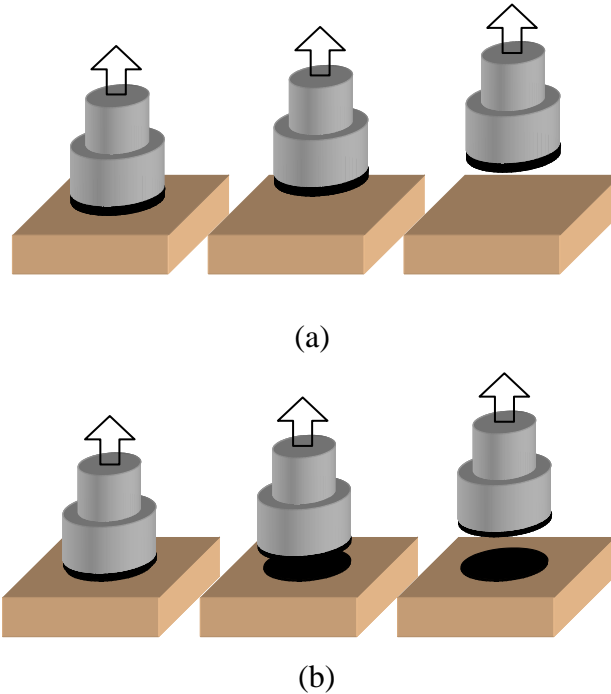


Fig. 8.2.2: (a) Adhesive bond failure (b) Cohesive bond failure

The remaining samples are conditioned in a moisture bath. For the moisture conditioning it is important to keep the water level below the aggregate-mastic interface, as to avoid moisture infiltration from the sides of the interface or through the mastic film itself. At pre-determined intervals, samples are removed from their moisture conditioning and the bond strength is directly measured via a direct tension test. By performing a series of such tests, a relationship between the aggregate-mastic bond strength and the moisture conditioning time is found, Fig. 8.2.3.

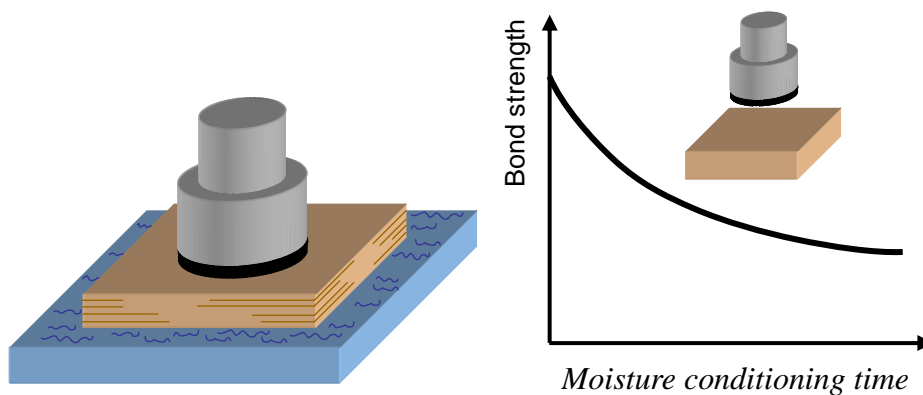


Fig. 8.2.3: Reduction of bond strength as a function of moisture conditioning duration

Obviously, this relationship is highly dependent on the geometry of the test-specimen and does not answer the question of the amount of moisture that is present in the interface at failure time. Therefore, moisture infiltration simulations are performed with RoAM for the test samples, using similar geometries and moisture boundary conditions.

Because the experiments give the degradation of bond strength versus moisture conditioning time, Fig. 8.2.4(a), and the simulations with RoAM give the moisture content in the interface region over time, Fig. 8.2.4(b), the combination of the two curves gives the wanted relation, i.e. the bond strength degradation as a function of moisture content in the interface, Fig. 8.2.4(c).

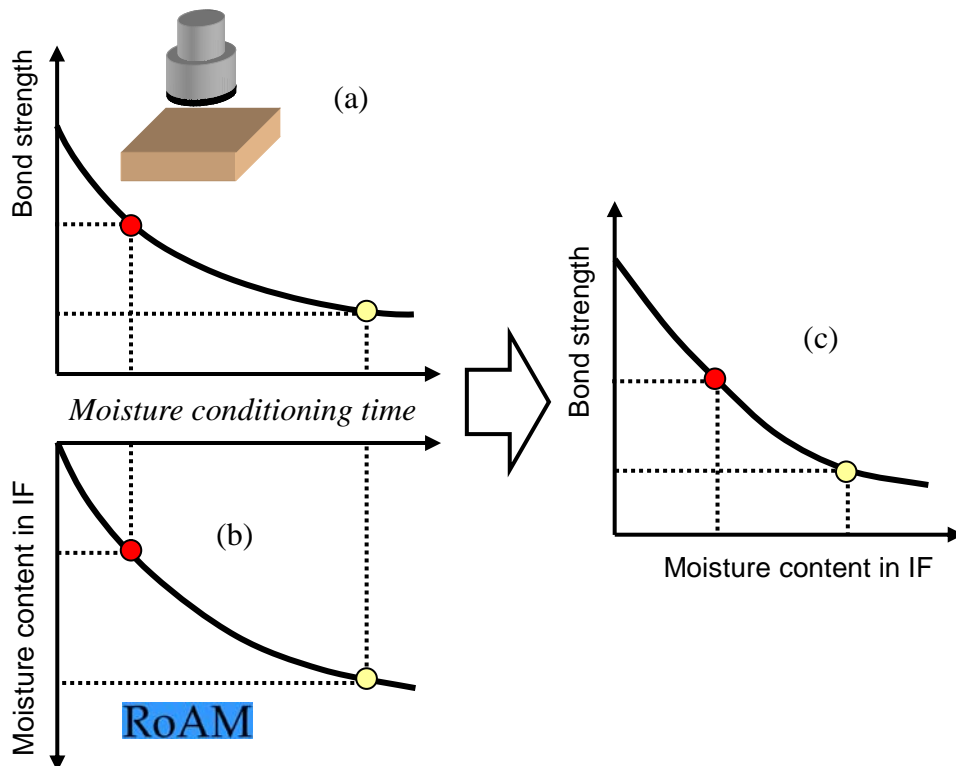


Fig. 8.2.4: Methodology overview

(a) Experimental results (b) RoAM simulations

(c) Bond strength as a function of moisture content

The test were performed at the Turner Fairbanks Research Centre of the US Federal Highway Administration.

In the following a demonstration of the results is given.

8.3 Experimental results

8.3.1 Sample preparation

Strategic Highway Research Program (SHRP) core asphalt AAD (PG58-28) was used to make the mastic. Diabase material, passing the #200 sieve (75 μm), was used as mineral filler to combine with the asphalt binder to make the mastic. Filler in the amount of 30% by volume was chosen, based on the fact that the fine aggregate passing the #200 sieve is approximately 27-28% volume of the binder in most fully graded aggregate systems. The mastic is prepared by heating measured quantities of binder and filler to 165° C for approximately two hours. The binder was removed from the oven and stirred for one minute at 600 rpm with a mechanical stirrer. The filler is added and the mixture is stirred at 600 rpm for an additional two minutes. The mastic is stored at ambient conditions, approximately 22° C, until the samples are made.

Diabase stone was used as the substrates in the pull-off test. Cobble-sized samples of diabase rock were obtained from a quarry in Sterling, VA. The rocks were cut into plates using a 33 cm diamond-tip, water-cooled saw. The geometry of the rock plates vary due to the varying sizes of rocks obtained from the quarry, the cutting process and meeting the requirements of pull-off test specifications for substrate size. However, the geometry of each stone plate was approximately square or rectangular in shape and its geometry was measured. The rock plates were polished using a 600-grit resin bonded diamond grinding disc. All reusable stone plates were oxidized to a temperature of 482° C. The oxidized plates were rinsed with distilled water, allowed to dry overnight, and then stored in an oven at 60° C until they were used to make the samples.

A sample of approximately 5.0 g mastic was mixed with one percent (by weight) glass beads. The beads ensured a uniform film thickness of 200 μm is attained. Youtcheff and Aurilio [1997] and Nguyen et al [1996] found that this method for controlling film thickness is convenient and reduces the time to prepare the test specimens. The mastic, was heated to approximately 100° C and applied to the loading fixture. The test operator pressed the loading fixture automatically onto the aggregate substrate. The specimens were allowed to cure at 20 ± 1 ° C for at least twenty-four hours.

After twenty-four hours of equilibration, dry specimens were tested. The other specimens were immersed in a water bath of distilled water at 24 ± 1 ° C. The specimens were withdrawn from the water bath after fourteen, twenty-four, and thirty-seven hours and immediately tested. The water height of the water bath was kept below the mastic-aggregate interface to ensure moisture diffusion through the aggregate substrate to the mastic-aggregate interface. Two different water depths (8 and 16 mm) were chosen based on specimen's thicknesses.

8.3.2 Direct tension test results

Using a direct tension device, which is pneumatically controlled, the burst pressure necessary to debond the specimen (unconditioned or conditioned) at a temperature of 21 ± 1 ° C was measured.

Table 1 shows the measured tensile bond strength results of the specimens exposed to moisture including their soak times, the height of the water bath measured from the bottom, and specimen geometries.

Table 1: Bond strength measurements & their conditioning

Spec ID	Moisture Conditioning		Specimen Geometry		Strength [MPa]
	Soak Time [hrs]	Water Height [mm]	Surface [mm x mm]	Thickness [mm]	
A14	14	8	48.06 x 46.92	16.84	0.767
B14	14	8	55.89 x 53.44	13.39	1.01
C14	14	8	52.29 x 43.07	14.10	1.01
A24	24	16	45.10 x 38.27	23.19	1.12
B24	24	16	63.17 x 56.15	18.92	1.15
C24	24	16	55.33 x 45.63	26.75	1.22
A37	37	8	47.27 x 46.66	15.68	0.56
B37	37	8	51.79 x 46.47	16.79	0.59
C37	37	8	47.54 x 50.17	16.93	0.767

The average tensile bond strength of four specimens, tested at dry conditions, was 1.3 MPa. Almost all tested specimens experienced a clear adhesive failure; i.e. they left very little or no mastic on the stone substrate and the surface of the mastic layer on the ceramic stub was observed to be smooth (i.e. no cavitations). Only specimens A24 and B24 showed a slight mixed failure mode, by leaving behind a small amount of mastic (5-10%) on the rock substrate in the center of the test area.

8.3.3 RoAM moisture simulation results

For the RoAM moisture infiltration simulations, it was assumed that moisture infiltrates into the aggregate via diffusion. For the moisture diffusion analyses a molecular diffusivity of $0.6 \text{ mm}^2/\text{hr}$ was used for the diabase aggregate [Bradbury 1982]. Since all specimens had different geometries and water tables (as shown in Table 1), a new finite element mesh was made for each specimen that simulates the specific geometry and moisture conditions given for that specimen. Fig. 8.3.1 shows the geometry and the moisture diffusion for specimen A37 at 0 and 37 hours.

Fig. 8.3.2 shows an analysis of the moisture profiles, over time, on the surface of the middle cross-section of specimen A37. From the profiles, it can be seen that the region of the stone to which the mastic film is adhered, is exposed to a fairly uniform moisture front. Simulations of the moisture diffusion into the specimens can be seen in Fig. 8.3.3, where the moisture content depicted in the graphs is measured at the center of the top surface of the diabase specimen.

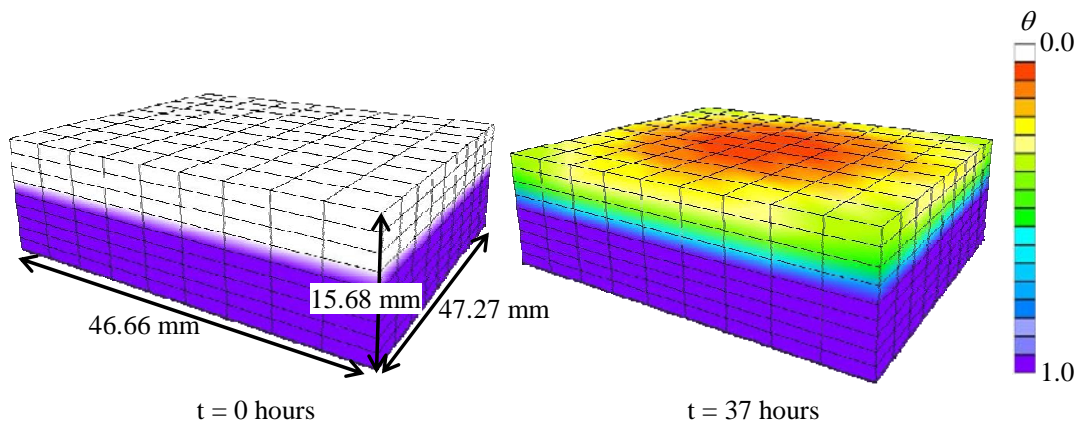


Fig. 8.3.1:: Moisture diffusion simulation in specimen A37.

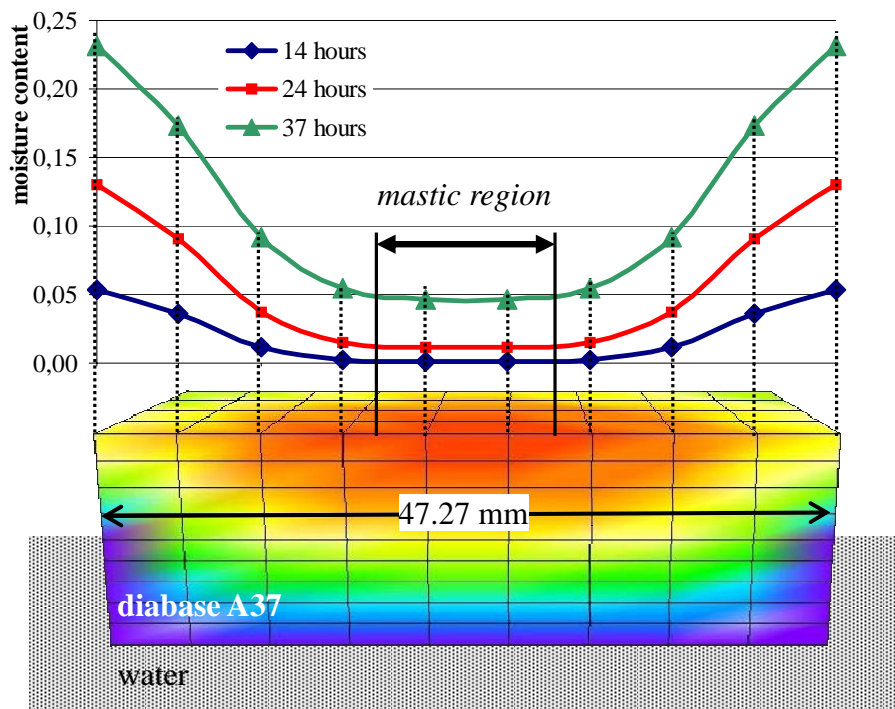


Fig. 8.3.2: Moisture content profiles for specimen A37 at substrate surface cross-section.

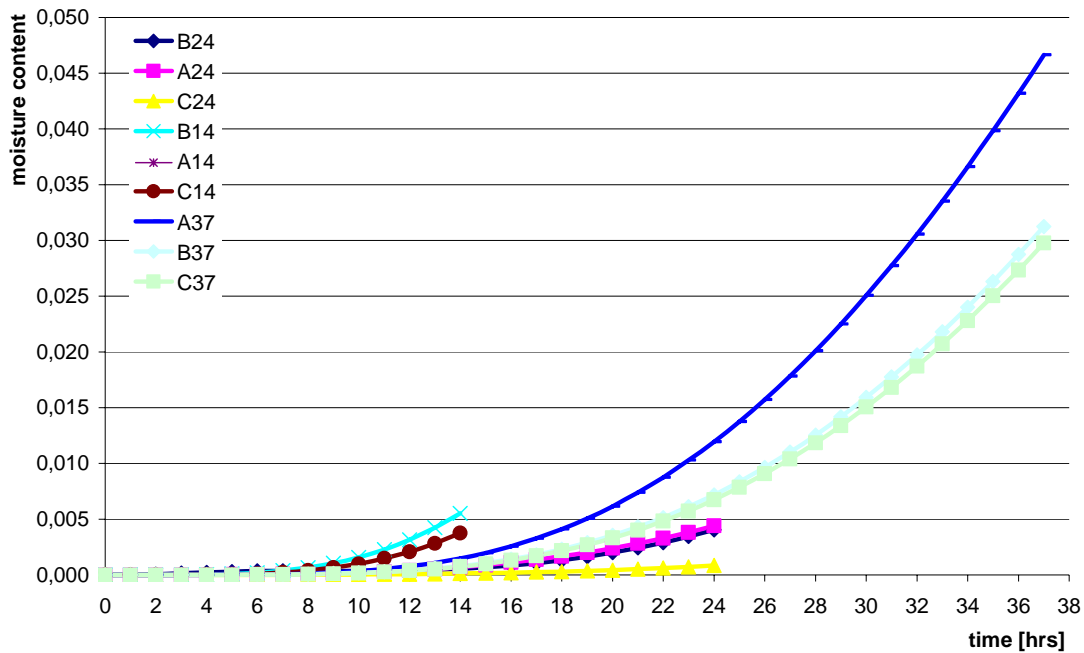


Fig. 8.3.3: Moisture diffusion simulations for the test specimen.

8.3.4 Mastic-aggregate bond strength degradation

As explained in Fig. 8.2.4, the procedure for determination of the aggregate-mastic bond strength and moisture content is based on a combination of experimental results and finite element simulations. This methodology is applied to all specimens and the results are plotted in Fig. 8.3.4. As can be seen, the overall result seems to confirm the hypothesis that moisture at the interface reduces the bond strength. The results of specimen A14 were excluded due to an unexpectedly low tensile strength value that is believed to be a result of specimen preparation.

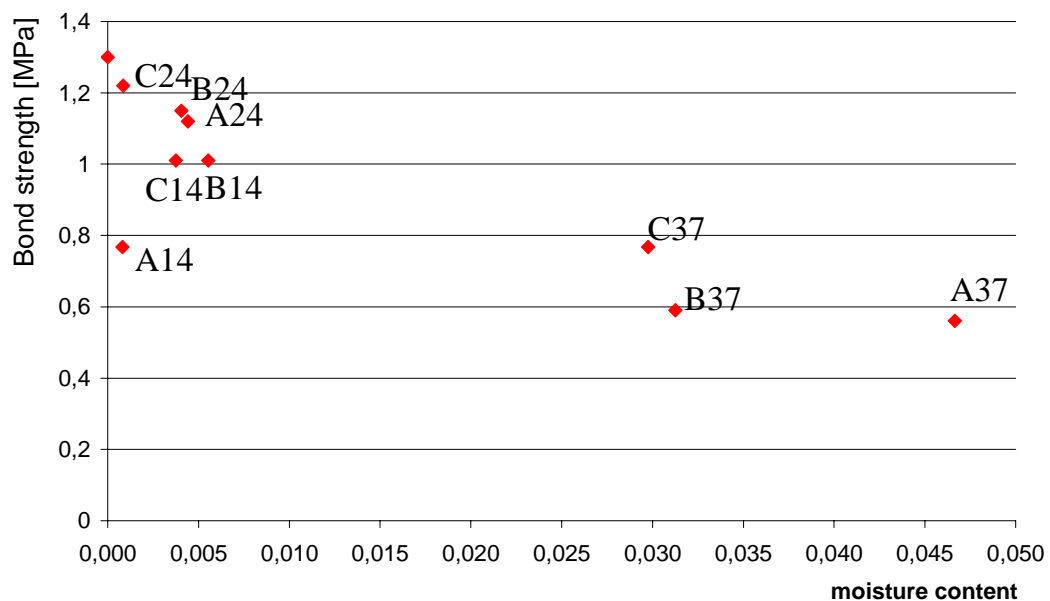


Fig. 8.3.4: Measured bond strength versus computed moisture content for all specimens

As shown in Fig. 8.3.5, on the basis of regression analysis the relationship between the aggregate-mastic bond strength and moisture content was determined as

$$S_{if} = e^{(0.30 - 3.76 \sqrt{\theta})} \quad (8.1)$$

This can be rewritten to indicate the percentage of bond strength, as a function of moisture content in the interface, Fig. 8.3.6, as

$$\%S_{if} = 100 e^{-3.76 \sqrt{\theta}} \quad (8.2)$$

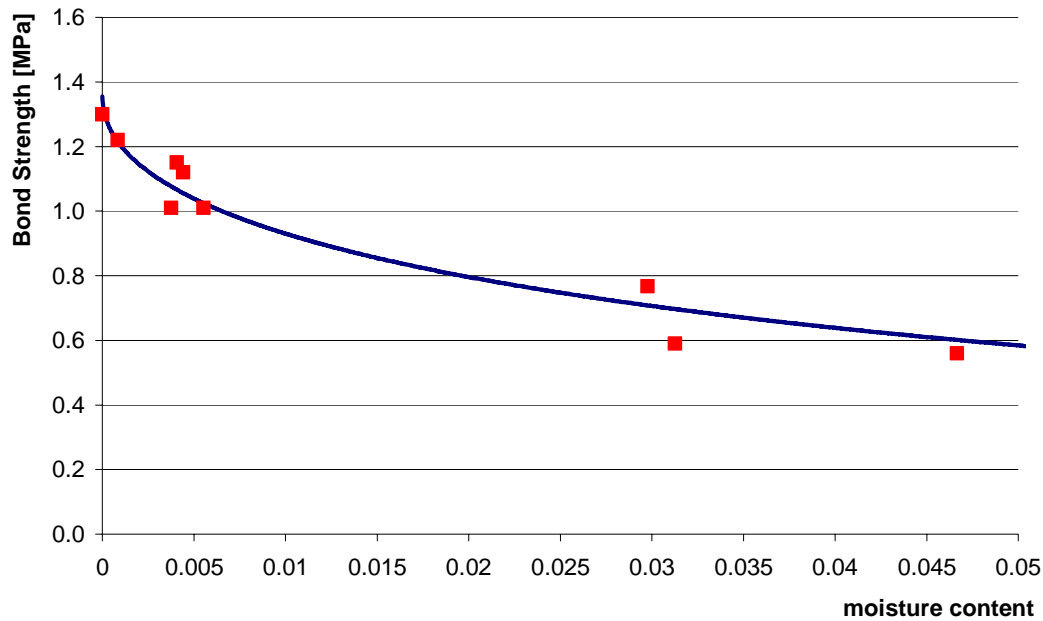


Fig. 8.3.5: Relationship between interface strength and moisture content

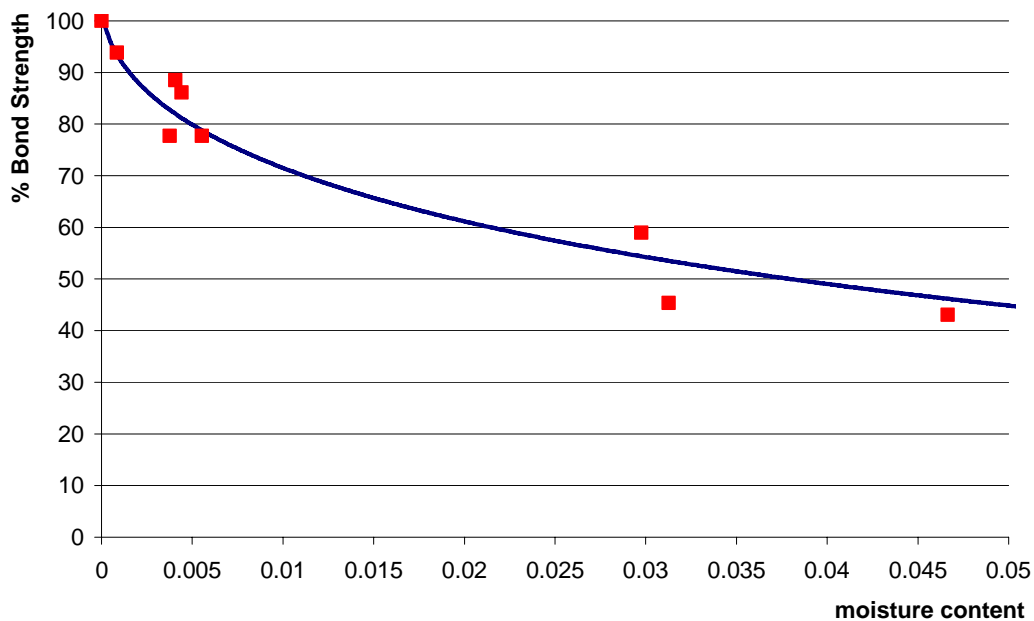


Fig. 8.3.6: Relationship between reduction of strength and moisture content

On the basis of Eq.(8.1) and Eq.(8.2) the evolution of moisture damage as a function of moisture content, Fig. 8.3.7, can be determined as

$$\xi_m(\theta) = 1 - e^{-3.76\sqrt{\theta}} \quad (8.3)$$

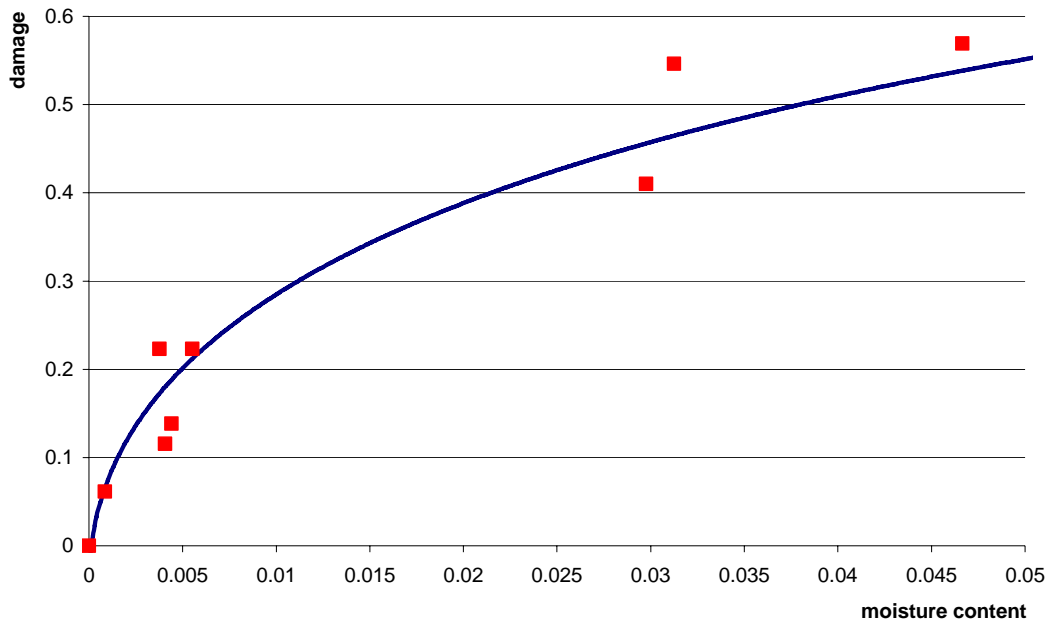


Fig. 8.3.7: Relationship between interface bond damage and moisture content

8.4 Conclusions

In the above, a new methodology is presented to determine the mastic-aggregate bond strength as a function of moisture content at the interface. Direct tension tests were shown and utilized to determine the moisture induced damage in the bond. The damage relationship that was determined, and is shown in Eq. (8.3), shall be utilized in the next chapter.

Physical-Mechanical Moisture Induced Damage Model

9.1 Introduction

The aim of this research is the development of a computational tool for the fundamental analysis of moisture induced damage of asphaltic mixes which includes both physical and mechanical moisture damage inducing processes. To achieve this aim, in the previous chapters of this dissertation the physical and mechanical moisture induced damage processes are identified, the controlling parameters are discussed, the finite element based simulation tools are developed and an experimental framework to quantify most of these parameters is set-up.

In this chapter, the physical and the mechanical moisture induced damage processes are brought together in the final combined physical and mechanical moisture induced damage model, Fig. 9.1.1. To do so, the physical moisture induced damage parameters are identified which alter the mechanical material properties, the adjustments to the constitutive formulations of the asphalt components, as shown in chapter 6, are given and the coupling procedure between RoAM and CAPA-3D is discussed. Finally, via several computational simulations with the developed tool using a micro-scale finite element mesh, it is shown how changing the moisture susceptibility properties of the asphalt components will lead to different failure patterns of the mix.

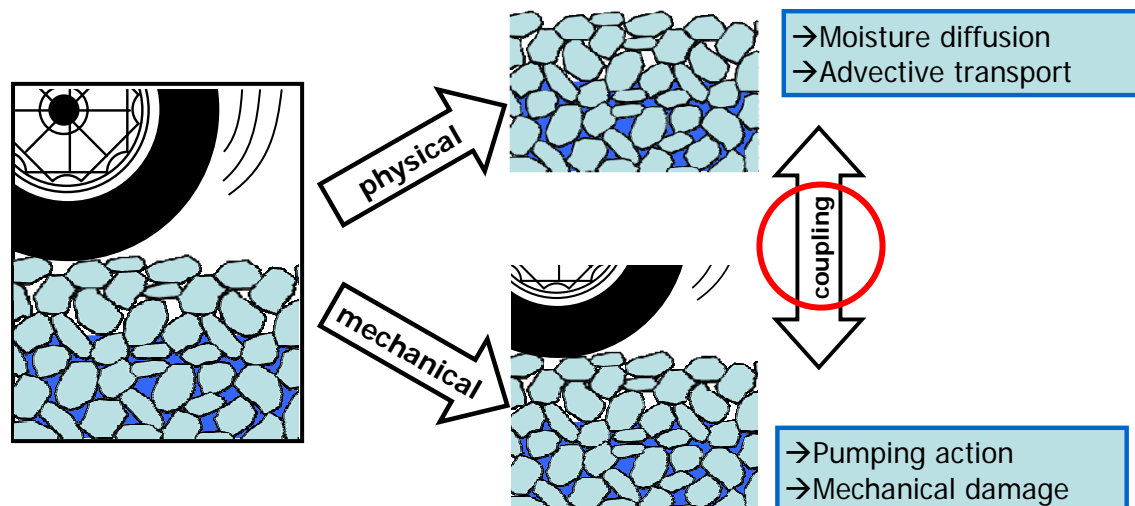


Fig. 9.1.1: Schematic of the new approach towards moisture induced damage

9.2 Physical moisture induced damage parameters

Moisture infiltration weakens the cohesive properties of the mastic and the adhesive properties of the aggregate-mastic bond. To model the damage on the material properties, caused by the moisture infiltration, damage parameters are defined which can go from 0 (no damage) to 1 (complete damage), following the Kachanov formulation.

The first physical moisture induced damage parameter is related to moisture diffusion into the asphalt components

$$d_{\theta} = f(\theta) \quad (9.1)$$

where θ is the moisture content, defined as the fraction of moisture concentration $C_{\theta}(x, t)$ w.r.t. the maximum moisture concentration C_{θ}^{\max} that a material can absorb, i.e.

$$\theta(x, t) = \frac{C_{\theta}(x, t)}{C_{\theta}^{\max}} ; \quad 0.0 \leq \theta \leq 1.0 \quad (9.2)$$

The function $f(\theta)$ needs to be determined experimentally, and has to satisfy

$$\begin{aligned} f(0) &= 0.0 \\ 0.0 &\leq f(1) \leq 1.0 \end{aligned} \quad (9.3)$$

This function should be determined for all the asphalt components, i.e. the mastic, the aggregate and the aggregate-mastic interface.

The second physical moisture induced damage parameter is postulated for only the mastic, which is based on the erosion of the mastic due to a water pressures. To keep the Kachanov damage parameter range (going from 0 for no damage to 1 for complete damage) the second physical moisture induced damage parameter has a slightly different form than the previous, namely

$$d_{\hat{\rho}} = 1 - f(\hat{\rho}) \quad (9.4)$$

Where $\hat{\rho}$ is the normalized value of the mastic density

$$\hat{\rho}(x, t) = \frac{\rho(x, t)}{\rho_0} ; \quad 0.0 \leq \hat{\rho} \leq 1.0 \quad (9.5)$$

In this, ρ_0 is the undamaged, reference, mastic density and $\rho(x, t)$ is the current, updated, mastic density. The mastic erosion function $f(\hat{\rho})$ can be determined experimentally and has to satisfy

$$\begin{aligned} f(1) &= 1.0 \\ f(0) &= 0.0 \end{aligned} \quad (9.6)$$

As an example, a type of mastic which is highly susceptible to moisture damage, would have moisture damage parameters which are more like the red curves in Fig.

9.2.1 and a less moisture damage susceptible mastic would have moisture damage parameters which develop more like the blue curves in Fig. 9.2.1.

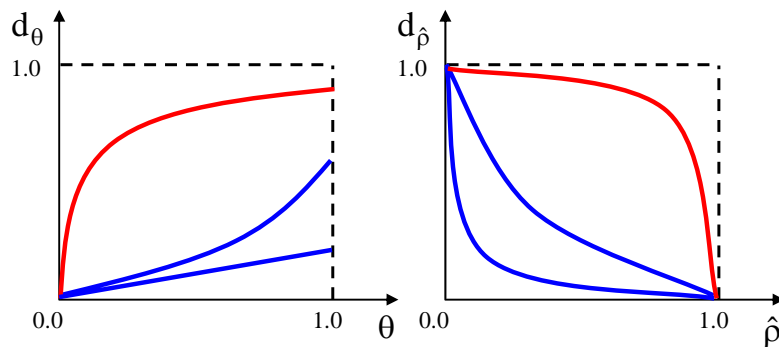


Fig. 9.2.1: Schematic of possible moisture damage parameter relations

Nevertheless, a mastic which has moisture damage parameters such as the red curves, may in practice still behave very well as long as the time scale in which the moisture damage parameters become considerable, is relatively long enough. In such a case, it is very likely that the asphaltic mix has failed under another type of damage long before moisture induced damage ever became an issue.

It is therefore very important in moisture damage susceptibility studies, either purely experimentally orientated ones or computationally based ones, to indeed take into account the time issue, otherwise a perfectly well behaving mix may be disregarded for the wrong reasons, and visa versa.

9.3 Mechanical moisture induced damage

As discussed in chapter 2, a combination of a (partially) saturated asphaltic mix, exposed to traffic loading, can cause a ‘pumping action’ effect inside of the asphaltic mix, Fig. 9.3.1. The excess pore pressures contribute to extra stresses within the asphaltic mix, which may cause added permanent deformation within the asphalt components. In addition to this (mechanical) damage, pumping action may contribute to the physical moisture induced damage, since the increased water pressure in the macro-pores, Fig. 9.3.1(b), may result locally into fast flow fields, Fig. 9.3.1(c), which increases the advective transport damage.

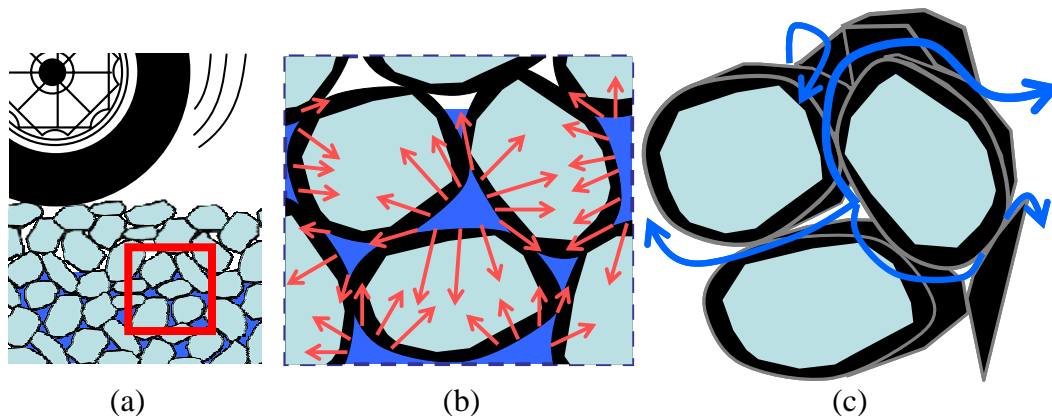


Fig. 9.3.1: Pumping action on a pavement causing fast flow field
 (a) traffic loading (b) excess pore pressures (c) fast water flow

The formulations of the mechanical damage which is generated in the mix by imposing (traffic) loading, is discussed in the constitutive model description in chapter 7 in the form of the equivalent plastic deformation parameter ξ . The locally high water pressures due to the pumping action, however, follow directly from the coupling between CAPA-3D and RoAM. The macro-pores in the asphaltic mix are simulated in CAPA-3D by using a porous-media formulation [Liu, 2003]. By applying traffic loading on the asphaltic mix, the coated aggregates shall slightly rearrange themselves, causing a reduction in the volume of the macro-pores. For the macro-pores which are saturated with water, this action shall locally generate high water pressures. These water pressures are communicated to RoAM, which simulates, based on these pressures, the flow field and the subsequent damage to the mastic film.

In the following the coupling between RoAM and CAPA-3D is discussed in detail.

9.4 Coupling of RoAM with CAPA-3D

For the coupling between RoAM and CAPA-3D, a staggered algorithm is utilized, mainly because of the differences in time scales. For instance, the passing of a wheel load over a pavement happens in such a short time, that it is justified to pose that during this time, no moisture diffusion shall take place.

Therefore, RoAM simulates the processes contributing to the physical moisture induced damage (i.e. moisture flow, moisture diffusion and loss of mastic concentration), and based on the physical changes of the components, RoAM communicates the updated material characteristics to CAPA-3D, which then performs the damage simulations for that time step. After which, the deformed mesh and the traffic induced water pressures (i.e. the pumping action) are communicated back to RoAM, who updates the parameters and communicates them back to CAPA-3D, which then performs the next time step. This procedure continues until the end of the simulation time. This process is schematically shown in Fig. 9.4.1.

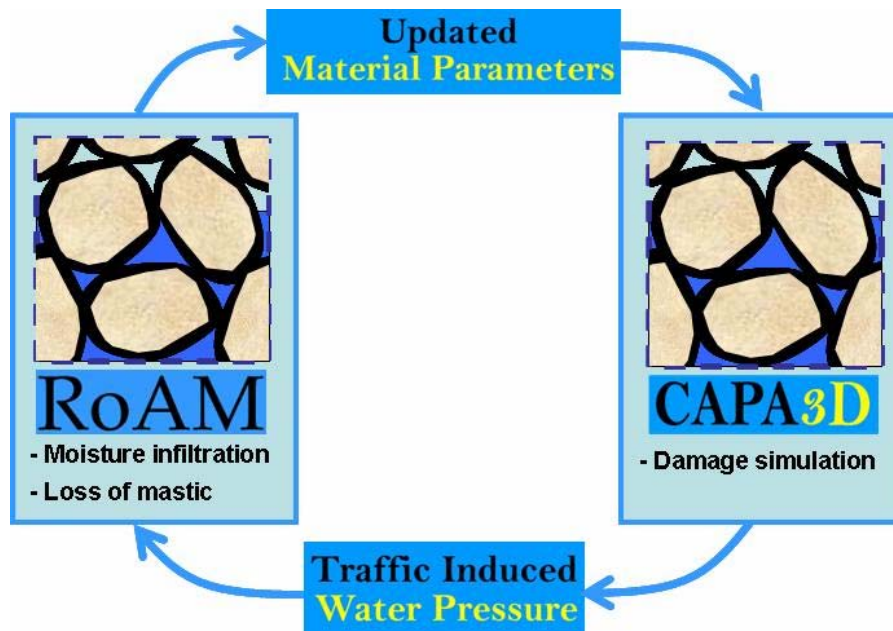


Fig. 9.4.1: Combined Physical-Mechanical Moisture Induced Damage of Asphaltic Mixes Finite Element System

Suppose that for a time t an asphalt mix is not exposed to traffic loading but it is exposed to moisture, after which the traffic loading continues. In the proposed coupling scheme, it is possible to perform simulation with RoAM for a time t , and start communicating the updated material characteristics for the time steps in which traffic loading is again applied. The staggered algorithm therefore allows for a time-efficient computation of the combined physical-mechanical moisture induced damage.

In the following section, the constitutive formulation for the asphalt components, based on the formulations in chapter 7 and the damage parameters postulated in 9.2, is derived.

9.5 Combined physical and mechanical moisture induced damage constitutive model

9.5.1 Introduction

In this section, the constitutive model, as derived in chapter 7 is adjusted to incorporate the moisture induced damage parameters d_θ and $d_\hat{p}$ which were defined earlier.

When the material property X is reduced from its original, undamaged, value X_0 due to moisture diffusion, the updated, or damaged, value X_d^θ can be determined as a function of its undamaged value and the damage parameters

$$X_d^\theta = f(X_0, d_\theta, \alpha) \quad (9.7)$$

Assuming that for zero damage (i.e. $d_\theta = 0.0$) the original property is maintained and for total damage (i.e. $d_\theta = 1.0$) the original property is reduced to zero, the function $f(X_0, d_\theta)$ may be postulated as

$$f(X_0, d_\theta, \alpha) = (1 - d_\theta)^\alpha X_0 \quad (9.8)$$

where α determines the nonlinearity of this relation, Fig. 9.5.1.

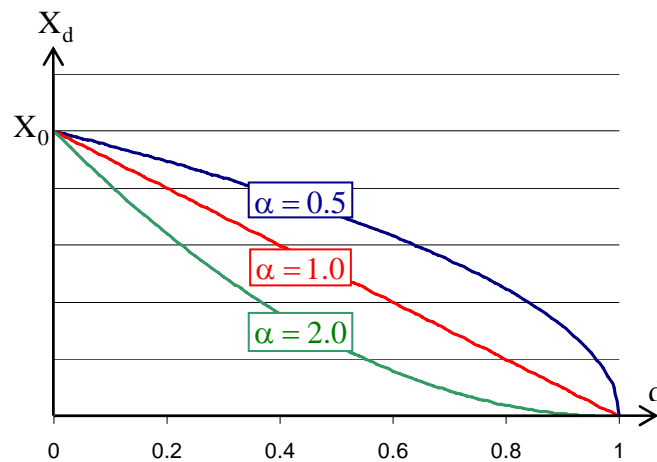


Fig. 9.5.1: Influence of damage parameter d on material property X

In the following formulations, it is assumed for simplicity that $\alpha = 1.0$.

If the property X_0 is additionally reduced due to an erosion action, similar to the above, the updated property could be found from

$$X_d = (1 - d_\hat{p}) X_d^\theta \quad (9.9)$$

Substituting Eq. (9.7) and Eq. (9.8) into Eq. (9.9) gives the total updated property

$$X_d = (1 - d_\theta)(1 - d_\hat{p}) X_0 \quad (9.10)$$

In this, the damage induced by moisture infiltration into the system is expressed by the term $(1-d_\theta)(1-d_{\hat{\rho}})$ or, writing this expression explicitly, $(1-d_\theta-d_{\hat{\rho}}+d_{\hat{\rho}}d_\theta)$.

In order to simplify the following equations, whereby maintaining the damage scale as defined earlier, the two damage processes can be represented by one damage parameter d_m

$$d_m = d_\theta + d_{\hat{\rho}} - d_\theta d_{\hat{\rho}} \quad (9.11)$$

where the last term on the r.h.s. shows the coupling between the two damage processes.

Utilizing Eq. (9.11), allows for the expression

$$(1-d_m) = (1-d_\theta)(1-d_{\hat{\rho}}) \quad ; \quad 0 \leq d_m \leq 1 \quad (9.12)$$

In Table 9.5.1 a few examples are given of the moisture damage parameters.

Table 9.5.1: Example moisture damage parameters

d_θ	$d_{\hat{\rho}}$	d_m	Moisture damage %
0.2	0.5	0.6	60 %
0.5	0.5	0.75	75 %
0	0	0	0 %
1	0	1	100 %
0	1	1	100 %
1	1	1	100 %

In the following, the coupled physical-mechanical constitutive model is shown, in which Eq. (9.12) is utilized.

Similarly to chapter 7, first the formulations of the elasto-plastic component and then the visco-elastic components are derived.

9.5.2 Elasto-plastic component

In the intermediate configuration, for the elasto-plastic component of the model and accounting for the physical moisture induced damage, the Helmholtz free energy can be set up as

$$\Psi_d = (1-d_m)\Psi(\mathbf{C}_\infty, \xi) \quad (9.13)$$

Therefore, the time derivative of the free energy function becomes

$$\begin{aligned} \dot{\Psi}_d &= (1-d_m)\dot{\Psi} - \Psi\dot{d}_m \\ &= (1-d_m)\left[\frac{\partial\Psi}{\partial\mathbf{C}_\infty}:\dot{\mathbf{C}}_\infty + \frac{\partial\Psi}{\partial\xi}:\dot{\xi}\right] - \Psi\dot{d}_m \end{aligned} \quad (9.14)$$

For the proposed staggered solution scheme between RoAM and CAPA-3D the physical moisture induced damage parameter d_m does not change during the simulation time step, and therefore $\dot{d}_m = 0$.

Using the relations $\dot{\mathbf{C}}_\infty = 2\mathbf{F}_\infty^T \dot{\mathbf{F}}_\infty$ and $\dot{\mathbf{F}}_\infty = \dot{\mathbf{F}} \mathbf{F}_p^{-1} + \mathbf{F} \dot{\mathbf{F}}_p^{-1}$ from Eq. (7.6)-(7.7), Eq. (9.14) can be further elaborated as

$$\begin{aligned} \dot{\Psi}_d &= (1-d_m) \left[\frac{\partial \Psi}{\partial \mathbf{C}_\infty} : 2\mathbf{F}_\infty^T \dot{\mathbf{F}}_\infty + \frac{\partial \Psi}{\partial \xi} : \dot{\xi} \right] \\ &= (1-d_m) \left[2\mathbf{F}_\infty \frac{\partial \Psi}{\partial \mathbf{C}_\infty} : \left(\dot{\mathbf{F}} \mathbf{F}_p^{-1} + \mathbf{F} \dot{\mathbf{F}}_p^{-1} \right) + \frac{\partial \Psi}{\partial \xi} : \dot{\xi} \right] \\ &= (1-d_m) \left[2\mathbf{F}_\infty \frac{\partial \Psi}{\partial \mathbf{C}_\infty} : \dot{\mathbf{F}} \mathbf{F}_p^{-1} + 2\mathbf{F}_\infty \frac{\partial \Psi}{\partial \mathbf{C}_\infty} : \mathbf{F} \dot{\mathbf{F}}_p^{-1} + \frac{\partial \Psi}{\partial \xi} : \dot{\xi} \right] \end{aligned} \quad (9.15)$$

which can be rearranged as

$$\dot{\Psi}_d = (1-d_m) \left[2\mathbf{F}_\infty \frac{\partial \Psi}{\partial \mathbf{C}_\infty} \mathbf{F}_p^{-T} : \dot{\mathbf{F}} - 2\mathbf{C}_\infty \frac{\partial \Psi}{\partial \mathbf{C}_\infty} \mathbf{F}_p^{-T} : \dot{\mathbf{F}}_p + \frac{\partial \Psi}{\partial \xi} : \dot{\xi} \right] \quad (9.16)$$

so that the Clausius-Planck local dissipation inequality reads

$$\begin{aligned} \mathcal{D} &= \mathbf{P}_d : \dot{\mathbf{F}} - \dot{\Psi}_d \\ &= \left[\mathbf{P}_d - 2(1-d_m) \mathbf{F}_\infty \frac{\partial \Psi}{\partial \mathbf{C}_\infty} \mathbf{F}_p^{-T} \right] : \dot{\mathbf{F}} + 2(1-d_m) \mathbf{C}_\infty \frac{\partial \Psi}{\partial \mathbf{C}_\infty} : l_p + (1-d_m) q \dot{\xi} \geq 0 \end{aligned} \quad (9.17)$$

from which by standard argumentation the first Piola-Kirchhoff stress tensor, including physical moisture induced damage, is obtained as

$$\mathbf{P}_d = 2(1-d_m) \mathbf{F}_\infty \frac{\partial \Psi}{\partial \mathbf{C}_\infty} \mathbf{F}_p^{-T} \quad (9.18)$$

and the dissipation inequality

$$(1-d_m) \left[2\mathbf{C}_\infty \frac{\partial \Psi}{\partial \mathbf{C}_\infty} : l_p + q \dot{\xi} \right] \geq 0 \quad (9.19)$$

After defining the Mandel stress tensor

$$\boldsymbol{\Sigma}_d = 2(1-d_m) \mathbf{C}_\infty \frac{\partial \Psi}{\partial \mathbf{C}_\infty} = (1-d_m) \mathbf{C}_\infty \mathbf{S}_\infty \quad (9.20)$$

with \mathbf{S}_∞ the second Piola-Kirchhoff stress tensor defined in the intermediate configuration, inequality (9.19) can be expressed as

$$\boldsymbol{\Sigma}_d : l_p + q_d \dot{\xi} \geq 0 \quad (9.21)$$

with $q_d = (1-d_m)q$

For completeness the push-forward operation of $(1-d_m)\mathbf{S}_\infty$ is reiterated

$$\boldsymbol{\tau}_d = \mathbf{J} \boldsymbol{\sigma}_d = \mathbf{F}_\infty (1-d_m) \mathbf{S}_\infty \mathbf{F}_\infty^T \quad (9.22)$$

On the basis of inequality Eq. (9.21) the following constrained minimization statement can be set up

$$\begin{aligned} & \text{minimize} \quad -\left(\boldsymbol{\Sigma}_d : \boldsymbol{l}_p + q_d \dot{\boldsymbol{\xi}} \right) \\ & \text{subject to} \quad f(\boldsymbol{\Sigma}_d, q_d) \leq 0 \end{aligned} \quad (9.23)$$

which is equivalent to the following set of plastic evolution equations

$$\begin{aligned} \boldsymbol{l}_p &= \dot{\mathbf{F}}_p \mathbf{F}_p^{-1} = \lambda \mathbf{N}_d \\ \dot{\boldsymbol{\xi}} &= \lambda \left(\frac{\partial f}{\partial q_d} \right) \\ \lambda &\geq 0 \quad ; \quad f(\boldsymbol{\Sigma}_d, q_d) \leq 0 \quad ; \quad \lambda f(\boldsymbol{\Sigma}_d, q_d) = 0 \end{aligned} \quad (9.24)$$

in which again λ is the plastic consistency parameter, $\mathbf{N}_d = \partial f / \partial \boldsymbol{\Sigma}_d$ and $f(\boldsymbol{\Sigma}_d, q_d)$ is a flow surface function. The implemented flow surfaces are discussed in Appendix 7.2.

The flow rule expressed by Eq. (9.24)₁ can be written as

$$\frac{\partial \mathbf{F}_p}{\partial t} = \lambda \mathbf{N}_d \mathbf{F}_p \quad (9.25)$$

9.5.3 Visco-elastic component

Similarly to the elasto-plastic component, the Helmholtz free energy function of the visco-elastic component can be reformulated

$$\Psi_d = (1-d_m) \Psi(\mathbf{C}_e) \quad (9.26)$$

$$\dot{\Psi}_d = (1-d_m) \frac{\partial \Psi}{\partial \mathbf{C}_e} : \dot{\mathbf{C}}_e - \Psi \dot{d}_m \quad (9.27)$$

Again, for the proposed staggered solution scheme between CAPA-3D and RoAM, the physical moisture damage parameter does not change during a time step, and therefore $\dot{d}_m = 0$

Since from Eq. (7.7) it can be found that $\dot{\mathbf{C}}_e = 2 \mathbf{F}_e^T \dot{\mathbf{F}}_e$, therefore

$$\frac{\partial \Psi}{\partial \mathbf{C}_e} : \dot{\mathbf{C}}_e = 2 \frac{\partial \Psi}{\partial \mathbf{C}_e} : \mathbf{F}_e^T \dot{\mathbf{F}}_e = 2 \mathbf{F}_e \frac{\partial \Psi}{\partial \mathbf{C}_e} : \dot{\mathbf{F}}_e \quad (9.28)$$

Substituting this into Eq. (9.27) and using from Eq. (7.6) the relation $\dot{\mathbf{F}}_e = \dot{\mathbf{F}} \mathbf{F}_v^{-1} + \mathbf{F} \dot{\mathbf{F}}_v^{-1}$, the rate of the free energy function can be written as

$$\begin{aligned}
\dot{\Psi}_d &= 2(1-d_m) \mathbf{F}_e \frac{\partial \Psi}{\partial \mathbf{C}_e} : \dot{\mathbf{F}}_e \\
&= 2(1-d_m) \mathbf{F}_e \frac{\partial \Psi}{\partial \mathbf{C}_e} : (\dot{\mathbf{F}} \mathbf{F}_v^{-1} + \mathbf{F} \dot{\mathbf{F}}_v^{-1}) \\
&= 2(1-d_m) \mathbf{F}_e \frac{\partial \Psi}{\partial \mathbf{C}_e} : \dot{\mathbf{F}} \mathbf{F}_v^{-1} + 2(1-d_m) \mathbf{F}_e \frac{\partial \Psi}{\partial \mathbf{C}_e} : \mathbf{F} \dot{\mathbf{F}}_v^{-1}
\end{aligned} \tag{9.29}$$

Utilizing the tensor identity $\mathbf{A}:\mathbf{BC} = \mathbf{AC}^T:\mathbf{B}$ for the first term on the r.h.s. of Eq. (9.29), it results

$$2(1-d_m) \mathbf{F}_e \frac{\partial \Psi}{\partial \mathbf{C}_e} : \dot{\mathbf{F}} \mathbf{F}_v^{-1} = 2(1-d_m) \mathbf{F}_e \frac{\partial \Psi}{\partial \mathbf{C}_e} \mathbf{F}_v^{-T} : \dot{\mathbf{F}} \tag{9.30}$$

By means of the identity $\dot{\mathbf{F}}_v^{-1} = -\mathbf{F}_v^{-1} \dot{\mathbf{F}}_v \mathbf{F}_v^{-1}$ and the identity $\mathbf{F}_e = \mathbf{F} \mathbf{F}_v^{-1}$ the second term on the r.h.s. of Eq. (9.29) can be written as

$$\begin{aligned}
2(1-d_m) \mathbf{F}_e \frac{\partial \Psi}{\partial \mathbf{C}_e} : \mathbf{F} \dot{\mathbf{F}}_v^{-1} &= -2(1-d_m) \mathbf{F}_e \frac{\partial \Psi}{\partial \mathbf{C}_e} : \mathbf{F} (\mathbf{F}_v^{-1} \dot{\mathbf{F}}_v \mathbf{F}_v^{-1}) \\
&= -2(1-d_m) \mathbf{F}_e \frac{\partial \Psi}{\partial \mathbf{C}_e} : \mathbf{F}_e \dot{\mathbf{F}}_v \mathbf{F}_v^{-1}
\end{aligned} \tag{9.31}$$

Utilizing the tensor identity $\mathbf{A}:\mathbf{BC} = \mathbf{B}^T \mathbf{A}:\mathbf{C}$ for Eq. (9.31) it results

$$\begin{aligned}
-2(1-d_m) \left(\mathbf{F}_e \frac{\partial \Psi}{\partial \mathbf{C}_e} \right) : \mathbf{F}_e \dot{\mathbf{F}}_v \mathbf{F}_v^{-1} &= -2(1-d_m) \mathbf{F}_e^T \left(\mathbf{F}_e \frac{\partial \Psi}{\partial \mathbf{C}_e} \right) : \dot{\mathbf{F}}_v \mathbf{F}_v^{-1} \\
&= -2(1-d_m) \mathbf{C}_e \frac{\partial \Psi}{\partial \mathbf{C}_e} : \dot{\mathbf{F}}_v \mathbf{F}_v^{-1}
\end{aligned} \tag{9.32}$$

which can be further simplified by means of the identity $\mathbf{A}:\mathbf{BC} = \mathbf{AC}^T:\mathbf{B}$

$$-2(1-d_m) \mathbf{C}_e \frac{\partial \Psi}{\partial \mathbf{C}_e} : \dot{\mathbf{F}}_v \mathbf{F}_v^{-1} = -2(1-d_m) \mathbf{C}_e \frac{\partial \Psi}{\partial \mathbf{C}_e} \mathbf{F}_v^{-T} : \dot{\mathbf{F}}_v \tag{9.33}$$

Substituting Eq. (9.33) and Eq. (9.30) into Eq. (9.29)

$$\dot{\Psi}_d = 2(1-d_m) \mathbf{F}_e \frac{\partial \Psi}{\partial \mathbf{C}_e} \mathbf{F}_v^{-T} : \dot{\mathbf{F}} - 2(1-d_m) \mathbf{C}_e \frac{\partial \Psi}{\partial \mathbf{C}_e} \mathbf{F}_v^{-T} : \dot{\mathbf{F}}_v \tag{9.34}$$

so that the Clausius-Planck local dissipation inequality reads

$$\begin{aligned}
\mathcal{D} &= \mathbf{P}_d : \dot{\mathbf{F}} - \dot{\Psi}_d \\
&= \mathbf{P}_d : \dot{\mathbf{F}} - 2(1-d_m) \mathbf{F}_e \frac{\partial \Psi}{\partial \mathbf{C}_e} \mathbf{F}_v^{-T} : \dot{\mathbf{F}} + 2(1-d_m) \mathbf{C}_e \frac{\partial \Psi}{\partial \mathbf{C}_e} \mathbf{F}_v^{-T} : \dot{\mathbf{F}}_v \\
&= \left[\mathbf{P}_d - 2(1-d_m) \mathbf{F}_e \frac{\partial \Psi}{\partial \mathbf{C}_e} \mathbf{F}_v^{-T} \right] : \dot{\mathbf{F}} + 2(1-d_m) \mathbf{C}_e \frac{\partial \Psi}{\partial \mathbf{C}_e} : \dot{\mathbf{F}}_v \mathbf{F}_v^{-1} \\
&= \left[\mathbf{P}_d - 2(1-d_m) \mathbf{F}_e \frac{\partial \Psi}{\partial \mathbf{C}_e} \mathbf{F}_v^{-T} \right] : \dot{\mathbf{F}} + 2(1-d_m) \mathbf{C}_e \frac{\partial \Psi}{\partial \mathbf{C}_e} : \mathbf{l}_v \geq 0
\end{aligned} \tag{9.35}$$

from which by standard argumentation the first Piola-Kirchhoff stress tensor, including physical moisture induced damage, is obtained as

$$\mathbf{P}_d = 2(1-d_m) \mathbf{F}_e \frac{\partial \Psi}{\partial \mathbf{C}_e} \mathbf{F}_v^{-T} \tag{9.36}$$

and the dissipation inequality

$$2(1-d_m) \mathbf{C}_e \frac{\partial \Psi}{\partial \mathbf{C}_e} : \mathbf{l}_v \geq 0 \tag{9.37}$$

Again, after defining the Mandel stress tensor

$$\boldsymbol{\Sigma}_d = 2(1-d_m) \mathbf{C}_e \frac{\partial \Psi}{\partial \mathbf{C}_e} = (1-d_m) \mathbf{C}_e \mathbf{S}_e \tag{9.38}$$

with \mathbf{S}_e the second Piola-Kirchhoff stress tensor defined in the intermediate configuration

Inequality Eq. (9.37) can then be expressed as

$$\boldsymbol{\Sigma}_d : \mathbf{l}_v \geq 0 \tag{9.39}$$

In similarity to Eq. 7.91 the following evolution law can be found

$$\mathbf{l}_v = \mathbb{C}_v^{-1} : \boldsymbol{\Sigma}_d \tag{9.40}$$

with

$$\mathbb{C}_v^{-1} = \frac{1}{2\eta_D} \left(\mathbb{I} - \frac{1}{3} \mathbf{I} \otimes \mathbf{I} \right) + \frac{1}{9\eta_V} \mathbf{I} \otimes \mathbf{I} \tag{9.41}$$

while η_D and η_V are the deviatoric and volumetric viscosities which may be deformation dependent

$$\eta_D = \eta_D(\boldsymbol{\Sigma}_d) > 0 \quad ; \quad \eta_V = \eta_V(\boldsymbol{\Sigma}_d) > 0 \tag{9.42}$$

Therefore

$$\mathbf{l}_v = \dot{\mathbf{F}}_v \mathbf{F}_v^{-1} = \mathbb{C}_v^{-1} : \boldsymbol{\Sigma}_d \tag{9.43}$$

Which can be written as

$$\frac{\partial \mathbf{F}_v}{\partial t} = \left(\mathbb{C}_v^{-1} : \boldsymbol{\Sigma}_d \right) \mathbf{F}_v \tag{9.44}$$

9.5.4 Stress Reduction Procedure

The stress reduction procedures for the elasto-plastic and visco-elastic components of the model is similar to the formulation described in section 7.2.5 and 7.2.7, using the above described tensors which include the physical moisture induced damage, and is not repeated here.

In the following the above described combined physical-mechanical moisture induced system is demonstrated via several numerical simulations, using the experimentally determined parameters.

9.6 Numerical parametric study of moisture induced damage

9.6.1 Introduction

The combined physical-mechanical moisture induced damage model, as presented in the previous sections, is demonstrated in this section.

First, the time aspect regarding aggregate-mastic bond degradation in the presence of moisture is highlighted. In the developed methodology for determination of bond strength in the presence of moisture, as discussed in chapter 8, moisture is reaching the interface through the aggregate mastic film. Therefore, the bond degradation times which are determined from the experiment cannot be used for bond degradation times in practice. Rather, it is fair to assume that, in practice, moisture would most of the time diffuse through the mastic to reach the aggregate-mastic interface. Therefore, the diffusion coefficient of the mastic and mastic film thickness become important in assessing the bond degradation time.

Then, a micro-scale asphalt mix is used to demonstrate the damage development within the components, when exposed to the combined action of traffic loading, moisture diffusion and pumping action. Via several computational simulations it is demonstrated that completely different damage patterns may result for different moisture susceptibility parameters of the asphalt components.

In the following, first a parametric study is performed in which the generation of bond strength reduction as a function of time is simulated. In the study, the mastic film thickness, the mastic moisture diffusion coefficient and the aggregate-mastic bond moisture damage susceptibility parameter are varied.

9.6.2 Mastic film thickness versus aggregate-mastic bond strength reduction

As was mentioned before, the time scale in which moisture induced damage develops within an asphaltic mix is of paramount importance in the assessment of moisture susceptibility of an asphaltic mix. Therefore, in order to assess the time-scale in which aggregate-mastic bond strength reduction becomes relevant in practice, in the following, simulations are given of aggregate-mastic samples that are exposed to moisture from the outside of the mastic film, with varying:

- mastic film thicknesses
- mastic moisture diffusivity coefficients
- moisture damage susceptibility parameters of the aggregate-mastic bond

As discussed in chapter 3, the rate of moisture diffusion is controlled by the diffusion coefficient of the material. However, the maximum moisture concentration C_m^{\max} which a material may absorb can be different and should be determined experimentally. The implication of the above is that, for instance, a material with a high diffusion coefficient may absorb more moisture in the beginning of the diffusion process, see the red curve in Fig. 9.6.1(a), but shall ultimately absorb less moisture than a material which has a lower diffusion coefficient but a higher C_m^{\max} , see the blue curve in Fig. 9.6.1(a).

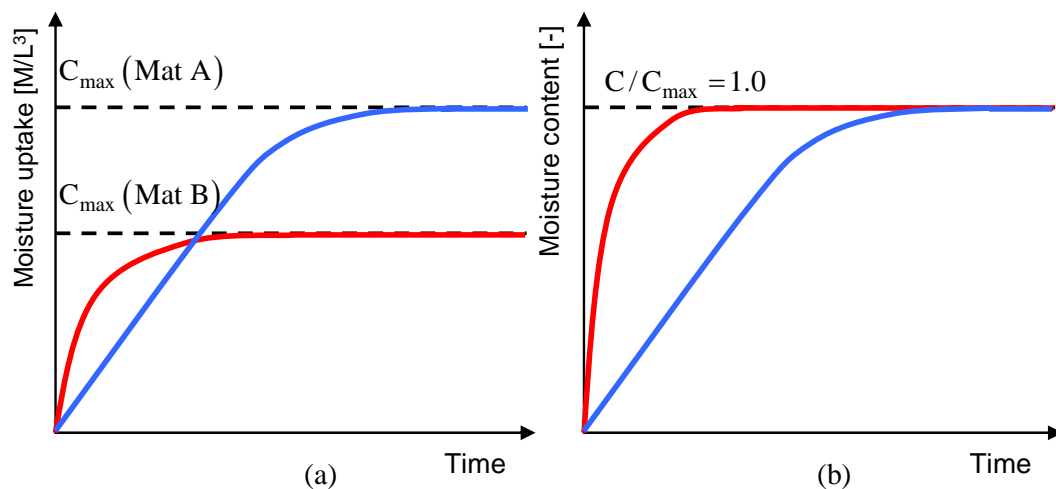


Fig. 9.6.1: Moisture uptake schematic for two materials

As mentioned earlier, to enable the comparison between materials, in the following analyses, the normalized values of the moisture concentrations $C_m(t)/C_m^{\max}$ are used, Fig. 9.6.1(b), and shall be referred to as the moisture content $\theta(t)$.

In chapter 8 the aggregate-mastic bond strength was determined as a function of moisture content for a particular type of aggregate-mastic combination. From this, the moisture induced damage parameter $d_\theta = f(\theta, \alpha)$ was determined for the aggregate-mastic bond as

$$d_{\theta} = 1 - e^{-\alpha\sqrt{\theta}} \quad (9.45)$$

where for the tested samples, it was determined that $\alpha = 3.76$

In the following analyses, the assumption is made that the moisture damage development of all aggregate-mastic bonds is of the exponential form depicted in Eq. (9.45), which is controlled by the *moisture damage susceptibility parameter* α .

Three types of aggregate-mastic moisture damage evolution are postulated, type I, II and III with a moisture damage susceptibility parameter of $\alpha_I = 0.1$, $\alpha_{II} = 1.0$ and $\alpha_{III} = 5.0$, respectively.

In Fig. 9.6.2 the development of the moisture damage d_{θ} as a function of moisture content $\theta(t)$ is plotted for the three moisture damage evolution types.

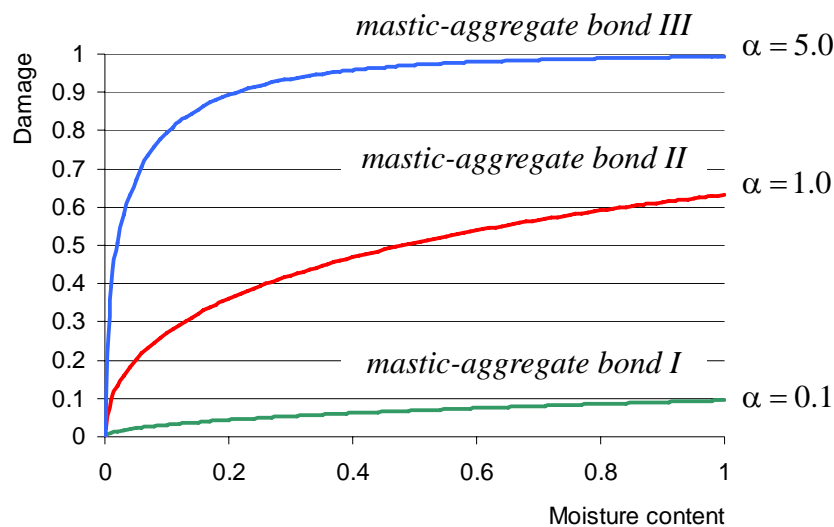


Fig. 9.6.2: Postulated mastic-aggregate moisture susceptibility

From Fig. 9.6.2 it can be seen that the mastic-aggregate bond type III damages severely, even for low moisture content values, type II loses approximately 60% of its bond when the maximum moisture content is reached and type I suffers very little moisture damage, with a maximum of 10% damage at full saturation.

Moisture diffusion measurements are still not performed very commonly for asphaltic materials. There are two main test procedures being utilized to date. The first is an overall measurement of the increase of weight as a sample is exposed to a controlled moisture conditioning [Cheng 2002]. The second is a slightly more complicated procedure using a Fourier transform infrared spectroscopy [Nguyen 1992]. It is quite challenging, though, to utilize the available test data, since the values can be considerably different.

For instance, for the type AAD-1 asphalt binder (i.e. pure bitumen), values have been published from a wide range of $2.88 \cdot 10^{+6} \text{ mm}^2/\text{hr}$ [Little 2003] to $4.79 \text{ mm}^2/\text{hr}$ [Cheng 2002] to $9.0 \cdot 10^{-5} \text{ mm}^2/\text{hr}$ [Nguyen 1992].

Comparing these values with published diffusion coefficients of, for example, rubber $D = 1.44 \cdot 10^{-4} \text{ mm}^2/\text{hr}$, PVC $D = 8.28 \cdot 10^{-3} \text{ mm}^2/\text{hr}$ and polyethylene $D = 8.28 \cdot 10^{-2}$

mm²/hr [Abson 1979], the lower range diffusion values for asphalt binders seems to be more plausible. Since the mastic in an asphaltic mix generally consists of asphalt binder as well as sand particles and fine aggregate filler material, a higher diffusion value than for the binder alone can be expected, as was demonstrated in chapter 6.

To cover the wide-spread values of the diffusion coefficients, within reason, and to show their implications for the aggregate-mastic bond strength reduction, in the following, a parametric analysis with RoAM is given, where mastic diffusion coefficients ranging from the extreme value of 1 mm²/hr to 1.0 10⁻⁰⁵ mm²/hr are utilized.

In Table 9.6.1 an overview is given of the various aggregate-mastic simulation types.

Table 9.6.1: Overview of aggregate-mastic simulation types

Moisture Damage Susceptibility	Mastic Diffusion Coefficients [mm ² /hr]			
	D _I = 1.0	D _{II} = 1.0 10 ⁻²	D _{III} = 1.0 10 ⁻⁴	D _{IV} = 1.0 10 ⁻⁵
$\alpha_I = 0.1$	A	B	C	D
$\alpha_{II} = 1.0$	E	F	G	H
$\alpha_{III} = 5.0$	J	K	L	M

In the RoAM diffusion analyses, moisture diffusion into the mastic film is simulated and the moisture content θ in the aggregate-mastic interface is monitored, Fig. 9.6.3

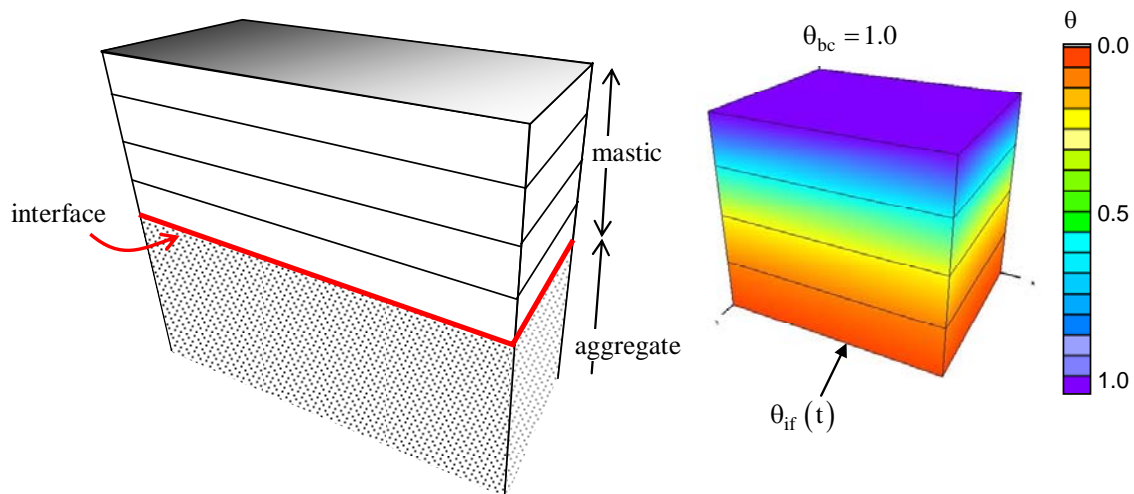


Fig. 9.6.3: Simulation of moisture into the mastic towards the interface (if)

In the analyses it is assumed that:

- during the entire simulation time, moisture is freely available from the outside environment, i.e. a continuous moisture boundary condition of $\theta_{bc} = 1.0$;
- moisture can only reach the aggregate-mastic interface via a diffusion process through the mastic film;

- once the mastic has reached its maximum moisture capacity, i.e. $\theta(t)=1.0$, no additional damage is generated;
- moisture at the aggregate-mastic interface is not accumulating;
- moisture is not causing any swelling in the mastic;
- moisture diffusion stagnates once the concentration gradient in the mastic diminishes to zero;
- no other damage process is occurring.

For the aggregate-mastic combination types A-M, the time in which 10 %, 25 %, 50 %, 75 % and 100 % bond strength reduction is generated, is computed for mastic films of a thickness of 50 μm , 100 μm , 500 μm , 1.0 mm and 5.0 mm and is summarized in Table 9.6.1 through Table 9.6.6.

From the tables it can be concluded that accurate determination of the moisture diffusion coefficient of the mastic film and its maximum moisture capacity are of essence in determining the life time of asphaltic mixes. Moreover, it can be recommended to choose mastic-aggregate combinations, which minimize the mastic moisture diffusion coefficients D and the aggregate-mastic moisture damage susceptibility parameter α .

Table 9.6.2: Time in which 10% bond strength reduction is generated

	Mastic Film Thickness				
	50 μm	100 μm	500 μm	1.0 mm	5.0 mm
A	< 1.0 min	< 1.0 min	36 min	2.4 hrs	9 days
B	1 hr	2.3 hrs	2.5 hrs	12 days	13 months
C	2.6 days	9.7 days	8.5 months	33 months	50 yrs
D	3 months	11 months	15.3 yrs	102 yrs	2.3 10^3 yrs
E	< 1.0 min	< 1.0 min	< 1.0 min	2.6 min	1.2 hrs
F	< 1.0 min	2.5 min	30 min	2.4 hrs	5 days
G	1.3 hrs	4.4 hrs	4.2 days	17 days	1.4 yrs
H	13 hrs	2 days	1.8 months	6.9 months	14.6 yrs
J	< 1.0 min	< 1.0 min	< 1.0 min	< 1.0 min	20 min
K	< 1.0 min	< 1.0 min	9 min	54 min	1.9 days
L	28 min	1 hr	2 days	4.2 days	6.5 months
M	4.6 hrs	18 hrs	19 days	2.5 months	5.3 yrs

Table 9.6.3: Time in which 25% bond strength reduction is generated

	Mastic Film Thickness				
	50 μm	100 μm	500 μm	1.0 mm	5.0 mm
A	never	never	never	never	never
B	never	never	never	never	never
C	never	never	never	never	never
D	never	never	never	never	never
E	< 1.0 min	< 1.0 min	1.8 min	6.6 min	2.8 hrs
F	< 1.0 min	7 min	3 hrs	10 hrs	12 days
G	3 hrs	11 hr	10 days	46 days	3.3 yrs
H	28 hrs	4.7 days	3.9 months	1.3 yrs	32.4 yrs
J	< 1.0 min	< 1.0 min	< 1.0 min	2 min	45 min
K	< 1.0 min	2 min	20 min	1.6 hrs	3.5 days
L	51 min	3 hrs	2 days	12 days	12 months
M	8.5 hrs	33 hrs	2.1 months	4.6 months	9.8 yrs

Table 9.6.4: Time in which 50% bond strength reduction is generated

	Mastic Film Thickness				
	50 μm	100 μm	500 μm	1.0 mm	5.0 mm
A	never	never	never	never	never
B	never	never	never	never	never
C	never	never	never	never	never
D	never	never	never	never	never
E	< 1.0 min	< 1.0 min	6 min	22 min	9 hrs
F	6 min	22 min	10 hrs	1.7 days	1.3 months
G	10 hrs	1.5 days	38 days	5 months	10 yrs
H	3.8 days	15 days	13 months	4.2 yrs	105 yrs
J	< 1.0 min	< 1.0 min	< 1.0 min	4 min	1.5 hrs
K	< 1.0 min	< 1.0 min	1 hr	2.8 hrs	6.4 days
L	1 hr	6 hrs	6 days	25 days	1.8 yrs
M	15 hrs	2.5 days	2.1 months	8.5 months	17.7 yrs

Table 9.6.5: Time in which 75% bond strength reduction is generated

	Mastic Film Thickness				
	50 μm	100 μm	500 μm	1.0 mm	5.0 mm
A	never	never	never	never	never
B	never	never	never	never	never
C	never	never	never	never	never
D	never	never	never	never	never
E	never	never	never	never	never
F	never	never	never	never	never
G	never	never	never	never	never
H	never	never	never	never	never
J	< 1.0 min	< 1.0 min	1.5 min	6.6 min	2.8 hrs
K	< 1.0 min	7 min	3 hrs	10 hrs	11.3 days
L	3 hrs	11 hrs	10 days	46 days	3 yrs
M	27 hrs	29 days	3.8 months	1.3 yrs	31.4 yrs

Table 9.6.6: Time in which 100% bond strength reduction is generated

	Mastic Film Thickness				
	50 μm	100 μm	500 μm	1.0 mm	5.0 mm
A	never	never	never	never	never
B	never	never	never	never	never
C	never	never	never	never	never
D	never	never	never	never	never
E	never	never	never	never	never
F	never	never	never	never	never
G	never	never	never	never	never
H	never	never	never	never	never
J	< 1.0 min	< 1.0 min	< 1.0 min	2.4 hrs	19 hrs
K	1 hr	2.3 hrs	2.5 days	12 days	2.6 months
L	2.6 days	10 days	8.4 months	33 months	22 yrs
M	8 days	1 month	2.2 yrs	8.8 yrs	218 yrs

9.6.3 Combined physically and mechanically generated damage on a micro-scale asphalt mix

9.6.3.1 Introduction

Traffic loading causes quite a complex stress pattern on an asphaltic pavement, given its dynamic nature, the high velocities and its combined compressive, frictional and tension loading due to tire-pavement interactions. Tools are currently being developed to accurately simulate the dynamic wheel-asphalt pavement loading [Kasbergen 2007]. For the asphaltic mix behavior, generally, a continuum approach is used to simulate the material response.

To explicitly include the response of all the asphalt components, it is also possible to develop micro-scale finite element meshes whereby each component has its own constitutive model and the interaction is simulated via interface elements [Milne 2004], Fig. 9.6.4.

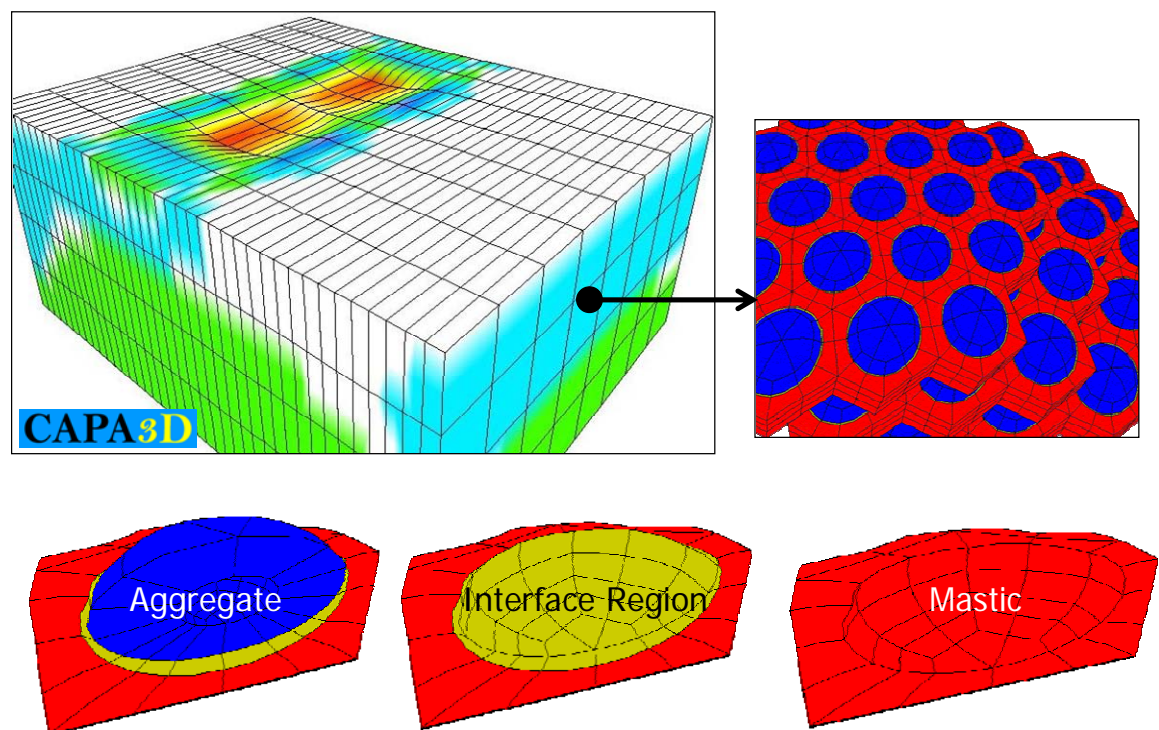


Fig. 9.6.4: Different scales of simulating asphaltic materials

The use of such an approach to simulate the actual behavior of a pavement makes for interesting analyses, even though the computational effort and times involved are of such a large scale that even with the current computing power this remains an unattractive option. Other approaches, which benefit from the computational efficiency of the continuum mechanics approach, while at the same time, including the directionality of the aggregate types and shapes within the material model, are also being developed [Scarpas 2006[b]].

In this dissertation, the asphalt mix is indeed approached on a micro-scale level, though the current objective is not to use the developed model to simulate the pavement response. Rather, the objective is to show the combined physical-mechanical phenomena that can now be simulated with the developed tool and to

demonstrate the importance of each of these moisture induced damage processes on the eventual developed damage pattern.

It therefore suffices to demonstrate the developed tool on a simplified representation of an asphaltic mix. In Fig. 9.6.5 and Fig. 9.6.6 the geometry and set-up of the finite element mesh is shown. The mesh consists of two stones, coated with a mastic film and a macro-pore which may contain moisture. The aggregate-mastic interface is also modeled to simulate the bond response.

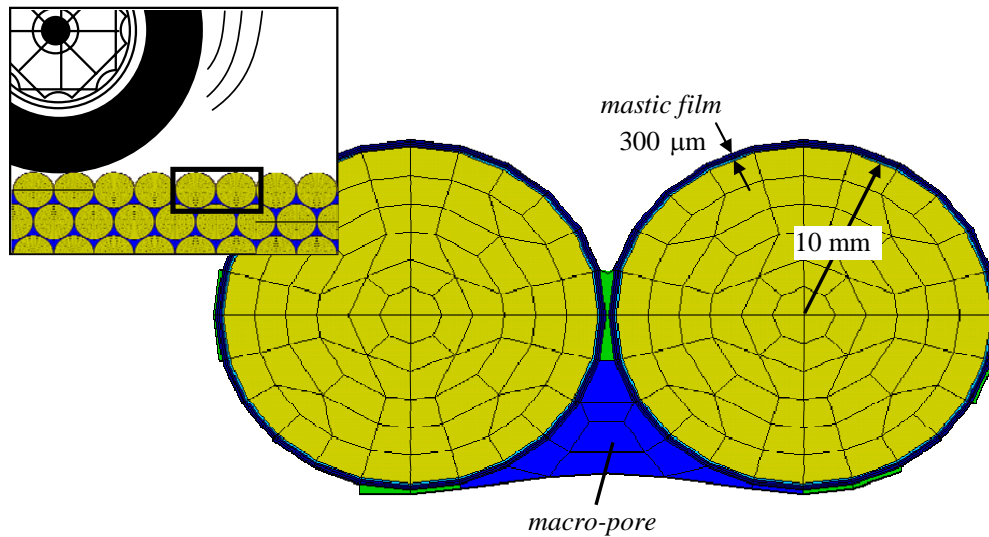


Fig. 9.6.5: Finite element mesh for the micro-scale analyses

The (green) cohesive mastic boundary elements, Fig. 9.6.6, are in fact mastic patches which connect one coated aggregate to the next one, and are assigned the same material properties as the mastic film.

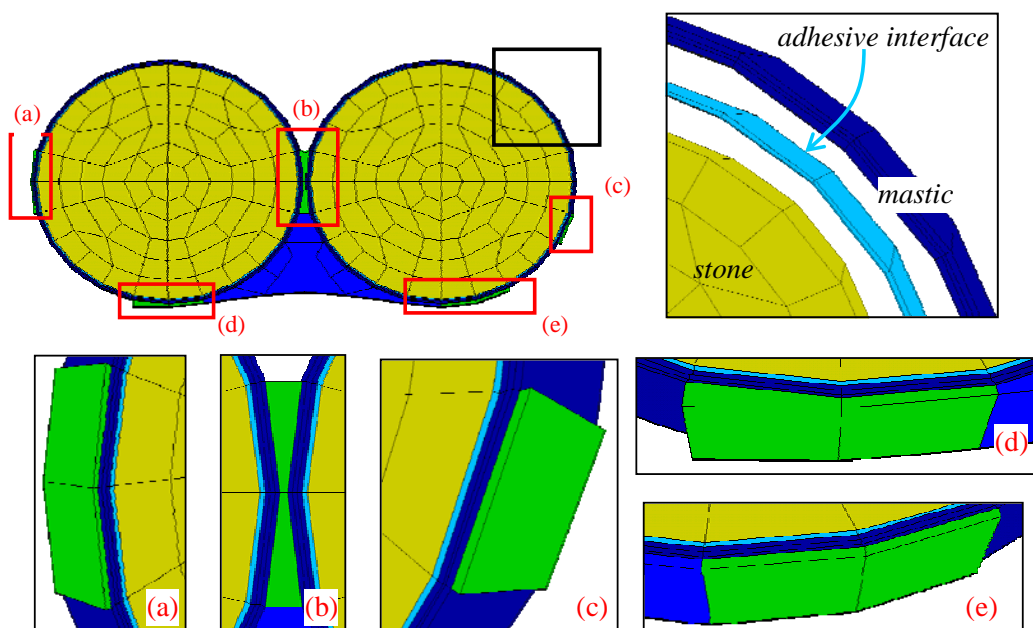


Fig. 9.6.6: Details of the mesh. Topright: adhesive interface.
Bottom: details of cohesive mastic boundary elements

The purpose of these elements is to simulate the constraints from the surrounding aggregates on the movement of the two aggregates. Boundary elements (a) and (c) are restrained in the horizontal movement and (d) and (e) are restrained in the vertical movement. The bottom nodes of the macro-pore element are also restrained from moving vertically. The mastic patch between the two aggregates, detail (b), simulates the connecting mastic between the two aggregates and is not given any extra restrains.

Even though the developed model is fully three dimensional, for demonstration purposes here only the two dimensional response in the micro-scale finite element mesh is discussed.

9.6.3.2 Mechanical loading conditions

Since the two aggregates are at the surface of the pavement, they are in direct contact with the traffic loading. To simulate the tire-pavement interaction, a loading cycle is applied, which consists of 0.02 s pulses per tire, with 0.06 s period between the tires and 0.1 s between the next car loading [Al-Qadi 2007]. In the simulation, the loading of the stones in time is simulated with a compressive and shear pulse on the front and back side of the stones, with a time-lag of 0.01 s. In the simulation, traffic is assumed to move from the right to the left. The maximum applied compressive and shear stress is 0.7 MPa and 0.3 MPa, respectively. A complete loading cycle takes 0.2 s and is considered to be two wheel passes and one rest period, Fig. 9.6.7.

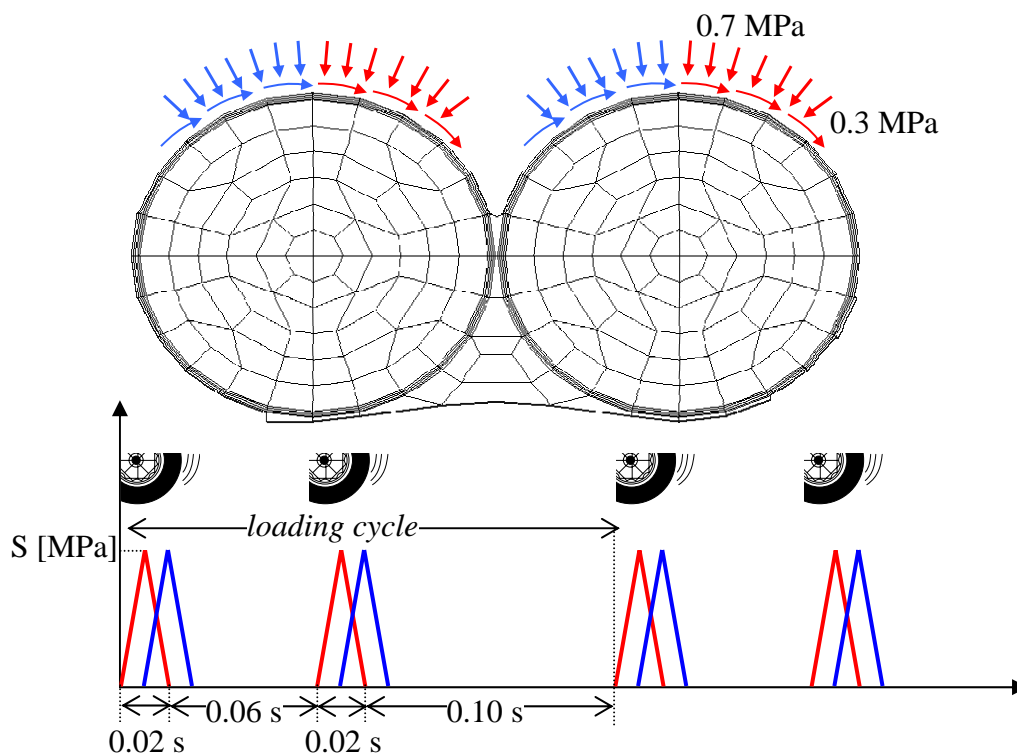


Fig. 9.6.7: Time scheme of applied loading cycle, with applied compressive loading $F_{yy} = 0.7 \text{ MPa}$ and shear loading $F_{xy} = 0.3 \text{ MPa}$

In Fig. 9.6.8 the deformation of the mesh, due to the applied mechanical loading is shown. From the pictures it can be seen there is a tendency for the aggregate to rotate under the applied loading, which applies a severe deformation on both the mastic between the stones and the aggregate-mastic interfaces near the boundaries.

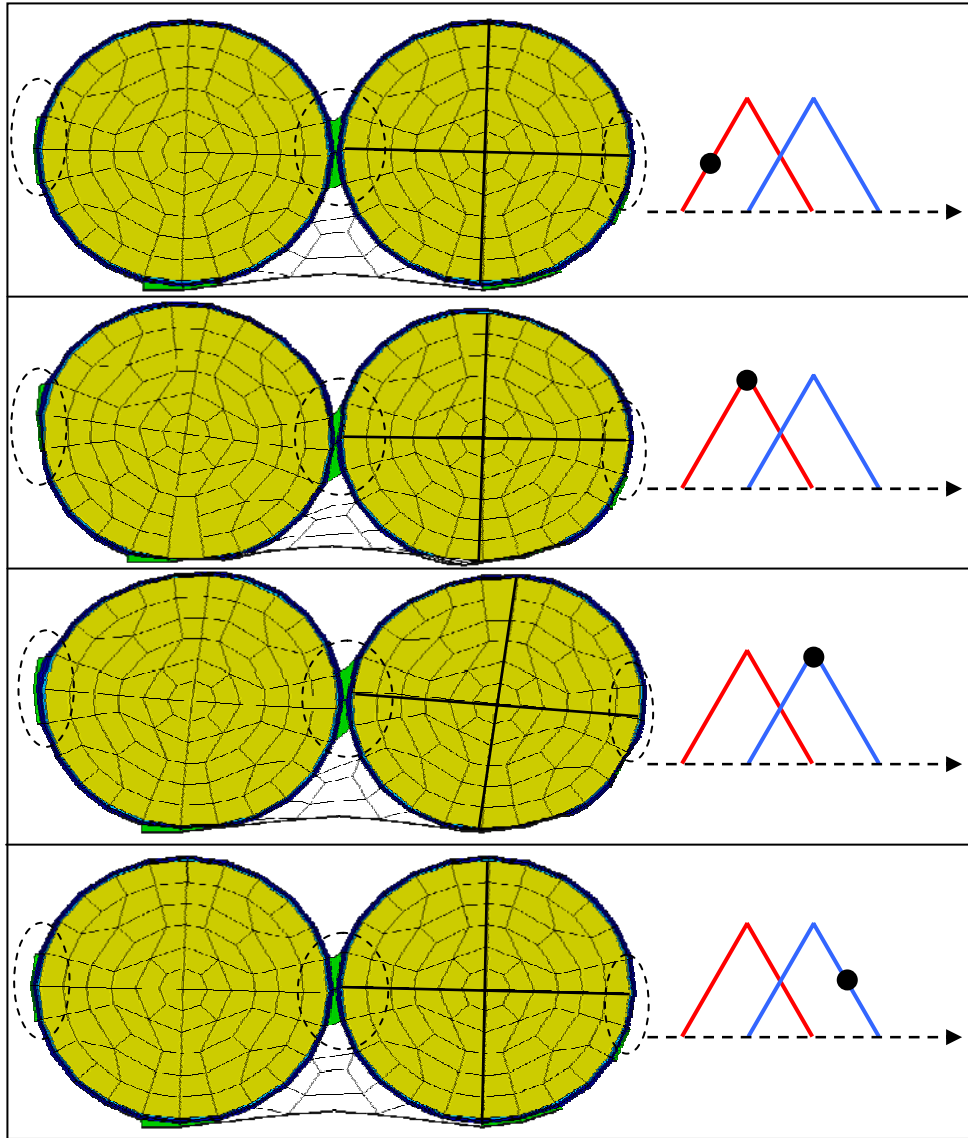


Fig. 9.6.8: Deformation due to applied loading (magn. 200x)

The applied loading is not meant as an actual representation of the tire-pavement interaction as would occur in practice. In such a case, dynamic phenomena and 3D effects should certainly be included. Rather, the chosen loading times, the magnitude of the applied compression and shear stresses and the contact area's are chosen in such a way, to show the punishment that the individual components may suffer from and the versatility of the stresses and strains that different locations in the asphalt mix may be exposed to, given sensible loading assumptions.

In the following, 13 different cases are simulated in which the diffusion of moisture, the erosion of mastic, the mechanical damage and the moisture susceptibility parameters are varied in a systematic way. It is the intention that these cases demonstrate that the consideration of physical moisture induced damage, together with mechanically generated damage, will lead to predictions of damage patterns which may differ considerable had they not been included. It furthermore shows the importance of determining the various moisture susceptibility parameters.

9.6.3.3 Parametric simulation scheme

In Table 9.6.7 the parameters of the various cases are shown.

Table 9.6.7: Parametric simulation scheme

Case name	Moisture conditioning	Moisture susceptibility parameters	
		Mastic	Aggregate-mastic bond
Case 0: Dry	-	-	-
Case I: Diff	42 days diffusion	$D_{mst} = 3 \cdot 10^{-3} \text{ mm}^2 / \text{hr}$ $\alpha_{\theta}^{mst} = 0.5$	$\alpha_{\theta}^{if} = 0.7$
Case II: Diff	42 days diffusion	$D_{mst} = 1.5 \cdot 10^{-2} \text{ mm}^2 / \text{hr}$ $\alpha_{\theta}^{mst} = 0.5$	$\alpha_{\theta}^{if} = 0.7$
Case III: Diff	42 days diffusion	$D_{mst} = 1.5 \cdot 10^{-2} \text{ mm}^2 / \text{hr}$ $\alpha_{\theta}^{mst} = 0.0$	$\alpha_{\theta}^{if} = 1.2$
Case IV: Diff	42 days diffusion	$D_{mst} = 1.5 \cdot 10^{-2} \text{ mm}^2 / \text{hr}$ $\alpha_{\theta}^{mst} = 1.2$	$\alpha_{\theta}^{if} = 0.0$
Case V: Dry PA	PA (pumping action) No diffusion No erosion	$K_d = 0.0 \text{ mm}^3 / \text{g}$, $\alpha_{\rho} = 0.0$	-
Case VI: Advec	PA and erosion No diffusion	$K_d = 1.0 \text{ mm}^3 / \text{g}$, $\alpha_{\rho} = 2.0$	-
Case VII: Advec	PA and erosion No diffusion	$K_d = 1.0 \text{ mm}^3 / \text{g}$, $\alpha_{\rho} = 5.0$	-
Case VIII: Advec	PA and erosion No diffusion	$K_d = 5.0 \text{ mm}^3 / \text{g}$, $\alpha_{\rho} = 5.0$	-
Case IX: All	PA, erosion and 42 days diffusion	$K_d = 5.0 \text{ mm}^3 / \text{g}$, $\alpha_{\rho} = 5.0$, $\alpha_{\theta}^{mst} = 0.5$ $D_{mst} = 1.5 \cdot 10^{-2} \text{ mm}^2 / \text{hr}$	$\alpha_{\theta}^{if} = 0.7$
Case X: All	PA, erosion and 42 days diffusion	$K_d = 1.0 \text{ mm}^3 / \text{g}$, $\alpha_{\rho} = 5.0$, $\alpha_{\theta}^{mst} = 0.5$ $D_{mst} = 1.5 \cdot 10^{-2} \text{ mm}^2 / \text{hr}$	$\alpha_{\theta}^{if} = 0.7$
Case XI: All	PA, erosion and 42 days diffusion	$K_d = 1.0 \text{ mm}^3 / \text{g}$, $\alpha_{\rho} = 5.0$, $\alpha_{\theta}^{mst} = 0.0$	$\alpha_{\theta}^{if} = 1.2$

		$D_{mst} = 1.5 \cdot 10^{-2} \text{ mm}^2 / \text{hr}$	
Case XI: All	PA, erosion and 42 days diffusion	$K_d = 5.0 \text{ mm}^3 / \text{g},$ $\alpha_{\hat{\rho}} = 5.0, \alpha_{\theta}^{mst} = 1.2$ $D_{mst} = 1.5 \cdot 10^{-2} \text{ mm}^2 / \text{hr}$	$\alpha_{\theta}^{if} = 0.0$

9.6.3.4 Material properties

To monitor the damage development within the asphalt mix more carefully, six locations are selected, for which stress, strain and damage values can be compared in time for the various cases, Fig. 9.6.9. Gauss points A, B and C are located within the mastic and D, E and F are located in the aggregate-mastic interface.

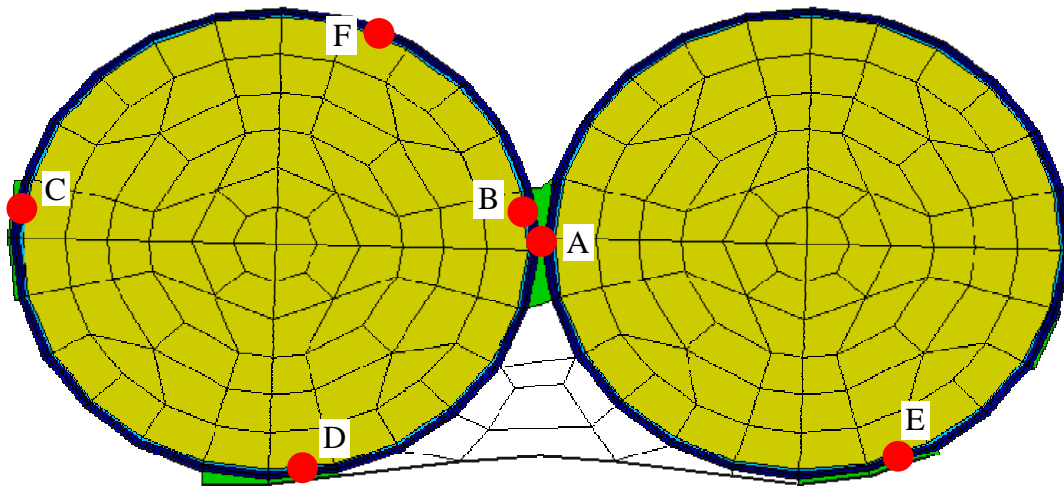


Fig. 9.6.9: Monitoring locations

For the material response of the individual components, the elasto-visco-plastic model, as presented in chapter 7 is utilized. Hereby, for the mastic, the parameters as determined in chapter 7 are used. The stones are assumed hyper-elastic, with a $E = 3000 \text{ MPa}$ and $\nu = 0.3$. The aggregate-mastic bond is simulated, assuming an approximately 20% weaker material than the mastic. A Drucker-Prager yield surface is used for the response of the plastic component. In section 7.3.1 a detailed description of this yield surface and its parameters is given.

In Table 9.6.8 a summary is given of the material parameters, which are utilized in the analyses.

Table 9.6.8: Material parameters for visco-elasto-plastic model

<u>Material</u>	<u>Visco-elastic component</u>	<u>Elasto-plastic component</u>
Mastic	$E = 176 \text{ MPa}, \nu = 0.3$ $\eta_d = 110 \text{ MPa} \cdot \text{s}, \eta_v = 1000 \text{ MPa} \cdot \text{s}$	$E = 176 \text{ MPa}, \nu = 0.3$ $c_{y_0} = 0.12 \text{ MPa}, c_{y_\infty} = 0.35 \text{ MPa}$ $\phi = 0.25 \text{ rad}, \delta = 90$
Aggregate-mastic bond	$E = 100 \text{ MPa}, \nu = 0.3$ $\eta_d = 70 \text{ MPa} \cdot \text{s}, \eta_v = 1000 \text{ MPa} \cdot \text{s}$	$E = 176 \text{ MPa}, \nu = 0.3$ $c_{y_0} = 0.09 \text{ MPa}, c_{y_\infty} = 0.35 \text{ MPa}$ $\phi = 0.15 \text{ rad}, \delta = 90$

9.6.4 Moisture induced damage simulations

Case 0: dry response

To enable the comparison between the added damage which is induced by the moisture, first a zero case simulation is performed for the dry material. The dry response of the mesh is evaluated during several loading cycles at the six locations as shown in Fig. 9.6.9.

In Fig. 9.6.10 the damage development at the six locations is plotted against time, for 137 loading cycles. Ksi is the measure of damage development which is used in all the analyses, and is the equivalent plastic strain ξ , defined in Eq. 7.40.

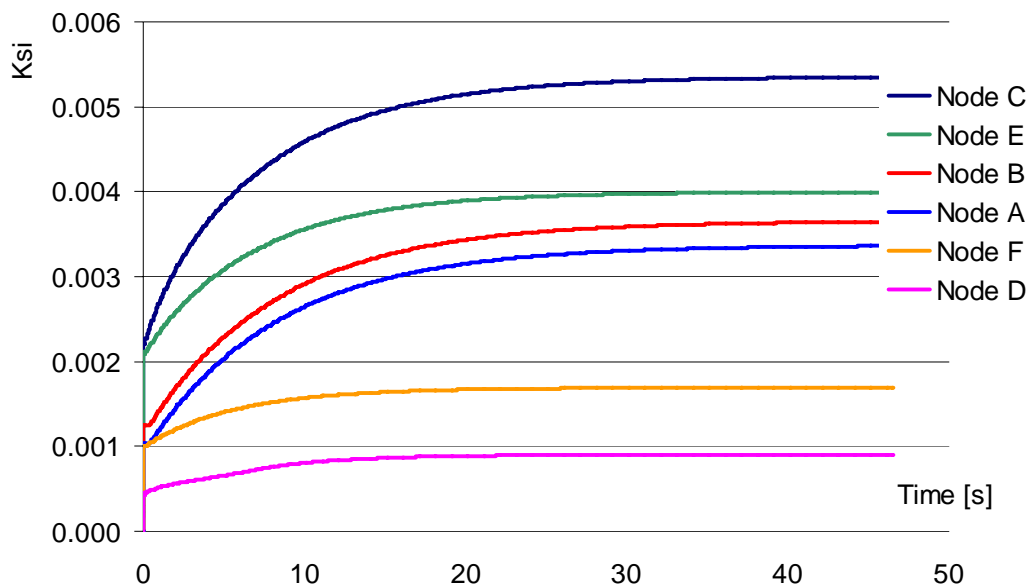


Fig. 9.6.10: Damage generation for the dry mix, 250 loading cycles

As can be seen from the graphs, most damage is generated in node C and E after 250 loading cycles, which are both located near a boundary with a next aggregate, Fig. 9.6.9.

The cyclic response of node C, node A and node D are plotted for 250 loading cycles in Fig. 9.6.11 through Fig. 9.6.13, respectively. In these, the top graph shows the response of the nodes, plotted in stress space (where I_1 and $\sqrt{J_2}$ are the first and second stress invariants, see Eq. 7.141 and Eq. 7.142), and the bottom graph shows the vertical stress-strain response. The ‘unhardened Drucker-Prager’ line, shown in the top graphs, indicates the original yield response of the material, before hardening. The plastic hardening of the material is modeled via a cohesion hardening, and is explained in more detail in Appendix 7.2.

As can be seen from the graphs, each node is exposed to a complex stress field, depending on the location in the mesh and its material properties.

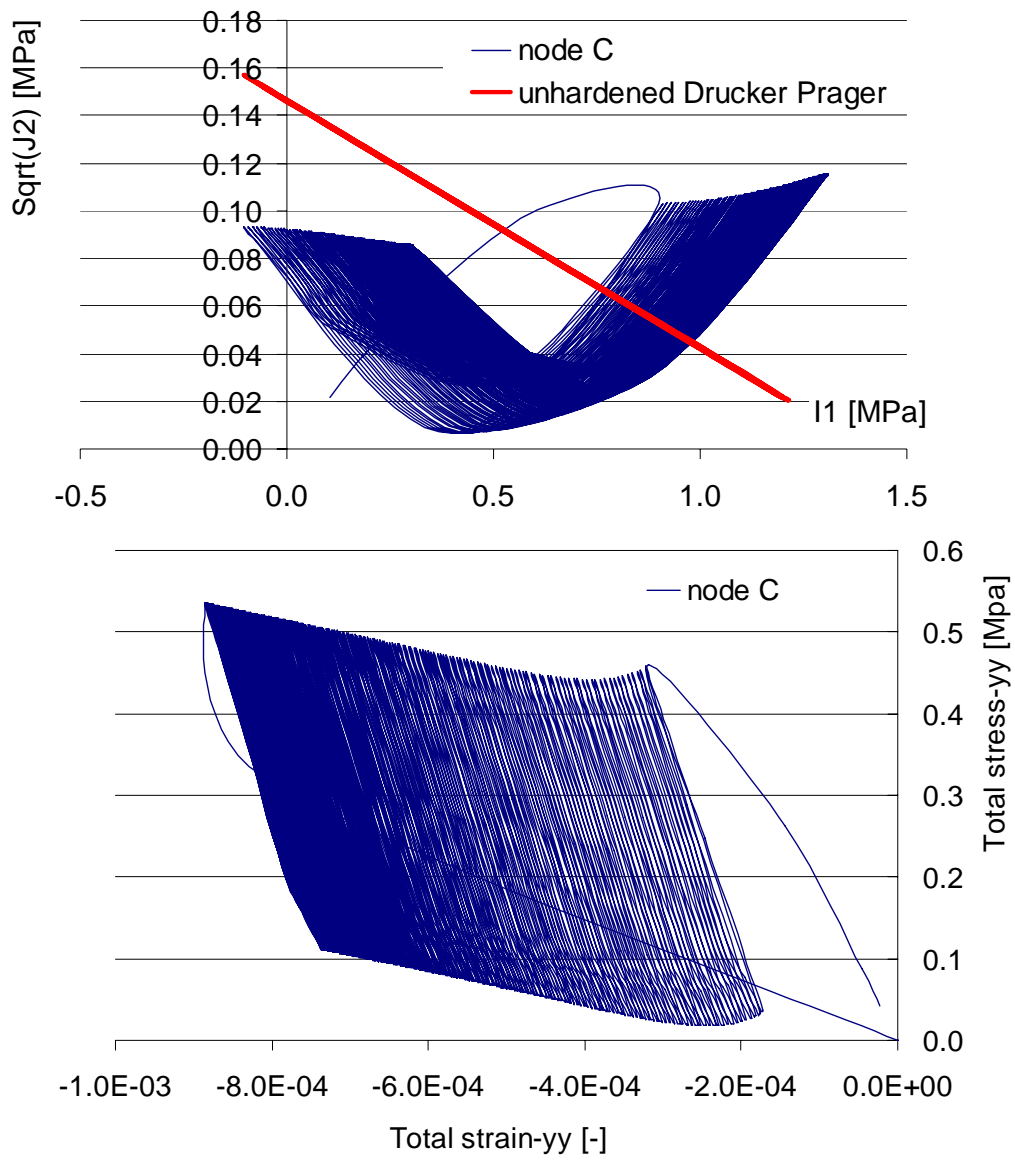


Fig. 9.6.11: Cyclic response of node C for the dry case

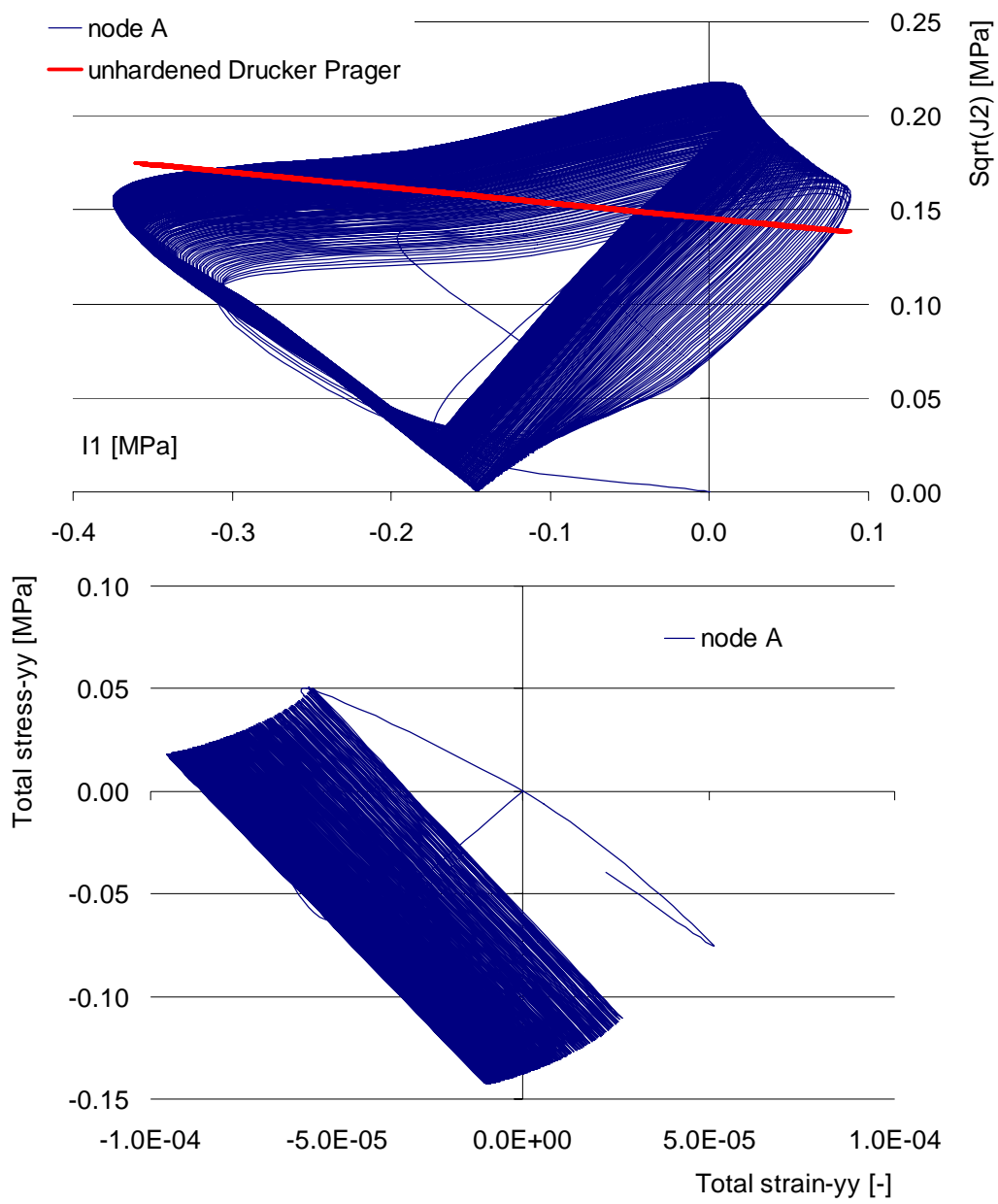


Fig. 9.6.12: Cyclic stress-strain response of node A, for the dry case

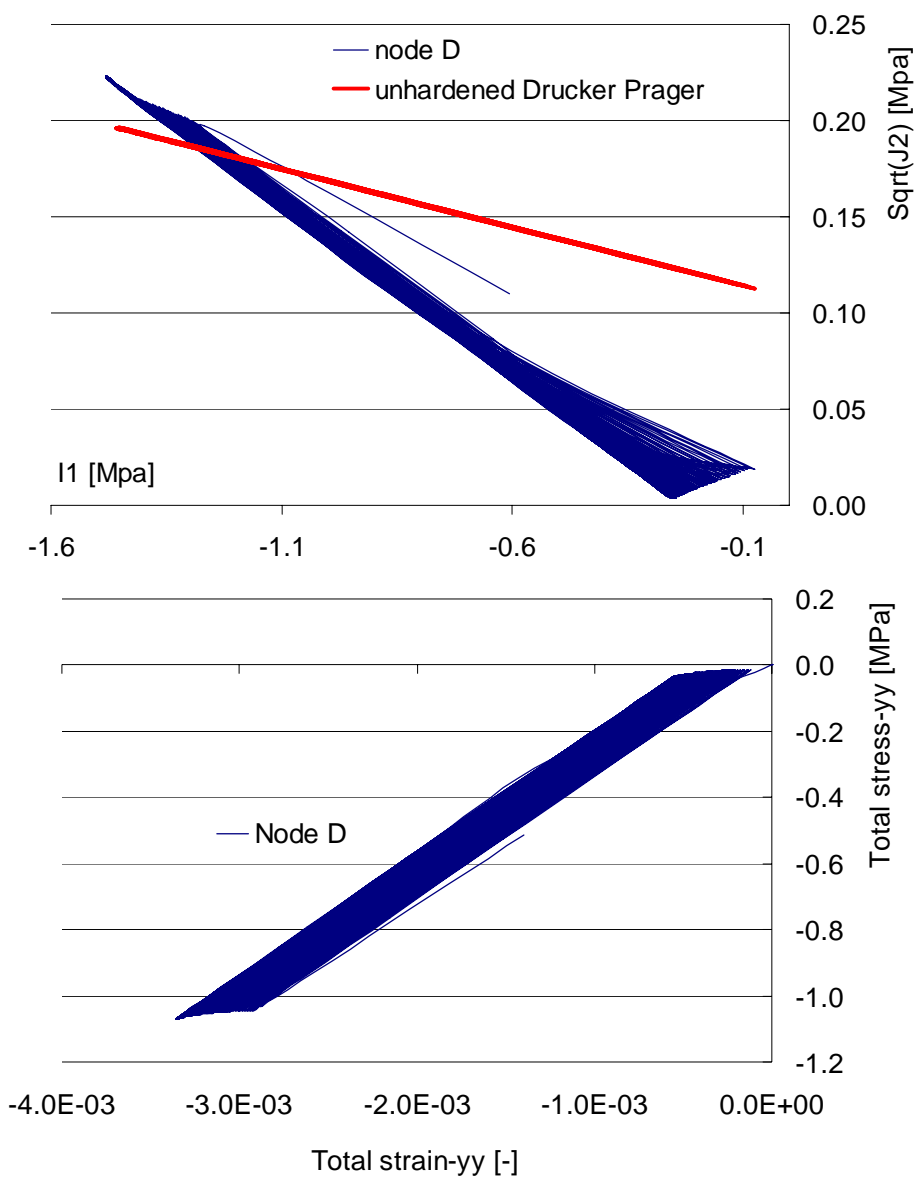


Fig. 9.6.13: Cyclic stress-strain response of node D, for the dry case

Case I & II: diffusion, with varying diffusion coefficients

As described in chapter 8 and section 9.6.2, the development of the moisture damage of the aggregate mastic bond interface, was defined as

$$d_{\theta}^{\text{if}} = 1 - e^{-\alpha_{\theta}^{\text{if}} \sqrt{\theta}} \quad (9.46)$$

where θ is the moisture content and $\alpha_{\theta}^{\text{if}}$ is the moisture susceptibility parameter of the aggregate-mastic interface.

For simplicity, and because of the lack of experimental evidence, the moisture damage development of the mastic, due to the presence of moisture is, similarly to the aggregate-mastic interface, defined as

$$d_{\theta}^{\text{mst}} = 1 - e^{-\alpha_{\theta}^{\text{mst}} \sqrt{\theta}} \quad (9.47)$$

where $\alpha_{\theta}^{\text{mst}}$ is the moisture susceptibility parameter of the mastic.

For the Case I and II, the moisture susceptibility parameters for the mastic and the aggregate-mastic bond are chosen as $\alpha_{\theta}^{\text{mst}} = 0.5$ and $\alpha_{\theta}^{\text{if}} = 0.7$, Fig. 9.6.14

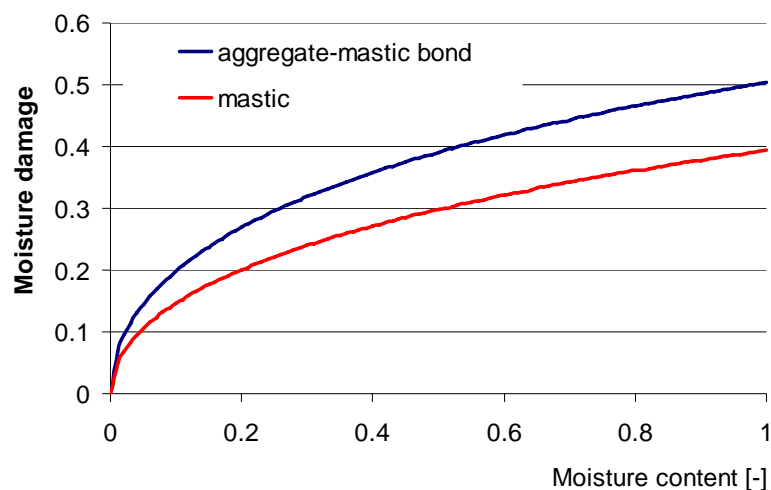


Fig. 9.6.14: Moisture damage development for Case I & II

For Case I a diffusion coefficient of $D_{\text{mst}} = 3 \cdot 10^{-3} \text{ mm}^2 / \text{hr}$ is used, based on a bitumen with moisture diffusivity $D_{\text{bit}} = 1 \cdot 10^{-4} \text{ mm}^2 / \text{hr}$ with 25%/by volume filler content with $D_{\text{fill}} = 1 \cdot 10^{-2} \text{ mm}^2 / \text{hr}$.

For Case II a diffusion coefficient of $D_{\text{mst}} = 1.5 \cdot 10^{-2} \text{ mm}^2 / \text{hr}$ is chosen, which is based on the same bitumen and filler percentage as in Case I, but with a filler with $D_{\text{fill}} = 1 \cdot 10^{-1} \text{ mm}^2 / \text{hr}$. In section 6.3.4 more details are given as to how these values were determined.

For both cases, it is assumed that the elements of the macro-pore, Fig. 9.6.5, are saturated with moisture. Numerical diffusion simulations are performed with RoAM, which shows the moisture infiltration into the mastic film, and eventually, the

aggregate-mastic interface. In the analyses, the elements which represent the aggregate-mastic interface are simulated with cubic elements and are given the same moisture diffusivity as the mastic film. The aggregate is assumed to have a diffusivity of $D_{agg} = 0.01 \text{ mm}^2 / \text{hr}$.

In Fig. 9.6.15 the gradual increase in moisture content in the asphalt mix for Case II is shown at several times.

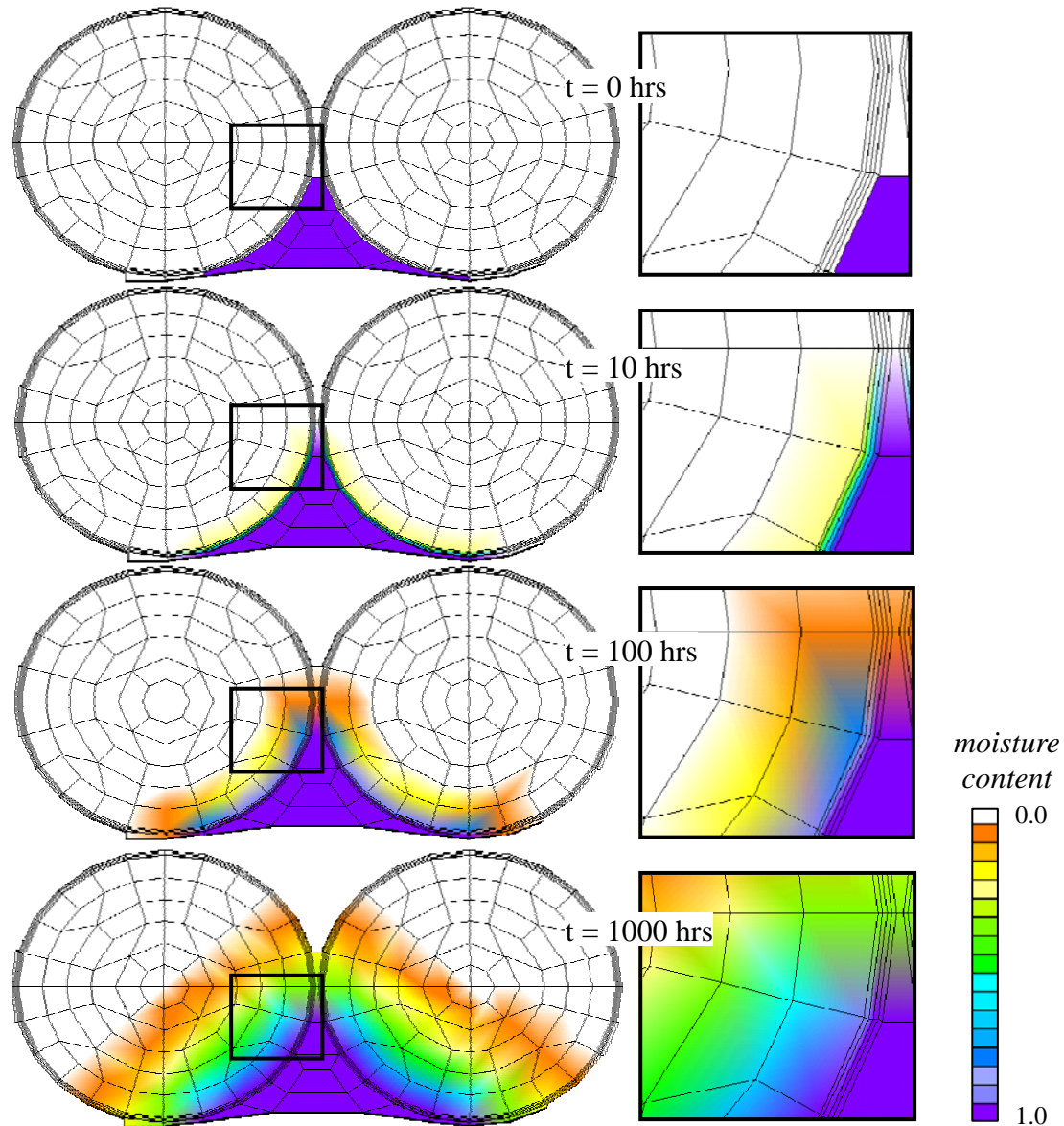


Fig. 9.6.15: Moisture diffusion for diffusion case II
with $D_{agg} = 0.01 \text{ mm}^2 / \text{hr}$ and $D_{mastic} = 0.015 \text{ mm}^2 / \text{hr}$

It can be seen that after 1000 hours (i.e. ~42 days) the mastic film, which was in direct contact with the macro-pore, has reached almost its maximum moisture capacity, whereas the mastic film further away from the macro-pore has reached 0 -50% of its maximum capacity.

Depending on the moisture susceptibility parameter α_θ of the asphalt components, different levels of moisture damage shall be reached after similar diffusion times. In Fig. 9.6.16 the moisture damage d_θ is shown for Case II after 42 days of moisture diffusion, utilizing the moisture damage development functions, as defined in Eq. (9.46) and Eq. (9.47).

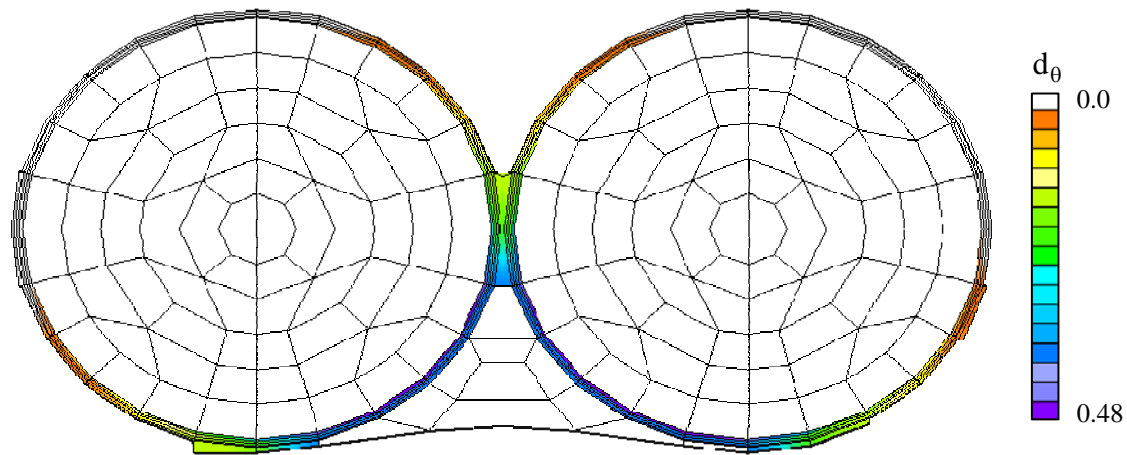


Fig. 9.6.16: Moisture damage after 42 days of moisture diffusion for Case II, i.e. $D_{\text{mst}} = 0.015 \text{ mm}^2 / \text{hr}$, $\alpha_\theta^{\text{if}} = 0.7$ and $\alpha_\theta^{\text{mst}} = 0.5$

Because the moisture damage development within the aggregates themselves is not considered in this study, i.e. $\alpha_\theta^{\text{agg}} = 0.0$, no moisture damage shall be generated in the aggregates, regardless of their moisture content.

In principle, the moisture diffusion processes and the mechanical loading cycles occur simultaneously. However, given the fast nature of the mechanical loading cycle, and the slow nature of the diffusion process, it does not make much computational sense to actually simulate the processes in parallel for only a few loading cycles. Rather, it is assumed in the parametric studies that the asphalt has already been exposed to moisture (from the macro-pore) for 42 days, after which it is subjected to mechanical loading.

Since Case I and II have different mastic diffusivity properties, after 42 days of moisture diffusion, the asphalt mix shall show a different behavior for the two cases, when exposed to the mechanical loading cycles.

In Fig. 9.6.18 and Fig. 9.6.17 a comparison is given between the response of Case 0, I and II, after being exposed to 42 days of moisture diffusion and 10 loading cycles. The comparisons are made for location A and D, which are located in the cohesive mastic area between the two stones and in the (adhesive) aggregate mastic interface area, respectively.

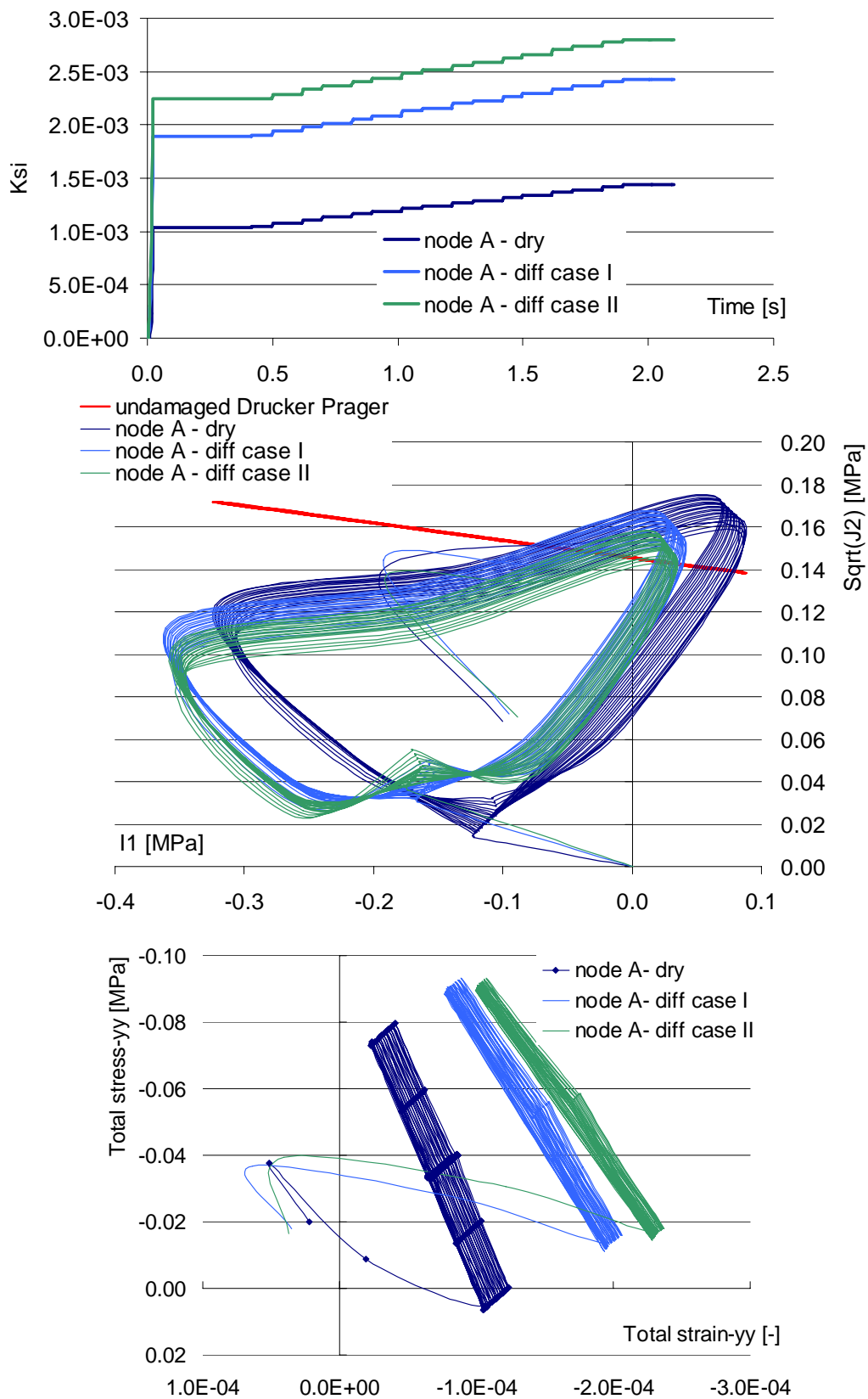


Fig. 9.6.17: Comparison of the response of node A, for the dry case 0 and case I and II with moisture diffusion conditioning

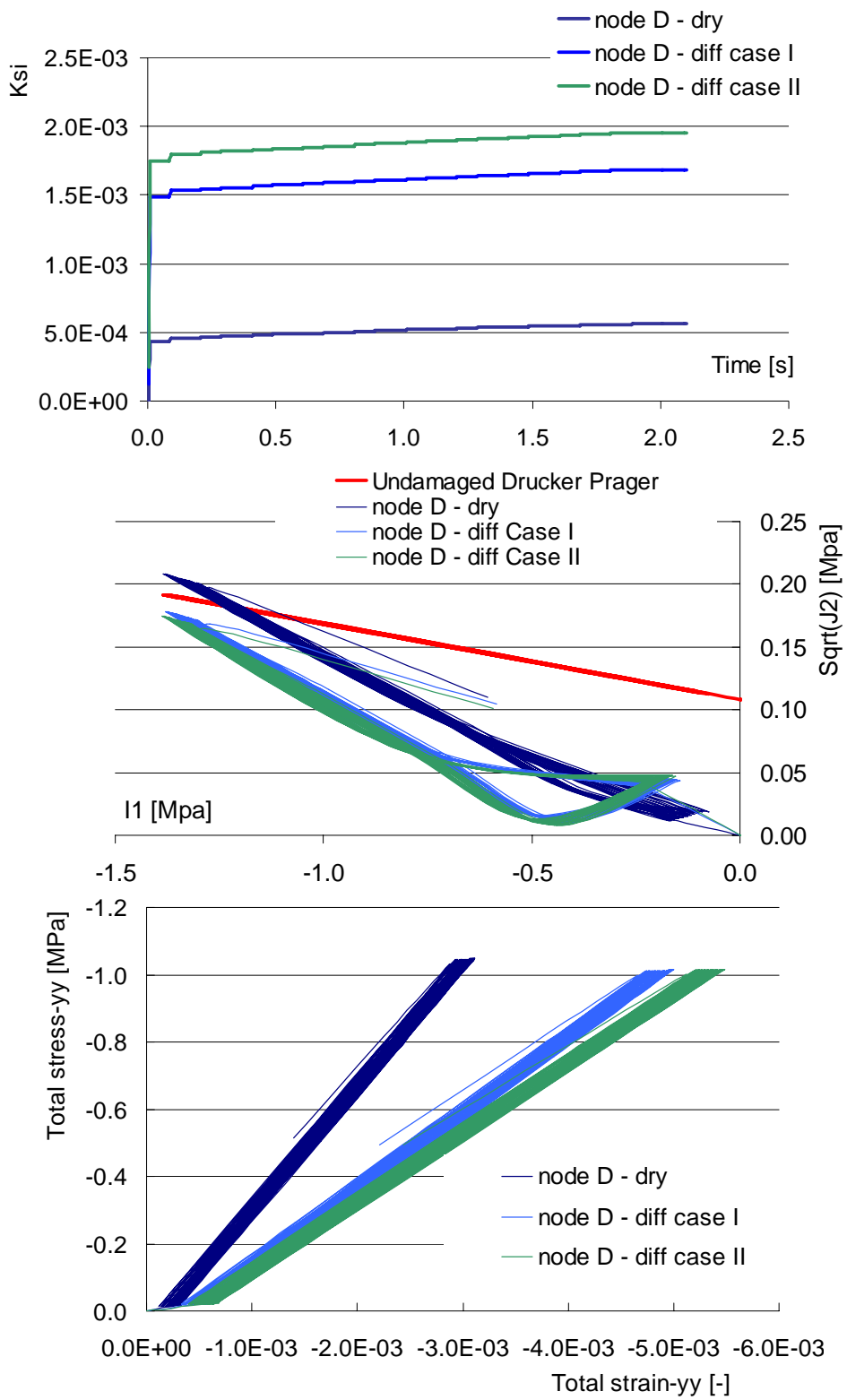


Fig. 9.6.18: Comparison of the response of node D, for the dry case and case I and II with moisture conditioning

From both graphs it can be seen that the moisture diffusion conditioned Case I & II develop a significant increase of damage (i.e. equivalent plastic strain) at both locations. Furthermore, the effect of the mastic diffusion coefficient on the damage development can be noticed by comparing the response of Case I and II.

In Fig. 9.6.19 the permanent deformation is shown at several locations for Case II.

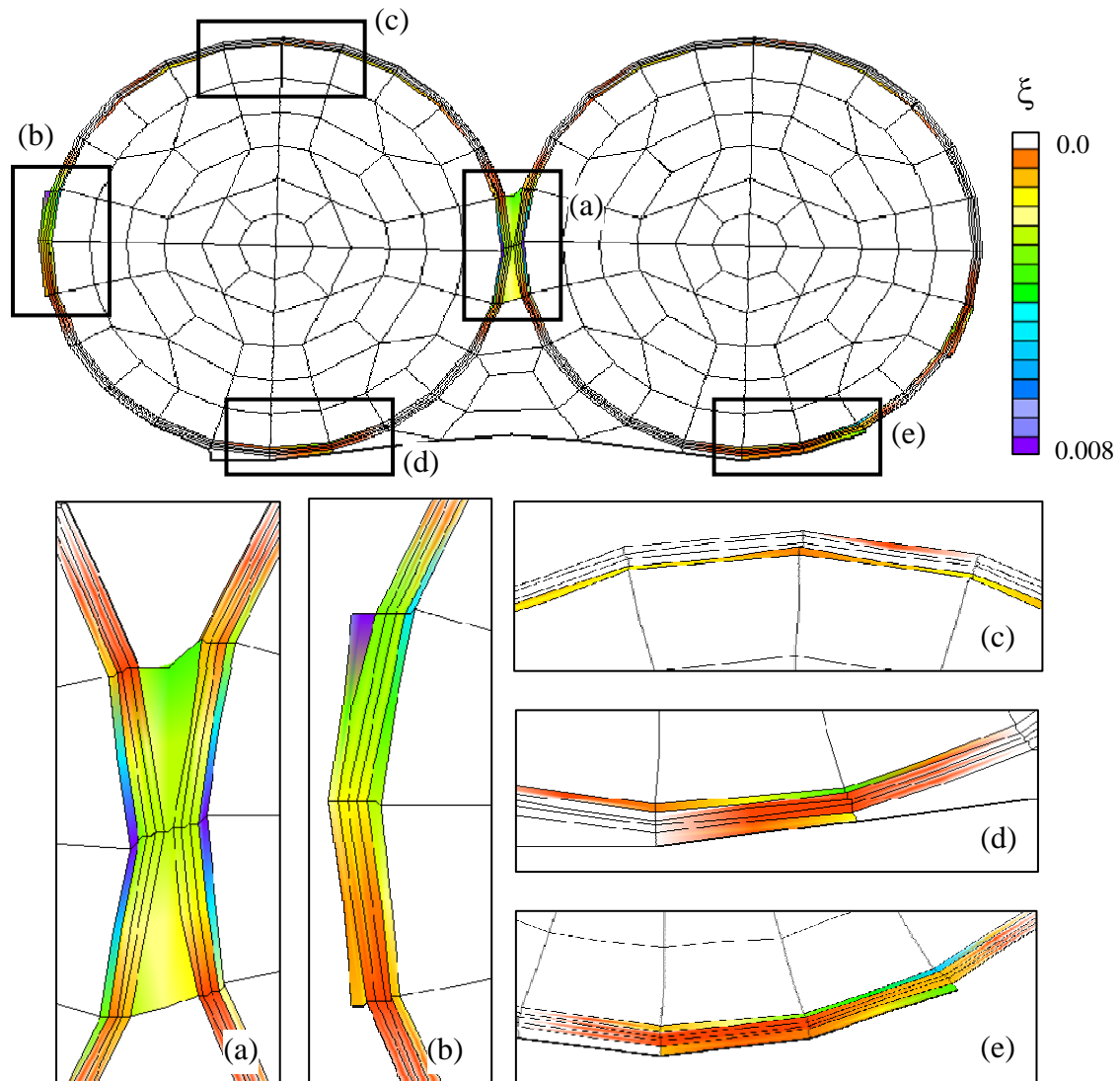


Fig. 9.6.19: Damage in the mastic and aggregate-mastic bond for Case II, after 42 days of moisture conditioning and 10 loading cycles (magn. 200x)

It can be seen from the figure that considerable damage is generated in the aggregate-mastic interfaces, which would indicate the onset of a ravelling process. Additionally, the mastic film between the stones and near the boundaries starts to generate damage.

Case III& IV: diffusion, with varying moisture susceptibility parameters

To demonstrate the effect of the moisture susceptibility parameters, in Case III and IV, the mastic diffusion coefficient is kept constant at $D_{\text{mst}} = 1.5 \cdot 10^{-2} \text{ mm}^2 / \text{hr}$, similar to Case II. The moisture susceptibility parameters for the mastic and the aggregate-mastic interface are chosen as $\alpha_{\theta}^{\text{mst}} = 0.0$ and $\alpha_{\theta}^{\text{if}} = 1.2$ in Case III and as $\alpha_{\theta}^{\text{mst}} = 1.2$ and $\alpha_{\theta}^{\text{if}} = 0.0$ in Case IV.

Case III represents an asphalt mix with a mastic type through which moisture does diffuse, but does not affect its properties, and an aggregate-mastic bond which degrades in the presence of moisture. Case IV represents an asphalt mix which has an aggregate-mastic bond which is not affected by moisture, even though the mastic is moisture susceptible.

Again, location A and D are used to show the effect of the moisture susceptibility parameters on the material response, Fig. 9.6.20 and Fig. 9.6.21.

It can be seen that the ‘cohesive interface’ between the stones (location A) damages most in Case IV and the adhesive interface (location D) damages most in Case III. Since they correspond to locations within the mastic and the aggregate-mastic area, respectively, this makes perfect sense given that Case IV is not susceptible to moisture damage in the interface and Case III is not susceptible to moisture damage in the mastic.

However, it can also be noticed that, because of the interactions between the materials and the redistributions of stresses internally, due to locally weakened materials, the interface response is still slightly affected in the non-moisture susceptible interface case and the same goes for the mastic in the non-moisture susceptible mastic case.

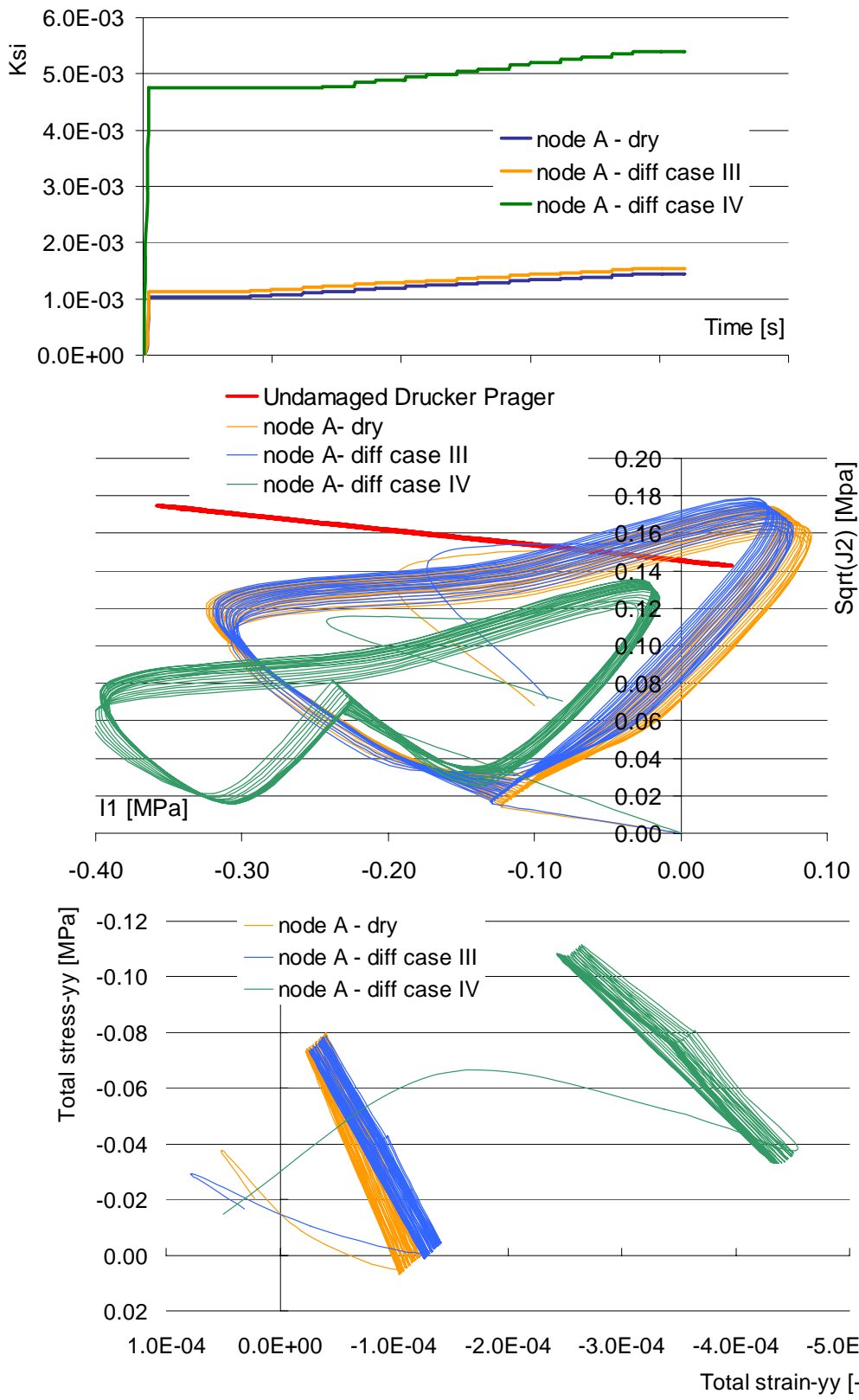


Fig. 9.6.20: Comparison response of node A, between case 0 and diffusion case III and IV

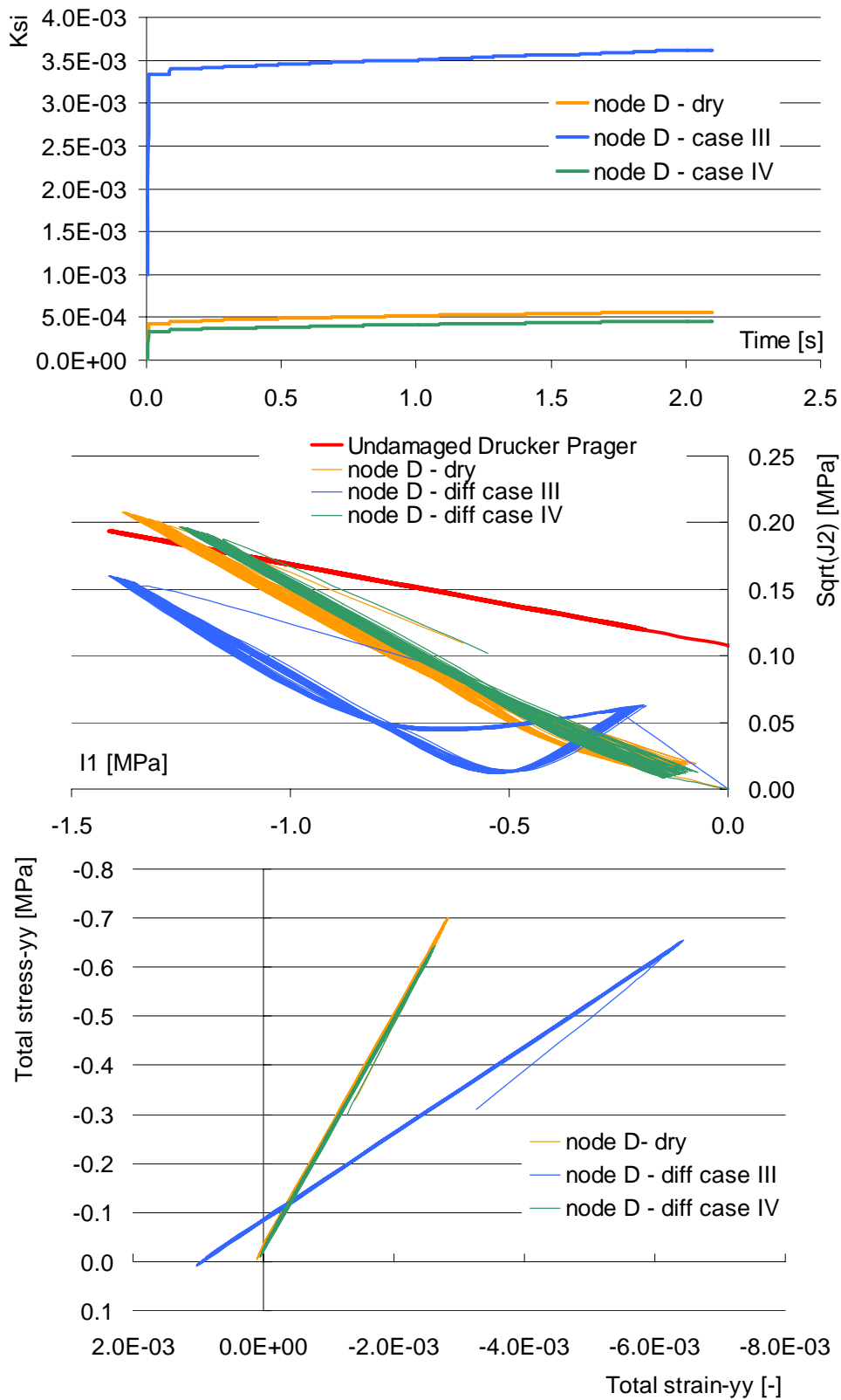


Fig. 9.6.21: Comparison of response of node D, between case 0 and diffusion case III and IV

In Fig. 9.6.22 and Fig. 9.6.23 the response of node D and node A after 3000 loading cycles is compared for the dry case (Case 0) and case II and Case III.

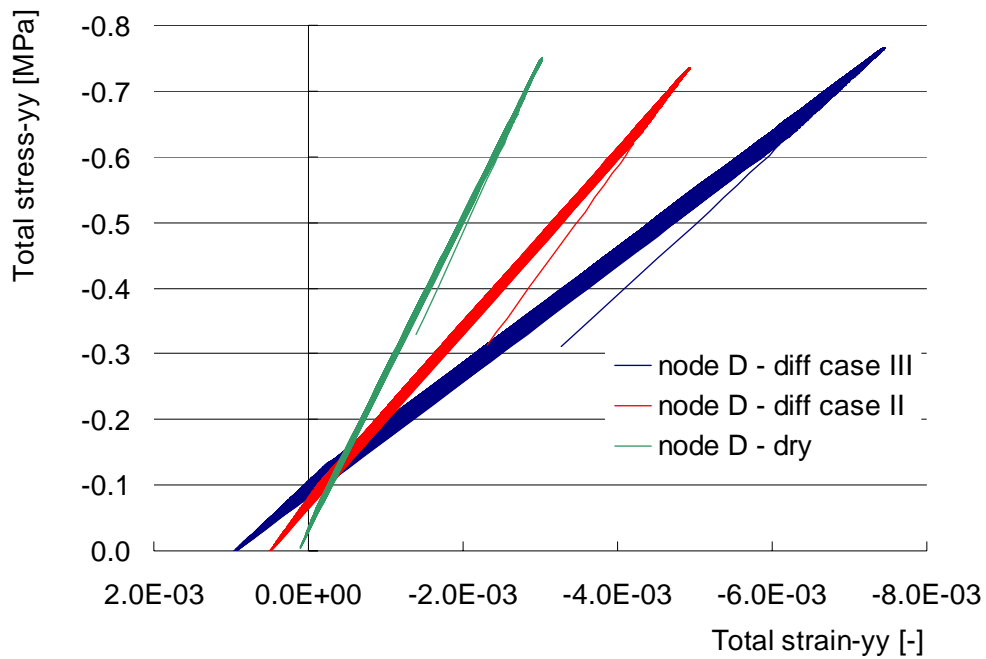


Fig. 9.6.22: Stress-strain response of node D for Case0, Case II and Case III for 3000 loading cycles

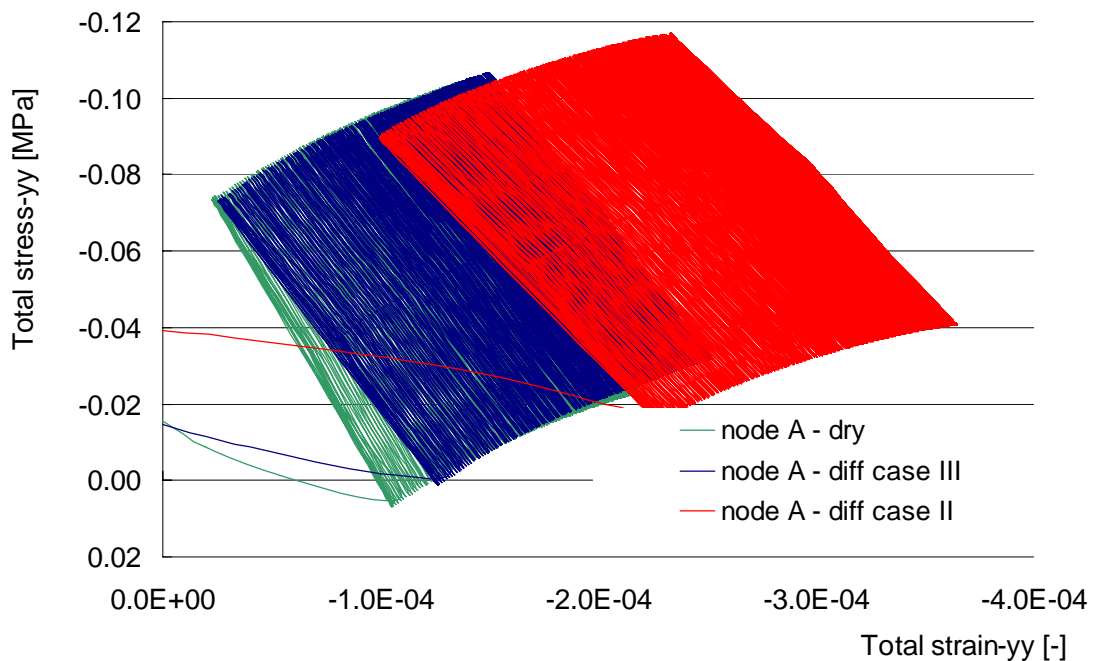


Fig. 9.6.23: Stress-strain response of node A for Case 0, Case II and Case III for 3000 loading cycles

It can be seen that node A is more affected in case II and node D in case III. This would be expected, since node A is part of the mastic and node D is part of the

interface. In Fig. 9.6.24 a visual comparison is given between the permanent deformation at the location between the two simulated stones for Cases 0- IV.

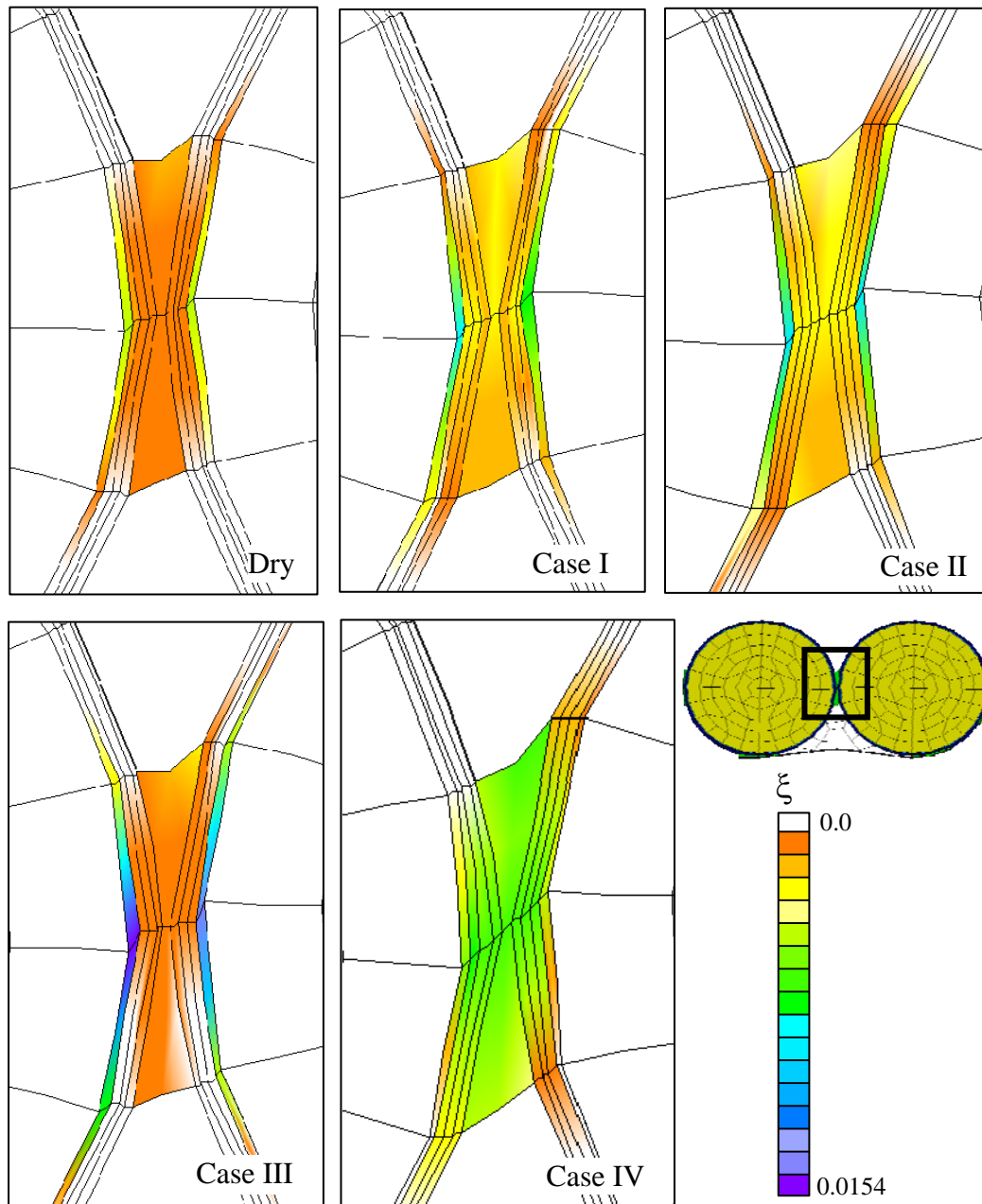


Fig. 9.6.24: Comparison of damage development for the various cases after 10 loading cycles (magn. 300x)

From the comparison between the accumulated damage and the resulting deformation, it can be concluded that the materials with the moisture susceptibility characteristics used in Case III would most likely show an adhesive failure in the field (i.e. raveling of the mix), whereas Case IV would show a more pronounced cohesive failure within the mastic films. From the comparison between Case II and III it can be concluded that for materials with a given moisture (damage) susceptibility, the moisture diffusion coefficients become the dominant parameter which decided which failure pattern would occur in the field. The normal and shear stress distribution within the

mesh is shown for Case II, during the second loading cycle, Fig. 9.6.25 and Fig. 9.6.26 respectively.

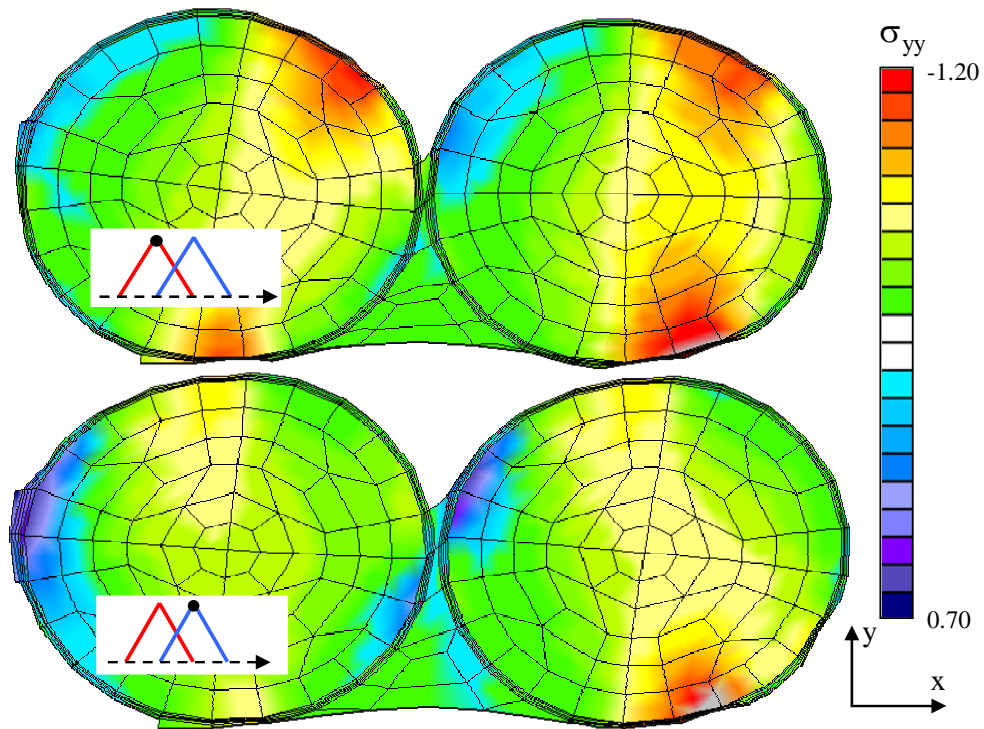


Fig. 9.6.25: Stress-yy development within the materials for Case II, during the second loading cycle

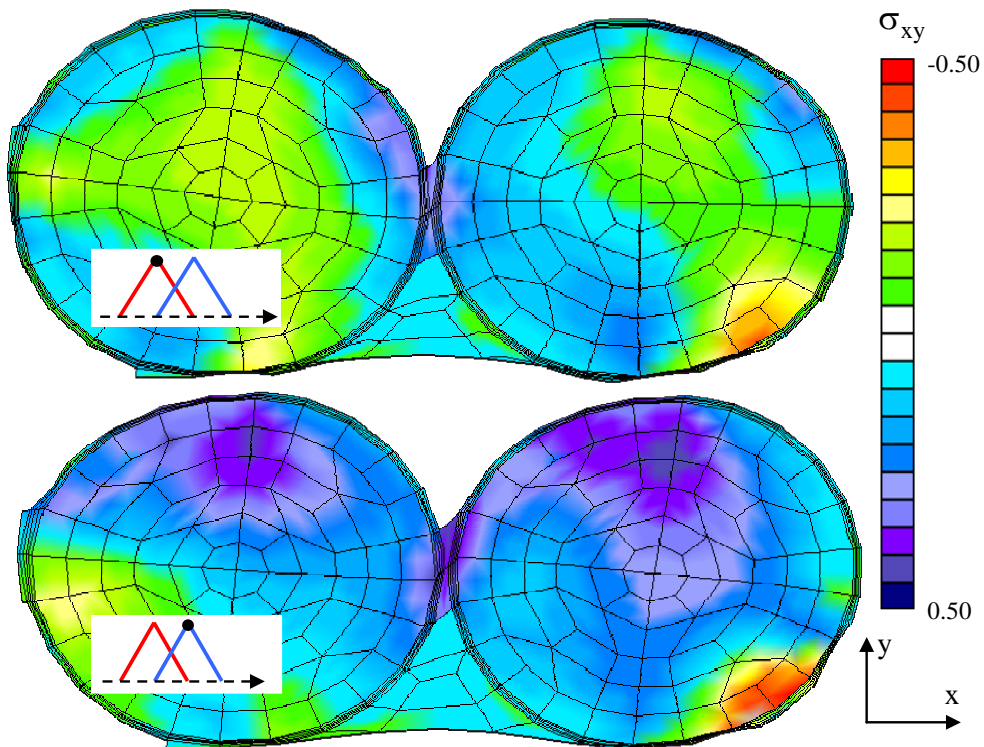


Fig. 9.6.26: Stress-xy development within the materials for Case II, during the second loading cycle

It was mentioned earlier that in the dry simulation (Case 0) location C was generating most damage. Since this location is not nearby the area of the macro-pore, less moisture induced damage is generated in location C, in comparison with the other locations. As can be seen from Fig. 9.6.27, in Case I and II node E is generating most damage, followed by node C. In Case III most damage occurs in node E and F and in Case IV most damage is generated in locations B and A.

From the comparison between the changing order of dominant damage development locations between the Cases, it can be concluded that for different moisture susceptibility parameters of the individual components and their bond, *completely different damage patterns may be generated within the asphalt mix*. In Case 0, damage would probably start from an aggregate dislodging effect from the mix, and in Case I & II it may be a combined cohesive and adhesive failure which would develop. In Case IV, most likely failure would first occur between the two stones, whereas in Case III, failure would probably start from a stripping action between the mastic and the stone. Improvement of the asphalt mix performance would therefore imply improvement of different parameters in the various cases.

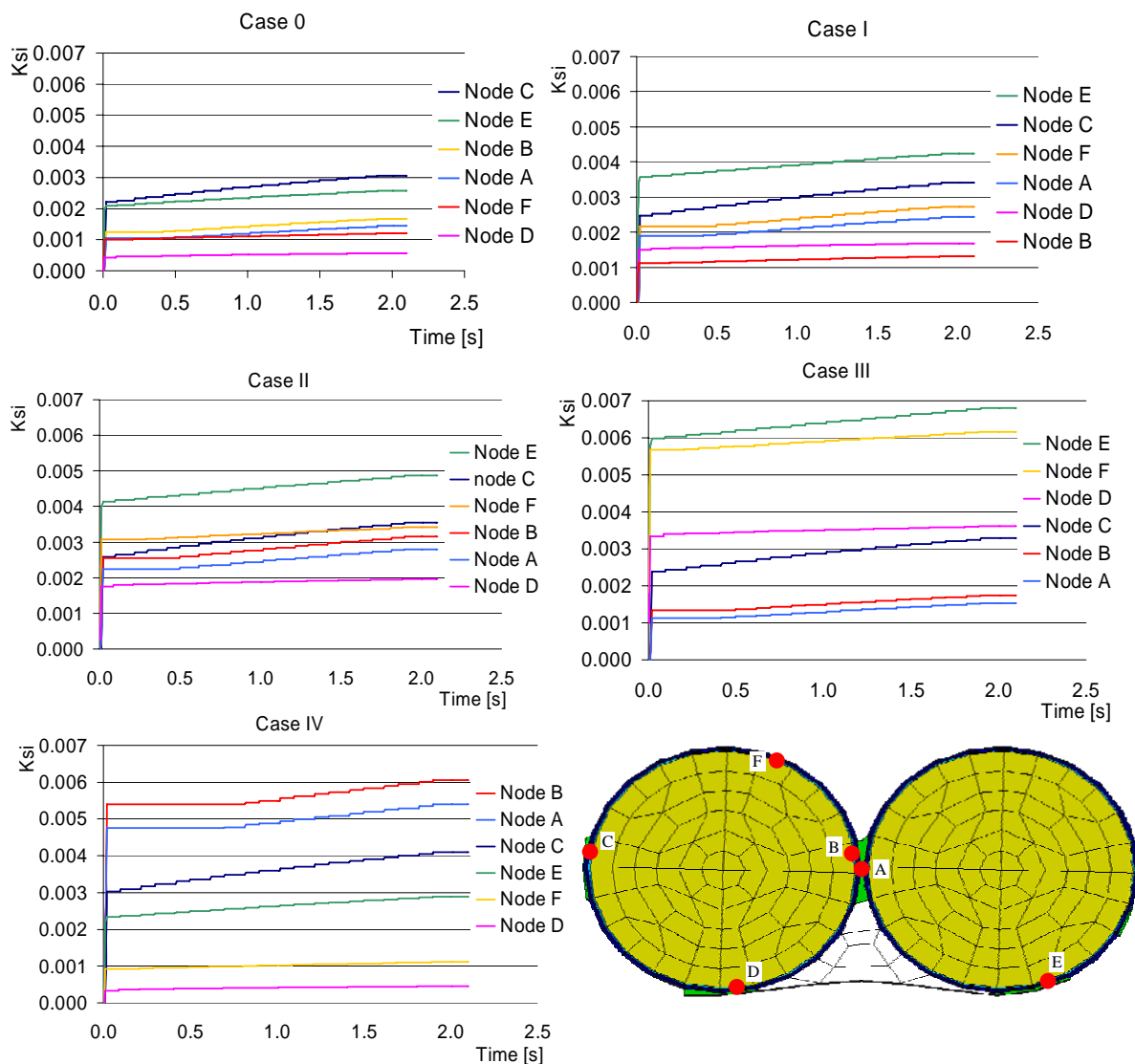


Fig. 9.6.27: Dominant damage development for Case 0 - IV

Case V- VIII: Pumping action

In Case I through IV, moisture damage was induced via a moisture diffusion process. Because of the time differences in which mechanical loading occurs and moisture diffusion progresses, in the simulations, the asphalt was preconditioned by exposure to moisture, before mechanical loading was applied. As discussed in previous sections, in addition to moisture induced damage due to diffusion, another type of moisture induced damage that may occur and which influences the damage patterns which would ultimately develop, is an erosion of the mastic due to high water pressures.

In addition to the loss of mastic, the water pressure may cause additional stresses on the mix, which may cause added plastic deformation (i.e. mechanical damage), Fig. 9.6.28. The first process is considered in this research as a *mechanical* and the latter as a *physical* moisture induced damage process.

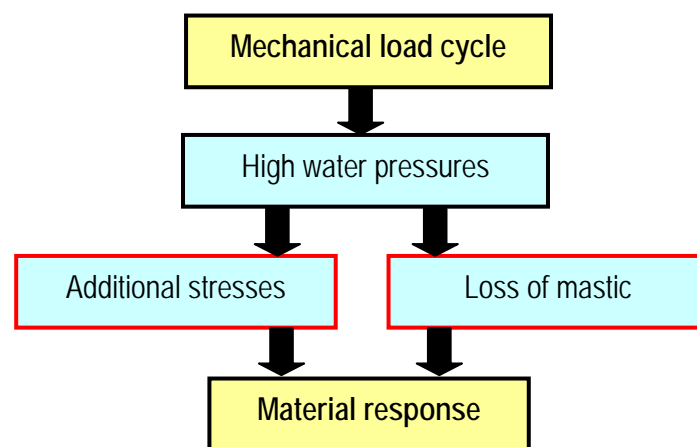


Fig. 9.6.28: Principle of damage due to pumping action

Unlike the moisture diffusion process, which occurs over a longer timeframe, the erosion of mastic due to the pumping action occurs on the same timeframe as the mechanical loading process, since one is a direct consequence of the other.

In Case V the mechanical moisture induced damage process is addressed, without physical damage to the mastic due to moisture diffusion or erosion. In Cases VI through VIII the combined action of the mechanical and physical moisture induced damage due to the pumping action is shown, again without considering moisture diffusion. Then, in Case IX through XII the combined action of moisture diffusion, erosion and mechanical loading is demonstrated.

Case V: Pumping Action: added mechanical damage

To simulate the (mechanical) damage which is generated by the pumping action of the traffic load, the elements of the macro-pore of the mesh, Fig. 9.6.5 , are simulated as fully saturates porous-media elements [Liu 2003]. Therefore, imposing the mechanical loading cycle on the mesh, water pressure is generated within the macro-pore elements. Fig. 9.6.29 shows that, under the imposed loading cycle, the water pressure builds up to maximum value of 0.20 MPa and drops to zero when the loading is reduced.

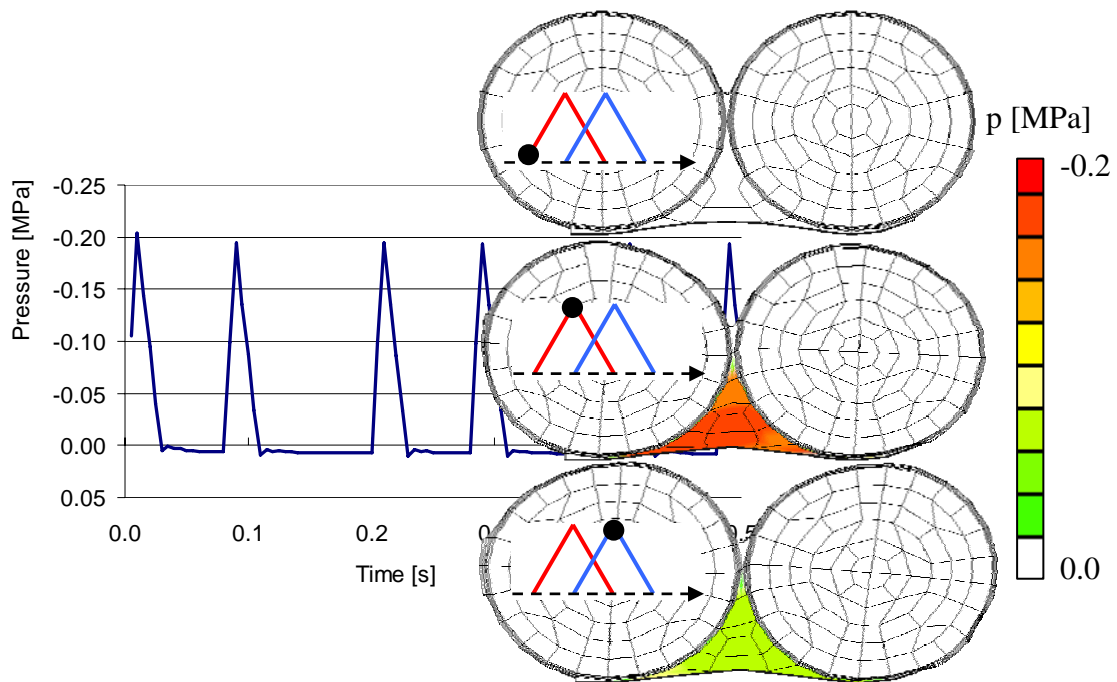


Fig. 9.6.29: Water pressure in the macro-pore

In the analyses, the hydraulic conductivity and the porosity of the macro-pore is maximized, in order to simulate the characteristics of the pore-space. To verify that the water pressure in the macro-pore of the micro-scale mesh is of the correct order of magnitude, also a macro-scale finite element porous media analysis was performed. In this analysis, the traffic loading was applied on the top of the asphalt wearing surface via a moving load simulation. The material properties of the asphalt were kept as close as possible to the micro-scale mesh properties. From this analyses it followed, that the water pressure was indeed in the same range as found in the micro-mesh.

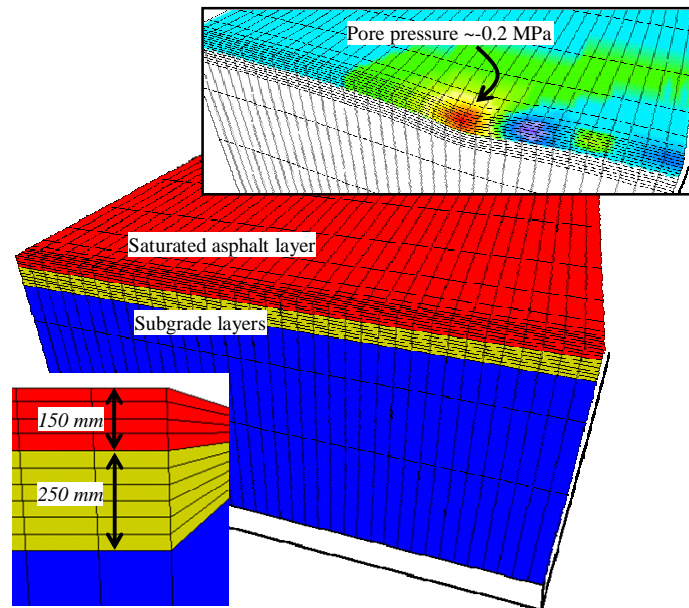


Fig. 9.6.30: Simulation of moving wheel load to confirm pore pressure loading, due to the pumping action of the wheel load

Comparing the damage which is generated after 10 loading cycles in the dry mesh (Case 0) with the mesh including the water pressure in the macro-pore (Case V), it is found that in some locations more damage is generated (node A and B), in some there is no added damage due to the water pressures (node F) and in others there is actually a reduction in damage, compared to the dry simulation (node C, D and E), Fig. 9.6.31.

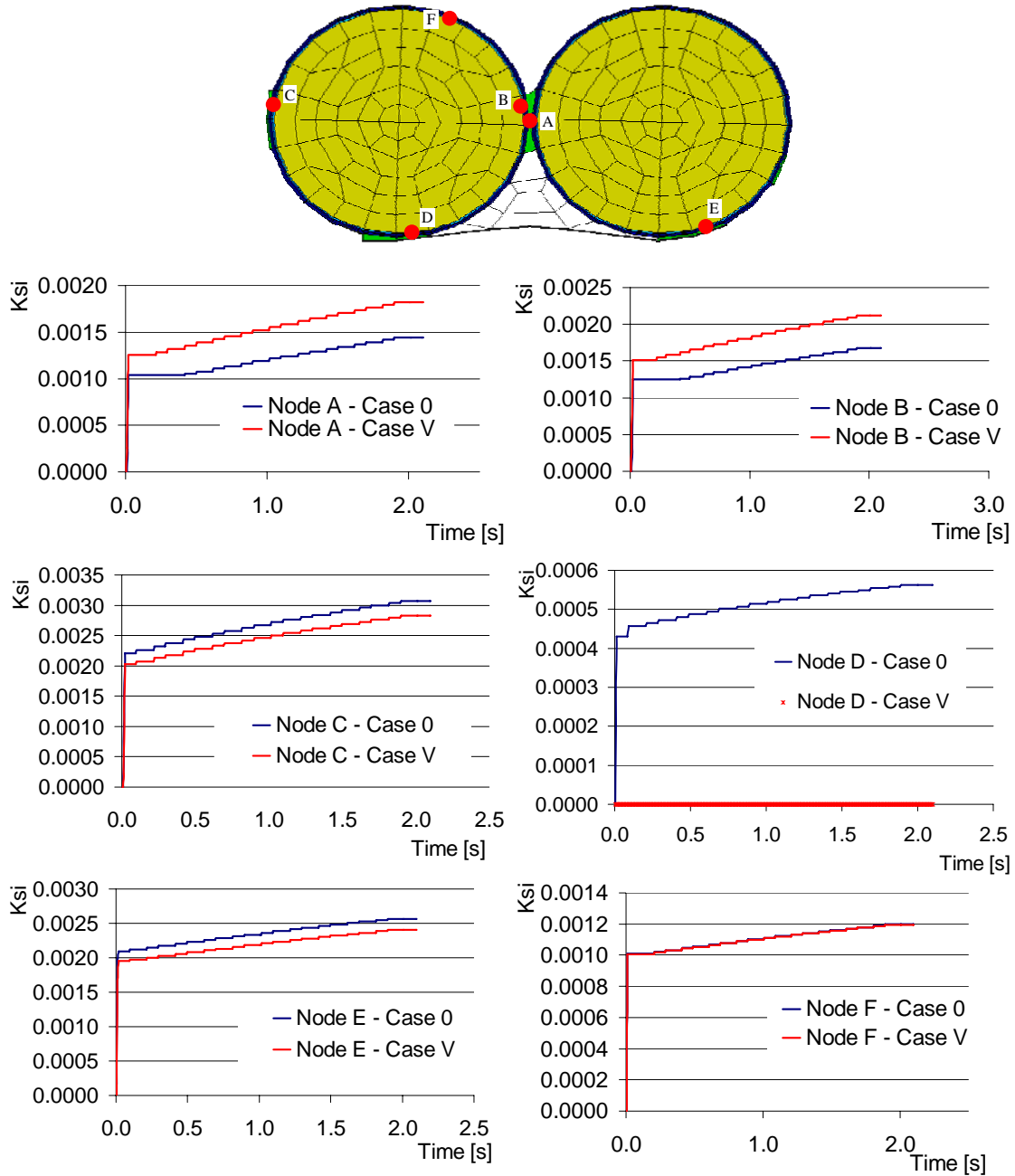


Fig. 9.6.31: Comparison plastic deformation generation Case 0 and Case V

It can therefore be concluded that the added mechanical damage in the case of a pumping action on the asphalt, based only on mechanical moisture induced damage processes, is *mainly harmful for the cohesive connection between the aggregates*. In the case of the particular geometry of the chosen mesh and boundary conditions, it can also be seen that the water may actually absorb some of the stresses near the boundaries to other aggregates, with this reducing the generation of damage at these locations. It should be noted, however, that with a changing geometry and locations of the macro-pores, the mechanical punishment may be differently distributed.

Case VI & VII: Pumping action with physical and mechanical damage

In Case V, the only added damages which would arise from the water in the asphalt's macro-pores, would be additional (mechanical) damage to the material, due to the locally high water pressure. As explained earlier, these pressures may also cause an erosion of the mastic due to an advective transport process. In Case VI and VII the erosion of mastic is included in the analyses, where the mastic desorption coefficient is chosen as $K_d = 1.0 \text{ mm}^3 / \text{g}$.

Depending on the moisture damage susceptibility parameter of the mastic as a function of the changing density, mastics with similar desorption coefficients may show different damage patterns. The loss of mastic concentration was expressed earlier in the normalized mastic density value

$$\hat{\rho} = \frac{\rho(x, t)}{\rho_0} \quad (9.48)$$

where ρ_0 is the original, undamaged, mastic density. In other words, when $\hat{\rho} = 1.0$, no mastic has been lost, and in the extreme case of $\hat{\rho} = 0.0$, all mastic is lost.

The relationship between the actual weakening of the material as a function of mastic density, does not have to be linear. In the analyses, the damage in the mastic film, due to loss of mass, is expressed as

$$d_{\hat{\rho}} = 1 - \hat{\rho}^{\alpha_{\hat{\rho}}} \quad (9.49)$$

where $\alpha_{\hat{\rho}}$ is the moisture damage susceptibility parameter of the mastic in the presence of water pressure gradients.

For Case VI and VII, $\alpha_{\hat{\rho}}$ has been chosen as 2.0 and 5.0, respectively, Fig. 9.6.32.

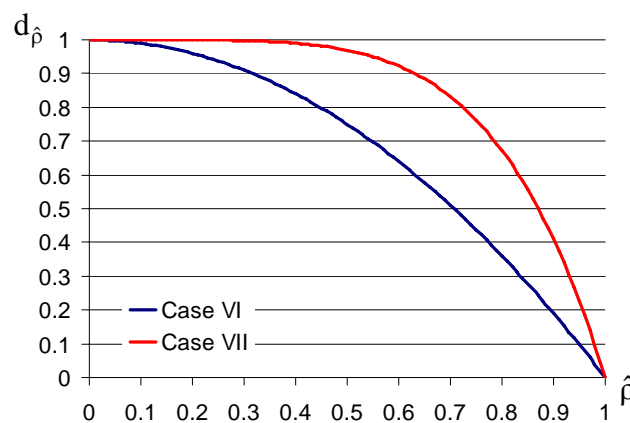


Fig. 9.6.32: Mastic damage development $d_{\hat{\rho}}$ as a function of loss of concentration

In Fig. 9.6.33 the erosion of mastic over time in Case VI and VII is shown.

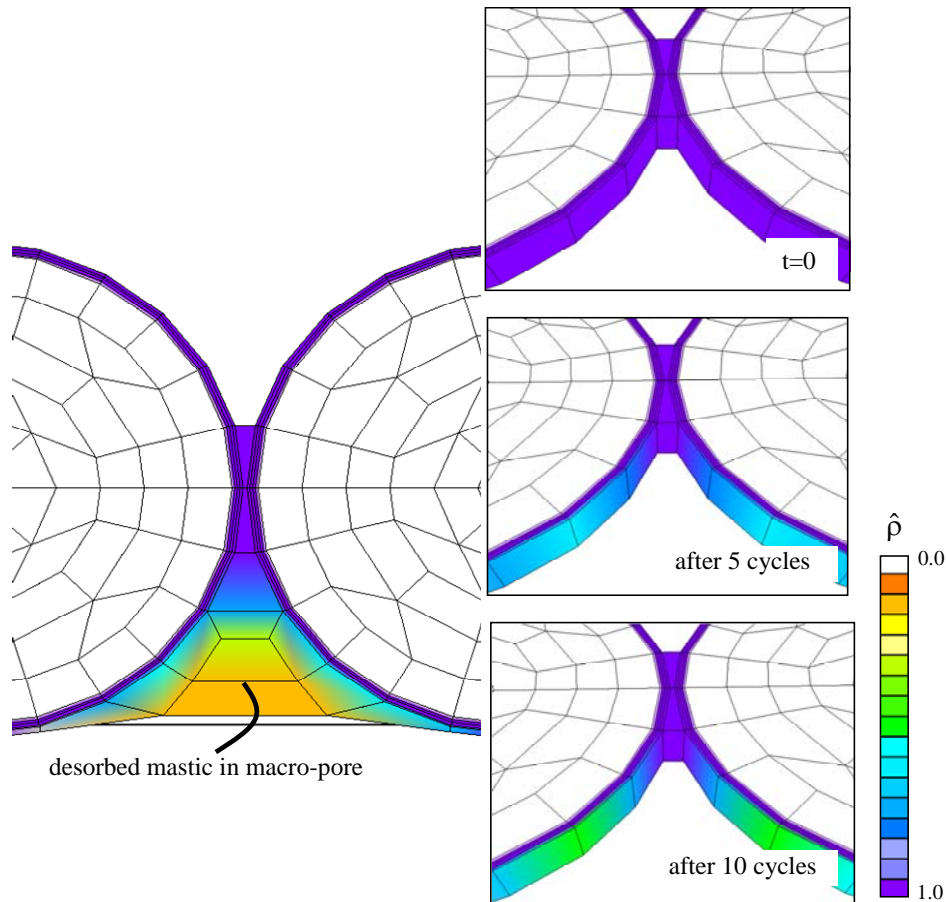


Fig. 9.6.33: Erosion of mastic for 10 loading cycles, $K_d = 1.0 \text{ mm}^3 / \text{g}$

In Fig. 9.6.34 and Fig. 9.6.35 a comparison of the response of node A and B is shown, respectively, for Case V, VI and VII. Node A is located in the mastic patch between the two stones and node B is located in the mastic film adjacent to the macro-pore.

What is most noticeable about the response in Case VI and VII in both locations, is the gradual increase of equivalent plastic damage per cycle. This follows from the coupling between RoAM and CAPA-3D, which updates the (mechanical) material properties for at a prescribed set of times, depending on the loss of mastic due to the erosion effect. Since each loading cycle will decrease the mastic density, and therefore increase the damage parameter $d_{\hat{\rho}}$, depending on the desorption parameter K_d of the mastic and the moisture damage susceptibility parameter of the mastic $\alpha_{\hat{\rho}}$, increased plastic deformation and a weakened response will result.

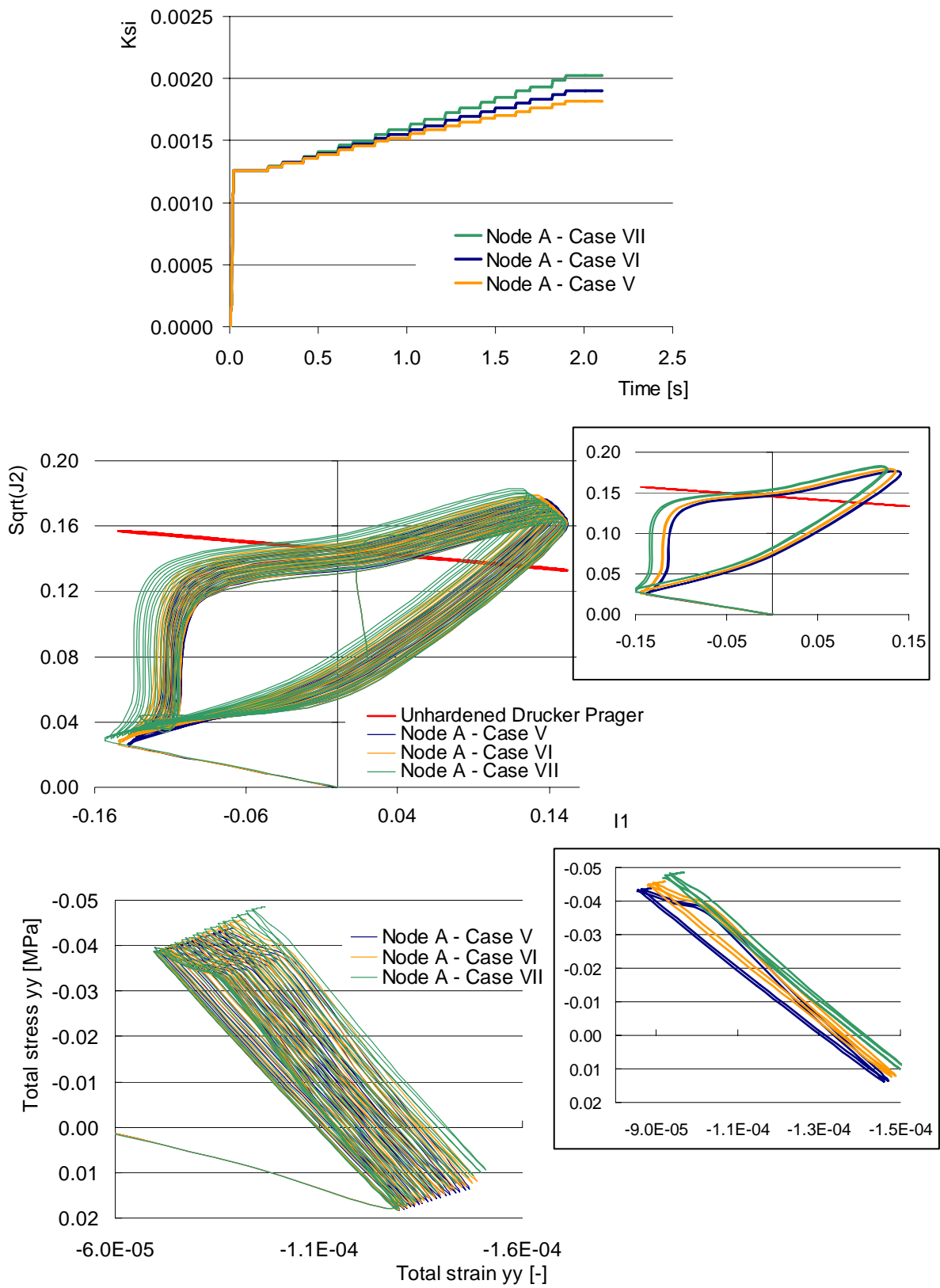


Fig. 9.6.34: Comparison response of node A for Case V, Case VI and Case VII

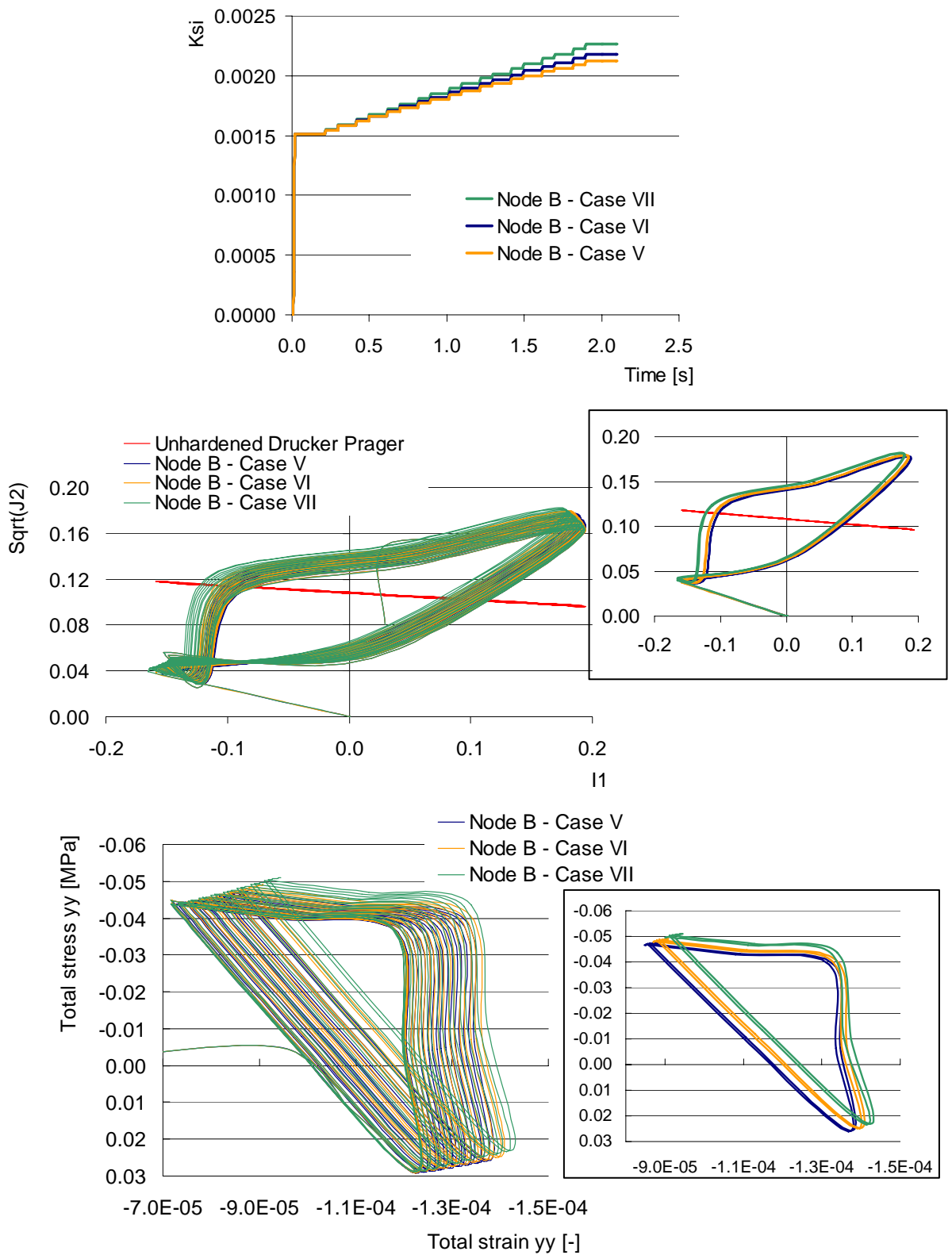


Fig. 9.6.35: Comparison response of node B for Case V, Case VI and Case VII

Case VII & VIII: Pumping action with physical and mechanical damage

To show the possible impact of the desorption (erosion) coefficient of the mastic, a comparison is made between Case VII and Case VIII, in which both cases have a mastic moisture susceptibility parameter $\alpha_{\hat{\rho}}$ of 5.0, but Case VIII has a higher mastic desorption coefficient of $K_d = 5.0 \text{ mm}^3 / \text{g}$.

These two cases, together with Case V which does not include physical damage, are compared in Fig. 9.6.36 and Fig. 9.6.37 for node A and B.

From the graphs it can be seen that for both A and B a significant increase in generated equivalent plastic strain can be seen for case VIII, in comparison to case VII and V. This shows the impact of more significant erosion parameters of the mastic. It should be noted that the other nodes do not show a similar impact, which is logical given their distance from the macro-pore.

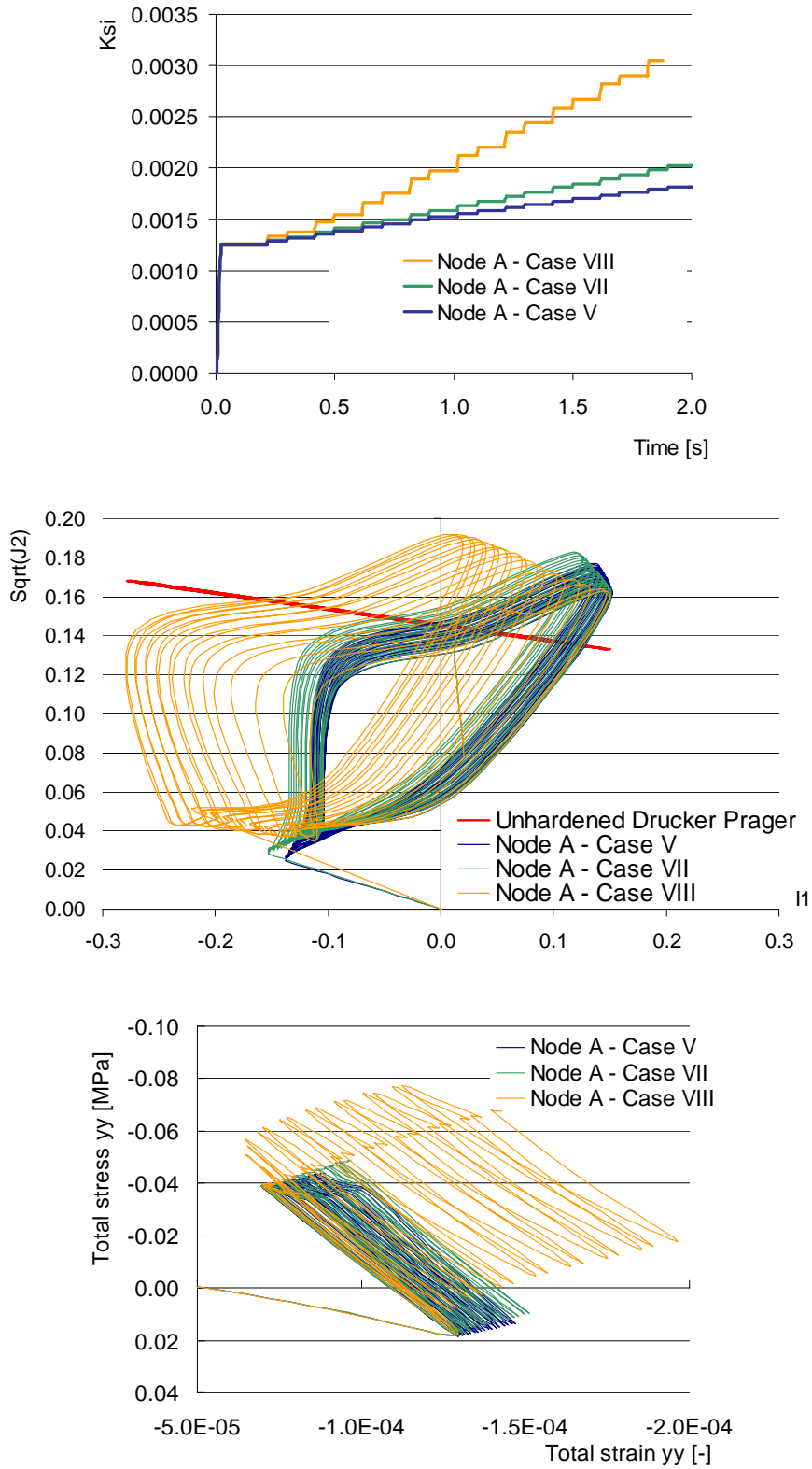


Fig. 9.6.36: Comparison response node A for Case V, VII and VIII

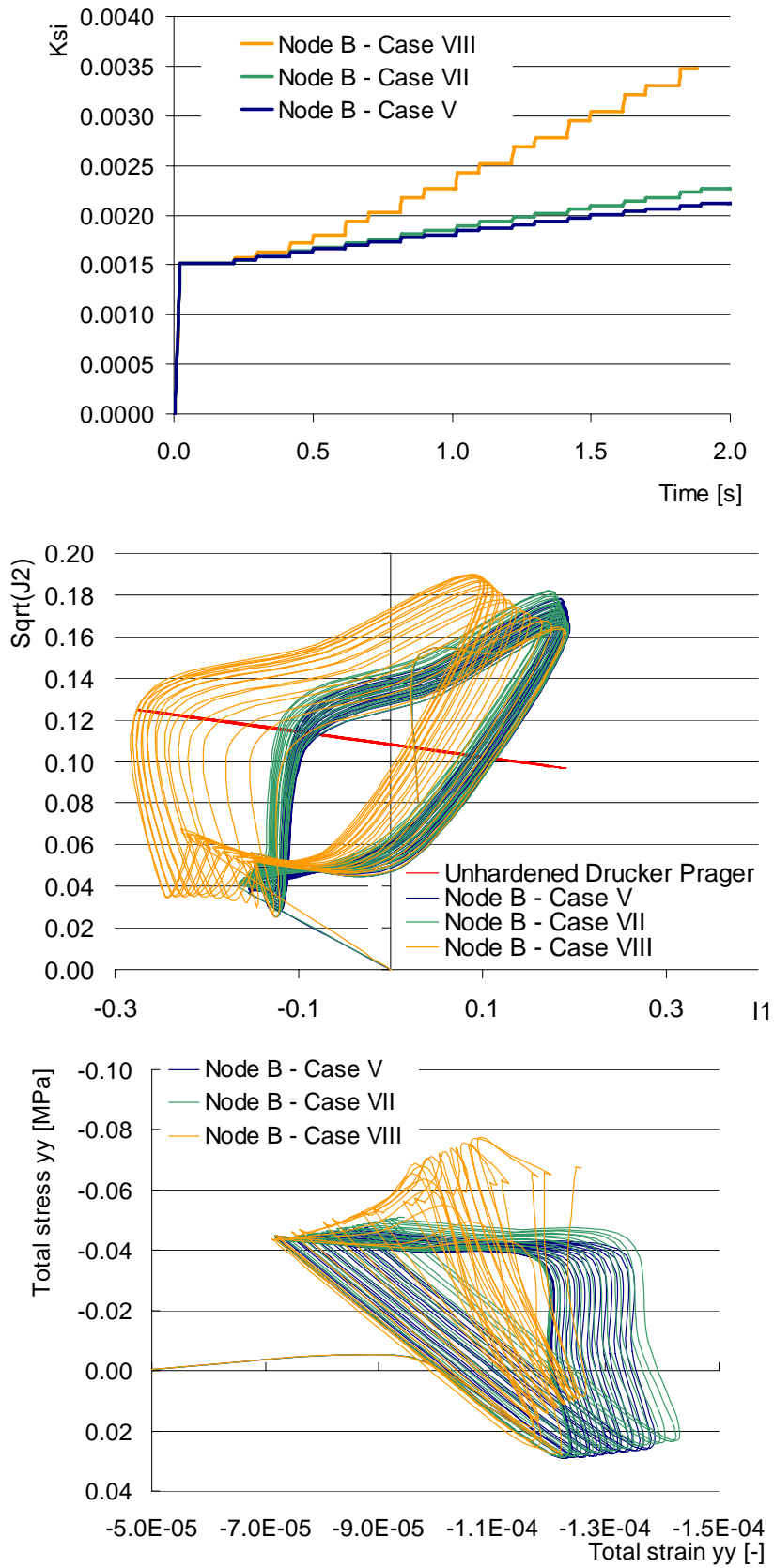


Fig. 9.6.37: Comparison response node B for Case V, VII and VIII

By comparing the equivalent plastic strain, which is generated in Case V through VII, Fig. 9.6.38, it can be seen that for all cases node A and B are most affected by the mastic erosion. This is understandable, since the other nodes are further away from the macro-pore and shall therefore not be exposed to an erosion effect, and node A and B are also exposed to considerable stresses due to the pumping action.

In Case V through VII, damage is most pronounced in nodes C and E, which indicates a combined adhesive and cohesive failure pattern. In Case VIII, for which more severe desorption properties of the mastic were defined, the asphalt shall eventually show most likely a cohesive failure pattern in the mastic between the stones.

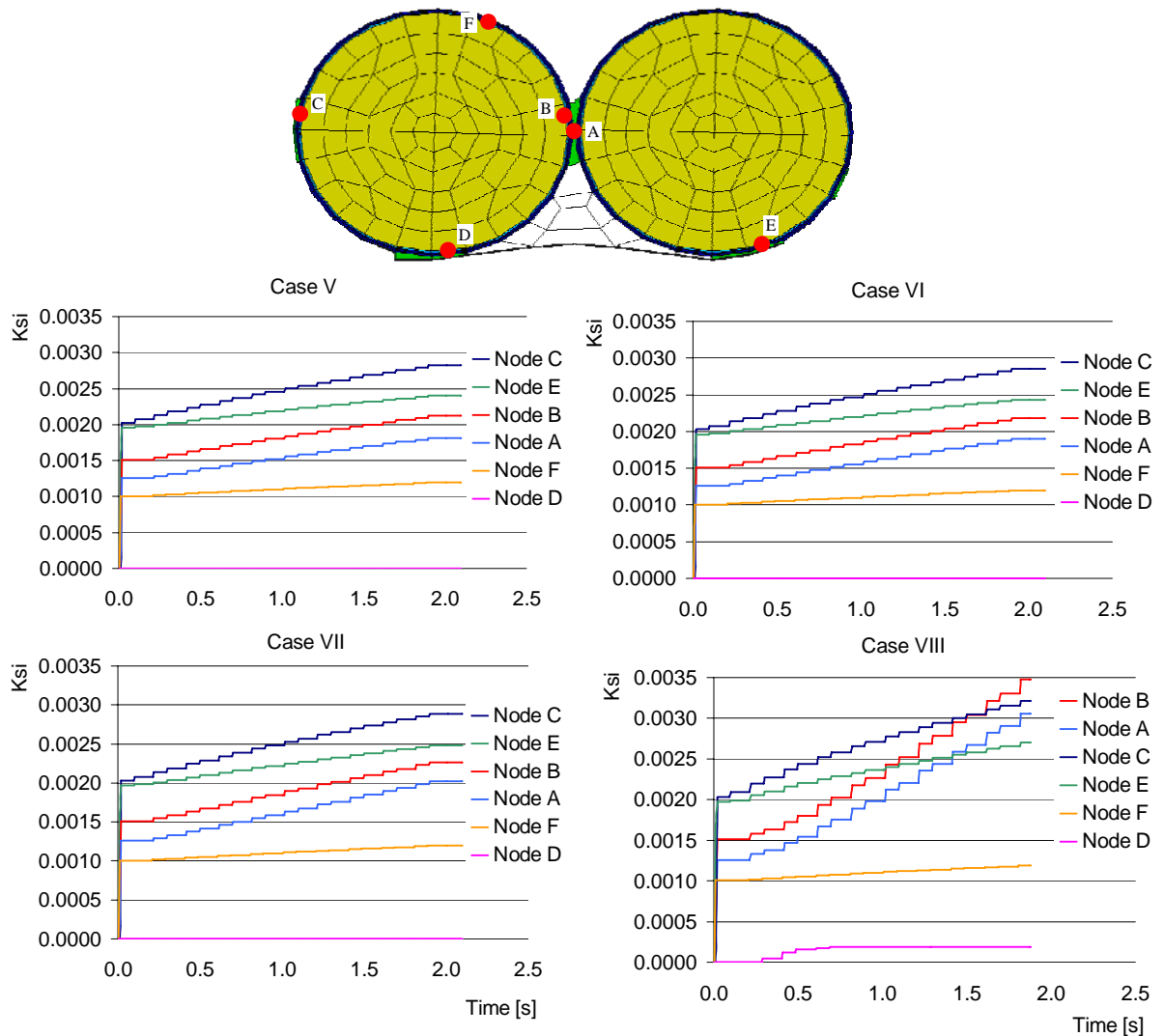


Fig. 9.6.38: Comparison generated equivalent plastic strain ξ for Case V - VIII

In the following, the combined effect of moisture induced damage due to diffusion, erosion and mechanical damage is shown.

Case IX through XII: Moisture induced damage due to diffusion, erosion and mechanical loading.

In Case IX through the combined effect of all the identified moisture induced damage processes is shown. For this, in Case IX the (pumping action) parameters of Case VIII and the (diffusion) parameters of Case II are combined. For Case X through XIII, the (pumping action) parameters of Case VII are combined with the (diffusion) parameters of Case II through Case IV respectively. A summary of the parameters is shown in Table 9.6.7.

In Fig. 9.6.39, Fig. 9.6.40 and Fig. 9.6.41 a comparison is made for the response of node A, C and D, respectively, for Case 0, which is the dry case, Case II, which only included diffusion and Case IX which included all processes. What becomes noticeable in the three figures is that different locations in the asphalt mix get a different impact from the combined damage processes. It seems logical to assume that including more moisture induced damage processes into the analyses would lead to an overall increase in damage.

In the Case of Node A a clear increase in damage can be seen, when comparing the graphs, whereas in the case of node C only a little effect can be seen. In the case of Node D, more equivalent plastic strain was generated in the diffusion only case than in the case which also includes pumping action. A clear explanation can be found in figure Fig. 9.6.31, which shown that the presence of water in the macro-pore absorbs some of the stresses, leading to less deformations in Node D.

It could therefore be concluded that in Case IX a pronounced damage pattern shall start from the mastic between the aggregates, thereby supporting a cohesive failure.

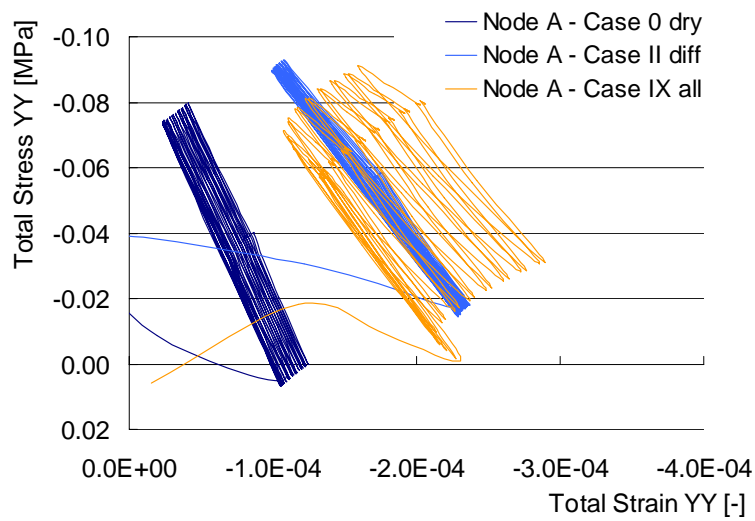
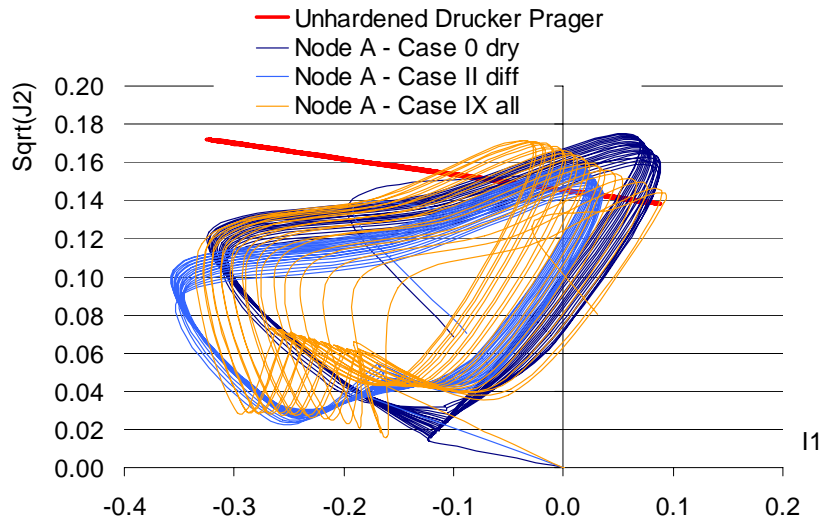
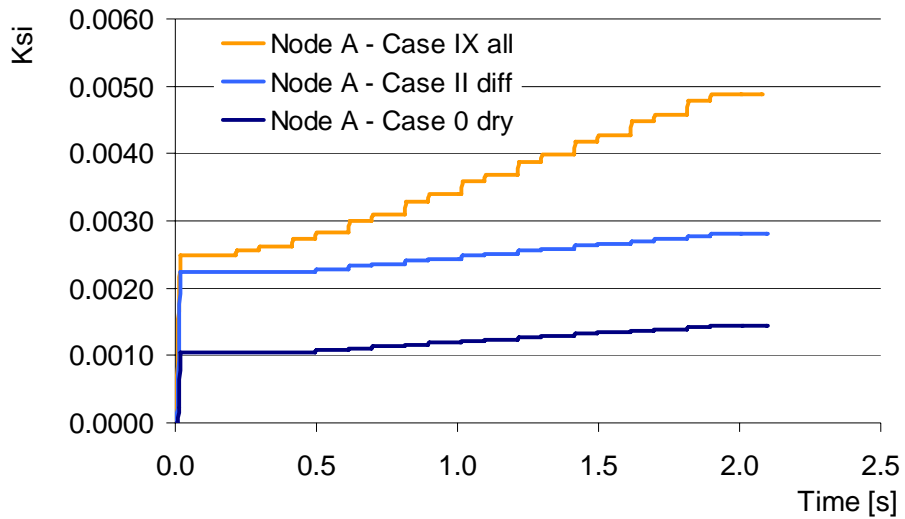


Fig. 9.6.39: Comparison response node A for Case 0 (dry), Case II (diffusion) and Case IX (diffusion & pumping action)

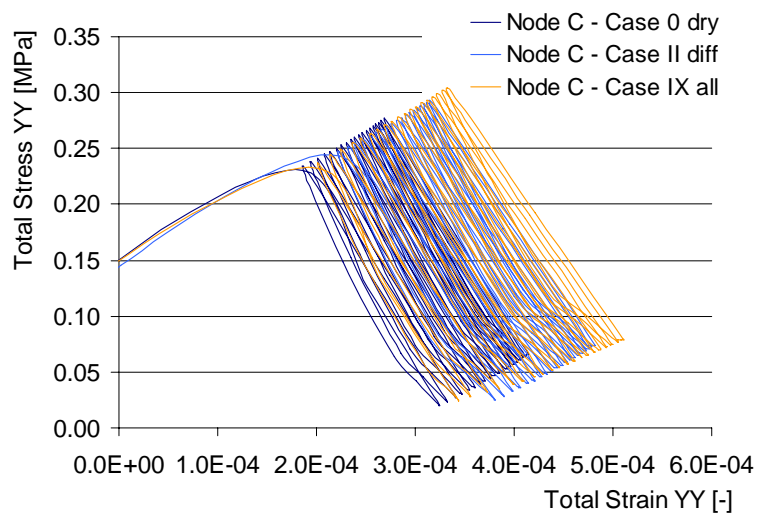
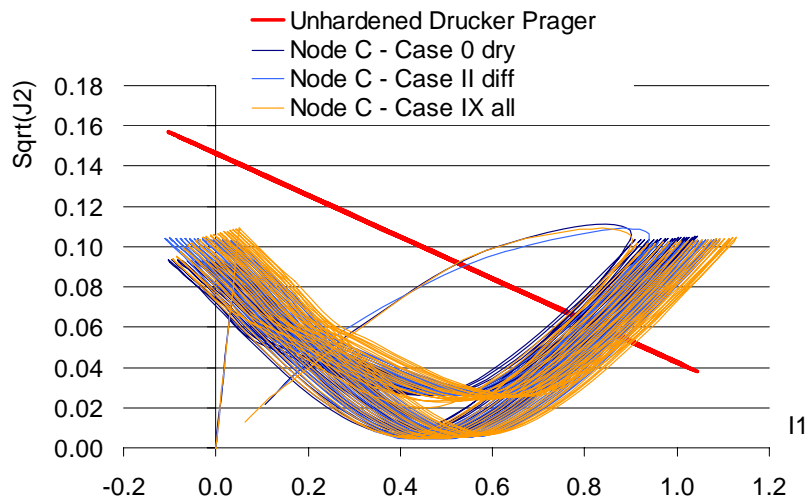
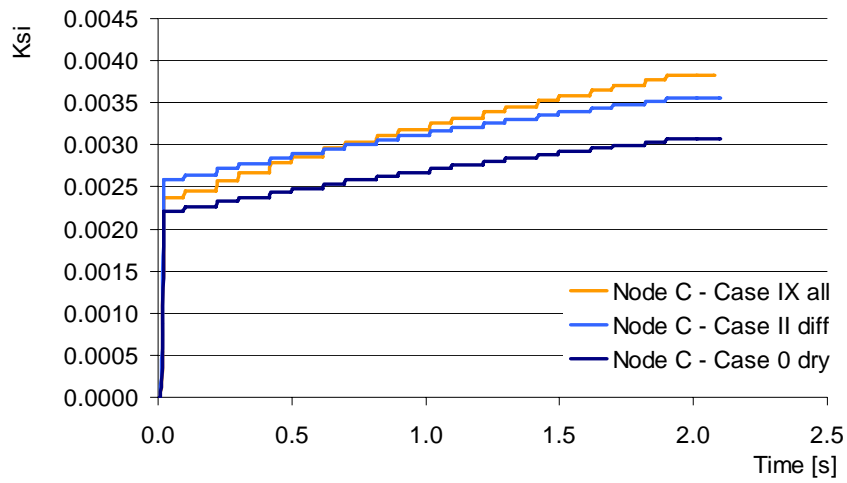


Fig. 9.6.40: Comparison response Node C for Case 0 (dry), Case II (diffusion) and Case IX (diffusion & pumping action)

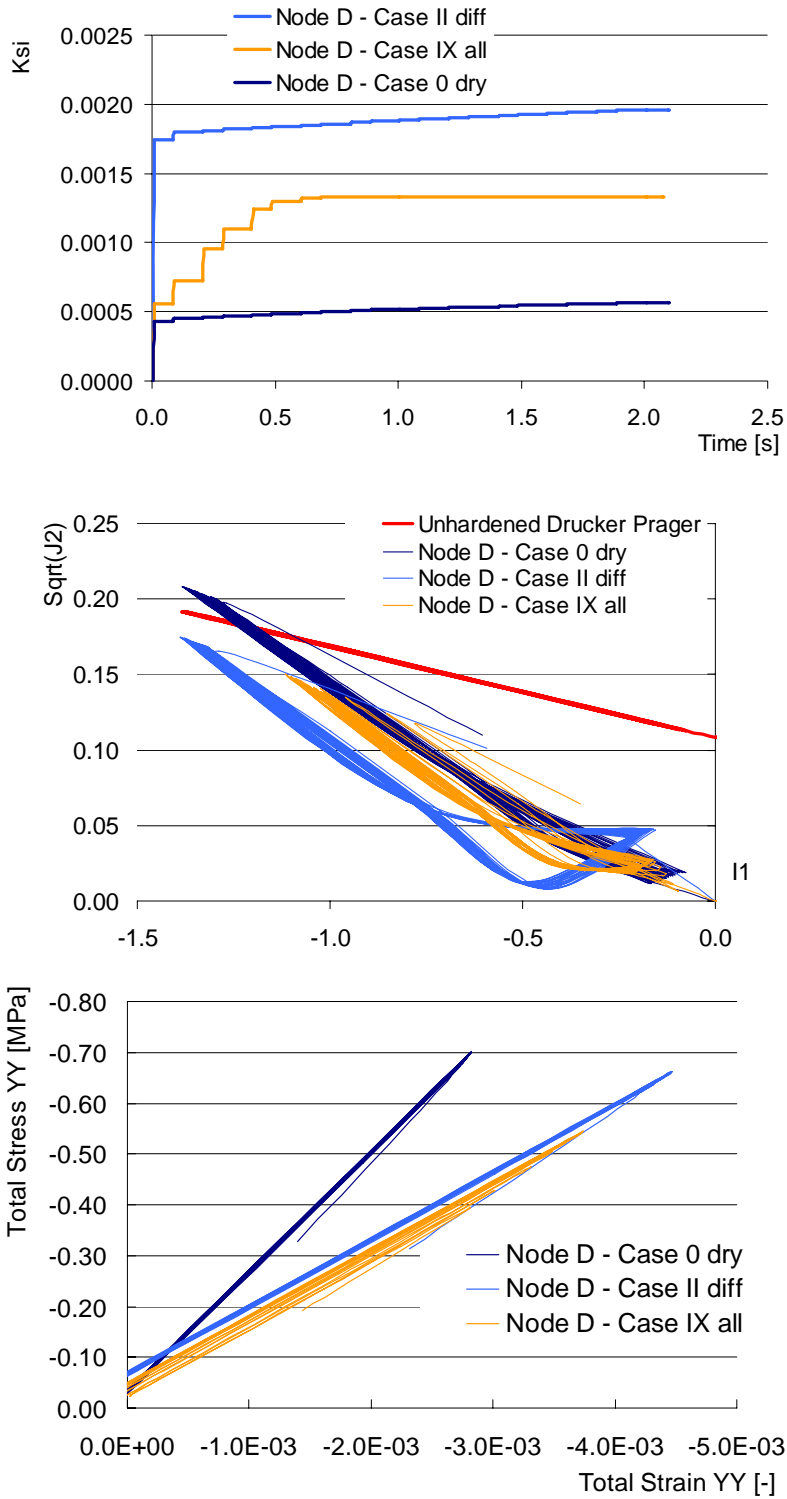


Fig. 9.6.41: Comparison response Node D for Case 0 (dry), Case II (diffusion) and Case IX (diffusion & pumping action)

In Fig. 9.6.42 the overall damage developments for Case IX through XII is compared.

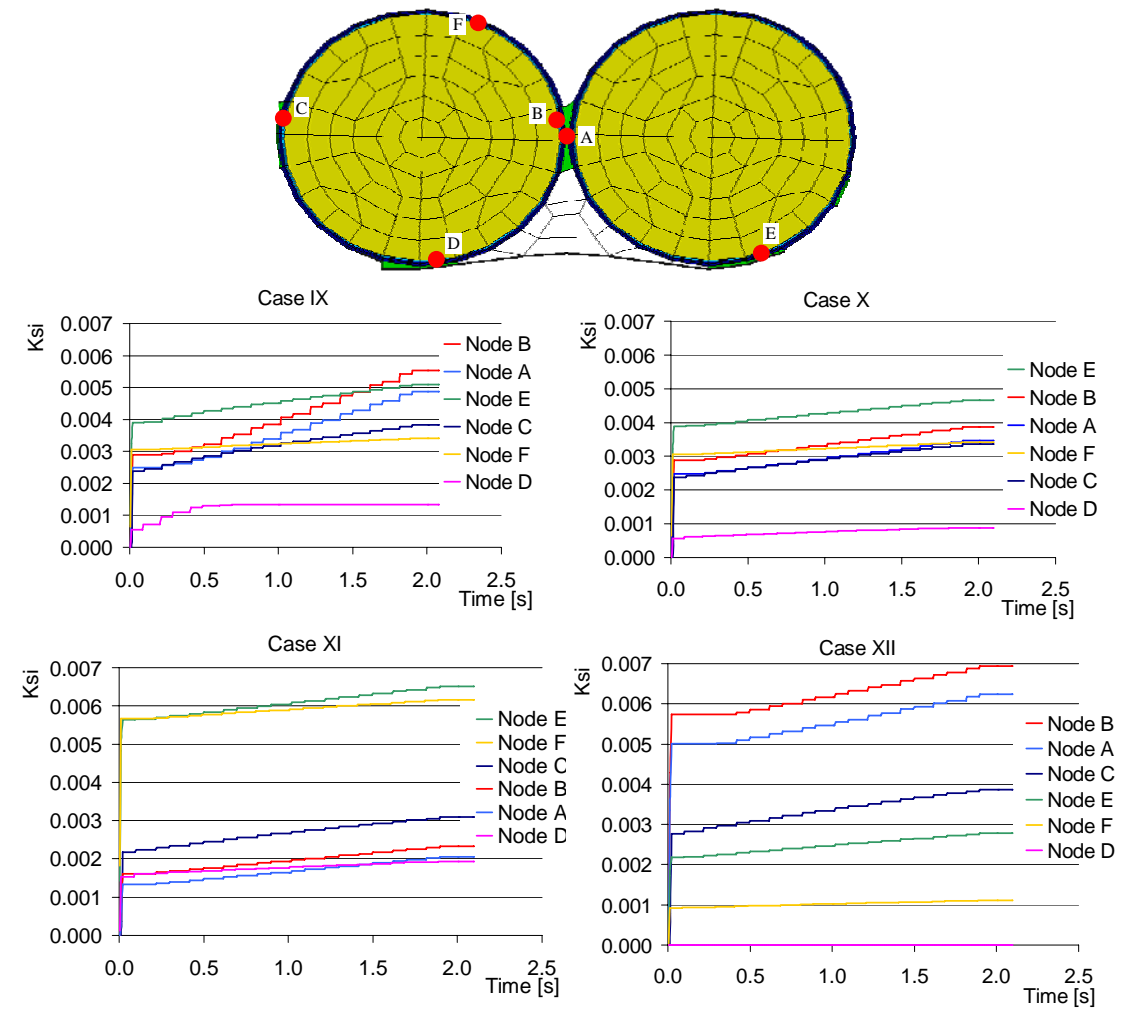


Fig. 9.6.42: Comparison generated equivalent plastic strain ξ for Case IX - XII

It can be seen that for the chosen moisture susceptibility parameters, Case IX and Case XII generate most damage in the mastic and would therefore lead to a pronounced cohesive failure. In Case XI node E and F show an impressive equivalent plastic strain, and comparing to the response in the other nodes, this asphalt would certainly have a pronounced raveling damage. In Case X, even though most damage occurs in Node E, which is in the interface, the other nodes show a similar trend in damage development. This would indicate a combined cohesive-adhesive failure pattern of this mixture.

Similar observations could be made from Fig. 9.6.43.

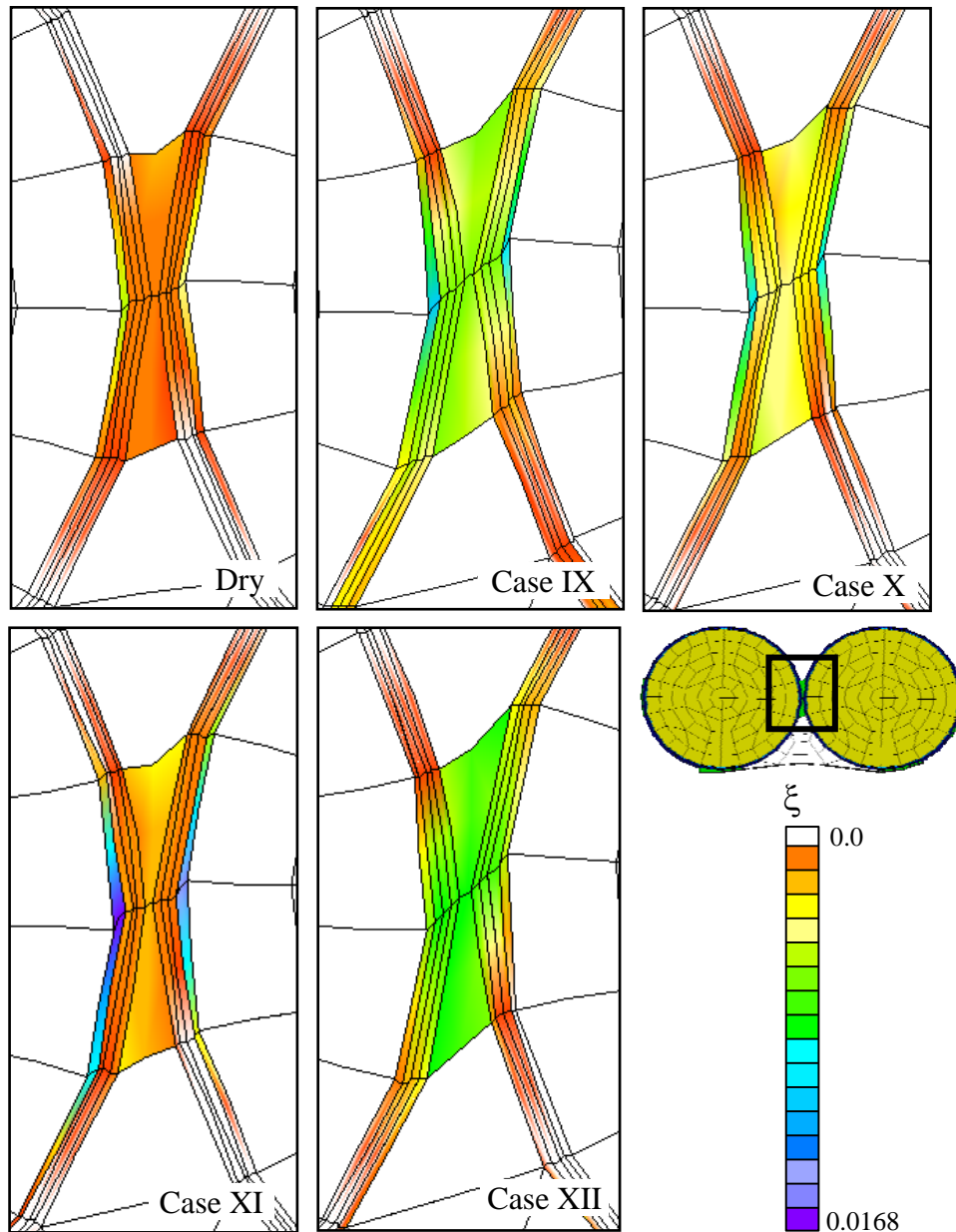


Fig. 9.6.43: Comparison of damage development for Case IX- XII after 10 loading cycles (magn. 300x)

In the above computational cases it has been shown that, depending on the moisture susceptibility and damage parameters, moisture induced damage in an asphaltic mix can occur quite differently. It was shown that unfavorable aggregate-mastic moisture susceptibility will lead to a raveling of the asphalt mix and, likewise, moisture susceptible mastic would lead to damage patterns starting from the mastic. It was also shown that direct access to moisture and fully saturated macro-pores in the asphalt mix can cause a redistribution of stresses, which also contributes to the damage pattern.

Conclusions and Recommendations

The aim of this research was the development of a computational tool for the fundamental analysis of combined mechanical and moisture induced damage of asphaltic mixes which includes both physical and mechanical moisture damage inducing processes. Such a tool will contribute greatly to the understanding of the dominant material parameters which cause moisture induced failures, such as ravelling, and would help in improving material selection procedures.

In this dissertation, physical and mechanical moisture induced damage processes were identified, procedures to determine the controlling parameters were developed, an experimental framework to quantify these parameters was set-up and the numerical tools were developed and demonstrated.

On the basis of these, in the following, conclusions are presented and recommendations are made.

Moisture susceptibility tests:

To assess moisture damage of asphaltic mixes, currently two main categories of moisture susceptibility tests are in use: The classical immersion tests, in which the asphalt/aggregate mixtures are not subjected to mechanical loading while they are exposed to moisture. The second series of test procedures introduce damage in the mastic by applying a load to a saturated mixture specimen.

It has frequently occurred that asphalt mixes pass the first category of tests and fail in the second or visa versa [King 2007]. So far, the reasons for this could not be explained, and as a result, Departments of Transportation (DOT's) would only approve mixes which perform well under the most severe testing conditions, and reject those that do not pass the test or they would only prescribe one set of tests and ignore the other.

Based on the research performed in this dissertation, failure of an asphalt mix when exposed to solely moisture without any mechanical forces can be explained by moisture diffusion into the mix. Failure due to a combined action of moisture infiltration and mechanical loading can also be explained as a combined action of diffusion, erosion and mechanical loading.

Therefore, based on the methodologies developed in this dissertation, it may be concluded that seemingly 'mysterious asphalt failures' can be explained on the basis of a set of material properties: diffusion coefficients, desorption coefficients and damage parameters which relate moisture content and erosion to mechanical weakening (i.e. d_{θ}^{if} , d_{θ}^{mst} and d_{ρ}^{mst} in the context of this dissertation).

It is therefore recommended that, in addition to the standard moisture susceptibility experiments which are currently performed, one starts determining these physical and physio-mechanical parameters. A great benefit of such an approach would be that, instead of rejecting asphalt mixes because they fail an empirical test, one starts understanding which material property should be improved upon. The long-term

benefit of this shall be that, it becomes possible to ‘engineer’ the asphalt mixes, based on fundamental knowledge, rather than empirical speculations. This would change the pavement material selection procedures from a ‘backward looking’ approach to a ‘forward looking’ one, and will lead to better maintenance strategies, longer performing and cost efficient pavements.

Material selection

Based on the research performed in this dissertation, it is concluded that it is important, when selecting the aggregates and bitumen for an asphalt mixture, to keep in mind the following:

- the bitumen should have as low as possible moisture diffusion coefficients;
- the amount of filler of the mastic should be decided on the basis of the mechanical properties of the mastic, the diffusion coefficients of the filler and the bitumen, mastic erosion in the presence of water and mastic moisture damage parameters (d_{θ}^{mst} and $d_{\hat{\rho}}$);
- the aggregate-mastic bond strength should be maximized by keeping the moisture susceptibility parameter α (see Eq. 9.45) as low as possible;
- combinations of mastics with low moisture diffusion coefficients and low moisture susceptible aggregate-mastic bonds should be preferred. However, if the moisture diffusion coefficient of the mastic is low enough, moisture concentrations in the aggregate-mastic interface will never reach critical values, eliminating thus the need for a moisture resistant aggregate-mastic bond;
- it should be avoided at all times to introduce moisture into the mix before and during the time of mixing.
- if the stones were exposed to a moist environment, they should be adequately dried before added to the mix. If moisture is remaining in the stones when it is mixed with the mastic, it can be expected that moisture will diffuse towards the aggregate-mastic interface and may cause a premature debonding, which will result into ravelling;
- it is common practise to add extra components to the asphaltic mix to enhance the performance, such as polymers, phosphoric acids, hydrated lime or liquid anti-stripping agents. Before choosing additives, it should be ensured that by adding them to mix, the fundamental moisture susceptibility parameters are not degraded (diffusion coefficients, desorption coefficients, moisture damage parameters, etc.).

Time scales

In addition to moisture, asphalt pavements are exposed to many other influences which may lead to damage (i.e. settlements, cracks, ageing etc.). It is therefore important in moisture damage susceptibility studies, either purely experimentally orientated ones or computationally based ones, to always take into account the time frame over which moisture damage may be generated in comparison to other failures.

If, for a particular mix, it is concluded that other damage failures are more likely to occur before moisture induced damage becomes an issue, focus should be placed on

improving the dominant material parameters which control these, and less effort should be spent to improve the moisture susceptibility characteristics of the mix.

An estimate of the timeframe over which moisture damage may occur can be found by determining

- the mastic moisture diffusion coefficient,
- the maximum moisture capacity of the mastic,
- the moisture susceptibility of the mastic and the aggregate-mastic bond as a function of moisture concentration and
- the mastic film thickness.

Finally, it can be concluded from the computational analyses that the identified moisture susceptibility parameters can be of paramount importance to the resulting failure pattern. Determination of the dominant moisture susceptibility material parameters which were identified in this research, can lead to better failure predictions and improved asphalt mixtures.

The pavement engineering community, the material suppliers, the road-authorities and the society at large would benefit tremendously from better controllable and longer lasting asphalt pavements. Identifying specific issues, and dedicating focussed research on tackling these, is the only way to come with novel solutions and to progress the industry in a way where all parties involved in developing infrastructural systems can benefit from each others knowledge and put it to practise.

References

- Abson G. and Burton C, *Physical tests and range properties, Bituminous Materials: Asphalts, Tars and Pitches*, Vol.1, Krieger Publishing Compagny, N.Y. 1979
- Airey G., Young-Kyu Choi, State of the Art Report on Moisture Sensitivity Test Methods for Bituminous Pavement Materials, *Journal of Road Materials and Pavement Design*, 2002
- Al-Qadi I, *Pulse Loading Response: Measured vs. 3D Finite Element Analyses*, presentation for the Expert Task Group on Fundamental Properties and Advanced Modeling of Bituminous Materials of the Federal Highway Administration, Arizona, February 2007.
- Anderson D., Dukatz E.L. and Petersen J.C., The Effect of Antistrip Additives on the Properties of Asphalt Cement, *Journal of the Association of Asphalt Paving Technologists*, Vol. 51, 1982
- Atluri S.N., *The Meshless Local-Petrov-Galerkin Method for Domain and DIE Discretization*, Encino: Tech Science Press, 2004
- Baptista A.M., Adams E.E. and Stolzenback K.Dd, The 2-D Unsteady Transport Equation Solved by the Combined Use of the Finite Element Method and the Method of Characteristics, *Proceedings of the 5th International Conference on Finite Elements in Water Resources*, Springer-Verlag, 1984
- Bhasin, A., *Development of Methods to Quantify Bitumen-Aggregate Adhesion and Loss of Adhesion Due to Water*. Ph.D. thesis, Texas A&M University, College Station, Texas, 2006.
- Bathe K., *Finite Element Procedures*, Prentice-Hall, 1996
- Bear J. and Bachmat Y. *Theory and Applications of Transport in Porous Media*, Volume 4, Kluwer Academic Publishers, 1990.
- Bear J., *Dynamics of fluids in porous media*. Elsevier, New York, 1972.
- Belytschko T., Liu W.K. and Moran B., *Nonlinear Finite Elements for Continua and Structures*, John Wiley & Sons, 2001
- Boyce W. and DiPrima R., *Elementary Differential Equations and Boundary Value Problems*, John Wiley & Sons, Sixth Edition, 1997
- Bradbury M.H., Lever D. and Kinsey D., *Aqueous Phase Diffusion in Crystalline Rock, Scientific Basis for Radioactive Waste Management V*, Werner Lutze (edit.), Elsevier, 1982
- Brooks A.N. and Hughes T.J.R., Streamline upwind/Petrov-Galerkin method for advection dominated flows, *Proceedings Third International Conference on Finite Elements in Fluid Flow*, Banff, Canada, 1980
- Carslaw H.S. and Jaeger J.C., *Conduction of heat in solids*, Clarendon Press, Oxford, 1959
- Casulli V., Euler-Lagrangian Methods for Hyperbolic and Convection Dominated Parabolic Problems, *Computational Methods for Nonlinear Problems*, edit. C. Taylor, D.R.J. Owen and E.E.Hinton, Pineridge, 1987
- Casulli V., *Numerical Simulation of Shallow Water Waves, Computational Methods in Surface Hydrology*, edit. G.Gambolati, A. Rinaldo, A. Brebbia, W. Gray and G. Pinder, New York: Springer-Verlag, 1990
- Cheng D., Little D.N., Lytton R. and Holste J.C., Moisture Damage Evaluation of Asphalt Mixtures by Considering Both Moisture Diffusion and Repeated-Load Conditions,

- Transportation Research Record: Journal of the Transportation Research Board*, No. 1832, TRB, NRC, 2003
- Cheng D., Little D.N., Lytton R. and Holste J.C., Use of Surface Free Energy Properties of the Asphalt-Aggregate System to Predict Damage Potential, *Journal of the Association of Asphalt Paving Technologists*, Vol.71, 2002
- Coleman B.D. and Gurtin M., Thermodynamics with Internal Variables, *Journal of Chemical Physics*, Vol. 47, 1967
- Coleman B.D. and Noll W., The Thermodynamics of Elastic Materials with Heat Conduction and Viscosity, *Archives of Rational Mechanics & Analysis*, Vol. 13, 1963
- Copeland A., Kringos N., Youtcheff J. and Scarpas A., Measurement of Aggregate - Mastic Bond Strength in the Presence of Moisture: A Combined Experimental - Computational Study, *Proceedings 86th Transportation Research Board Meeting*, 2007
- Copeland A., Kringos N., Scarpas A. and Youtcheff J., Determination of Bond Strength as a Function of Moisture Content at the Aggregate-Mastic Interface, *Proceedings 10th Conference of the International Society for Asphalt Pavement (ISAP)*, 2006.
- Copland J.S., Epps J.A. and Quilici L., Anti-strip Additives: Background for a Field Performance Study, *Transportation Research Record: Journal of the Transportation Research Board* 1115, 1987
- Crank J., *The Mathematics of Diffusion*, Oxford Science Publication, second edition, 1975.
- Curtis C.W., Ensley K. and Epps J., *Fundamental Properties of Asphalt Aggregate Interactions Including Adhesion and Adsorption*, SHRP A-003B, 1991
- Curtis C.W., Ensley K. and Epps J., *Fundamental Properties of Asphalt Aggregate Interactions Including Adhesion and Adsorption*, SHRP A-341,1993
- Davidson D. and Ernyes J., Stripping: a Laboratory Study, *Proceedings of the Canadian Technical Asphalt Association*, Vol. 38, 1993
- Douglas J and Ruseel T., Numerical Methods for Convection Dominated Diffusion Problems Based on Combining the Method of Characteristics with Finite Element of Finite Difference Procedures, *SIAM Journal Numerical Analyses*, Vol. 19, 1982
- Epps J.A., *Compatibility of a Test for Moisture-Induced Damage with Superpave Volumetric Mix Design*, NCHRP 444, TRB, 2000
- Erkens S. Raveling in the Netherlands. *Proceedings of the International Workshop on Moisture Induced Damage of Asphaltic Mixes*, ISBN-13: 978-90-816396-1-1, 2005
- Erkens S., *Asphalt Concrete Response: Determination, Modeling and Prediction*, ISBN: 90-407-2326-5, 2002
- Fini E., Discussion on work of adhesion to determine moisture susceptibility of AC, *Journal of Association of Asphalt Paving Technologists*, 2006, Vol. 75.
- Franca L.P., Hauke G. and Masud A., Revisiting stabilized finite element methods for the advective-diffusive equation, *Computational Methods in Applied Mechanics and Engineering*, 2005
- Fromm H.J., The Mechanism of Asphalt Stripping from Aggregate Surfaces, *Journal of the Association of Asphalt Paving Technologists*, Vol.43, 1979
- Fwa T.F. and Ong B.K., Effect of Moisture in Aggregates on Performance of Asphalt Mixtures, *Transportation Research Record: Journal of the Transportation Research Board* 1454, NRC, 1994
- Galeati G., Gambolati G. and Neuman S.P., Coupled and Partially Coupled Eulerian-Lagrangian Model of Freshwater-Seawater Mixing, *Water Resources Research*, 28, 1992

- Ganzha V.G. and Vorozhtsov E.V., *Computer Aided Analysis of Difference Schemes for Partial Differential Equations*, New York: Wiley, 1998
- Graf P., Factors Affecting Moisture Susceptibility of Asphalt Concrete Mixtures, *Journal of the Association of Asphalt Paving Technologists*, Vol.55, 1986
- Harman T., *Development of a National Asphalt Roadmap*, presentation FHWA Expert Task Group Meeting, Illinois, October 2006
- Heinrich J.C. Huyakorn P.S. and Zienkiewicz C., An Upwind Finite Element Scheme for Two Dimensional Convective Transport Equation, *International Journal for Numerical Methods in Engineering*, Vol 11, 1977
- Hicks R.G., *Moisture Damage in Asphalt Concrete*, NCHRP Synthesis of Highway Practice 175, TRB, NRC, 1991
- Holzaphel G., *Nonlinear Solid Mechanics: A Continuum Approach for Engineering*, John Wiley & Sons, 2001
- Huber G. Tenderness Caused by Moisture, *Proceedings of the International Workshop on Moisture Induced Damage of Asphaltic Mixes*, ISBN-13: 978-90-816396-1-1, 2005
- Hughes T., *The Finite Element Method: Linear and Static Dynamic Finite Element Analysis*, Dover Publications, 1987
- Huyakorn P.S. and Pinder G.F., *Computational Methods in Subsurface Flow*, Academic Press, 1983.
- Ishai I. and Craus J., Effect of Filler on Aggregate-Bitumen Adhesion Properties in Bituminous Mixtures, *Journal of the Association of Asphalt Paving Technologists*, Vol. 41, 1972
- Kachanov L.M., *Introduction to Continuum Damage Mechanics*, Martinus Nijhoff Publishers, Dordrecht, 1986
- Kandhal P., Field and Lab Investigation of Stripping in Asphalt Pavements: State-of-the-Art, *Transportation Research Record: Journal of the Transportation Research Board* 1454, NRC, 1994
- Kandhal P., *Moisture Susceptibility of HMA Mixes: Identification of Problem and Recommended Solutions*, NCAT Report 92-1, 1992
- Kandhal P., Premature Failure of Asphalt Overlays from Stripping: Case Histories, *Journal of the Association of Asphalt Paving Technologists*, Vol. 70, 2001
- Kandhal P., The New Generation Open-Graded Asphalt Friction Courses, *Journal of Public Works*, Vol.132, No.13, 2001
- Kanitpong K. and Bahia H., Role of Adhesion and Thin Film Tackiness of Asphalt Binders in Moisture Damage of HMA, *Journal of the Association of Asphalt Paving Technologists*, Vol. 72, 2003
- Kasbergen C and Scarpas A, *Development of a General 3D Contact Algorithm to Model Tire-Pavement Interaction*, Proceedings of the International Conference on Advanced Characterisation of Pavement and Soil Engineering Materials, June 2007, Athens, Greece
- Kennedy T.W. and Ping W.V., Comparison Study of Moisture Damage Test Methods for Evaluating Antistripping Treatments in Asphalt Mixtures, *Transportation Research Record: Journal of the Transportation Research Board*, No. 1323, NRC, 1991
- Khosla N., Birdsall B. and Kawaguchi S., Evaluation of Moisture Susceptibility of Asphalt Mixtures: Conventional and New Methods, *Transportation Research Record: Journal of the Transportation Research Board*, No. 1728, NRC, 2000

- Kiggundu B.M. and Roberts F.L., *Stripping in HMA Mixtures: State-of-the-Art and Critical Review of Test Methods*, NCAT Report No. 88-2, 1988
- King G, Discussion on moisture susceptibility characterization procedures, *Journal of the Association of Asphalt Paving Technologists*, Vol. 76, 2007
- Kinzelbach W., *Methods for the Simulation of Polutant Transport in Groundwater, Proceedings of the Conference on Solving Groundwater Problems with Models*, Colorado, 1987
- Kringos N. and Scarpas A. Simulation of Combined Mechanical-Moisture Induced Damage in Asphaltic Mixes, *Proceedings of the International Workshop on Moisture Induced Damage of Asphaltic Mixes*, ISBN-13: 978-90-816396-1-1, 2005
- Kringos N. and Scarpas A., Development of a Finite Element Tool for Simulation of Raveling of Asphalt Mixes, *Proceedings of the 12th International Conference on Computational and Experimental Engineering and Sciences*, Tech Science Press, 2004.
- Kringos N. and Scarpas A., Raveling of asphaltic mixes: Computational identification of controlling parameters, *Transportation Research Record: Journal of the Transportation Research Board*, No. 1929: 79-87, 2005
- Kringos N. and Scarpas A., Ravelling of asphaltic mixes: Computational identification of controlling parameters., *Transportation Research Record: Journal of the Transportation Research Board*, No. 1929, Bituminous Paving Mixtures 2005, p.79-87
- Kringos N. and Scarpas A., Simulation of Combined Mechanical-Moisture Induced Damage in Asphaltic Mixes, *Proceedings of the International Workshop on Moisture Induced Damage of Asphaltic Mixes*, Delft, 2005
- Kringos N. and Scarpas A.. Numerical Simulation of the Physical Processes Inducing Moisture Damage in Asphaltic Mixes, *Proceedings 10th Conference of the International Society for Asphalt Pavement (ISAP)*, 2006.
- Kringos N., Scarpas A and Kasbergen C., Three Dimensional Elasto-Visco-Plastic Finite Element Model for Combined Physical-Mechanical Moisture Induced Damage in Asphaltic Mixes, *Journal of the Association of Asphalt Paving Technologists*, Vol. 76, 2007
- LeVeque R.J., *Numerical Methods for Conservation Laws*, Basel-Birkhauser Verlag, 1992
- Little D.N. and Epps J.A., The Benefits of Hydrated Lime in Hot Mix Asphalt, *National Lime Association*, 2001
- Little D.N. and Jones IV D.R., Chemical and Mechanical Processes of Moisture Damage in Hot-Mix Asphalt Pavements, *Proceedings of the Moisture Sensitivity of Asphalt Pavements - - a National Seminar*, TRB, California, 2003
- Liu X., *Numerical Modelling of Porous Media Response under Static and Dynamic Load Conditions*, Delft University of Technology, 2003, ISBN: 90-9017195-9
- Lobo Ferreira J., A Comparative Analysis of Mathematical Mass Transport Codes for Groundwater Pollution Studies, *Groundwater Flow and Quality Modelling*, 1987
- Lottman R., Laboratory Test System for Prediction of Asphalt Concrete Moisture Damage, *Transportation Research Record: Journal of the Transportation Research Board*, No. 515, NRC, 1974
- Lottman R.P. and Brejc S., Moisture Damage Cutoff Ratio Specifications for Asphalt Concrete, *Transportation Research Record: Journal of the Transportation Research Board*, 1269, 1990
- Lytton R., *Mechanics and Measurement of Moisture Damage*, *Proceedings of Moisture Damage Symposium*, WRI, Wyoming, July 2002

- Lytton, R.L., Masad, E., Zollinger, C., Bulut, R., and Little, D.N., *Measurements of Surface Energy and Its Relationship to Moisture Damage*. Technical Report, Project FHWA/TX-05/0-4524-2, 2005 (Texas Transportation Institute: College Station).
- Majidzadeh K and Brovold F., *State-of-the-Art: Effect of Water on Bitumen-Aggregate Mixtures*, HRB Special Report No. 98, 1968
- Masad E., Lytton R. and Little D., Moisture Induced Damage in Asphaltic Mixes, In: *Proceedings of the International Workshop on Moisture Induced Damage of Asphaltic Mixes*, ISBN-13: 978-90-816396-1-1, 2005
- Masad, E., Zollinger, C., Bulut, R., Little, D., and Lytton, R., Characterization of HMA Moisture Damage Using Surface Energy and Fracture Properties. *Journal of the Association of Asphalt Paving Technologists*, 2006b, 75, 713-754.
- Maupin G.W., *Laboratory Investigation of Hydrated Lime as an Anti-Stripping Additive*, FHWA Report No. VA84-14, 1983
- Mcgennis R.B., Kennedy T.W. and Machemehl R., *Stripping and Moisture Damage in Asphalt Mixtures*, FHWA Report TX 85, Dept. Of Highways and Public Transportation, Texas, 1984
- Milne T, *Towards a performance related seal design method for bitumen and modified seal binders*, PhD dissertation, University of Stellenbosch, 2004
- Molenaar J.M.M., *Evaluatie van ZOAB op knooppunten*, DWW-2006-003, Ministerie van Verkeer en Waterstaat, februari 2006 (in Dutch)
- Morton K.W., *Numerical Solutions of Convection-Diffusion Problems*, London: Chapman and Hall, 1996
- Neuman S.P., A Eulerian-Lagrangian Numerical Scheme for the Dispersion-Convection Equation Using Conjugate Space-Time Grids, *Journal of Computational Physics*, 41, 1981
- Neuman S.P., Adaptive Eulerian-Lagrangian finite element method for advection-dispersion, *International Journal of Methods in Engineering*, 20, 1984
- Nguyen T., Byrd W., Bentz D and Seiler J.Jr., *Development of a Technique for In Situ Measurement of Water at the Asphalt/Model Siliceous Interface*, SHRP report NISTIR 4783, 1992
- Nguyen T., and Byrd E., *Development of a Method for Measuring Water-Stripping Resistance of Asphalt/Siliceous Aggregate Mixtures*, IDEA Program, NCHRP-ID002, Transportation Research Board, National Research Council:1-31,1996
- Press W. et.al., *Numerical Recipes: The Art of Scientific Computing*, Cambridge University Press, 1989
- Quarteroni A. and Valli A., *Numerical Approximations of Partial Differential Equations*, Berlin: Springer, 1997
- Reese S., and Govindjee S., A Theory of Finite Viscoelasticity and Numerical Aspects, *Int. J. Solids and Structures*, 1998, Vol. 35, pp. 3455–3482.
- Rice J.M., *Relationship of Aggregate Characteristics to the Effect of Water on Bituminous Paving Mixtures*, ASTM STP No. 240, 1958
- Riedel W. and Weber H., *On the Adhesiveness of Bituminous Binders on Aggregates, Asphalt and Teer*, 1953
- Scarpas A., *CAPA-3D Finite Element System Users Manual I, II and III*, a Delft University of Technology Publication, 2000
- Scarpas A., Kasbergen C. and Kringos, N. Course Notes, *International Course on Advanced Constitutive Modeling of Asphaltic Materials*, January 2005(a), Maryland, USA

- Scarpas A., *A Mechanics based Computational Platform for Pavement Engineering*, ISBN 90-9019040-6, 2005(b)
- Scarpas A., Kasbergen, C. and Kringos, N. Energy based, *Three Dimensional Elasto-Visco-Plastic Constitutive Model for Asphalt Concrete Response*, Research Progress Report, Section of Structural Mechanics, Faculty of Civil Engineering and Geosciences, Delft University of Technology, June 2006(a), p.73.
- Scarpas A., *Micro-Mechanical Modeling of Large Deformations and Texture Evolution in Stone-Based Infrastructure Materials*, NSF Workshop on Micromechanics of Stone Based Infrastructure Materials, October 2006(b), Virginia, USA
- Scholz T.V., Terrel R.L., Al-Joaib A. and Bea J., *Water Sensitivity: Binder Validation*, Report SHRP-A-402, NRC, 1993
- Scott J.A., Adhesion and Disbonding Mechanisms of Asphalt Used in Highway Construction and Maintenance, *Journal of the Association of Asphalt Paving Technologists*, Vol. 47, 1978
- Selvadurai A.P.S. and Dong W., A Taylor-Galerkin Approach for Modelling a Spherically Symmetric Advective-Dispersive Transport Problem, *Communications in Numerical Methods in Engineering*, 2006
- Selvadurai A.P.S. and Dong W., A Time Adaptive Scheme for the Solution of the Advective Equation in the Presence of a Transient Flow Velocity, *Computer Methods in Engineering and Science*, Vol.1, no.1., 2000
- Selvadurai A.P.S. and Dong W., The Numerical Modelling for Advective Transport in the Presence of Fluid Pressure Transients, *International Journal for Numerical and Analytical Methods in Geomechanics*, Vol. 29, 2005
- Selvadurai A.P.S., *Calibration of Computational Schemes for Solving Advective Transport Processes*, in preparation
- Selvadurai A.P.S., *Partial Differential Equations in Mechanics*, Vol 1 & 2 Berlin: Springer-Verlag, 2000
- Smith H.A., *Performance of Open Graded Friction Courses*, NCHRP Synthesis of Highway Practice 180, TRB, NRC, 1992
- Stuart K., *Moisture Damage in Asphalt Mixtures- State-of-the-art*, Report FHWA-RD-90-019, FHWA, VA 22101-2296, 1990
- Takerkhani H., *Experimental Characterisation of the Compressive Permanent Deformation Behaviour in Asphaltic Mixtures*, University of Nottingham, Department of Civil Engineering, 2006
- Takkalou H.B., Stripping of Asphalt Pavements: State-of-the-Art, *Transportation Research Record: Journal of the Transportation Research Board*, 84-6, 1984
- Taylor M.A. and Khosla N.P., Stripping of Asphalt Pavements: State-of-the-Art, *Transportation Research Record: Journal of the Transportation Research Board*, 911, 1983
- Terrel R.L. and Al-Swailmi S., *Water Sensitivity of Asphalt-Aggregate Mixes-Test Selection*, SHRP-A-403, 1994
- Thelen E., *Surface Energy and Adhesion Properties in Asphalt-Aggregate Systems*, HRB Bulletin 192, 1958
- Thunqvist E.L., Long Term Effects of Deicing Salt on the Roadside Environment: Part II: Groundwater and Surface Water, *Proceedings of the 9th Maintenance Management Conference*, Alaska, 2001
- Tunniclif D.G., Performance of Antistripping Additives, *Journal of the Association of Asphalt Paving Technologists*, Vol. 66, 1997

Wei, J. and Youtcheff, J. Ongoing research to determine moisture diffusion coefficients of asphalt binders, *FHWA internal report*, Jan 2007

Wang Y. and Hutter, K., Comparisons of Numerical Methods With Respect to Convectively Dominated Problems, *International Journal Numerical Methods Fluids*, Vol. 37, 2001

White T.D., Stripping in HMA Pavements, *Hot Mix Technology*, 1987

Youtcheff J. and Aurilio V., Moisture Sensitivity of Asphalt Binders: Evaluation and Modeling of the Pneumatic Adhesion Test Results, *42nd Annual Conference of Canadian Technical Asphalt Association*, Ottawa, Ontario, Polyscience Publications Inc., 1997

Zollinger, C., *Application of Surface Energy Measurements to Evaluate Moisture Susceptibility of Asphalt and Aggregates*. MSc Thesis, Texas A&M University, College Station, Texas, 2005.

Summary

Moisture induced damage in asphaltic mixes is recognized as a major issue, resulting to the need for frequent maintenance operations. This does not only imply high maintenance costs, but also temporary closure of traffic and hence increased road congestion. Given the high costs for the road authorities and the inconvenience for the road users, it is greatly desired to shift the solution from a repair philosophy to a prevention one.

Moisture induced damage in asphalt can not be solved by mechanical considerations alone. Clearly, our current asphalt wearing surfaces show that moisture has an effect on the material characteristics of the asphalt components and their bond. This implies that moisture makes a physical change to the material, which exhibits itself in the early development of damage patterns which, without the moisture, may have not occurred or may have occurred in a much later stage of its service life.

The aim of this dissertation is the development of a computational tool for the fundamental analysis of combined mechanical and moisture induced damage of asphaltic mixes which includes both physical and mechanical moisture damage inducing processes. Such a tool can greatly contribute to an improved material selection procedure and give insight into the various competing damage inducing processes within the asphalt mix.

To achieve this aim, the physical and mechanical moisture induced damage processes were identified, procedures to determine the controlling parameters were developed, an international experimental framework to quantify these parameters was set-up and numerical tools were developed and demonstrated in this dissertation.

From the numerical simulations it becomes clear that it is very important to know the moisture susceptibility parameters of the components of the mix, and the moisture susceptibility of its bond. It was shown that, for different parameters, completely different damage patterns may occur in the asphalt.

Based on the phenomena that were demonstrated in this thesis, it is therefore highly recommended that from purchase time on, the asphalt engineering community starts determining:

- the moisture diffusion coefficients of the aggregates and the mastic and the moisture capacity the materials can hold;
- the changing material response, in time, as a function of moisture content;
- the bond strength of the aggregate-mastic combinations, with and without moisture;
- the loss of concentration of the mastic, in the presence of high water pressures.

A better awareness of the fundamental material properties of the asphalt components will not only contribute to improving the currently produced asphalt mixes, but will assist the development of better, new mixes which come with their own well-defined maintenance schedule.

The pavement engineering community, the material suppliers, the road-authorities and the society at large would benefit tremendously from better controllable and longer lasting asphalt pavements. Identifying specific issues, and dedicating focussed research on tackling these, is the only way to come with novel solutions and to progress the industry in a way where all parties involved in developing infrastructural systems can benefit from each others knowledge and put it to practise.

Waterschade in asfaltmengsels is een belangrijke schadepost die bijdraagt aan de frequente onderhoudsacties die uitgevoerd moeten worden aan de asfaltdeklagen. Dit resulteert niet alleen in hoge onderhoudskosten maar ook in een toename van de filevorming omdat de wegen vaak afgesloten moeten worden. Het is daarom van groot belang voor zowel Rijkswaterstaat als de weggebruikers om deze reparatie filosofie om te zetten in een schadepreventiefilosofie.

Waterschade in asfalt kan niet alleen opgelost worden met mechanische overwegingen. Het blijkt duidelijk uit de schade aan de weglagen dat water een effect heeft op de materiaaleigenschappen van de asfaltcomponenten en hun binding. Dit impliceert dat vocht een fysische verandering van het materiaal tot stand brengt, die zichzelf uit in vroegtijdige schadevorming die zonder de aanwezigheid van water nooit of pas veel later opgetreden was.

Het doel van deze dissertatie was de ontwikkeling van een eindige elementen programma voor de fundamentele analyse van mechanisch-fysische waterschade in asfaltmengsels. Een dergelijk programma kan een grote bijdrage betekenen voor het ontwikkelen van verbeterde materiaalselectieprocedures voor de industrie en het verkrijgen van inzicht in de verschillende concurrerende schadeprocessen die zich binnen het asfalt kunnen afspelen.

Om dit computerprogramma te kunnen ontwikkelen, zijn verscheidene fysische en mechanische schadeprocessen geïdentificeerd, zijn procedures ontwikkeld waarin de dominante materiaalparameters bepaald kunnen worden, is een internationaal experimenteel netwerk opgezet voor het bepalen van deze parameters en zijn de eindige-elementenroutines ontwikkeld die in deze dissertatie gedemonstreerd worden.

Uit de numerieke simulaties wordt het duidelijk dat het van groot belang is om de waterschadegevoeligheidsparameters te bepalen van alle individuele asfaltcomponenten. Het is gedemonstreerd, dat voor verschillende waterschade gevoeligheidsparameters, compleet andere schadebeelden kunnen optreden

Uit dit onderzoek komt duidelijk naar voren dat het zeer aan te raden is om vanaf het begin van de aankoop van de individuele componenten van de asfaltmengsels, de volgende parameters te bepalen:

- de vochtdiffusiecoëfficiënten en de maximale vochtopnamecapaciteit van de aggregaten en de mastiek;
- het veranderende materiaalgedrag in de tijd, als een functie van de vochthoeveelheid;
- de bindingssterkte van de verscheidene aggregaat-mastiek combinaties, met en zonder de aanwezigheid van vocht;
- het verlies van massaconcentratie van de mastiek, in de aanwezigheid van hoge waterdrukken.

Een verbeterd bewustzijn van de fundamentele materiaaleigenschappen van de asfaltcomponenten zal niet alleen bijdragen aan de ontwikkeling van verbeterde materiaalselectieprocedures, maar zal tevens assisteren in de ontwikkeling van

verbeterde, nieuwe asfaltmengsels die hun eigen goedgedefinieerde onderhoudsbeschrijving met zich meedragen.

De wegbouwkunde wereld, de asfaltproducenten, Rijkswaterstaat en de maatschappij als geheel zal veel profijt hebben van beter controleerbare and langer houdbare asfaltwegen. Het identificeren van kritieke problemen en deze opdragen als onderzoeksvraagstukken aan gespecialiseerde wetenschappers, is de enige mogelijkheid om in de toekomst met innovatieve oplossingen te komen, om de industrie op een hoger niveau te brengen, waar alle partijen kunnen profiteren van ieders specifieke kennis en deze oplossingen daadwerkelijk in de praktijk kunnen brengen.

Curriculum Vitae

Name	Nicole Kringos
1979	Born in Utrecht, the Netherlands
1998	Propedeuse degree in Civil Engineering, TU Delft
1999 - 2000	Geotechnical Staff Member, Fugro Engineersbureau bv, Leidschendam
2000	First Dutch Civil Engineering degree, TU Delft
2000 - 2001	Erasmus exchange student, Department of Geodynamics, National Technical University of Athens, Greece
2003	Master of Science in Civil Engineering (Cum Laude), TU Delft Specialization: Structural Mechanics
2003	Junior researcher Section of Structural Mechanics, Faculty of Civil Engineering and Geosciences, TU Delft
may 2003...	PhD candidate Section of Structural Mechanics, Faculty of Civil Engineering and Geosciences, TU Delft

Awards

2003	Cum Laude Master of Science in Civil Engineering
2006	PhD award Association of Asphalt Paving Technologists